UNIVERSITY OF SOUTHAMPTON

Faculty of Engineering and the Environment

The Effects of Random Vibration on the Dimensional Stability of Space-Based Precision Structures

by

Ruben Edeson

Thesis for the degree of Doctor of Philosophy

July 2012

ABSTRACT

Low-cost Earth-imaging instruments typically require high performance structures to ensure that critical alignments of optical components are maintained between the assembly phase, and the on-orbit operational phase. There are a number of threats to structural dimensional stability, including thermal cycling, moisture desorption and launch vibrations.

This last area is the subject of this thesis. The main aim of the research described here is to better understand the effects of random vibration on the dimensional stability of precision structures.

The first part of this research considered the degree to which random vibration is a problem - this was assessed by comparing its effects on dimensional stability with those of other typical environmental stressors. This was accomplished by performing a series of environmental tests on an optical breadboard structure, and measuring the dimensional stability throughout.

These tests showed that random vibration could indeed pose a significant threat. The second part of the research aimed to better understand the dimensional stability response of specific structural elements - namely materials and bolted joints - to random vibration. This required the development of novel test setups and metrology techniques. Controlled tests were performed in both these structural areas, and a number of useful conclusions were drawn.

The final part of the research was to investigate the empirical results using FEA methods. A significant challenge was to develop a modelling technique that is capable of predicting dimensional stability responses to random vibration. In the case of the material tests, the response of the test samples was correctly predicted using FEA with cyclic plasticity properties and parameters identified from static tests.

This research has produced a number of relevant findings for space-based stable optical bench structures. These have been condensed into a series of recommendations for design, analysis, testing, metrology and bedding-in vibration for future optical payload projects.

Contents

List of Figures

DECLARATION OF AUTHORSHIP

I, Ruben Edeson

declare that the thesis entitled

“The Effects of Random Vibration on the Dimensional Stability of Space-Based Precision Structures”

and the work presented in the thesis are both my own, and have been generated by me as the result of my own original research. I confirm that:

- this work was done wholly or mainly while in candidature for a research degree at this University;
- where any part of this thesis has previously been submitted for a degree or any other qualification at this University or any other institution, this has been clearly stated;
- where I have consulted the published work of others, this is always clearly attributed;
- where I have quoted from the work of others, the source is always given. With the exception of such quotations, this thesis is entirely my own work;
- I have acknowledged all main sources of help;
- where the thesis is based on work done by myself jointly with others, I have made clear exactly what was done by others and what I have contributed myself;
- parts of this work have been published (or have been accepted for publication) as:

    1. Edeson R. L., Aglietti G. S., Tatnall A. R. L., "Conventional stable structures for space optics: The State of the Art" *Acta Astronautica*, 66, (1-2), 13-32. (doi:10.1016/j.actaastro.2009.06.015), 2010.
    2. Edeson R. L., Morris N., Aglietti G. S., Tatnall A. R. L., "Dimensional Stability Testing of a Space Optical Bench Structure", *AIAA Journal* Vol 47, No 1, Jan 2009.
    3. Edeson R. L., Aglietti G. S., Tatnall A. R. L., "Dimensional Stability Loss in Structures Subject to Random Vibration", *COMPDYN Thematic*

Conference on Computational Methods in Structural Dynamics and Earthquake Engineering, Corfu, Greece, 2011.

4. Edeson R. L., Aglietti G. S., Tatnall A. R. L., "The Effects of Random Vibration on the Dimensional Stability of Precision Structures", 12th *European Conference on Spacecraft Structures, Materials and Environmental Testing,* Noordwijk, The Netherlands, 2012.
5. Edeson R. L., Aglietti G. S., Tatnall A. R. L., "The Dimensional Stability of Materials Subject to Random Vibration", *Precision Engineering*, 2012, http://dx.doi.org/10.1016/j.precisioneng.2012.10.001.

Signed: ……..

Date:…….

Acknowledgements

I would like to thank the following people for their help and understanding during this research project:

- My long-suffering wife Sophie who will be very glad when this is all over!
- My boys Arthur – who often asks what work I am doing after he goes to bed; William – who has spent far too much of this time in hospital; and Laurence – who can't yet type but at the age of 1½ is very enthusiastic with a keyboard.
- Adrian and Guglielmo for all their help and support over the last five years.
- Nigel Morris, for letting me use the RALCam-4 project as part of this research, and for many words of wisdom and advice.
- Martin Whalley, for his help and support.
- The STFC Centre for Instrumentation, who funded the material and bolted joint test work.
- MDA Orbital Optics Ltd for funding the Breadboard Model Camera.
- Simon Canfer, Alan Pearce, Dave Rippington and Giles Case for all their practical help.

Definitions, Abbreviations, Nomenclature

α	back stress term in Kinematic Hardening model
AIV	Assembly, Integration and Verification
Arcminute	an angle of 1/60th of a degree
Arcsecond	an angle of 1/3600th of a degree
BBM	Breadboard Model
C_1	initial hardening modulus
CAD	Computer Aided Design
CFRP	Carbon Fibre Reinforced Polymer
CME	Coefficient of Moisture Expansion
CMM	Coordinate Measurement Machine
CTE	Coefficient of Thermal Expansion
dB	decibel
ε^{pl}	plastic strain
FEA	Finite Element Analysis
FEM	Finite Element Model
Fn	Normal Force
FM	Flight Model
FPA	Focal Plane Assembly
Fs	Shear Force
γ_1	Parameter controlling the rate of decrease of hardening modulus
GFRP	Glass Fibre Reinforced Polymer
GPa	Gigapascal
GSD	Ground Sampling Distance
HM	High Modulus
K	elastic limit
M1	Primary Mirror
M2	Secondary Mirror
MPa	Megapascal
MTF	Modulation Transfer Function
MYS	Microyield Strength (stress causing 10^{-6} permanent strain)
PDF	Probability Distribution Function
PEL	Precision Elastic Limit

PPM	Parts Per Million
PSD	Power Spectral Density
RAL	Rutherford Appleton Laboratory
RH	Relative Humidity
RMS	Root Mean Square
RTV	Room Temperature Vulcanising
STFC	Science and Technology Research Council
UTS	Ultimate Tensile Strength
μstrain	microstrain (10^{-6} strain)

1 Introduction

1.1 Background and Objectives

The early years of the space age did not see any dedicated civil programmes to deliver Earth imagery, instead concentrating on astronomical observation and the lunar landings[1]. The first Earth images were taken by astronauts during the Mercury and Gemini missions. The first dedicated Earth Observation (EO) program was initiated in 1966, and the first launch was Landsat-1 in 1972[2]. The MSS (Multispectral Scanner System) camera on this mission produced images with a ground sampling distance (GSD, or spatial resolution) of 80m. This was followed by Landsat-4 in 1982 (GSD 30m), SPOT-1 in 1986 (GSD 10m) and IKONOS in 1999 (1m GSD) amongst many others. An obvious trend here is the increase in resolving power over time. Most of these have been relatively large and heavy satellites, dedicated to Earth Observation. Since the turn of this century, there has been much interest in EO capabilities on "mini-sats", small platforms that are able to share launch costs or deliver a constellation of cameras. Such missions can put demanding requirements on optical bench structures, in terms of stiffness, mass, dimensional stability and cost.

This research project aims to improve the state of the art in low-cost conventional stable optical bench structures, primarily for Earth observation, but also with applicability to astronomical missions. It is focused on the dimensional stability response of structures to random vibration, as witnessed during the launch and ground-testing phases of a typical mission. There are three main objectives for the research:

- To better understand dimensional stability in structures subjected to random vibration, identifying key problem areas. Also to understand this in the context of a space-based structure that is subjected to a number of other environmental conditions that promote dimensional instability.
- To develop empirical methods for the quantitative assessment of dimensional instability in structures subjected to random vibration.

- To assess the potential for predicting dimensional instability under random vibration using FEA techniques.

For this research, "low-cost" is assumed to mean several £ million (<£5m) for a camera project, including detectors, optics, development models, testing and a flight model. "Conventional" construction follows from this – it precludes the use of exotic materials and structures which themselves require significant development (ie, silicon carbides, carbon-carbon), or very costly structural materials (ie beryllium). This definition effectively limits the available selection of materials to low expansion alloys and carbon and glass fibre composites, both widely used in this field. Notwithstanding these limitations, the structures of interest are typically subject to strict requirements on their dimensional stability in order to maintain crucial optical alignments during their operational lifetimes.

The main application for this class of camera is commercial high-resolution Earth imaging from a low Earth orbit (<2 m GSD) in the visible and near infrared wavelengths. This is an important and growing sector in the commercial space industry, with applications from border control, town planning and agricultural insurance assessment to consumer products such as Google Earth.

1.2 The Problem of Dimensional Instability

Typical space-based optical systems use two or more optical components and a focal plane. If the location of the detector's active surface deviates significantly from this focal plane, the resulting image will be out of focus. Similarly, there are ideal positions for the optical components, deviations from which will cause aberrations and degrade performance. This issue is usually tackled by attributing positional tolerances to each component, with tolerance values being determined by an optical sensitivity analysis. Obtaining adequate optical performances from visible wavelength Earth observation cameras in the 1m resolution class can result in positional tolerances on optical components in the 10 μm range and angular tolerances of less than 10 arcseconds for a low-mass, compact optical package. Conversely, a good degree of confidence in being able to achieve a particular level of stability would enable the optimisation of the optical design against this structural constraint.

Whilst these stability levels are easily achievable under laboratory conditions during an initial alignment process, maintaining them through a project's assembly, integration, verification, launch and on-orbit phases can be a challenge. There are a number of cases in the literature where costly stability failures have been induced by alignment and verification activities, and doubtless more that are not detailed in the literature.

The traditional problem areas for ultra-stable structures have been thermal expansivity and moisture desorption. Low expansion alloys such as Invar 36 have been addressing the first of these for over 100 years. Composite materials that use high-modulus carbon fibres in a resin matrix have been popular in lightweight stable structures work since the 1980s. However these are prone to hygral swelling during laboratory alignment operations and then shrinking during moisture desorption on-orbit. This issue has received much attention in the literature since the 1990s, and there are now several well-proven strategies to mitigate it.

The thermal and hygral expansion issues are now resolved to the extent that they no longer always pose the greatest threat to stability, and random vibration is now a key area. There are currently no suitable analytical methods for predicting the levels of instability introduced by random vibration in a structure, nor any bespoke empirical test data. The verification of dimensional stability is usually by all-up camera vibration testing at engineering model or protoflight model level.

In particular, random vibration testing which is intended to qualify a structure to survive launch loads is a problem. In this case, uncertainties in launch vehicle loads require that large margins are used on optical payload test specifications, and the resulting qualification levels can be substantially higher than those actually seen during launch. This, along with the uncertainties in the stability response of the structure to stress, can drive structures to be "over-designed" in order to meet stability requirements.

There are three obvious areas where instability can occur in a structure subject to dynamic loads: in structural materials, at joints, and in honeycomb panel inserts. None of these areas have received any significant attention in the literature.

The literature survey in this thesis (published as a review paper in Acta Astronautica[3]), as well as the breadboard tests described in Chapter 3, shows that stability loss due to random vibration is a real and significant issue for

conventional structures. It is argued that techniques for assessment and mitigation must be developed in order to achieve higher levels of dimensional stability than are currently considered the norm. In the first instance, this requires the gathering of empirical data and controlled experiments, as there are currently no tools or methods that are commonly used for predicting stability loss.

1.3 Addressing Vibration-Induced Dimensional Instability

The first part of the research seeks to enable a better understanding of the dimensional stability response of conventional space-based optical bench structures subject to random vibration, and identify typical problem areas. To this end, tests were performed on a typical optical bench structure to assess random vibration-induced dimensional stability loss. Also assessed were other causes of dimensional instability (ie thermal, vacuum, transport etc) in order to gauge their relative significance. The structure was a breadboard model of a 1-m resolution class low-cost camera. It made use of CFRP and low-expansion alloys, though aluminium mass-dummies were used for the optics. Metrology techniques included positional measurements using contact probes, laser interferometry, and in-situ angular measurements made optically. These tests found that stability loss was induced by a number of activities, including camera assembly and integration, handling and transport, vacuum, thermal changes, and of course, random vibration testing where a significant dimensional stability response was observed. This part of the project was the subject of a paper published in the AIAA Journal[4].

The next part of the research drew on the findings of the first part - the three key areas mentioned above (materials, joints and panel inserts) were identified for further investigation. They were examined using controlled tests of structural specimens. The structural specimens included CFRP and aluminium alloy samples, which were tested dynamically in a four-point bending configuration. Also tested were bolted joints, with a mass held in place by a single M4 screw. Random vibration was applied in a manner which would induce slight (but measurable) angular changes in the position of the mass due to micro-slipping. A third test was carried out only statically, assessing the movement of an insert within a honeycomb panel under load. It should be noted that the tests presented here are novel, and have not been

reported in the literature. A major goal of these tests, apart from gathering useful test data for materials and joints, was to assess and develop the test setups and metrology techniques. This assessment is also presented in detail.

Finally, the test results were assessed and compared with analysis where appropriate. In particular, some unexpected results were obtained from one of the material tests. Essentially, material samples subject to bending under random vibration were found to grow in length. This test was modelled accurately with an FEA model using cyclic plasticity material behaviour in a time-domain analysis. This analysis was able to predict the test results with reasonable accuracy, and has been hi-lighted as a useful analysis for future stable structures work. It was presented at the COMPDYN 2011 conference in Greece[5]. Other recommendations for the design, analysis and testing of future stable structures are also proposed. In particular, there are several observations made about the evolution of dimensional instability over a number of test cycles, that could be of great benefit in "bedding-in" stable structures during verification activities. From the industrial point of view, this is a "de-risking" activity, effectively enabling the verification of a structure early in an optical system program by design and analysis rather than by all-up testing at a later stage. A summary of this research was presented at the ESSMATS Conference in the Netherlands[6].

Conclusions are then drawn about the tests carried out, the results and the analysis work. Recommendations for future work are proposed. A brief protocol for dimensional stability maximisation in structures subject to random vibration is given in the Appendix.

1.4 Thesis Plan

A flowchart of this thesis, including the three main areas just described, is shown in Figure 1:

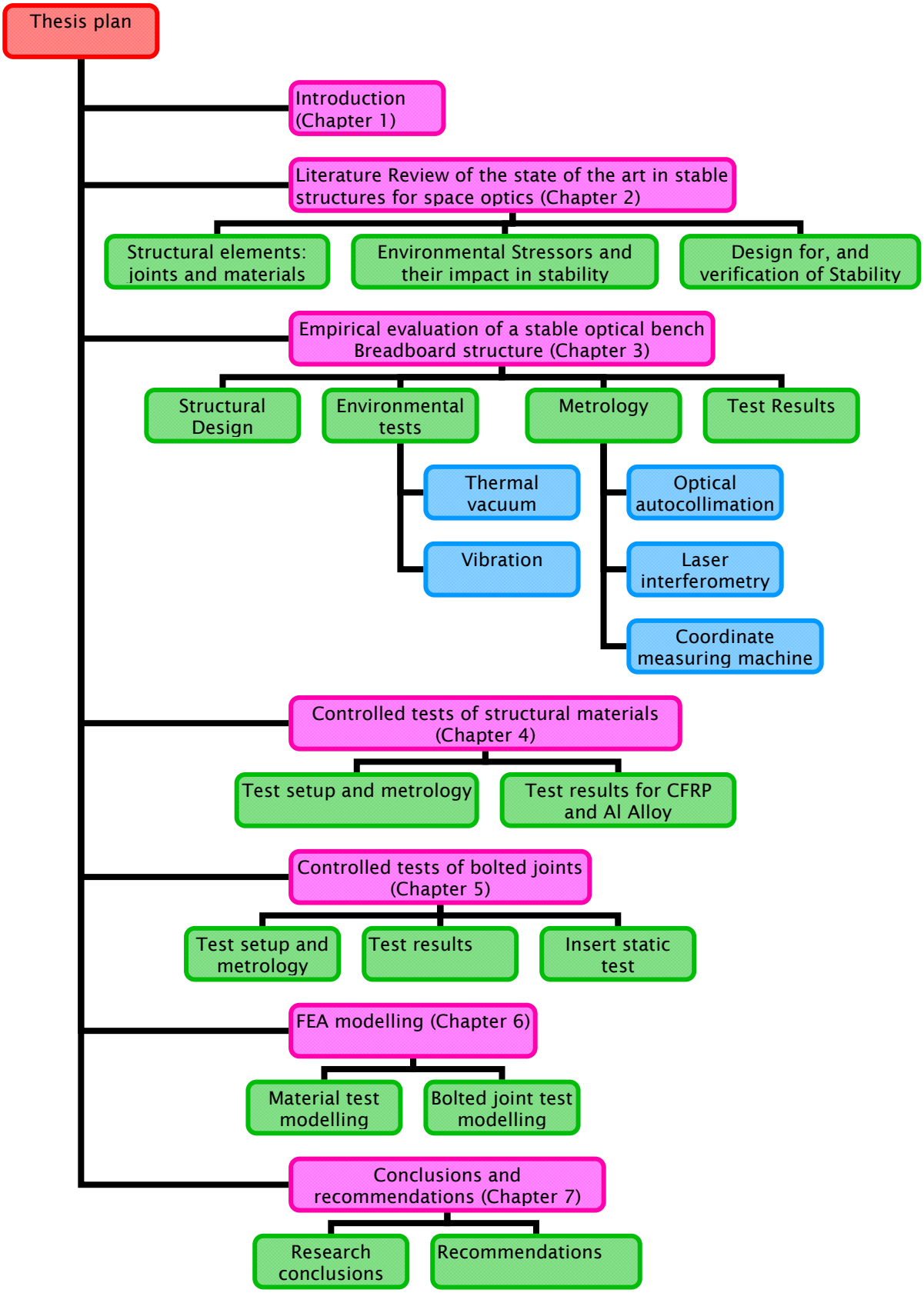

Figure 1. Flowchart showing the layout of this thesis.

The literature survey is presented in Chapter 2. It includes a summary of the various issues that affect dimensional stability, including environmental stressors, relevant properties of materials and joints, metrology and verification. It concludes highlighting the finding that while some areas of dimensional stability are well understood, a gap exists in the state of the art in dimensional stability loss due to random vibration.

Chapter 3 describes in detail the breadboard model test structure, the environmental test programme, and the metrology techniques used to assess dimensional stability throughout this programme. It then examines the results, including an assessment of experimental errors. It concludes that the effects of random vibration were indeed significant in comparison to thermal-vacuum and other environmental stressors.

The bespoke tests on materials samples under random vibration are described in Chapter 4. Firstly the test setup is described, along with the metrology techniques. Next the test procedure and results are presented in detail. The results are then analysed, and conclusions drawn about the dimensional stability response of these materials. The performance of the test setup and metrology methods is also examined in detail.

Chapter 5 describes the test setup used to assess micro-slipping at bolted interfaces under random vibration. Again the test setup, procedure and results are examined in detail, with a critical assessment of the setup and metrology techniques.

Chapter 6 presents two finite element analyses. The first is a nonlinear analysis of one of the material sample tests from Chapter 4. The aim of the analysis is to predict the dimensional stability behaviour witnessed during testing. The second analysis models the contact surfaces of the bolted joint test setup from Chapter 5.

Conclusions of this research, and recommendations for future research and test methodologies are presented in Chapter 7. Supporting material for this research is presented in the Appendix. Also presented in the Appendix is a simple guide for future stable space structure projects, with recommendations arising from this research.

2 Literature Review

2.1 Introduction

This literature review focuses on the technical aspects of dimensional stability in space structures, starting with a summary of the main environmental threats to stability and material properties relevant to dimensional stability.

It is apparent that there has not been very much work published in the literature on the subject of dimensional stability loss due to cyclic loading. This survey seeks to frame the issue as a gap in the state of the art. As well as focusing on the factors affecting dimensional stability of structures under cyclic loading, it considers the other aspects of dimensional stability. This is to put the vibration issue in context and to assess the relative maturity of work in the area.

Conventional materials and joints used in stable space structures are examined, and finally and the testing and verification of stable space structures is investigated. The importance of dimensional stability in optical structures is discussed in the Appendix.

2.2 Environmental Causes of Instability

During its life, a spacecraft structure is exposed to various environments that might cause microscopic movements within or between the parts that make up the structural assembly. Just to mention the most obvious situations: the structure/optical payload is assembled and calibrated in a clean room environment (i.e. 1g, and pressure and temperature controlled environments), then it will undergo vibration and thermal vacuum testing, it will be launched (where it will experience the real launch environment) and finally will operate in space thus subjected to its specific space environment (zero g, vacuum, thermal gradients, radiation etc). The following is a brief description of the intrinsic and environmental effects that are generally relevant when developing stable structures for space use.

Space-based optical instruments will invariably be required to operate at temperatures other than that at which they were assembled and aligned on the ground. This change in temperature may result in recoverable and non-

recoverable deflections in the structure. Cycling the temperature of the instrument may produce additional non-recoverable deformations – some materials display CTE hysteresis (with expansion and contraction occurring over different paths), and mechanical joints may ratchet into a position that relieves inbuilt strains. Deformations due to temperature changes occurring during imaging are also an issue. Typically the optical requirements for stability are much greater during imaging than between alignment and operations[7], a period when large amounts of heat may be produced in the focal plane subassembly of the instrument.

Marschall and Maringer[8] and Paquin[9] both note that material creep can give rise to unwanted distortions. Creep is the time-dependent deformation response of a solid under load. It can result in either time-dependent recoverable elastic strains, or permanent plastic strains[10]. An example of this could be a compliant gasket in a bolted joint – as the gasket deformation increases over time, the bolt deformation and therefore preload is reduced.

Launch vibrations are one of the most demanding environments with which a stable structure must contend. Small structural translations and rotations that would not be indicative of failure on a general spacecraft structure (i.e. non-stable structure) may be catastrophic on an optical bench structure.

Vibratory loads on spacecraft structures and their instruments are generated at several stages during launch. Depending on the launch vehicle, large amounts of acoustic noise from rocket engines can be reflected from the launch pad before lift-off. At transonic speeds, acoustic noise on the rocket nosecone can excite a significant structural response in the payload structure, as well as in the mounting structure (which is coupled to the payload). This acoustic pressure is typically in the range 20 – 8000 Hz[11]. Large transient loads can occur during stage separation events typically at lower frequencies (0 – 100 Hz). In addition, there is a significant random vibration response in the launch vehicle, which is transmitted to the payload at the interface between the two (20 – 2000 Hz.

The literature provides a number of examples of vibration tests causing problems during the development of stable structures:

- The flight model of the Mars Observer camera suffered a failure during random vibration testing[12]. The cause of the failure was found to be a

bonded joint, and the problem was rectified with retro-fitted joint strengthening.

- A development and test program was required to realise the necessary stability levels for the TopSat primary mirror mount assembly[13]. The final design included retro-fitted dowel pins.
- Alignment problems due to random vibration led to reinforcement of joints with higher-strength bolts and adhesives on the MAC camera for the Malaysian RazakSAT[14].
- Skullney et. al.[15] report structural "deflections somewhat higher than anticipated" as a result of static testing on the MSX ballistic missile tracking satellite. This is a large structure, composed mainly of CFRP struts with Titanium endfittings. The results were attributed to interfacial slipping.

Most space optics are aligned on the ground in a 1g environment, and must function in a 0g environment. For systems with large heavy optics, this gravity release can lead to misalignments. Even the surface shape of mirrors may be affected by sag effects. If it was polished in one orientation, surface errors may be introduced when tested in other orientations, or with different mounting systems.

Some materials release gaseous volatiles when in vacuum. As well as giving rise to potential cleanliness and contamination issues (especially with cold, sensitive optics), this process invariably results in a dimensional change. Similarly, hygroscopic materials that have spent time on Earth in a normal laboratory clean room environment (typically 50-60% RH) are likely to lose their moisture in space, with further dimensional changes resulting. Loss of trapped air from porous materials may also be a problem.

Neutron irradiation has been shown to affect the dimensional stability of some crystalline materials, by reducing the levels of internal stress or resulting in swelling[8]. In materials containing organic compounds, ionising radiation can cause physical and chemical changes that affect stability and other material properties. In particular, atomic oxygen in LEO has been identified as a problem, giving rise to surface damage on composite structures with polymer matrices[16].

Some studies have been made of the stability behaviour of materials over time, with no loads or varying environmental conditions. Many materials that

are useful for stable structures due to their low thermal expansion coefficients display signs of temporal dimensional instability (Steel [9]; Invar and Glass[17]; Composites[18]).

An aligned optical instrument may be subject to a series of unpredictable loads during handling and transport, the worst of which is shock due to being dropped. Most instrument transport containers incorporate shock sensors that will indicate whether this has happened and to what degree, but that doesn't necessarily help the optical alignment.

Vibrations on-orbit may be caused by reaction wheels, thrusters, other mechanical devices, or even thermal cycling. Luhia[19] and Do[20] investigate microvibrations induced in structures due to slipping in bolted joints and composite microcracking. When these vibrations induce imaging problems, they are referred to as "jitter"[21].

Some materials experience reversible dimension changes when exposed to magnetic or electric fields (electrostriction and magnetostriction)[8].

2.3 Materials for Stable Structures

To date, the best introduction to this area is by Marschall and Maringer[8]. Here all the main properties of interest for stable design are introduced, and a large amount of data for the materials that were widely used in this field at the time (much of which has not been significantly improved since) is provided. The main area that has seen substantial progress since their book publication is composites – these were only just starting to be used in this role at the time. Nonetheless, a modern equivalent has not yet been produced, and it remains highly cited to this day.

2.3.1 General Characteristics of Importance for Dimensional Stability

<u>Stiffness</u>

Most solids of interest behave elastically under load and, in general, for stable structures it is best to be as stiff as possible. This is for several reasons:

- The stiffer the structure for a given mass, the less effect gravity and its release will have on deformations.

- Stiffer structures generally behave more favourably under launch vibrations, as with higher frequencies, amplitudes and therefore stresses will be generally lower (structural resonances notwithstanding).
- Similarly, the dynamic response during operations is likely to have lower amplitudes, and jitter is reduced[21].

Anelasticity refers to the time-dependent behaviour of the stress-strain relationship[8]. On the application of a stress, strain does not occur instantaneously, but builds up over time. For most engineering materials, the time response is fast enough not to have a significant effect. It is in fact this "lag" that is thought to be responsible for most material damping under vibration. For some materials, such as RTV elastomers, the time response is significant, and they are best analysed with viscoelastic models.

Thus the specific stiffness, or ratio of Young's Modulus to density is an important factor to consider in material selection. Many common engineering alloys have similar specific stiffnesses though, and other material properties must also be considered. For example, given the choice between an aluminium alloy and a stainless steel, the high thermal conductivity of the former may be an attractive property for minimising thermal gradients.

Temperature Effects

Most solid materials will respond to a change in temperature with a change in size due to the amplitudes of atomic vibrations changing. The contraction/expansion property of materials is not linear, though it is often assumed to be for a small range of temperatures around room temperature. The secant gradient of the strain/temperature curve for a given temperature range is the CTE (see Table 1 for typical values). Even over this range, path dependency, rate dependency and hysteresis are observed in some materials[9]. Temperature effects that are hysteretic can have a significant cumulative effect on a structure due to the large number of thermal cycles it may experience in its operational lifetime. Thus for precision design work, a simple CTE value may not be sufficient and detailed displacement-temperature curves may be required.

Additionally, some materials will undergo phase changes which may result in a step change in dimensions. Precipitation and re-solution of alloying elements at different temperatures can result in further changes in size in

metals. Crystalline solids may also display slightly different expansivities in different directions due to the atomic lattice arrangement being anisotropic, though this effect can effectively be "averaged out" for a large number of randomly oriented crystals[22]. Note that this is relevant to other material properties such as Young's Modulus as well.

For extremely high levels of stability, another factor is thermodynamically-induced oscillations in structures above absolute-zero. These oscillations are due to atomic vibration exciting structural modes, the first of which is a uniform expansion-contraction of the structure. Dolgin, et. al.[23] calculate that for most materials, a 10m long rod weighing 1kg will oscillate with an amplitude of 10^{-12}m.

Material	Typical CTE (ppm/K)	Linear expansion over 1000mm/20°C (μm)
Aluminium	23.5	470
Titanium	8.6	172
SiC	4.5	90
C/Sic	2	40
Invar 36 (depending on heat treatment)	1 to 4	20 to 80
CFRP (in-plane, using a quasi-isotropic layup and high modulus fibres)	0 to 2	0 to 40
Zerodur	0.02	0.4

Table 1. Typical Materials CTE and expansion produced on a 1m specimen by a 20°C temperature variation

A high thermal conductivity is generally preferable for stable structures. Whilst the thermo-elastic behaviour of structures under temperature gradients can be assessed easily with techniques such as Finite Element Analysis, such gradients can lead to large stresses and unwanted distortions. In mirrors with small but nonzero CTEs, different areas being at different temperatures may introduce distortions.

Yield and Microyield

Material yield occurs when defects within the crystal structure of a material, or dislocations, move within the crystal lattice under load[10]. At a macroscopic level, the result is that on reaching a certain stress level, a non-recoverable (plastic) strain is observed. Typically the "yield" stress required to produce a plastic strain of 0.2% (the 0.2% proof strength) is quoted by material manufacturers and used when determining safety margins on gross failure. At this level, there is little variability in yield stress, which is reasonably repeatable amongst different samples and tests in most materials.

Yield at the 0.2% level is not particularly useful for precision instrument design because of the large strain that is observed – it equates to 2mm in every metre. The "elastic limit", or "proportional limit", where the stress-strain curve deviates from the linear can vary considerably depending on the resolution of the measurement. A yield definition more suited to dimensional stability problems is "microyield". It is usual to define a material's microyield strength (MYS) as the stress that will cause a 1×10^{-6} permanent strain in a material[8, 9, 16, 24] (some typical values are reported in Table 2), though some literature uses the term to describe different strain levels (ie, 5×10^{-5} reported by Bates and Bacon[25]), and in fact different terminology (the precision elastic limit, PEL is sometimes used interchangeably with the MYS[16]). The mechanisms for yield in the microstrain region are different in different materials, and include dislocation movements, dislocation generation at grain boundaries in polycrystalline metals and atomic displacements in noncrystalline materials that can occur without breaking bonds[16]. In composites, microyield can result from failures within the matrix, the fibres, or a failure at the interface, though usually it is microcracks that are transverse to the load direction that signal the onset of failure and cause a loss of dimensional stability.

Unlike yield at higher stress levels, microyield strength is not always repeatable. It depends strongly on the prior loading and heat treatment history of the material, and the way the test is carried out[8]. Furthermore, there is no relationship between traditional 0.2% yield and microyield, so one cannot use the former to infer the latter[9]. One way of producing microyield measurements is to repeatedly strain a sample to consecutively higher levels, relaxing the sample between each step to monitor the residual strain. Because of this, MYS figures are not particularly useful without the accompanying stress-strain curves.

Material	0.2% Yield Stress (MPa)	Micro Yield Stress (MPa)
Al-6061-T6	270	68.5
Ti-6-Al-4V	830	69 - 524
Invar-36	276	30 - 140

Table 2. Typical values of yield and micro yield stress

Moisture Effects

As previously mentioned, desorption of moisture and volatiles can give rise to dimensional changes. Organic compounds, and in particular epoxies and other composite matrix materials are vulnerable to this.

Hygral swelling typically occurs in a polymer solid when water molecules either react with hydrophilic (ie, highly polar) parts of the material to form a solution, or by occupation of (and transport through) sites of free volume[16]. After regions near the surface become saturated, moisture diffuses further into the solid, eventually reaching a steady-state saturation state which is dependent on the ambient humidity and temperature. It is generally assumed to follow Fick's law[26] which relates the rate of mass transport to the concentration gradient through the solid:

$$\frac{dc}{dt} = D\frac{d^2c}{dz^2}$$

Where c is moisture concentration (in units of density), t is time, D is a constant and z is the distance in the direction of diffusion. Note that this assumes diffusion in one direction only, normal to the solid's surface. Wolff[16] also discusses materials that display non-Fickian behaviour due to the addition of microstructural damage, or the leaching of organic volatiles from the solid. For most materials of interest though, this process does not usually result in microstructural damage, and is completely reversible.

For composite materials, a property that is frequently quoted and used for design calculations is the coefficient of moisture expansion, or CME. The CME is defined as the strain accompanying a given change in moisture content.

The time taken to reach steady state is important, as some projects ensure that stable structures are stored continuously in dry environments (ie, dry nitrogen), and removed only for short periods to perform critical alignment operations. Another way to prevent swelling effects is to coat the solid with an impervious moisture barrier[15] (discussed in detail in the Appendix).

Creep

Creep is a term used to describe a number of different material behaviours under load. Creep results in deformations in a solid that are time dependent, and can result from loads that are significantly lower than those one would expect from a traditional elastic-plastic analysis. It can be recoverable, non-recoverable, or partly recovered.

Creep is strongly temperature-dependent, and has been considered in the literature mostly for high-temperature applications. Room temperature creep in the microyield region has been observed for a number of materials – for metals, it is due to the atomic vibrations associated with temperature, which help to overcome barriers to dislocation movement. The longer a solid is left in a loaded state at a non-zero temperature, the greater the probability that this will occur[8].

Analytically, creep can be treated as a viscoelastic problem[10], and in the case of composites a superposition of an elastic fibre in a viscoelastic matrix. Unfortunately, there is little material information available, particularly in the microcreep region. In general, it needs to be handled by either performing bespoke tests to identify the material parameters required, or ensure that the design does not include substantially loaded members in a high-stability path.

Cyclic Plasticity

It stands to reason that vibratory loading which induces material stresses above the elastic limit (or the MYS) could pose a threat to dimensional stability. Unfortunately there seems to be a paucity of data in the literature regarding material dimensional stability after vibratory loading. Maringer, Cho and Holden[27] performed some tests on a number of material samples (for spacecraft applications) using a shaker to provide axial tension/compression

cycles that were controlled with a load cell. Stress cycles were sinusoidal, with amplitudes significantly less than the materials' MYS. Even so, significant changes in sample length were observed.

In examining cyclic plasticity, it is helpful to analyse a material's stress-strain curve in some detail around the elastic limit. The reversal of a stress that is above the elastic limit does not necessarily mean that the strain will be reversed. Most materials harden slightly when undergoing yield, and display the "Bauschinger Effect". This is where the onset of compressive yield is seen well below the initial tensile yield stress[10], following a tensile stress cycle and is illustrated in Figure 2. Starting at *a*, a tensile stress is applied which results in some yield. The stress peaks at *b* and is then reduced. Yield in compression begins to occur at *c* at an absolute level of compressive stress that is lower than the equivalent tensile yield stress. The stress is again reversed at *d*, and a hysteresis loop is formed.

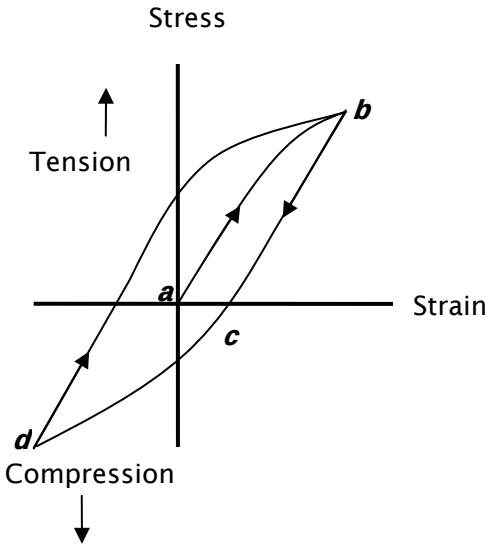

Figure 2. Bauschinger Effect and tension-compression hysteresis loop

Over a number of cycles, the hysteresis loop can change due to further cyclic hardening or softening. In the context of a cyclic stress, the result can be a strain that changes for each cycle but eventually reaches an asymptote.

If an additional static load is superimposed (ie gravity, or bolted joint tension), the alternating stress is not symmetric, and "ratchetting" or "shakedown" can occur, which result in progressive changes in strain for each

stress cycle (Figure 3). Often the post-yield portion of the curve is described linearly as the "hardening modulus", or with the Ramberg-Osgood strain hardening model, an exponential function with parameters identified from test results. Domber and Peterson[28] have been able to provide the constants for several engineering materials in the microyield regime from an extensive literature search.

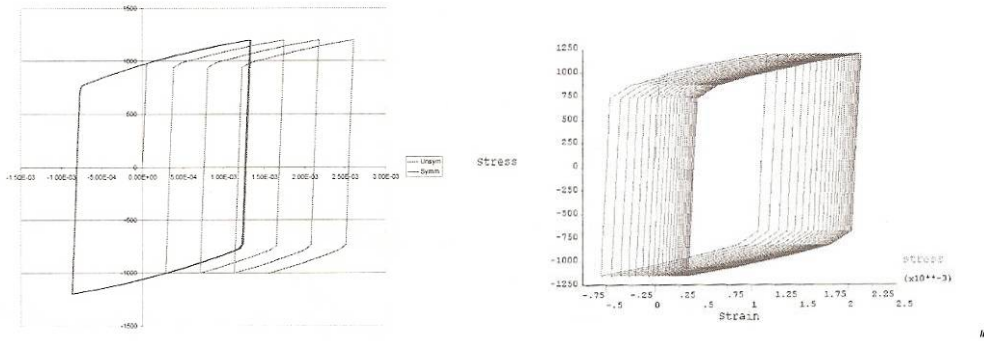

Figure 3. Stress-strain hysteresis for ratchetting (left) and shakedown (right) under asymmetric stress-controlled load reversals (from Ref. 29).

The nonlinear kinematic hardening model developed by Chaboche[10, 30] is designed to specifically model cyclic plasticity under asymmetric loading, and can predict both ratchetting and shakedown. It relies on bespoke material data being collected from the evolved hysteresis loop (ie, the final loop on the right of Figure 3) for several levels of cyclic stress. A minimum of three parameters are then determined which define the stress vs plastic strain curve. Further parameters can be added to improve the curve fit or increase its range of validity.

Residual Stresses

Most engineering materials contain some form of internal stress that is imparted during manufacture and processing. For metals that have undergone heat treatment, this typically means compressive stresses near the surface and tensile stresses in the centre. These stresses can cause problems when the material is machined, through long term stress relaxation, or through yield occurring locally at lower-than-expected levels of macroscopic stress.

Composite materials suffer from containing different materials that have different CTEs, and are often cured at high temperatures. The greater the

temperature change the material experiences with respect to the cure temperature, the greater the inherent inter-constituent stresses will be.

2.3.2 Metals Used in Stable Space Structures

Invar

The Invar group of alloys (which includes Invar-36, Unispan LR-35 and Super Invar) exhibit a near-zero CTE between about -50°C and +100°C[8]. The alloys consist of iron and nickel in an approximately 64-36 ratio. The unusual CTE behaviour is due to its ferromagnetic behaviour, which effectively reduces the gaps between atoms with an increase in temperature in a way that almost completely compensates for the increase in atomic vibration. This process is known as volume magnetostriction. The room temperature CTE of Invar is highly dependent on its history, with heat treatment, cold working and impurities all having some effect[31]. Typically, it can range from about +2 to -0.5 ppm/°C.

The MYS of Invar has been studied in some detail[8, 32, 33]. It ranges from about 30 MPa to 140 MPa depending on heat treatment and carbon content[33], and can be as high as 310 MPa if subjected to cold working. Some specific heat treatments are recommended in all the above references. Invar can tend to exhibit temporal instability, and can be prone to microcreep when subject to low levels of load, and even due to residual stresses induced during heat treatment. It can also require progressive stress-relieving heat treatments during machining. Usefully, it can be welded and then heat treated to give good properties[34].

Invar is easily available, and relatively cheap and easy to work with. It therefore has been in favour with stable structures designers for some time. It has been used as the primary material in the main structural metering components of space cameras[14], but tends to be used mainly for stable joints[35], composite tube endfittings[7] and inserts in honeycomb panels[21, 36], as well as mirror fixation bond-pads and flexures[37, 38]

Titanium

The main Titanium alloy of interest is Ti-6Al-4V, also known as “BS-TA 10, 11, 12 or 13”, “Grade-5” or “IMI-318” depending on conditioning. It has a relatively low CTE, 8.6 ppm/°C and moderate stiffness (113.8 GPa) and density

(4420 kg/m3). It is of most interest for flexures, bolts and components in highly-loaded joints, as it is very strong. After a precipitation hardening heat treatment, it is possible to achieve a 0.2% proof strength in excess of 1050 MPa[39].

The alloy is composed of two phases, an α phase - which acts as a matrix – and a brittle β phase. The proportion of these phases, as well as the overall microstructure is significantly affected by heat treatment and cold working. The mechanical properties, including those useful for stable structures are commensurately dependent on conditioning.

The MYS of the alloy has been reported as anything from 69 MPa[9] to 524 MPa[40]. Bates and Bacon[25] performed tests on the α phase at different temperatures and different impurity levels, and present stress-strain curves in the microyield region that are useful. Similar data for the α-β phase material with different microstructures is presented by Dudarev et. al.[41], who also investigate cyclic plasticity in the MYS region, and find that this is far more dependent on stress amplitude than the number of cycles. Bi-directional creep in this alloy was investigated by Imam and Gilmore[42]. They found that creep could occur at room temperature under stresses as low as 25% of the proof strength, and was highly dependent on prior heat treatment. An empirical power-law relationship is established in Ref. 8 for estimating creep strain in this alloy, which could be useful for design purposes.

Aluminium

Aluminium alloys are generally not used in dimensionally critical parts of structures because of their high CTEs (approx 23 ppm/°C). Low cost, easy machining and high thermal conductivity makes aluminium of interest though for structural items such as electronics boxes and focal-plane assembly boxes, and it usually ends up being used in most areas that are not dimensionally critical.

In structurally stable members, Al alloys still find uses in sandwich structures as the honeycomb material[13], as well as potted-inserts.

Stainless Steel

The stability of stainless steels in the microyield region has been studied extensively[8], though it is still not widely used due to its relatively high CTE (approximately 16 ppm/°C for an austenitic S/S) and high density

(approximately 8000 kg/m^3). Its main use in stable structures is for threaded fasteners and dowel pins, where various national and international standards are used to produce fasteners with very repeatable and predictable macroscopic mechanical properties that are very cheap and easy to obtain.

Beryllium

Beryllium alloys have some highly favourable mechanical properties, including a Young's Modulus in excess of 300 GPa, and a density of 1850 kg/m3. These materials have been successfully used in space, for both structural and optical components[43]. Unfortunately they are very expensive, and hazardous to work with due to their toxicity, so are rarely used in low-cost optical structures.

2.3.3 Conventional CFRP Composites for Stable Structures

Composites have found considerable favour in spacecraft structures due to their high specific stiffness, good dimensional stability and relatively low cost. The discussion here is focused on composites based on carbon fibres within a resin matrix. A more general discussion of composites is presented in the Appendix.

CFRP CTE

Most carbon fibres exhibit a slightly negative CTE at room temperature – pure graphite is -1.6 ppm/°C, and some of the high modulus (HM) fibres are not far away from this. In general the CTE becomes more negative with increasing Young's modulus. Using them, it is possible, and relatively easy, to produce a laminate that has quasi-isotropic properties and a near-zero CTE – ie it would effectively have a zero CTE in two mutually perpendicular directions, although the CTE perpendicular to the lay-up plane can be very large. Carbon fibres are not hygroscopic, and do not outgas volatiles in vacuum, making them very attractive for stable structures work.

Composite Failure

For gross composite failure, there are a number of possible mechanisms. The terminology for failure seems to vary almost as much as the mechanisms do. Generally speaking, gross failure can be the result of fibre failures, resin failures, or failures in the interphase. In tension, the main mechanisms for failure in an individual layer are fibre breakage, transverse crack formation in

the matrix, and shear failure in the matrix[44], commonly referred to as modes 1, 2 and 3. Under compression, fibre micro-buckling is another mechanism. In a built-up laminate, inter-laminar shear stresses present another common failure mode.

Failure analysis is therefore a complex field. There are no less than 19 different failure models presented in Ref. 45, and that was over 15 years ago. These range from independent limit conditions (ie, maximum stress in the *x* direction) to interactive criteria that incorporate the effects of multiple stress components acting simultaneously. More recently, an ESA-funded study known as the World Wide Failure Exercise[46] comprehensively compared a number of criteria with test results. The study recommended the "Puck" criterion as the most accurate. This criterion accommodates different independent sub-criteria for fibre and matrix failures.

Fatigue strength in composites is generally good compared with metals[47]. The mechanism for fatigue in metals is cyclic plasticity, while in composites it is transverse crack propagation. Composite fatigue behaviour in tension is different to compression, and therefore bending fatigue is complex. Most of the literature on low-strain composite fatigue is limited to microcracking induced by thermal cycling.

Transverse Microcracking

The main area of concern for stable structures under load is transverse microcracking[16]. Transverse microcracks are cracks that occur in the matrix and run through the thickness of an entire ply, parallel to the fibre direction. They are usually the result of thermal cycling or excursions to low temperatures – as the composite temperature deviates from the "cure" temperature, the matrix-fibre CTE differential results in compressive loading in the fibres and tension in the matrix. At a certain "critical temperature"[35], these stresses reach the level at which microcracks form. They are usually fairly short due to the accompanying stress relief.

Damage due to microcracking is typically measured in number of cracks per unit length of ply (crack density). The microcracking onset temperature can be measured using acoustic emission methods[48], (though the correlation between acoustic events and microcrack density is also disputed in the literature[49]). By measuring the strain induced and counting the number of cracks, the stress relief per crack can be estimated. The direct effect on

dimensional stability is an expansion of the composite (as additional cracks are effectively new voids) of the order of between 0 and 200 μstrain[16]. Attempts to quantify this have led to the Coefficient of Cracking Expansion, or CCE, which is the change in CTE due to cracking. Below the critical temperature, crack density can be more dependent on the rate of temperature change than the temperature extreme itself[50]. As well as temperature, the effects of moisture swelling need to be accounted for – as these swell the matrix they will tend to counteract the thermally induced residual stresses.

Microcracking affects other laminate properties as well. Cracks tend to reduce the tensile modulus of the laminate. As noted, laminate CTE can vary considerably due to microcracking[51], depending on the layup. Usually the CTE of a unidirectional ply will become closer to that of the fibre. The MYS is also sensitive to microcracking, reducing with increasing crack density[52]. The rate of moisture uptake is generally increased by microcracking.

Although there is an abundance of literature on laminate microcracking due to thermal cycling, and also some due to hygral cycling, there is very little on microcracking due to purely mechanical or vibratory loading. Nairn[53] notes that there is a fundamental difference between thermal and mechanical loading, in that the former is always biaxial, and the latter is often uniaxial. Some designers use "rule-of-thumb" methods to ensure that MYS stress levels are not exceeded – ie 1/3 of the theoretical laminate tensile strength[37]. Static MYS tests have been performed in the past[54], but these are obviously very laminate-specific and there seems to be very little information on this for modern materials.

Thus far, only metallic materials and composites have been discussed for stable structures. There are other classes of material that are suitable for stable structures, including glass and silicon carbides. For this research, these are precluded from the class of "conventional" structural materials, and are not assessed in any detail. Descriptions of these materials and their applications in stable structures are nonetheless presented in the Appendix.

2.4 Joints

Structural joints are required in various forms for all spacecraft structures. Even "monolithic" structures, making use for example of silicon carbide for both structure and optics, require devices that allow the alignment

and fixation of the optics and focal plane assembly. For low cost stable structures, typically joints are required amongst CFRP, glass and metallic components with different degrees of required stability. Most joints are best designed to be non-permanent. This is so they can be taken apart and re-assembled if required, and so small positional adjustments can be made if required during alignment processes.

2.4.1 Bolted

Bolted joints can generally be thought of as two elastic springs in parallel (though mathematically they are in "series"), with the "bolt" more compliant than the "joint". As the preload is applied, the bolt is stretched and the joint is compressed. The amount of preload is usually limited by the yield strength of the bolt material. It is usually applied by using a known torque. The relationship between torque and preload is linear, but depends very much on assumptions made about friction. Of the total torque applied, substantially more goes into overcoming friction in the threads and beneath the bolt head than is used to extend the bolt. Therefore, uncertainties in specific friction coefficients can result in a large uncertainty range in the actual preload applied.

After the initial loading, typically some of the preload relaxes over time[55]. This is due to embedding. At the joint interfaces, the actual areas of contact are very small - even for flat surfaces - and governed by local asperities on both surfaces. Over time, these highly-stressed areas can creep or slip into a slightly more "relaxed" position.

The load is transferred through the joint to the faying surface in a way that does not seem to be well understood. Historically, engineers have assumed for design calculations that the load is transferred through the joint in a pressure cone, as shown in Figure 4, which is used to calculate the stiffness of the joint. The correct angle to assume for this cone is debated in the literature, and ranges from about 25° to 45° [56, 57].

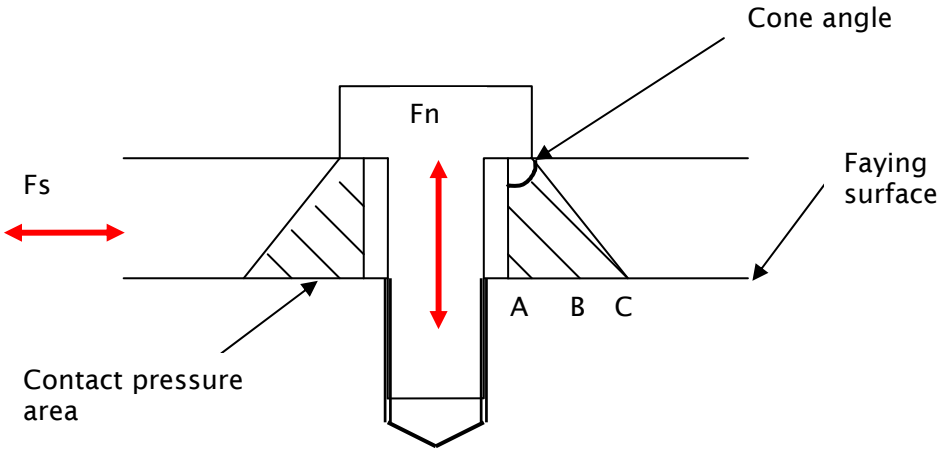

Figure 4. Bolted joint with pressure cone.

Contact Pressure Distribution

It is difficult to measure the exact shape of this pressure distribution experimentally, as any transducer that is added to the joint will have some effect on it. Recent experiments at the University of Sheffield have made use of the spatial response of the contact area to ultrasound to map the pressure distribution (see Figure 5 and Ref. 58. One of their results is shown below, for an M12 bolt torqued to 30Nm:

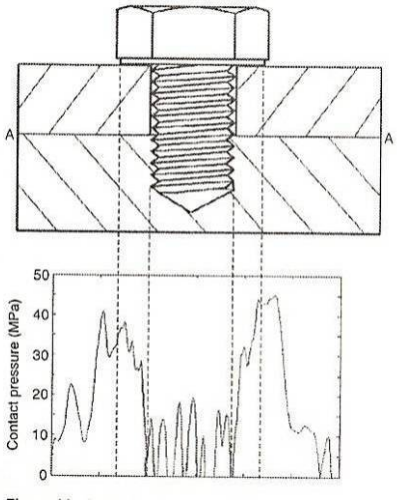

Figure 5. Actual pressure distribution (from Ref. 58).

The contact pressure is clearly not linear or even axisymmetric. The same study in fact found that the equivalent cone angle varied between 41° and 68°

depending on the interface roughness. Nonetheless, FEA models have been found to produce load distribution results that compare reasonably well with experiment[56]. When out-of-plane loads are applied, the pressure distribution is complicated even further.

Because exact solutions to bolted joint problems are complex, engineers tend to use simplifying assumptions and "rules of thumb" when designing bolted interfaces, which invariably lead to non-optimised designs.

Slip Resistance

The pressure distribution at the interface is important because it governs the frictional response of the joint to applied shear loading, and the degree of resistance to slipping. This in turn affects the dimensional stability of the structure.

Friction is usually assumed to follow the Coulomb pattern,

$$F_s = F_n * \mu.$$

Where F is force, the subscripts *s* and *n* are for the shear and normal directions, and μ is the friction coefficient. The friction coefficient is often assumed to be a constant for different material pairs, with a dynamic value and a static value. The static value is the load that is required to initiate shear motion, and the dynamic value refers to the load required to perpetuate it. Taking into account the pressure distribution at the interface, a more accurate expression might be:

$$F_s = \iint P(r,\theta)\mu dr d\theta$$

Where $P(r,\theta)$ is the pressure distribution as a function of distance from the bolt centreline *r*, and angular position θ.

The Friction Coefficient μ

Unfortunately μ does not behave in a manner that can be assumed constant. There is some evidence that it varies depending on contact pressure[59]. Values between 0.07 and 0.2 have been used for aerospace structures depending on the surface pressure[60]. This may be because of

changes in the asperity contact patterns. It is also time-dependent. Several studies[61] have found that the static friction coefficient gradually increases when the joint is left in a static state. When the joint slips, the friction coefficient decreases as an exponential function of the sliding distance[62], or velocity[63], then increases again once static. An empirically-derived exponential expression to predict the static friction coefficient of aluminium to glass as a function of time is presented by Panait et. al.[64]. Time dependency is probably due to thermally-activated relaxation processes[65]. Friction is also dependent on surface roughness, with higher coefficients to be expected at higher roughnesses. There is evidence that the RMS roughness is more important than the peak roughness[66].

Baylis[67, 68] performed a number of useful tests on material combinations used in the space industry, including titanium, CFRP and aluminium with various surface treatments. He treated sliding of the whole joint, or "macroslip", as failure, and determined a "slip coefficient" from the loading state at this point. One of his findings was that the thickness of the joint did not seem to have an effect on slipping. Another was that re-use of a joint tended to reduce the slip coefficient – probably because asperities became progressively more flattened. He also compared the results of dynamic testing with static testing, and found that the slip coefficient is substantially higher (up to twice) under dynamic shear loading than static shear loading. This behaviour did not appear to be frequency dependent. A similar study on aluminium joints for fighter aircraft found that harsh dynamic loading could increase the friction coefficient from 0.2 to 0.8 due to the faying surface oxide layers being destroyed[69]. To further complicate matters, vibratory loading can result in some preload loss[70] and damping loss[71], possibly due to ratchetting or shakedown in contacting asperities[72].

Microslipping

Partial slipping of the joint is called "microslip". As the shear force Fs increases, the parts of the joint with the lowest interface pressure slip first. In the diagram in Figure 4 region C would slip first, followed by B and A (at which point macroslip commences). Microslip has been studied extensively due to its contribution to structural damping. A large-scale test and analysis program has been running at Sandia National Laboratories[73, 74] for a number of years to characterise this effect. For dimensional stability, microslip may be important

for two reasons. Firstly, the structural connection that the joint is supporting is unlikely to be immediately adjacent to the bolt, and therefore subject to small displacements if microslip occurs – an effect that could be amplified in a structure with a number of joints under asymmetric loading. Secondly, under repeated loadings, the joint may "ratchet", especially if the alternating load is again asymmetric.

Modelling of Bolted Joints

Bolted joints can be modelled accurately with FEA using various contact algorithms[75]. The success of such models depends on the accuracy of the material and joint parameters, as well as the fidelity of the model. Because these models are nonlinear, solution times can be long. Detailed models of bolted joints are thus impractical for use in large structural models, that may incorporate hundreds of such joints. There does not seem to be adequate provision in current commercially available FEA programs for the large-scale modelling of nonlinear joints.

There are a number of methods proposed in the literature for simplified joint modelling, mainly for damping and nonlinear dynamic analysis. One of the most promising is the Iwan model[76], which assumes that both surfaces are attached with a large number of stick-slip elements in parallel with the loading direction. Each element has a critical force, at which it slips. The overall slipping behaviour is governed by a population distribution function whose parameters are identified by testing or FEA[74, 77]. One of the results of Iwan modelling is a prediction of the hysteresis curve (load vs displacement) for all points in the joint. This is sometimes called the Mindlin cycle[78], and the area under this curve is the energy dissipated per cycle, which is used to calculate damping. Iwan models have been compared to test results on the dynamic response of structures at Sandia National Laboratories[76, 79], and the University of Liverpool[80] with good success.

Other models for microslipping have been proposed. The LuGre model assumes that both surfaces are covered in small bristles that interact[20]. The Valanis model is based on nonlinear material behaviour[81], and the Bouc-Wen model is based on a differential equation that relates hysteretic slipping to a "restoring force"[82, 83].

Dowelling to Reduce Slipping

It should be noted that minimising microslipping may be dangerous in a structure, as less damping will lead to higher amplifications under launch vibration. It is estimated that up to 90% of damping in built-up structures is due to microslipping[83].

A fairly obvious method of preventing slippage is to apply a tight-fitting metallic dowel pin through the joint. This technique was used on TopSat[13] and the Hubble corrective optics[21]. Metrology on the latter showed that these pins did not prevent apparent movement across several of the primary mirror bolted interfaces under random vibration, and there was evidence of damage to pins.

One of the main issues with this approach is how it is done. Ideally, the instrument would be built and aligned perfectly, and then the dowel pins applied. Unfortunately this requires drilling and reaming holes in-situ, usually in close proximity to the aligned optics. There seems to be no literature at all on assessing quantitatively the effectiveness of dowel pins for dimensional stability in this way.

Often metallic inserts are bonded into glass or composite parts for the purpose of threaded fastening. It is possible that under load, these inserts would move due to yield or viscoelastic effects in the adhesive. Additionally, moisture swelling and thermal expansion may affect the stability of such joints. Though there has been much work done on insert design and testing for classical macroscopic failure[84], there is very little literature on the subject as regards dimensional stability. It is likely that detailed finite element models that take into account material nonlinearities and time-dependencies, would provide good insight into these effects.

Another commonly used method of making joints is by adhesive bonding. This method is discussed in the Appendix.

2.5 Structural Design for Stability

2.5.1 Structural Configurations

There are a number of configurations that have been used for metering structures in optical systems. For small structures, a simple tube or rod of a stable material between the main optics is sometimes used[40]. Truss structures

employing high-stiffness, low CTE truss members are popular. An example of this is the Serrurier Truss, in which the "front" and "back" ends of the structure deflect equally and parallel when the structure is simply supported at the centre and subject to gravity.

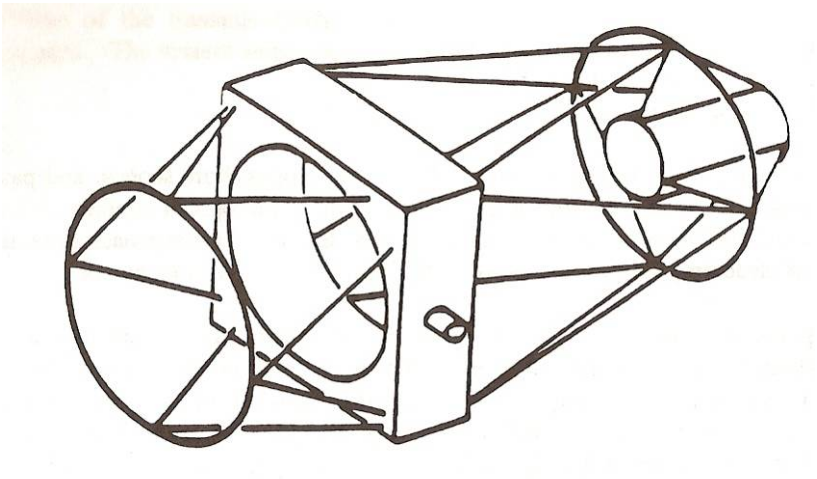

Figure 6. Serrurier Truss (from Ref. 40).

Another common approach for small space structures is a monolithic tube that acts as a structural support for the optics, a metering structure, and a stray-light baffle. A third class of structure makes use of flat panels with a honeycomb-sandwich construction[85]. Flat panels are easier to produce with CFRP than large cylinders, and offer more predictable and repeatable properties. The TopSat optical bench was essentially a box structure based on this approach[13].

It is possible to athermalise a structure by using structural elements of different materials in a way that cancels out their net thermal expansion at a location of interest. For example it is reasonably common for metering tubes with slightly negative CTEs to be attached by metallic endfittings with positive CTEs[86, 44], producing a structure whose overall thermal stability is excellent. While such structures are highly tolerant to isothermal temperature excursions, thermal gradients can be problematic.

2.5.2 Structural Conditioning

It has already been mentioned that thermal conditioning of composite structures is common to relieve manufacturing stresses. It is proposed that a

similar conditioning process, based on vibratory loading, could be used effectively to "bed-in" a built-up structure. This process would act to internally stress relieve materials in individual components, as well as inducing slipping at bolted interfaces that would result in a more stable state for the joints and the structure.

There is very little literature on this subject. Interestingly, tests performed in the 1970s to investigate vibratory stress relief in steel and aluminium samples found that the degree of stress relief in these materials was dependent on amplitude rather than number-of-cycles[87].

2.5.3 Jitter

Jitter can be caused by thrusters, and reaction wheels, but also by sudden stress releases on-orbit due to thermal cycling of bolted joints[88]. A detailed study of sudden stress release events due to thermal cycling was performed for the GOCE project[19]. The conclusion reached here was that many of the microvibration events observed were due to CFRP properties as well as joint slipping, and also that there was a significant settling in these events after the first thermal cycle. It has been proposed that liquid lubricants are purposely used on faying surfaces in ground based telescope joints, to prevent stick-slip induced jitter due to dissimilar materials under a thermal gradient[89].

2.5.4 Mirrors and Mounting

Most mirrors of interest are provided on large glass monolithic substrates. These can be reasonably heavy, and often require lightweighting to be practical. Traditional lightweighting involved machining the back of the mirror into a "single-arch" or "double-arch" shape. Modern lightweighting techniques involve making undercut-pockets in the back of the mirror using grinding tools and chemical etching. The resulting structure is effectively a glass honeycomb sandwich. Mass reductions of 70-80% are possible this way, though cost and risk rises substantially above about 50% lightweighting. It is also possible to create sandwich mirrors by fusing separate parts together at high temperature, though this technique does not seem to be available for glasses in the ULE and Zerodur class.

Recently, attempts have been made to fabricate optical surfaces from CFRP materials. A recent study by Romeo and Martin[90] successfully proved a ground-based astronomical telescope which made use of a mirror constructed

from CFRP. Interestingly, the fabrication process used did not make use of conventional polishing, instead relying on an optical-quality mould-tool to achieve the correct form and surface quality. This technique has enabled the construction of an all-CFRP Cassegrain telescope of 400mm aperture that weighs 10kg. Lightweight CFRP mirror segments can also be used in deployable telescopes – these are launched in a folded configuration, then deployed to produce an aperture that would be far too large to fit inside the nosecone of a rocket as a monolithic optic[91].

Mounting of mirrors is crucial to their stability. Most mirror mounts are kinematic, or semi-kinematic – that is they place individual constraints separately on all six degrees of freedom, without any overconstraint. Typically this is via three flexures mounted 120° apart around the circumference. Vukobratovich[40] recommends designing so that the mounting loads act through the centre-of-mass of the mirror, while Iraninejad et. al.[92] suggest that the neutral plane is best for this (invariably a good design would ensure both). The use of flexures for such designs is to prevent moment transfer, though equally ball joints, pin joints or hinges could be used[93] if they are deemed suitable for space use.

2.6 Verification of Stability

2.6.1 Material Testing

CTE testing can be done easily and cheaply on small test coupons one of three ways – using a contacting probe - or dialometer, using optical methods, or using electrical transducers[94]. Optical methods may require the bonding of mirrors either end of the test sample[95], but may be more accurate at temperature extremes where the temperature profile along any contacting probe is unknown[96]. Electrical transducers include strain gauges and capacitance probes, which have been used to good effect before in spacecraft structural testing[97].

Microyield tests require an accurate stress-strain measurement rig. It involves the application and relaxation of progressively increasing loads until 1ppm residual strain is observed[8].

CME can be measured in the same way as CTE, though tests might take much longer. Humidity control may be difficult in some test chambers, and

one approach is to boil the sample in water to saturate it. This method requires accurate measurement to determine the amount of water absorbed. Other methods to verify the design can be found for example in Ref. 98.

2.6.2 Assembly Level Tests

Vibration testing occurs at instrument level to verify that the structure will survive launch vibrations. There are two levels of vibration tests that are usually performed[99]. Qualification tests are used to qualify a payload design, and ensure that it is fit for purpose with some margin. Often bespoke qualification models of hardware – lacking electronics and realistic optics but structurally representative - are produced specifically for these tests. Acceptance tests are performed on flight hardware to screen for quality and workmanship defects prior to launch. These levels are lower than qualification levels, usually by 3 dB.

A typical test power spectrum is shown in Figure 7 (from Ref. 99). The test covers 20 – 2000 Hz, with a plateau between 100 and 300 Hz. The levels are tabulated in Table 3.

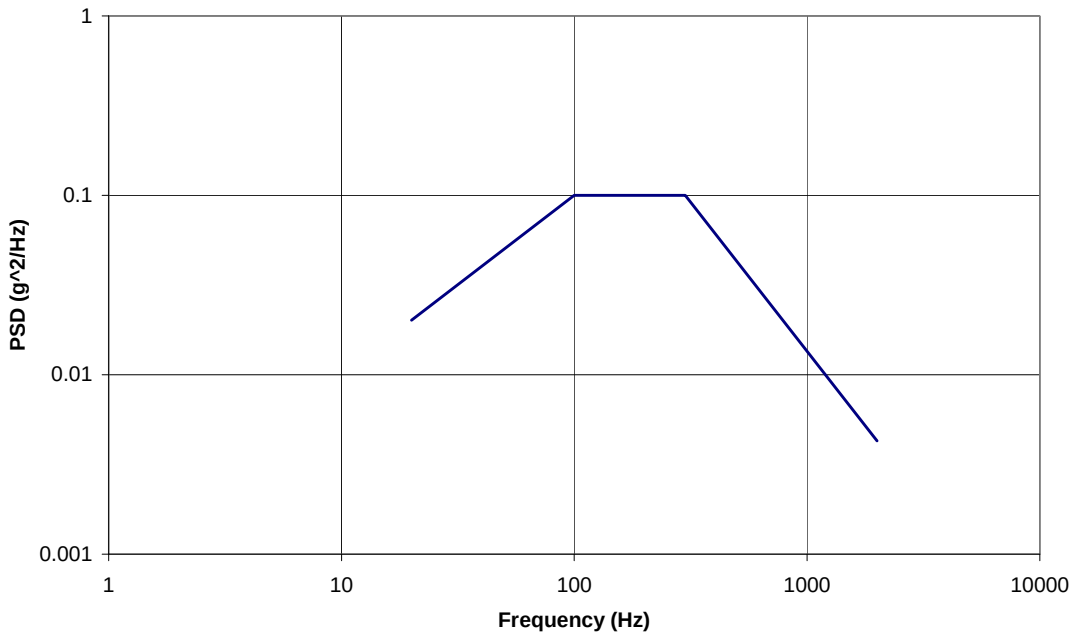

Figure 7. Typical PSD test curve

Frequency	Level
20-100 Hz	+3dB/oct
100-300 Hz	0.1 g^2/Hz
300-2000 Hz	-5dB/oct

Table 3. Typical PSD test levels

The level of the plateau varies from test to test, and is dependent on the mass of the equipment to be tested (with lighter equipment suffering higher test levels). The test duration is 2.5 minutes. This test spectrum was derived from Ariane and STS launch vehicle data, and is intended to provide an envelope which encompasses all possible dynamic loading events with a high degree of confidence (95%). Qualification also includes sinusoidal testing, swept from 5 – 100 Hz, though this is not necessarily as threatening to dimensional stability due to the low frequency cut-off, and the fact that it doesn't dwell at problematic frequencies, but sweeps through them relatively quickly.

It should be noted that the random test spectra are therefore always more harsh than the actual vibrations seen during launch. Where dimensional stability is limited by vibration loads, this process may impose unnecessarily difficult constraints on the structural design. The only way around this is through close cooperation between the instrument, spacecraft and launcher teams. Ideally, an acoustic test of the all-up spacecraft would be performed instead[100].

Thermal-vacuum testing typically takes place over a period of days to weeks, and gives the opportunity to observe the structural behaviour of the instrument in vacuum, and at temperature extremes and during thermal cycling. Typically several cycles are observed, with long soaks at temperature extrema to allow all areas of the structure to reach steady-state. Typically such tests are performed to ensure equipment functionality over the expected temperature range, qualify thermal systems, and correlate with thermal mathematical modelling.

2.6.3 Metrology

In order to assess the dimensional stability response of a structure to these environmental tests, bespoke metrology setups are required. These have been performed a number of ways:

One way to measure the stability response of a structure is to use a coordinate measurement machine (CMM) to physically probe discrete locations around a structure. Probe points can be realised with high-sphericity tooling balls bonded around the structure. This technique was used during TopSat development[13]. While it is possible to gauge the stability response accurately around various areas of the structure, it may be problematic to apply during actual tests, and is best suited to "before and after" snapshots of a structure. For the same project, a method based on an Invar frame around the instrument using LVDTs to make contact measurements was devised, but never used.

Very accurate in-situ measurements are possible (in a single direction) with a laser interferometry. Though this method is very accurate, and most errors are nulled by being "common mode", refractive-index differences need to be assessed if corner cube retroreflectors are used at different temperatures[101]. Note that such optical methods may require a glass window on the vacuum test chamber. To get around this issue, laser interferometers have been set-up entirely in vacuum[12].

Di Carlo and Usinger[102] used contacting probe measurements on dummy mirrors in a stable CFRP structure during thermal excursions in air. To do this, they built an "insulating tent" around the test structure, and heated it with bulb lamps.

Laser theodolites that make use of time-of-flight measurements of a laser beam are very attractive, though their accuracy may not be sufficient (10-30μm). A more advanced (and complex) technique is holographic interferometry[103], which interferes "before" and "after" waves of light to determine the influence of specific loads on a structure. Moiré interferometry is another more exotic technique – this requires the bonding of a diffraction grating to the structural area of interest, but gives very clear surface strain results[104]. A number of other techniques are presented by Wolff[16].

2.6.4 Analysis

FEA work is usually performed at two different levels for optical payload structures. All-up instrument models are generated to assess the dynamic

response, and highlight any particular areas of concern in terms of stress, while more detailed submodels are created of particular regions of concern such as mirror mounts and flexures.

For submodelling, the FEA package ANSYS offers some advanced material models that could be useful for stability predictions. In particular, there are several which are designed to capture cyclic plasticity (including nonlinear kinematic hardening), and modelling of material ratchetting and shakedown is possible[29, 105]. These models require bespoke material tests. Also, there are models that are well suited to bond-lines and CFRP matrix constituents, though not to whole composite sections.

ANSYS also provides a number of contact algorithms that would be useful for bolted joint evaluations. As mentioned, these techniques are mature and have been used extensively in the literature for parameter identification in simpler models. The "Augmented Lagrange" algorithm has been suggested as the best for bolted joints[60].

It is also possible to directly appraise the effect of structural distortion on the optical performance of the system analytically. By generating surface-fitting polynomials for the optical surfaces before and after distorting loads are applied, the direct impact on the aberrations can be found. The Zernike series of coefficients is designed for this – each term is directly associated with a particular aberration. ANSYS is not directly capable of generating these coefficients, but there is other commercial software available for it.

Though there are many good nonlinear models available for contact and material plasticity, these are only really suitable for small submodels. Their use in an "overall" instrument model would be prohibitive in terms of modelling effort and solution time using normal computers. The introduction of Iwan-type elements to commercial FEA packages will bring this goal much nearer. The current lack of a suitable technique for nonlinear dynamics was highlighted at a recent NAFEMS workshop[106]. NAFEMS have a special "Dynamics and Testing Working Group" currently looking that this area.

The other main problem encountered when performing random vibration analysis is comparing failure criteria with material parameters. This is due to the probabilistic nature of the input. The input loads are assumed to be Gaussian with a zero mean, and the resulting component (x, y and z direction) stresses also follow this distribution. The problem arises when these components are manipulated to form useful triaxial failure criteria, such as von

Mises. Some significant work has gone into assessing the probability distribution of von Mises equivalent stresses due to random vibration. Proposed solutions include estimating the number of standard deviations of the resulting distribution that are equivalent to 3-σ, or 99.8% probability for a normal distribution[107], estimating the probability of exceedance of a critical von Mises figure using "entropy maximisation"[108] or Monte Carlo Simulation.

2.7 Conclusion

Stable structures are becoming increasingly important for low cost, low mass high performance optical systems. Typically such systems rely on several large and heavy reflectors whose relative position must be maintained to within small tolerances in both rotational and distance degrees of freedom. These tolerances can be in the low 10s of microns and under 10 arcseconds. Optical performance may suffer if these limits are exceeded in the period between alignment operations on the ground and imaging operations in space. An alternative to using a stable structure is a re-focusing mechanism that can move one of the reflectors in those degrees of freedom to which image quality is sensitive. However such mechanisms add risk, cost and mass, and are not considered as part of a "low cost" solution for the purpose of this project.

There are a number of environmental conditions that a stable structure will see in the period between alignment and operation, which can contribute to instability. These include transport, thermal and hygral cycling on the ground, AIV and testing activities, launch vibrations, the vacuum environment, 0-g, orbital thermal cycling and atomic oxygen.

There are a number of material properties that are relevant to stability. These include thermal expansivity, moisture desorption, stiffness, microyield, fatigue and creep. In addition, joints can contribute to instability.

Some of these areas have been addressed very well in the literature. For instance thermal expansivity can be reduced to near-zero with the use of low expansion alloys (such as Invar 36), glasses and glass ceramics, and carbon fibre composites. This last material has found much favour in stable space structures due to its low density and high stiffness. Early problems with moisture desorption can be tackled using low-absorption resins (cyanate esters), moisture barriers, or careful humidity control during assembly.

Other areas have not received much attention. In particular the stability problems induced by launch vibration and vibration qualification testing. Although there are a number of instances in the literature where this has caused problems (see the Appendix), there is very little information on either the stability response of typical structures to vibration, or the stability response of the typical elements (ie, materials and joints) that make up those structures. Material microyield in the region that is relevant to stable structures has been studied in the context of static monotonic loads, but not dynamic cyclic ones. Studies of dynamic loading on structures tend to be focused on gross structural failure due to fatigue, rather than small plastic deformations. For bolted joints under cyclic loading, damping and energy loss are the main areas of interest. While interfacial slipping is relevant to this, it does not seem to have received much attention in its own right. In short, verification of dimensional stability in space structures seems to be by instrument level vibration testing of engineering models and protoflight models, rather than analysis or an assessment of the constituent parts of the structure.

The next part of this project was to assess the dimensional stability response of a conventional stable structure to a typical ground-test campaign, and determine the extent to which random vibration is a problem compared to other environmental stressors such as gravity sag, transport, thermal cycling and vacuum. A secondary goal was to identify any particular problem areas in the structure that require further attention.

3 The Breadboard Model Tests

3.1 Introduction

The aim of this part of the research is to achieve the first of the three main objectives outlined in the introduction to this thesis:

- "To better understand dimensional stability in structures subjected to random vibration, identifying key problem areas. Also to understand this in the context of a space-based structure that is subjected to a number of other environmental conditions that promote dimensional instability."

To this end, a conventional camera structural breadboard model (BBM) was designed, assembled and tested by the author. This model was structurally representative, and in many areas identical to, the structural design for flight. It was subject to a typical assembly, integration and verification (AIV) sequence that involved cleaning and baking parts, assembly, transport, optical alignment and environmental tests. During this time, its dimensional stability was assessed by test and observation. Particular attention was paid to dimensional stability during vibration testing and thermal-vacuum testing, with metrology rigs being used to quantify critical movements of dummy optics, and determine as far as possible which part of the structure was responsible for any stability loss.

3.2 BBM Structure

3.2.1 Structural Performance Requirements

The BBM was part of a larger design study funded by Orbital Optics Ltd, a subsidiary of Macdonald Dettwiler. The goal of the design study was a compact, low-cost (<£20m including launch) and low mass (<40 kg) camera which would be suitable for launch on a small satellite platform (<150 kg total). The driving performance requirement was the ability to produce images with a 1m ground sampling distance from a 600 km orbit in four spectral

channels with a 10 km swath. It was dubbed “RALCam-4”. The structural design, also performed by the author, is shown in Figure 8 and Figure 9.

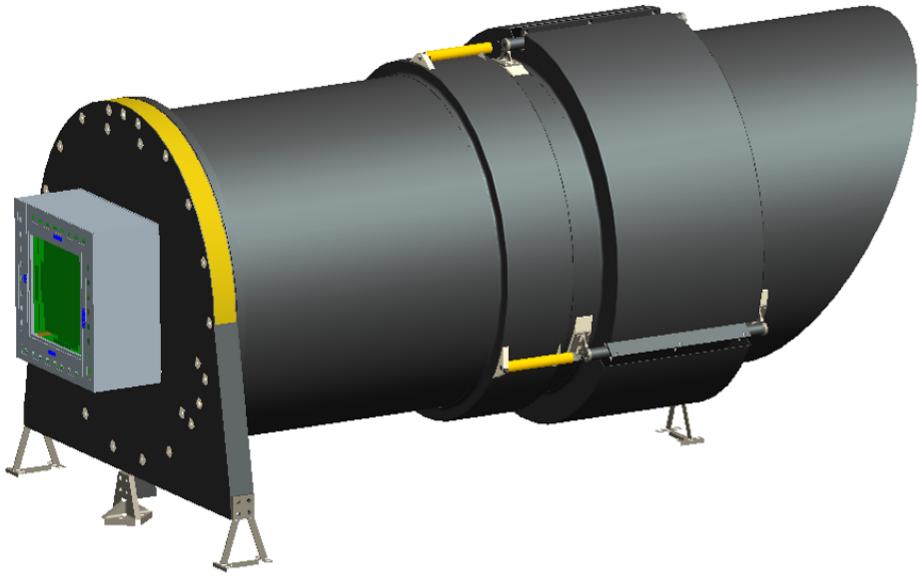

Figure 8. RALCam-4 camera CAD model showing the FPA attached to a stiff bulkhead panel.

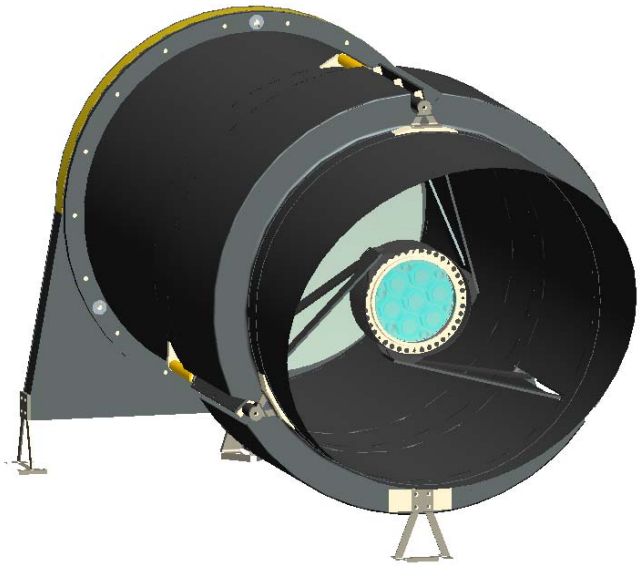

Figure 9. Front view of the RALCam-4 camera design showing the secondary mirror mounting spiders.

This performance requirement is challenging – typical cameras in this size class produce 2.5 – 5 m GSD images. To meet the requirement, a Ritchey-Chrétien (two-mirror Cassegrain) optical design was employed, with a 500 mm

diameter primary mirror and a 125 mm secondary mirror, located 0.9 m away. System performance was extremely sensitive to relative movements between these mirrors – tip and tilt tolerances were in the 10 arcsecond region, and axial displacement tolerances were below 10 μm. The dimensional stability of the system was seen as a major programme risk, hence the decision to fund the BBM design, analysis and testing to increase confidence in the camera design, and learn lessons for a flight programme.

3.2.2 Structural Design

The structural design and analysis was performed using the Pro/Engineer CAD package and ANSYS FEA program. The structural design made use of conventional – and relatively low-cost - material solutions that included CFRP, titanium and Invar 36. It has two primary parts – a stiff Bulkhead Panel and a large Tube (see Figure 10). The Bulkhead Panel is a sandwich structure with a honeycomb core and CFRP face skins. The tube is also of CFRP construction, with stiffening devices added at critical locations. An iterative design/analysis approach was taken, so the final design was well optimised for strength and stiffness.

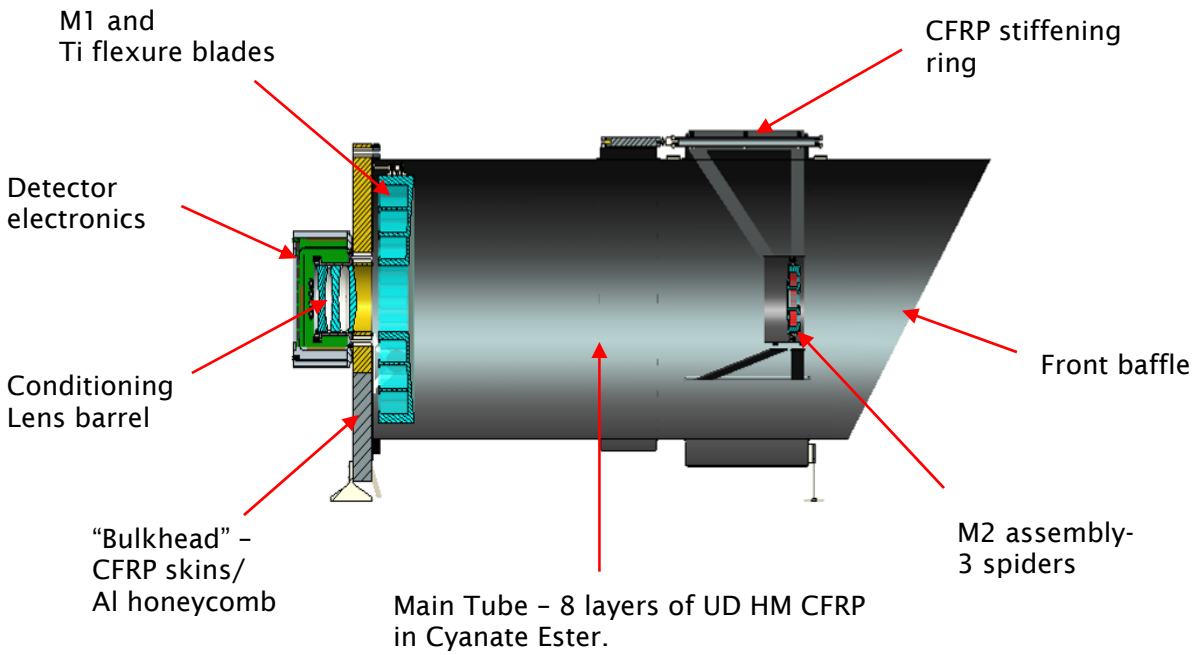

Figure 10. The RALCam-4 camera structure (CAD Model).

For the BBM, dummy masses were used to represent the optical components and focal plane assembly. Aluminium was used for these, as it has similar stiffness and density to the Zerodur glass-ceramic which would be used for the real optics. Mirror mounting flexures used Invar and titanium alloys. The primary structure used a quasi isotropic layup of M55J high modulus fibres in an Advanced Composites LTM123 Cyanate Ester resin system. The layup was chosen to minimise CTE, and the resin was chosen to minimise moisture expansivity. It was $(0, 90, 45, -45)_s$. A simple spreadsheet program based on the composite "rule of mixtures" (see Appendix) was used to derive this. The BBM structure was identical to the Flight Model (FM) design. The cure schedule included a low temperature cure with a long post-cure, in order to minimise pre-stress due to fibre-resin CTE mismatches. The structure is shown in Figure 11 and Figure 12.

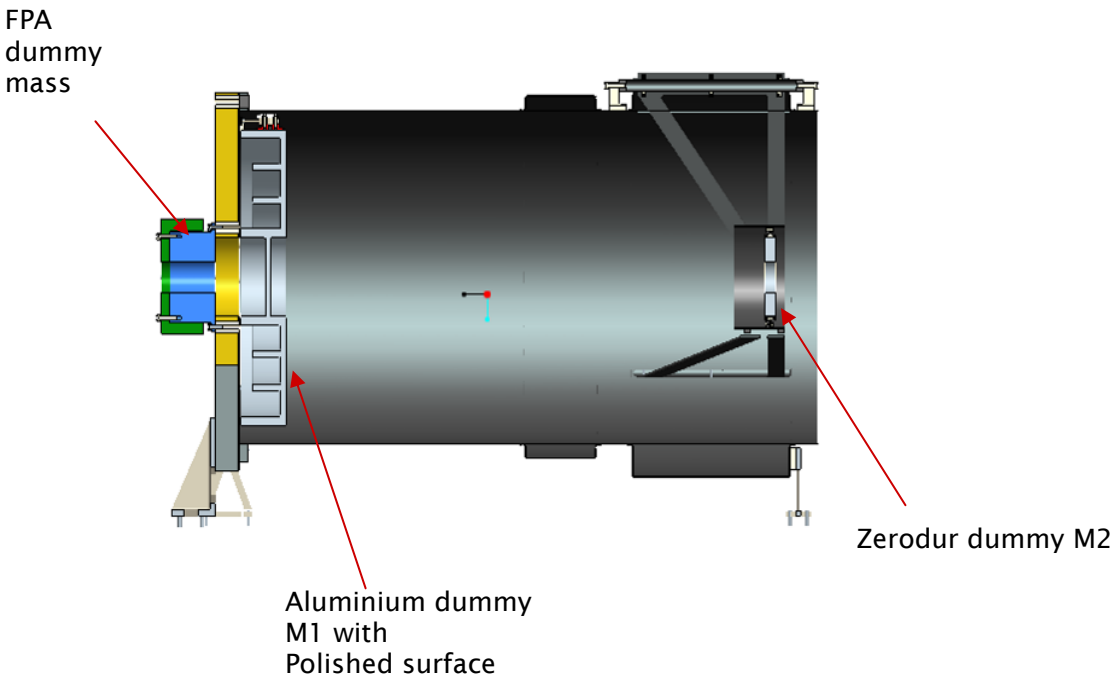

Figure 11. The BBM structure (CAD Model).

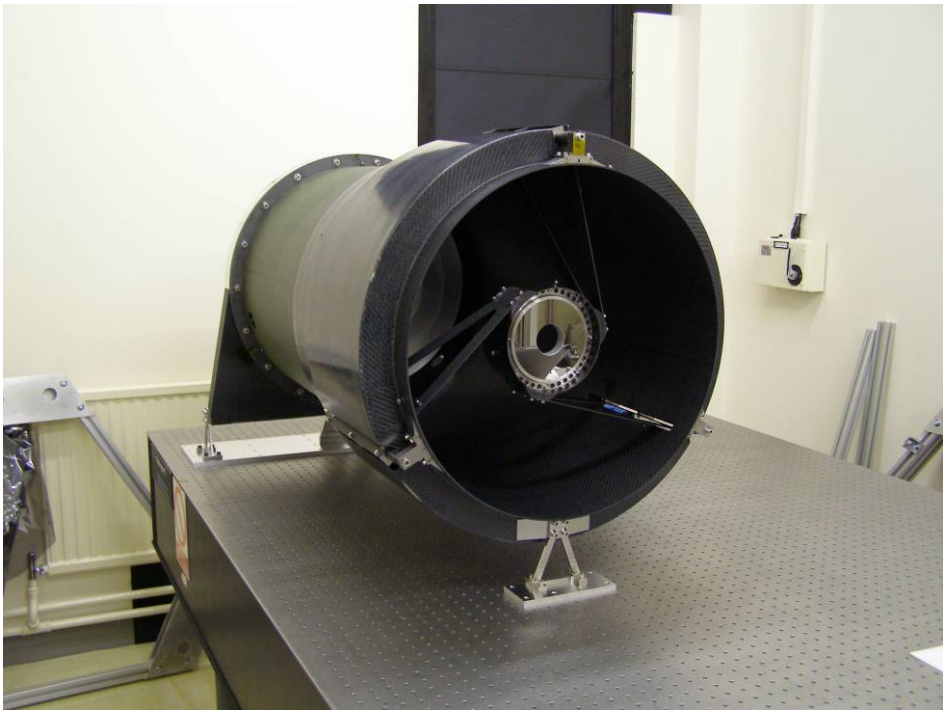

Figure 12. The complete BBM.

Finite element analysis was used to assess dynamic response, and strength under quasi-static loading. The first natural frequency was 81 Hz, helped by the addition of a large stiffening ring around M2 (Figure 13).

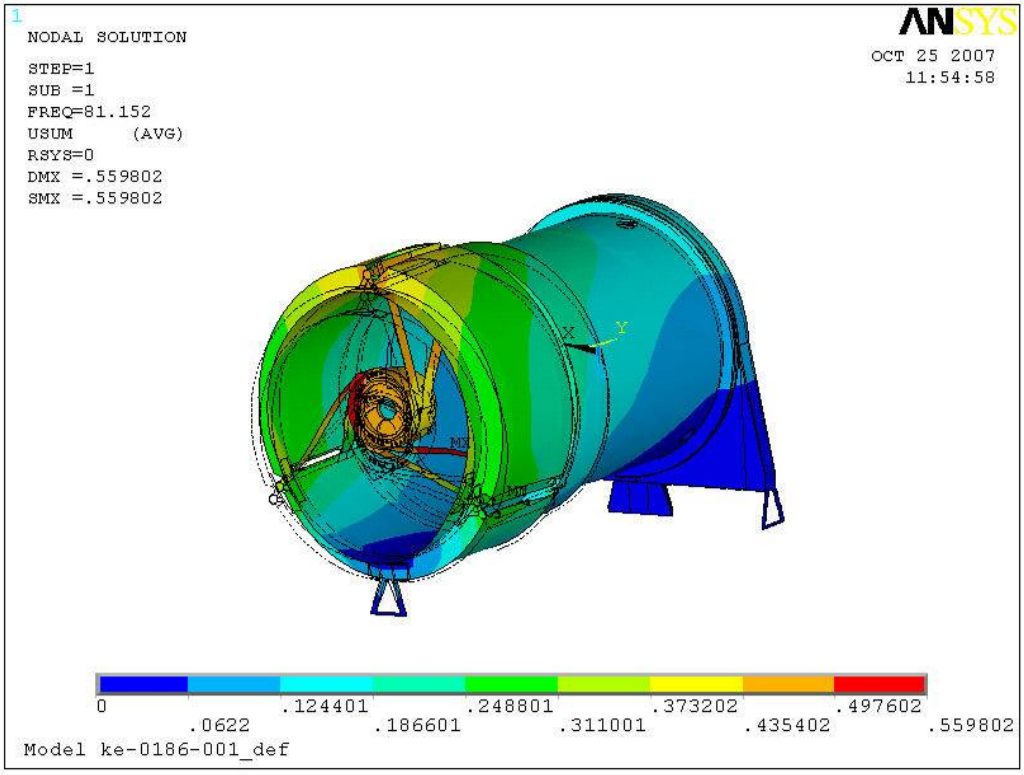

Figure 13. Predicted first modeshape.

3.3 Test Conditions

The assembly sequence is broadly the same as would be used for a flight instrument, though without the moisture absorption precautions. The approach was to sequentially "lock out" the degrees of freedom of the optical parts. Thus M1 is fixed in position within the structure, then M2 is fixed (this would occur following alignment, were real optics being used) with respect to M1, then the focal plane assembly is fixed with respect to the optics.

M2 was aligned with the BBM pointing vertically. An optical autocollimator was used to align a flat mirror bonded to the centre of M1 with a flat reflective surface on M2 to within several arcminutes in either direction. Part of the fixation process for M2 involved the in-situ drilling and reaming of dowel holes, and the fitting of dowel pins (there were 12 pins in this part of the assembly). This could not be done until M2 is aligned. Therefore one of the tests was to monitor the stability of M2 with respect to M1 during doweling operations.

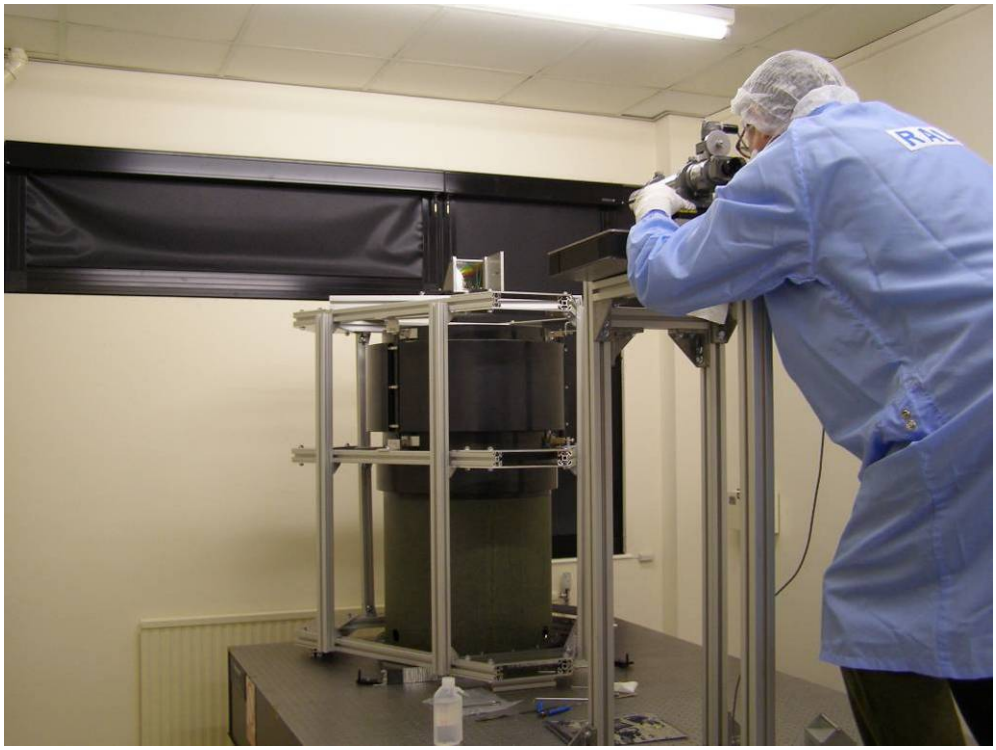

Figure 14. Using autocollimator to check alignment for gravity sag test.

The gravity release test was performed by assessing the relative alignment of the dummy mirrors whilst pointing both vertically and horizontally.

The test program relied on the use of facilities that were not all available on one site. After being built at RAL, the BBM was transported by road to the National Physical Laboratory in Teddington, UK three times for metrology, and once to Astrium in Stevenage, UK for vibration testing.

For transport, the BBM was mounted on a frame within a large transport box via commercial off-the-shelf anti-shock mounts.

The model was subject to random vibration testing in three directions. As no specific launcher or bus had been chosen, a generic qualification random power spectral density (PSD) curve was determined from Ref. 99, the ESA standard for structural testing. These levels are based on data from a number of ESA launches. For launches using other rockets, different spectra would be applicable. The levels used for random vibration testing gave 9.98 grms in the out-of-plane direction and 6.43 grms in the in-plane directions. The test sequence is listed in Table 4.

Test	Level	Duration
Resonance Search	0.5g	
Low Level Random PSD	-12 dB	30 s
Low Level Random PSD	-6 dB	30 s
Low Level Random PSD	-6 dB	30 s
Low Level Random PSD	-6 dB	30 s
Full Level Random PSD	-0 dB	60 s
Resonance Search	0.5 g	

Table 4. Random vibration test sequence for BBM.

Thermal-vacuum testing was performed in the RAL Space Test Chamber for a period of just over a week. During this period the BBM was continually under vacuum, and was subject to two thermal cycles between -10°C and +30°C with various plateaus at constant temperature, to represent the expected on-orbit thermal environment.

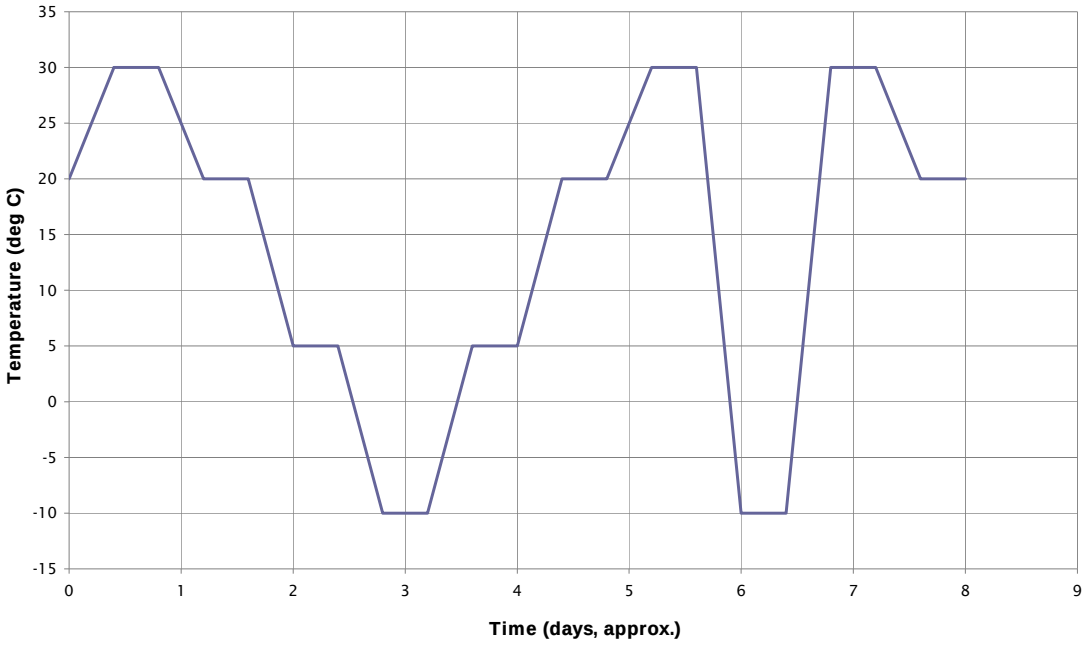

Figure 15. Temperature profile for thermal vacuum tests. Soak times are 3 hours at each plateau, and temperature ramp rates are 4°C/hour.

3.4 Metrology

The main goal was to quantify movements between M1 and M2. The degrees of freedom of importance are relative axial displacement, and relative rotations about the two axes orthogonal to the axial direction. Where movements of significance were observed, a secondary goal was to assess as far as possible which location(s) in the structure were responsible, and whether structural "bedding-in" could help improve performance.

Three primary metrology techniques were used to assess stability. The first was before-and-after CMM testing. The second was optical autocollimation to measure tilts between the dummy mirrors. The third was in-situ laser interferometry to measure axial displacement between them.

3.4.1 CMM

A coordinate measurement machine (CMM) at the National Physical Laboratory was used to assess structural movements. This is a machine that uses a highly accurate contacting probe to measure the locations points on the structure. Measurements were made at three inspection points – before vibration, between vibration and thermal vacuum testing, and after thermal vacuum testing.

To ensure that common points could be measured each time, silicon nitride tooling balls with a very high sphericity were attached around the structure. Epoxy was used to bond a washer to the structure at each point of interest, and then each washer was used as a seat for bonding the tooling ball (see Figure 16). During metrology, a number of points were probed around the surface of each ball, and its centre determined from a "best fit" approach.

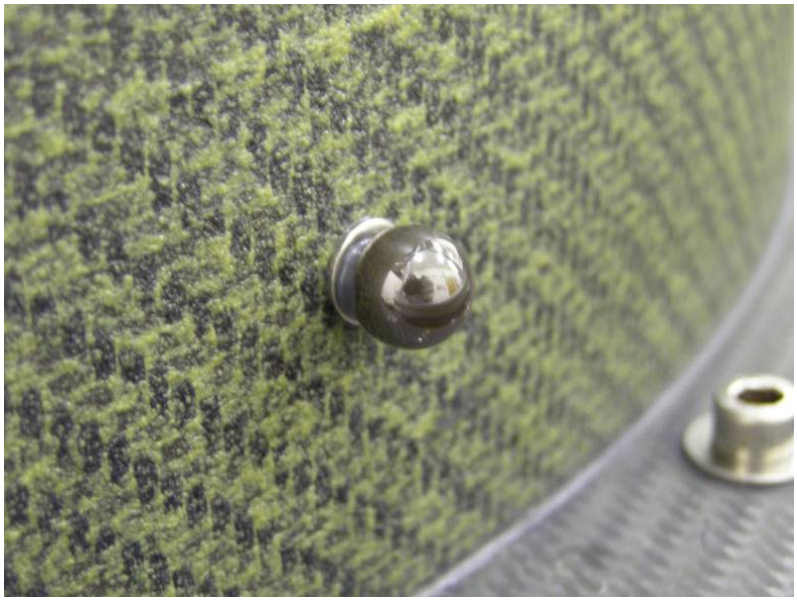

Figure 16. Tooling ball attachment.

For each set of measurements, the structure was mounted on a stable granite bench and given time to reach a steady-state thermal condition. Six sets of measurements were made for the centre position of each ball and the average result used.

3.4.2 Autocollimator

A two-axis autocollimator was used to measure relative tilts between M1 and M2. Flat reflectors were located at both reference planes for this. Measurements were manually recorded, again with five readings being taken for each. During vibration testing, measurements were made between each major shake. During thermal vacuum testing, the device was mounted outside a window in the test chamber, allowing measurements during testing. For the gravity release test, a 45° fold mirror was used to take measurements when the BBM optical axis was pointing vertically.

3.4.3 Laser Interferometer

An off-the-shelf Renishaw RLE-10 laser metrology system was used to measure axial displacement of M2 relative to M1. This system makes use of a pair of fibre-fed interferometer heads. Beam return from the target surface is by retroreflection (ie, using “cats eye” type reflectors), which avoided difficulties in aligning flat mirrors on the test item. The “corner-cube” retroreflectors were solid BK7 glass, mounted on bespoke Invar 36 fixtures.

One was located at M1 (with the beams passing through the central hole in M2), and the other was located on M2. Attachment of these was made with a 100 μm epoxy bond. The device had a resolution of 79 nm.

Both optical metrology methods are shown in Figure 17.

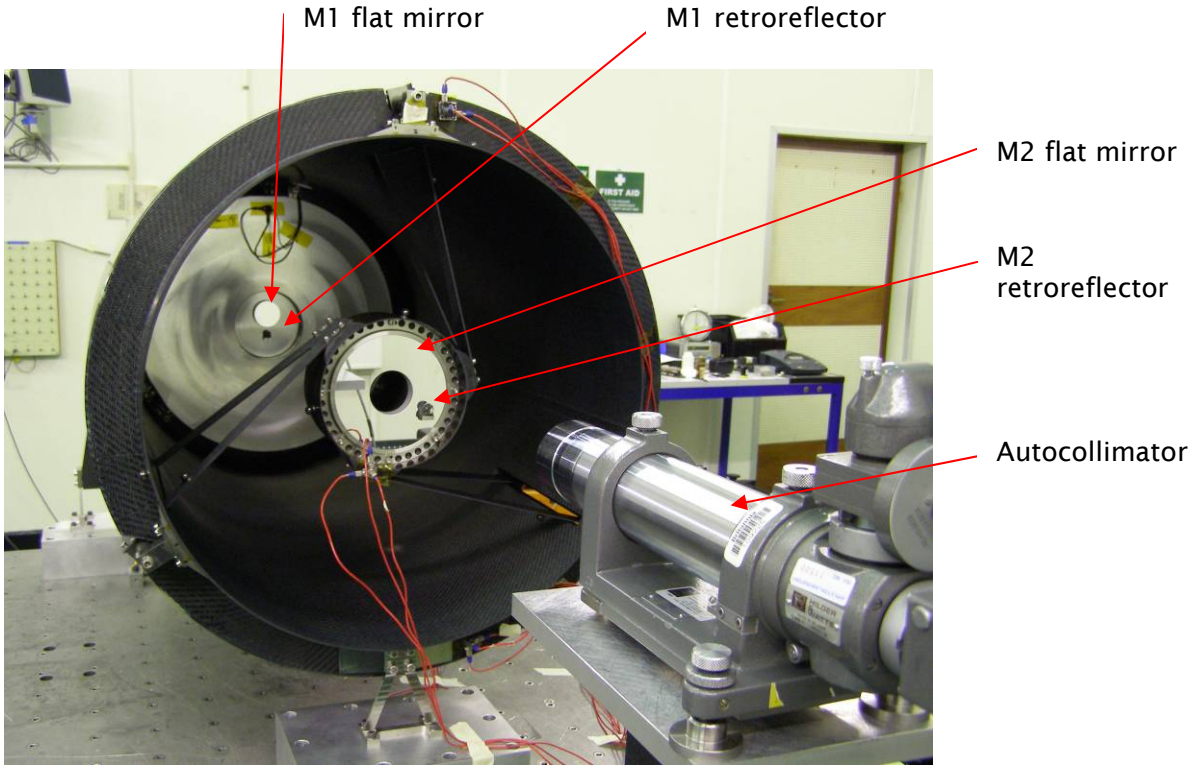

Figure 17. Optical metrology references.

This system was used during thermal vacuum testing. The BBM was mounted within the test chamber, aligned with the boresight pointing through a small optical quality vacuum window at one end. The pair of laser heads was mounted via a stiff fixture to the outside of the window flange, as shown in Figure 18. With this arrangement, any errors induced due to the CTEs of the retroreflectors, as well as refractive index changes, would be common-mode errors.

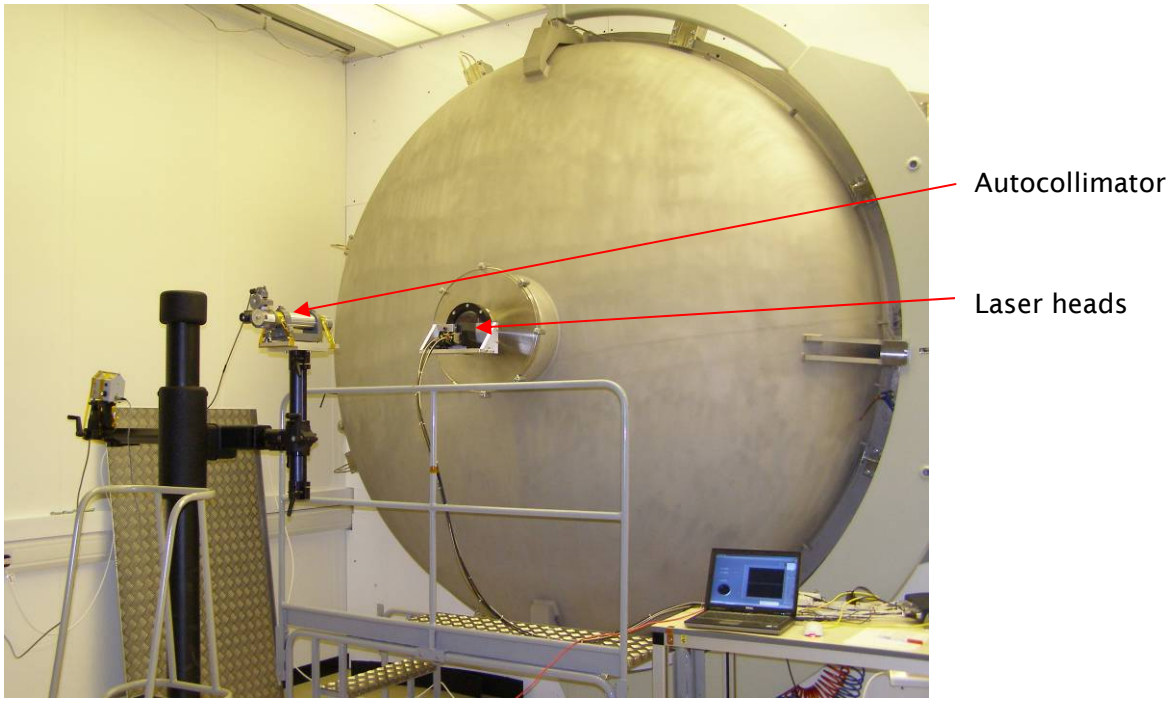

Figure 18. Thermal vacuum test chamber.

3.4.4 Scribe Marks

Scribe marks were made across bolted interfaces after they had been "locked". The marks were made over black, vacuum-compatible felt-tip marker, as shown in Figure 19. They were used to indicate whether gross slipping had occurred at these interfaces under vibration.

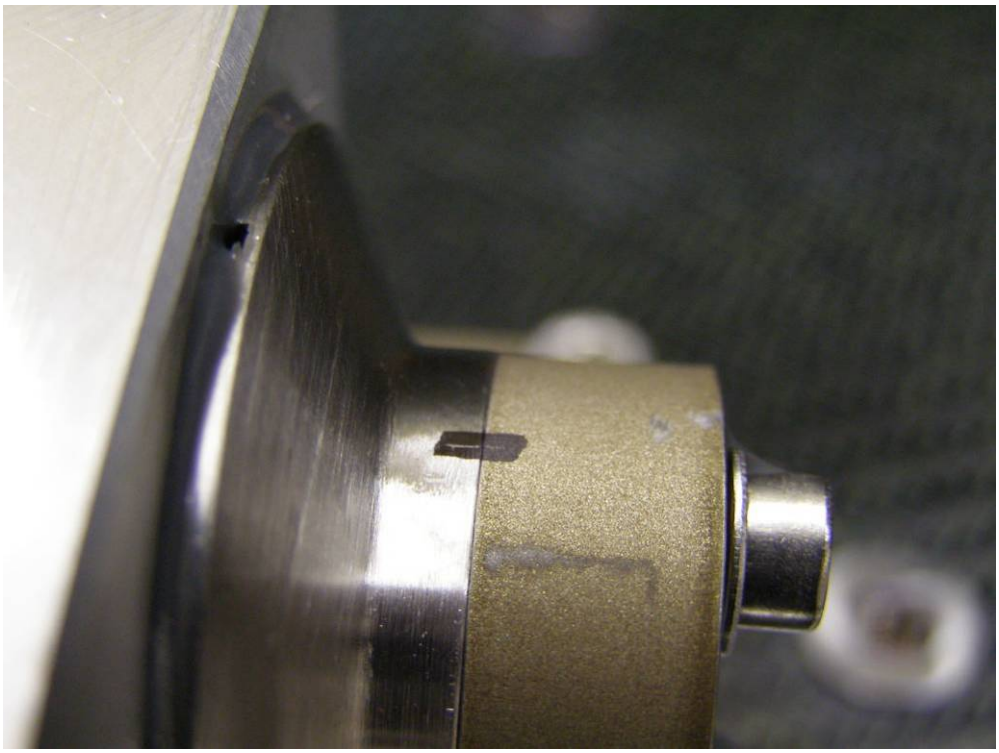

Figure 19. Scribe marks.

Table 5 summarises the metrology techniques used at various stages.

	CMM	Autocollimator	Laser Interferometer	Scribe Marks
Assembly		X		
Gravity Release		X		
Transport/Handling	X*	X		
Time		X		
Vibration	X	X		X
Thermal vacuum	X	X	X	

Table 5. Test and metrology matrix.

* The CMM measurements were only intended for assessing vibration and thermal vacuum movement, though transport of the test item was required to the CMM test facility.

3.5 Results

3.5.1 Assembly

Relative tilts between M1 and M2 during the assembly phase are summarised in Figure 20.

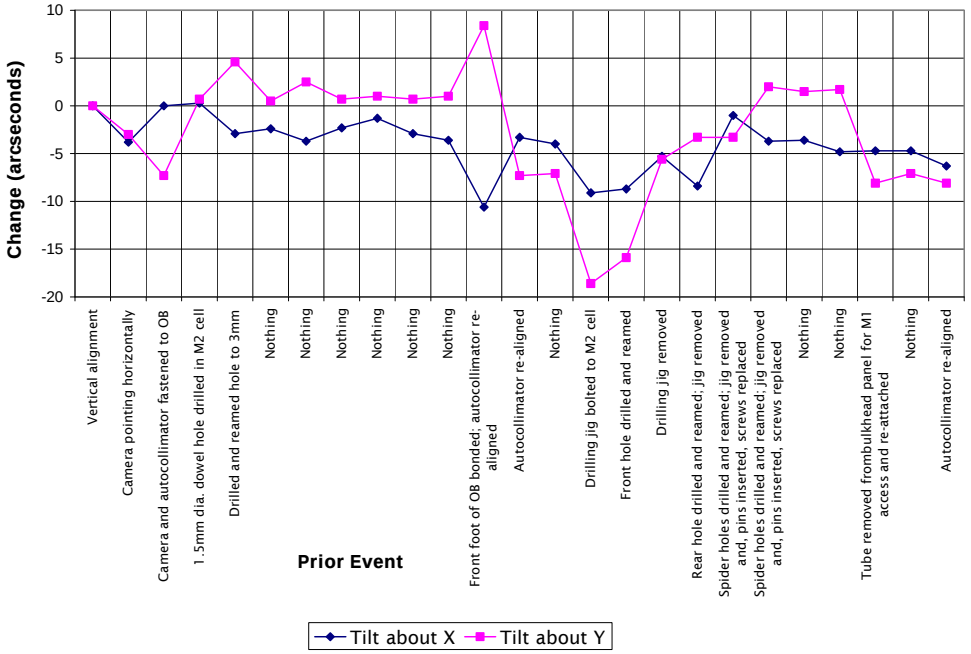

Figure 20. Tilts during assembly.

The effects of gravity release were 3 – 4 arcsecond tilts about each axis. The in-situ dowelling operations involved drilling, reaming and fitting of dowel pins. These had surprisingly little effect on alignment, less than 5 arcseconds in most cases. The attachment of a drilling jig to the M2 cell had a large (20 arcsecond) effect, though this was recovered when the jig was removed. The fastening of the BBM to a flat optics bench was found to induce tilts of up to 8 arcseconds even though this was done in a nominally strain-free way. The separating and reassembly of the two primary parts of the structure (the main tube and the bulkhead panel) induced a 10 arcsecond movement in one direction, and none in the other. It was found that transport in a van to and from another facility could impose tilts of up to 10 arcseconds. The entire assembly process lasted about a month after the dummy mirrors had been aligned and locked. Following the whole assembly sequence, the net movements were kept within 5 arcseconds and 10 arcseconds about both axes.

These tilts would have been acceptable for this type of optical system, with an overall tolerance budget of one arcminute per axis.

3.5.2 Vibration

The vibration test was successfully completed, with the low frequency behaviour correlating well with the FEM. Comparisons between the 0.5 g sine survey test and a harmonic response analysis are shown in Figure 21, Figure 22 and Figure 23. The point at which these responses was taken was the tri-axial accelerometer on the primary mirror. The analysis was only performed up to 300 Hz, in steps of several Hertz, with damping set globally at 2%.

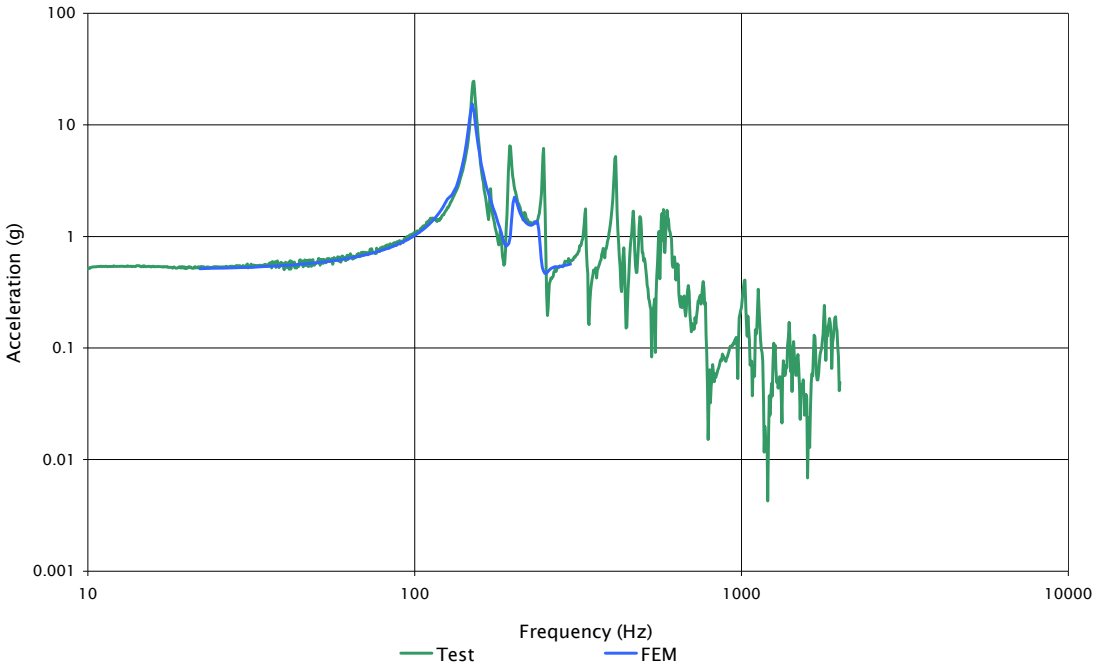

Figure 21. Comparison between test and analysis responses at M1 for sinusoidal excitation in the X direction.

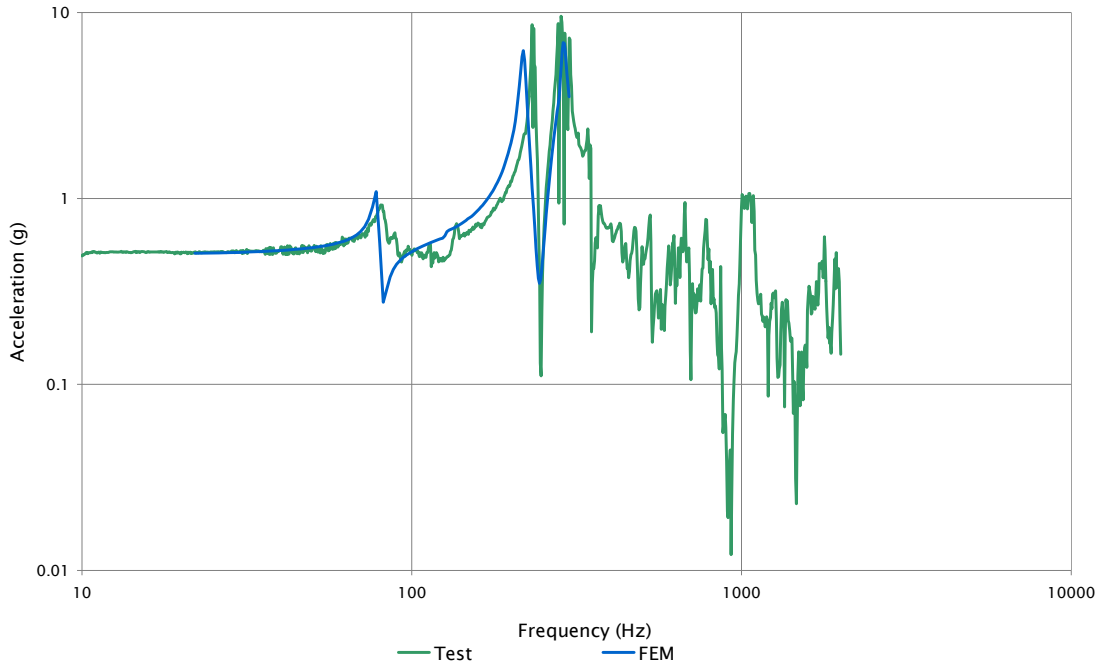

Figure 22. Comparison between test and analysis responses at M1 for sinusoidal excitation in the Y direction.

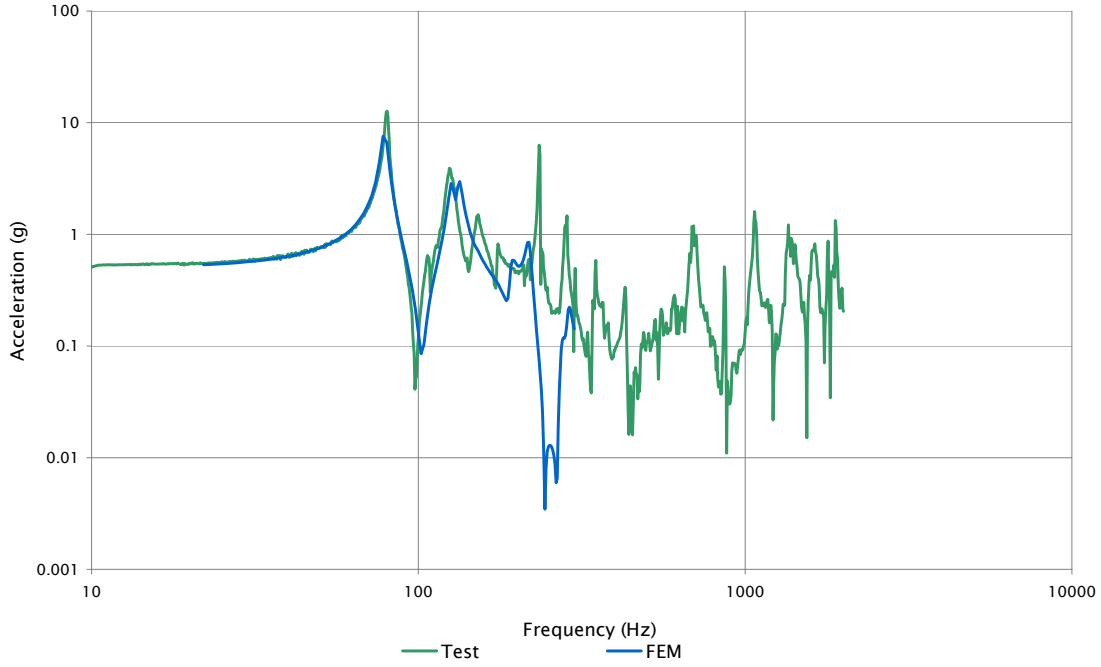

Figure 23. Comparison between test and analysis responses at M1 for sinusoidal excitation in the Z direction.

During vibration testing, the series of -6 dB shakes were to assess whether extra "bedding-in" shakes prior to final locking of optic positions could be used to improve stability. Unfortunately, during the final axis shake (X direction), it was found that an M6 screw had come loose at the connection between one of the spider frames with the main tube. Some very useful results were still obtained, though. A summary is shown in Figure 24.

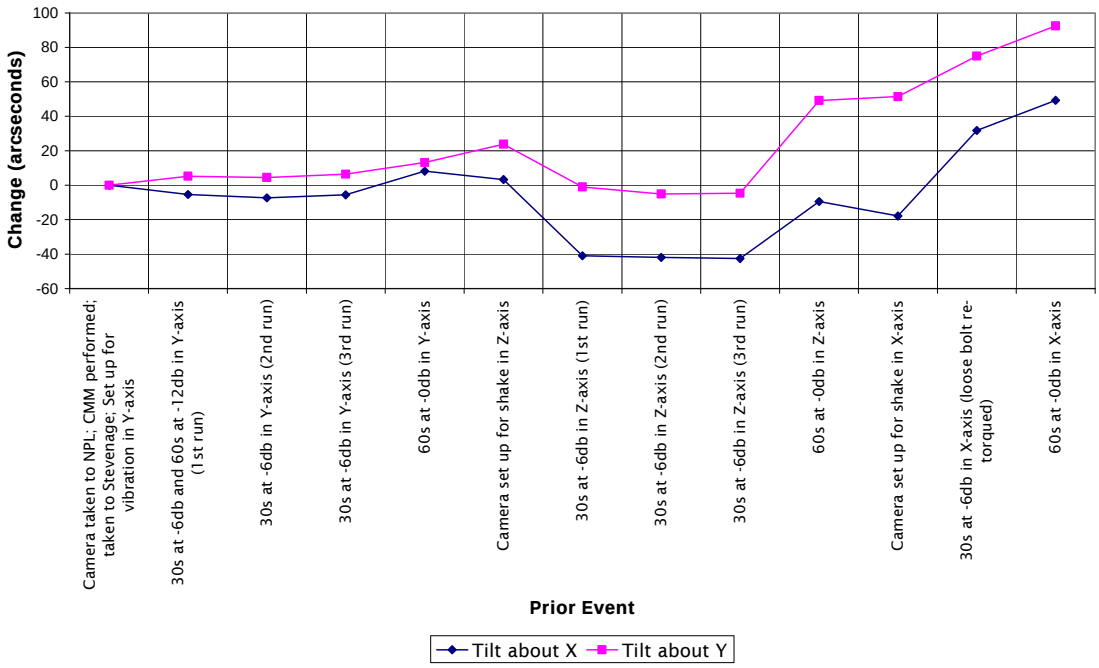

Figure 24. Tilts observed during vibration testing in all three directions.

The first direction of excitation was the Y direction, which is the out-of-plane direction and had the highest PSD levels (axis definitions are shown in Figure 25). The movements seen after the first -6 dB shake were about 5 arcseconds. This reduced to less than 2 arcseconds for the subsequent two -6 dB shakes. The full level shake in this axis produced movements of 8 arcseconds and 13 arcseconds.

The second axis was the Z direction, which is parallel to the breadboard's optical axis. Large movements of 25 arcseconds and 44 arcseconds were seen here on the first -6 dB shake, dropping to very low movements for the next two -6 dB shakes. Large movements were again seen after the full level shake in this direction.

During the third axis runs, the loose screw was discovered during the -6 dB shakes. It was re-tightened for the final -0 dB shake, which saw movements of 18 arcseconds in either direction.

It is interesting to note from the first two axes' results that induced movements appear to be dependent on power levels rather than duration of testing. If bedding-in vibration testing is proposed for a structure, short high-power shakes may therefore be the most effective approach.

For analysis of CMM results, the tooling balls were set up in groups of three to form six "planes" along the length of the BBM. These are shown schematically as the vertical lines in Figure 25. Each trio had balls in the 12 o'clock, 4 o'clock and 8 o'clock positions (the red circles in Figure 25). It was hoped that tilts and centroidal displacements along the tube could be easily assessed this way. A common datum for the measurements before and after environmental tests was defined as the centroid of the three tooling balls on the rear bulkhead pane skin.

The results show however that some of these planes did not behave as rigid bodies – the relative movements between "in-plane" balls were significant when compared with the movements of their centroids.

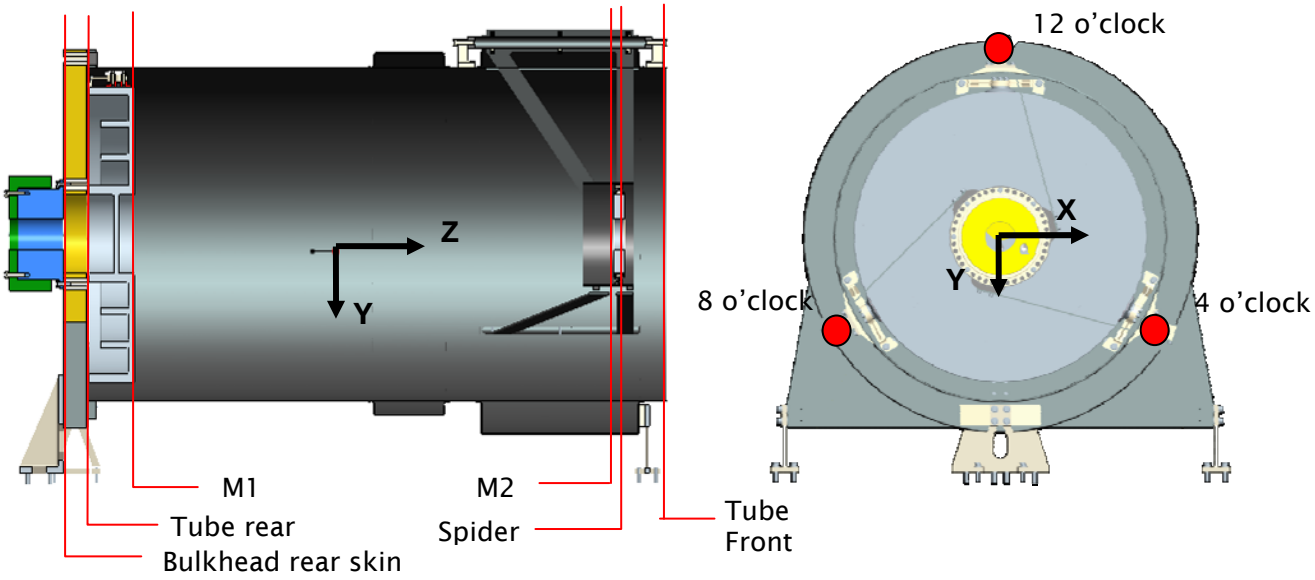

Figure 25. CMM metrology planes and tooling ball locations.

On the bulkhead panel rear skin, it was found that the two lower balls both moved upwards by about 5 μm, and the upper one downward (see Figure 26). This is commensurate with a permanent compressive strain in the vertical direction of 18 μm/m. There was no relative movement in the lateral direction, indicating that this effect was not a uniform in-plane expansion, and therefore

unlikely to be due to temperature or moisture effects due to the quasi-isotropic layup of the skin.

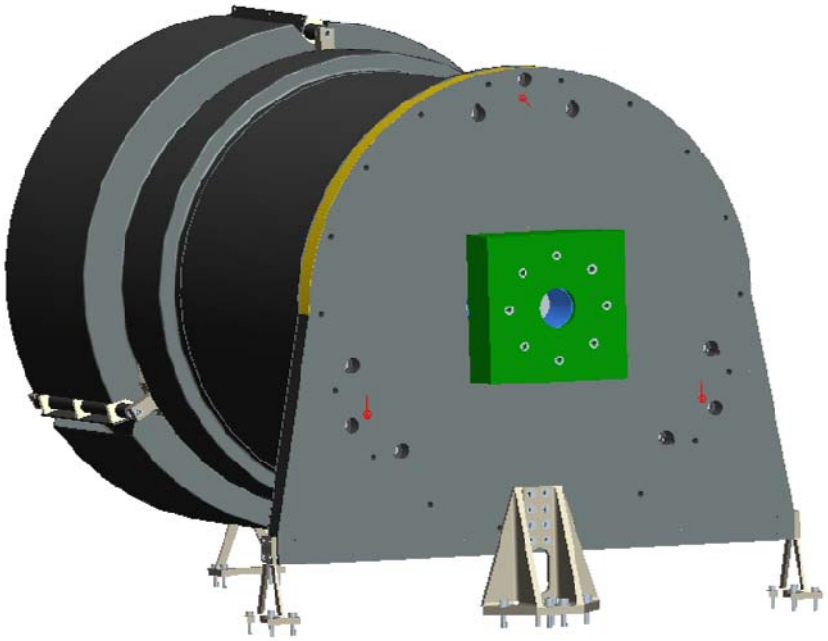

Figure 26. Movements on the rear of the bulkhead panel shown as red vectors.

The three balls at the front end of the tube show that this end became slightly ovalled, as well as tilting slightly about the lateral axis (the X axis in Figure 25), as though the whole tube had been bent. By comparing the results at pairs of balls mounted at either end of the tube in the same "clock" position, the longitudinal strain in the tube was determined. This was about 25 μm (or 26 μm/m) for both the lower clock positions in a tensile sense.

Large movements were seen at M2 (about 75 μm at the centroid) and the spiders, probably due to the loose screw. The tilt results at M2 produced by the CMM compared reasonably well with the in-situ autocollimator results (within about 10 arcseconds in either direction).

The M1 dummy mass behaved as a rigid body, though it did move with respect to the bulkhead panel. The net movement was equivalent to 68 arcseconds about the lateral X axis, 10 arcseconds about the vertical Y axis, and an axial movement at the centroid of the M1 surface of 27 μm. This movement was re-created in an exaggerated CAD model which is shown in Figure 27. There are two main interfaces where this could have occurred – the flexure-bulkhead panel interface, which was bolted and doweled, or the

flexure-M1 dummy mass interface which was just bolted. This is in addition to possible yield effects in the (titanium) flexure or the epoxy bondline to the dummy mass. A direct comparison between ball movements on the dummy mass and on the bulkhead panel (in adjacent positions) shows that movements occurred at all the flexure interface positions. The maximum of these was 95μm, and occurred in one of the stiff directions for the flexure, and in a direction that included a non-doweled bolted joint.

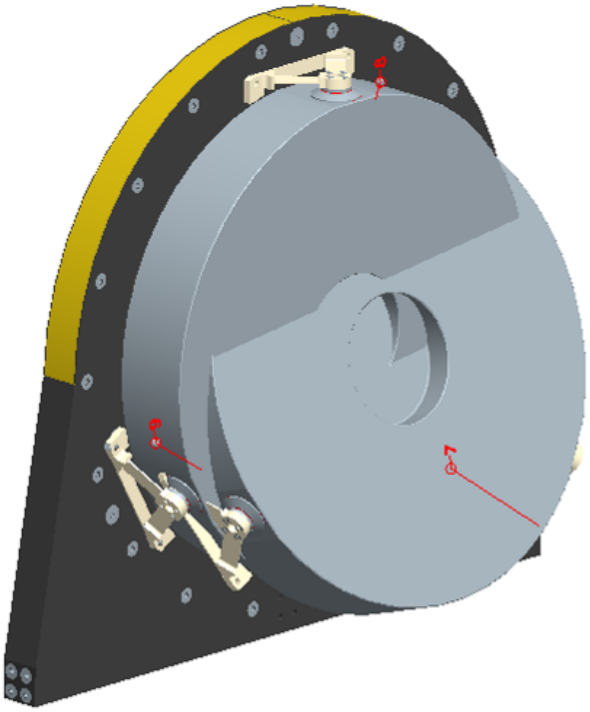

Figure 27. Exaggerated movements of M1.

Tooling ball measurements for the vibration test are shown in Table 6.

Plane	Tooling Ball Position	ΔX (μm)	ΔY (μm)	ΔZ (μm)
Rear skin of bulkhead panel	4 o'clock	-0.1	-4.8	0.0
	12 o'clock	-2.3	2.5	0.0
	8 o'clock	0.1	-4.8	0.0
Rear of tube	4 o'clock	21.4	-11.3	0.7
	12 o'clock	-2.6	-1.0	-3.5
	8 o'clock	-12.4	-9.2	5.0
M1	4 o'clock	26.9	42.6	94.6
	12 o'clock	43.9	39.1	-49.0
	8 o'clock	30.6	26.7	35.3
Front of Tube	4 o'clock	12.4	-34.9	23.2
	12 o'clock	4.3	-18.4	-1.2
	8 o'clock	6.4	-32.8	28.7
M2	4 o'clock	19.6	60.1	112.3
	12 o'clock	8.8	65.0	73.4
	8 o'clock	9.4	57.2	42.0
Spider	4 o'clock	78.7	-171.6	11.7
	12 o'clock	-90.6	73.0	46.1
	8 o'clock	-157.7	-128.3	29.0

Table 6. Summary of tooling ball results following vibration.

The scribe marks at the bolted interfaces were examined, though there were no signs of slipping at any interface. When the flexures were removed however, there were visible signs of fretting at most interfaces (dowelled and un-dowelled). This was manifested in black surface marks on both sides of the faying interface, and appeared to be worst around the two lower mounts. Interestingly, the dowelled interfaces showed no signs of fretting immediately around the dowel hole, but did around the screw hole (see Figure 28). This may be indicative of microslipping. This suggests that the addition of dowels to critical joints could reduce microslip.

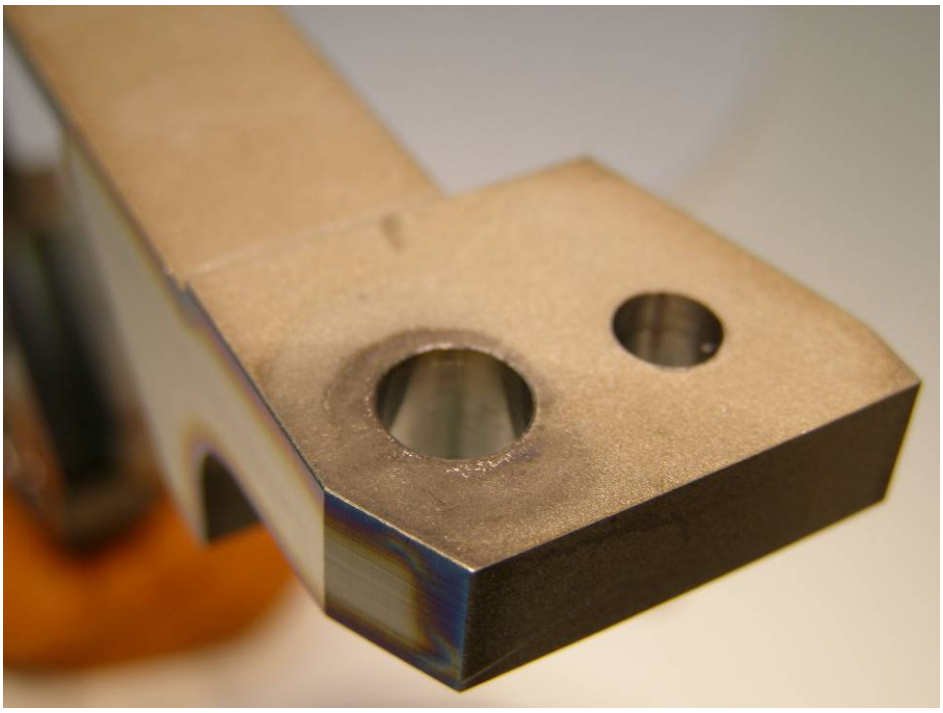

Figure 28. Fretting around the bolt hole (left) but not the dowel hole (right).

3.5.3 Thermal Vacuum

For thermal vacuum testing, the measurements made in-situ with the autocollimator and laser interferometer are summarised in Figure 29. The different displacement run numbers refer to different results files (discussed later). The commensurate temperature profile at various points in the structure is shown in Figure 30. The thermal tests included three hot cycles and two cold cycles. Temperature control was by radiative coupling to a shroud that surrounded the structure. A significant temperature lag was seen between the outer structure and the M1 dummy mass, as can be seen in Figure 30.

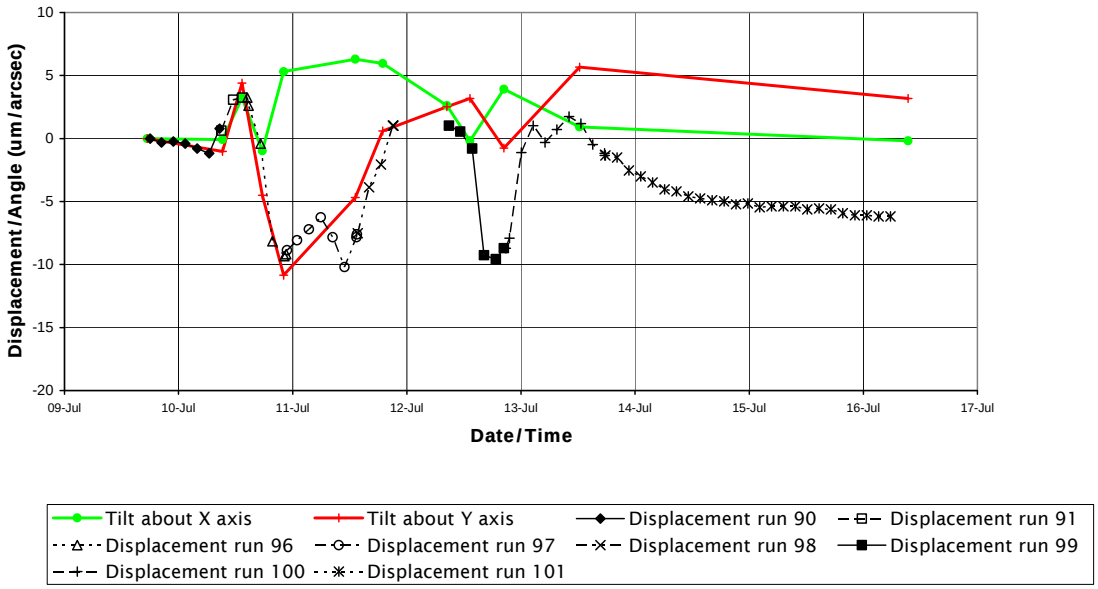

Figure 29. Displacement and tilt measurements over the test cycle.

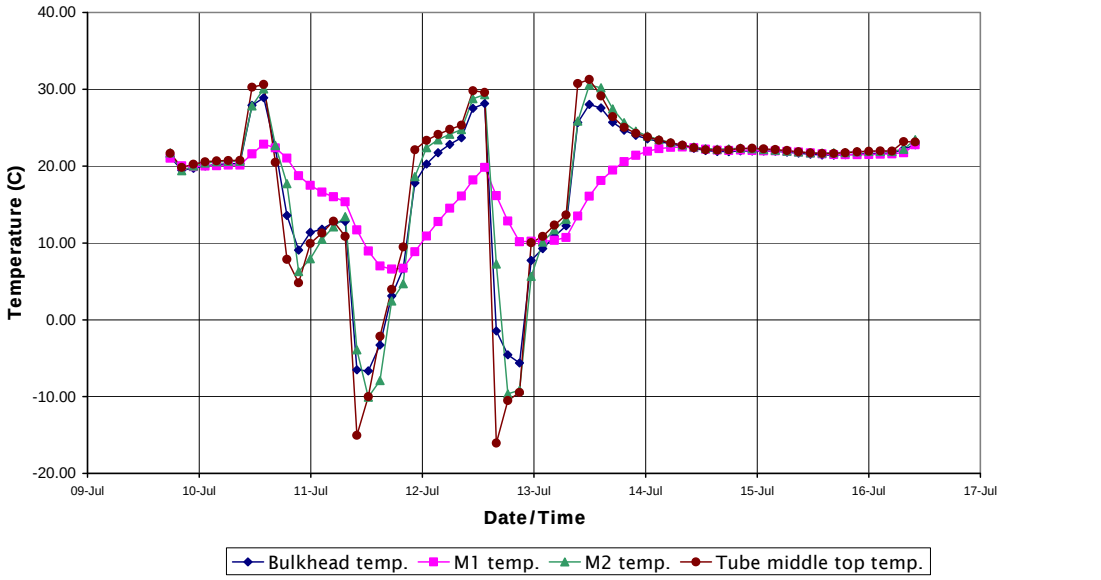

Figure 30. Temperature profile in various parts of the structure over the test cycle.

Small tilts about both axes were observed with the autocollimator throughout the tests. At the first 30°C plateau, both moved about 4 arcseconds. The largest tilts were seen during the first cooldown to -10°C, and were about 6 arcseconds about the X axis and 11 arcseconds about Y. These values decreased for the next thermal cycle. On returning to ambient, there

was no tilt about X but there was a residual tilt about Y of 3 arcseconds. An estimate of the sensitivity of tilt to temperature, determined using the final cooling curve from 30°C to 20°C is 0.1 arcsecond/°C about X and 0.25 arcsecond/°C about Y.

Laser interferometer readings were taken every 60s. Occasionally one of the beams would start to lose lock on its retroreflector, and the system required re-setting (resulting in a number of separate results files – the different runs shown in Figure 29). If this was done relatively quickly, there is no detrimental effect on the results. However data were lost for a period of about 12 hours on the night of the third day of the test. This means that the subsequent set of results (runs 99-101) cannot be directly related to the earlier runs. The start point for the resumption of data recording was set to the final data point before lock was lost.

For the first cycle, an expansion is seen on heating from 20°C to 30°C of about +3 μm. On cooling to -10°C, contractions were seen of about 14 μm. For periods of constant temperature, a gradual contraction was noticed. This is probably due to moisture expulsion. Initially the rate was about 2 μm/day, dropping to 1 μm/day by the end of the test. The total hygral swelling expansion was estimated to be 21 μm using manufacturer's CME (coefficient of moisture expansion) data.

The displacement vs temperature curves were generated using the main tube temperature as a reference. They are shown Figure 31.

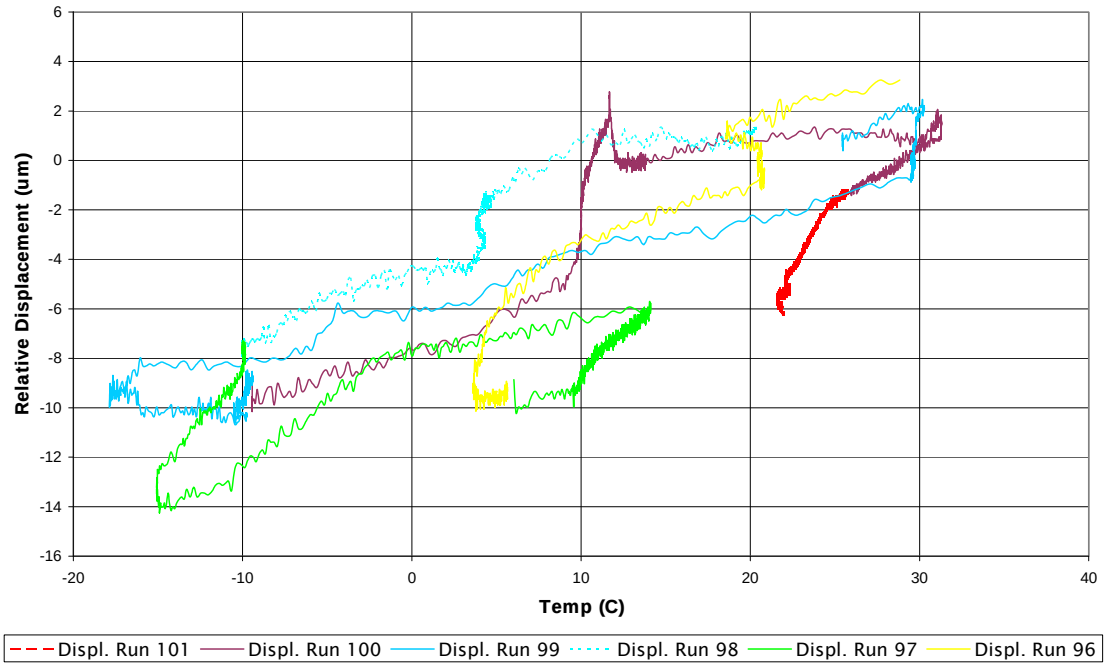

Figure 31. Displacement Vs temperature for the structure.

The gradient of the curves, normalised to the distance between the reference planes, is the CTE of the system. These results are quite linear over the range tested. From Run 99, the average CTE on cooldown from 30 to -10˚C is +0.215 ppm/˚C. From Run 100, the average CTE on warm-up from -10 to +10˚C is +0.299 ppm/˚C. The difference between these is within the experimental error described in the next section. For runs that have a slow temperature change, or a dwell, the gradient is seen to vary from this – for example Run 96 at around 4°C. This is probably due to moisture desorption having a greater net effect over these longer measurement periods. It should be stressed that this represents the CTE of the structural system, including flexures, spiders, dummy optic mounts, adhesive bondlines etc, rather than simply the CTE of the main tube.

Final CMM measurements showed that residual deformations due to thermal vacuum testing were small. A fairly uniform shrinkage along the tube was noticed, probably due to the different moisture content after vacuum testing. The residual axial displacement between M1 and M2 was 1.6 μm, and tilts were negligible about the X-axis and slightly over 3 arcseconds about the Y-axis. These again correlated well with the autocollimator results.

3.6 Error Estimation

During CMM metrology, six measurements were made on each ball for each result, with the average being used for analysis. The average standard deviation of ball position over all measurements was 1.78 μm, and the average spread over all 6 measurements was 4.99 μm. A set of measurements for the three tooling balls on M1 is presented in the Appendix to show the typical scatter in these results. The standard deviation and spread were lower for Y (vertical) direction measurements, and also lower for balls mounted at the bulkhead panel end of the BBM. The possibility of plasticity in the ball mounting adhesive was assessed with FEA, and the effect on stability found to be negligible for the relevant load cases.

For the autocollimator readings, the measurement technique evolved throughout testing to become more accurate. Taking measurements involved manually aligning pairs of fiducial marks and reading the angular difference from a Vernier scale. Three different people took measurements over the test period. In some test setups, the brightness of the reflected beam was very poor, and/or the test rig was slightly unstable. For each measurement five readings were taken of each position, and the average used. A typical measurement has a standard deviation of about 0.5 arcseconds, and a spread of about 1.3 arcseconds.

The resolution of the laser interferometer system was set to 79 nm. There was some noise on all the results, typically with a 0.2 - 0.3 μm amplitude. A spurious optical path difference is introduced within the retroreflectors as their temperature varies due to their thermal expansivity and a temperature-dependent refractive index. It was initially thought that the temperature difference between the reference planes would be negligible for most of the tests, and therefore this error would be common-mode.

However from Figure 30, it can be seen that there is a maximum temperature difference of about 10°C. The approximate size of the optical path difference due to this effect has been calculated to be 0.089 μm/Δ°C using manufacturer's material data for CTE and refractive index/temperature sensitivity. Additional errors due to the CTE of the retroreflector invar mounts and adhesive bondlines are estimated at 0.011 μm/Δ°C (again a negligible effect if both are at the same temperature). Therefore the likely error during the cold soaks, where the temperature difference is greatest, is about 1 μm (or

0.11 ppm/°C for the CTE), lower than the displacements observed. A cosine error due to the BBM axis being slightly angled relative to the laser beams was measured, and was found to be negligible.

3.7 Summary and Discussion of BBM Testing

A breadboard model was produced to test dimensional stability of a low cost Earth observation camera design. The structure was subjected to a typical sequence of environmental tests intended to qualify spacecraft instruments. The aim of this testing was to assess the dimensional stability of the structure under random vibration and compare it with stability loss due to the other environmental stressors.

The BBM optical bench structure showed good levels of stability during the assembly phase. The in-situ fitting of dowel pins, including drilling and reaming holes, introduced only very small movements, in the region of 5 arcseconds. Gravity release was responsible for 3 - 4 arcsecond tilts. The largest movements resulted from transport and handling events (10 arcseconds), even though these were performed with great care. The net tilts at the end of the process were 5 arcseconds to 10 arcseconds, which would have been just acceptable for the optical requirements of the structure.

Under thermal vacuum testing, the structure was very stable, with a structural CTE of under 0.3 ppm/°C. Tilts were observed of up to 11 arcseconds, though this was at a very low temperature. If the on-orbit thermal control system were able to maintain the structure's temperature between 0°C and 20°C, not an unreasonable requirement for a LEO mission, thermal expansion would be acceptable. The effects of moisture desorption were observed during this test, and would be significant without humidity control during AIV.

Large movements were seen during random vibration testing, even before the effects of the loose screw became apparent. Some of the movements occurred at jointed interfaces, while others occurred in the composite structure. In particular, permanent strains in the region of 15-25 μm/m were seen in the CFRP. This may be due to matrix yield or transverse microcrack initiation/propagation. On the subject of microplastic yield in CFRP, there is some discussion in the literature on the effects of low temperature thermal cycling and hygral cycling (which both tend to propagate transverse

microcracks[16]), but little on vibration load cases. These are necessarily different as they result from directional (and possibly complex) stress states rather than from the quasi-uniform expansion/contraction of the composite constituents. As noted in the literature survey, failure criteria for composites can be complex, and are designed for assessing gross structural failure rather than microyield induced by cyclic stresses. Dimensional stability loss in this material under random vibration is investigated further empirically in Chapter 4.

Interfacial movements were also observed, with a maximum 95 μm movement seen across a flexure interface to a dummy mass. Movements in the tens of microns were evident at interfaces that included dowel pins, and those that did not. Evidence of fretting was seen on some dowelled interfaces, though not directly around the dowel pins, suggesting that they still provide some resistance to interfacial sliding.

Under random vibration, there was a tendency for the structure to "bed-in". The degree of bedding-in was dependent on the amplitude of the input levels, rather than their duration. This is an important finding and has direct relevance for future stable structure development projects. Short duration bursts of random vibration could be used to condition high stability optical bench structures prior to the final locking of optical component positions.

A summary of the peak levels of dimensional instability observed for each environmental stressor is presented in Table 7.

Event	Approx Peak M1/M2 Tilt (arcsec)	Approx Peak Displacement (μm)
Assembly	5	N/A
Gravity Release	4	N/A
Transport/Handling	10	N/A
Vibration	92	158
Thermal Vacuum	11	14

Table 7. Summary of contributions of environmental tests to dimensional instability.

3.8 Conclusion of the BBM Tests

It was found that while it is relatively easy to design and build a space optics bench composite structure that is stable during assembly, under vacuum and under thermal cycling, random vibration testing may introduce significant non-recoverable instabilities. These are partly due to microyield in the composite structure, and partly due to movements at bolted interfaces. There is little in the literature on this subject, and it is an area where further work may help to improve the state of the art in stable structures. In particular, there are no data for the dimensional stability of materials or joints under random vibration, and no recommended test procedures for evaluating such data. Nor are there any analytical techniques for predicting instability in built-up structures. It is suggested that the development of bespoke techniques for empirically evaluating dimensional stability in material and joint samples in controlled tests would be of great value to practitioners of stable structures, and add substantially to the state of the art. The rest of this research is devoted to developing this theme. Chapters 4 and 5 cover the development of test setups and methods, while chapter 6 covers analytical methods.

4 Dimensional Stability Testing of Materials Under Random Vibration

4.1 Introduction

The next phase of the research was to address the second of the three goals outlined in the introduction to this thesis:

- "To develop empirical methods for the quantitative assessment of dimensional instability in structures subjected to random vibration."

This chapter looks at the first part of this goal (developing empirical methods). A later chapter addresses the second part (analytical methods).

To meet this first goal, specific areas of the structure were investigated in further detail, by performing controlled tests on individual structural elements. The BBM tests revealed that major areas responsible for stability loss under random vibration are in structural materials and at bolted interfaces. The literature review shows that the state of the art in these areas is not advanced, in terms of either predictive theories or test data. This chapter describes testing performed on material samples, and the following chapter describes joint tests

These tests required bespoke test setups. Such tests do not appear from the literature to have been attempted before. For the material sample tests, a single test setup that can accommodate different material test samples was possible.

As such tests have not been attempted before, a main aim of this phase of the project was to assess and validate the test setups and metrology techniques, as well as provide useful test data on specimens of structural elements. An additional aim was to assess variability in results – after all, the input loads are random, so some variability would be expected even for identical test samples. The final main aim was to assess the evolution of dimensional instabilities under random vibration, as knowledge of this could enable clear guidelines on bedding-in tests and qualification levels – the BBM test results definitely showed that this was a promising area of investigation.

A major challenge in dimensional stability testing is that movements of interest are generally sufficiently small as to make their measurement difficult. Whilst most tests for structural integrity would seek to measure permanent material strains of 2000 μstrain (0.2% proof, or "yield"), the strain levels of interest for stable structures are typically in the region of 1-100 μstrain.

The material tests made use of three identical samples – each was a thin panel with simple support. Masses were attached at two points. They were tuned to resonate at a particular frequency. At this frequency, the modeshape approximates a 4-point bend test configuration. Residual strains were measured using strain gauges, and by measuring the curvature of the beam optically. Coordinate measurement machine (CMM) measurements were also performed.

4.2 Test Description

4.2.1 Test Configuration

It was sought to develop a test setup that could used to mount material test samples on a shaker and excite them to levels that would result in dimensional instability. To this end, it was decided to use material samples in strip form, that would deform in bending when excited. This would enable relatively high stresses to be generated in relatively lightweight test samples, and would enable them to be easily "tuned" to respond at a target frequency. This form has the added benefit that it is reasonably easy to procure samples of most materials (including CFRP composites).

Several options were considered for the design of the rig. The first was a cantilever beam supporting a mass (ie, with the beam being the material strip sample). This was discounted since the peak bending moment (and hence the area of anticipated maximal residual strain) would be at the supported end. At this point, it may be difficult to separate the localised (contact) effects of the mounting arrangement from the bending effects of dynamic stress.

A second option was a variation on a classic three-point bend test. The beam would be simply supported, with a mass attached in the centre. This configuration was discounted for similar reasons to the cantilever option – that the peak bending moment would occur at the point of attachment of the mass, and the attachment technique affect the results.

The third method was a variation on a four-point bend test. A simply supported beam would have masses attached in the supported section, reasonably close to the supports. For an ideal four-point test, the peak moment would plateau in the region between the two masses. This is attractive since the peak bending moment occurs over a (potentially) long region of the beam, making a small residual strain easier to measure as a deformation. Although this peak stress occurs immediately adjacent to the pair of masses, most of this peak region is not in contact with support structure or attached masses. For the case of dynamic loading, the first mode shape departs slightly from the classic four-point test, giving a slightly elevated peak stress in the centre of the beam. It was this final configuration that was chosen for further study.

4.2.2 Test Setup

The test samples were strips of size 250 x 50 mm. Stainless steel masses were bonded 150 mm apart, and the supports were 200 mm apart. The sample test layout is shown in Figure 32.

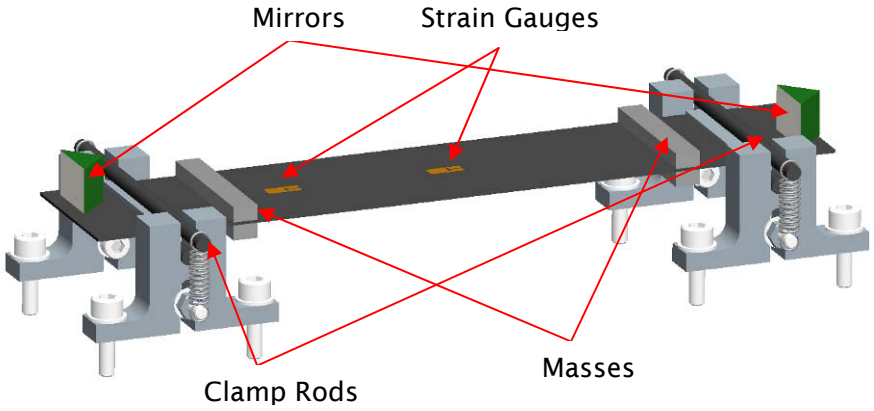

Figure 32. Material strip sample test setup.

The mounting concept was designed to provide simple support for the samples. There were several options to achieve this, including using rotary and linear bearings. However for simplicity, the method used was based on a knife-edge clamp concept to achieve a line-contact support at each end.

Rather than using sharp knife-edge devices, a pair of cylindrical rods were used at either end to clamp the test pieces. They were spring-loaded towards

each other using four extension springs (with preloads calculated to prevent gapping under the highest loads possible during the test). To avoid problems with high contact stresses at these interfaces, thin aluminium pads were bonded to the sample surfaces to distribute the force from the rods. The pads at one end were machined to be slightly concave (see Figure 33), in order to give some longitudinal location to the samples (this is equivalent to the axially-constrained end of a simply supported beam).

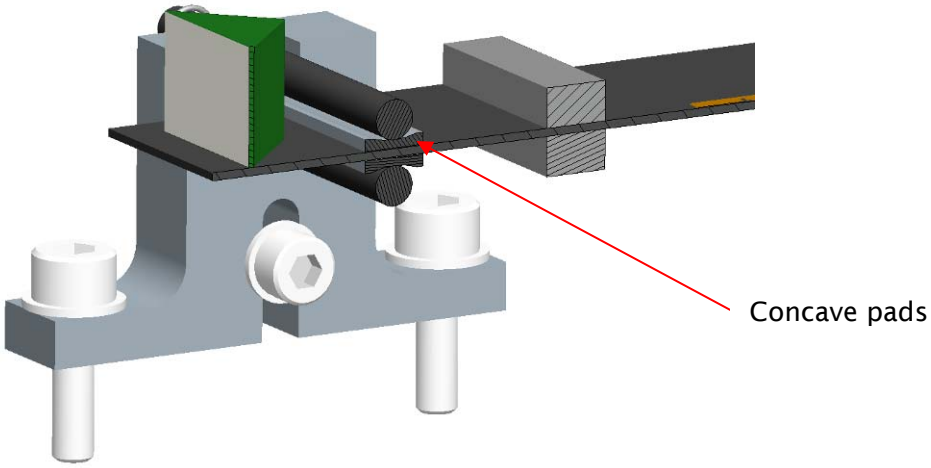

Figure 33. Cross section of sample support.

This setup relies on each pair of rods being aligned very well – if there is a slight offset between their contact lines' in the longitudinal direction, unwanted bending moments could be induced (0.1 mm offset would result in a 2.4 μstrain spurious strain). Tight clearances with fine tolerances on these rods within their housing mounts means that misalignments of this size are unlikely.

Extension springs were used, and the preload (20 N) set by adjusting the amount of extension (Figure 34).

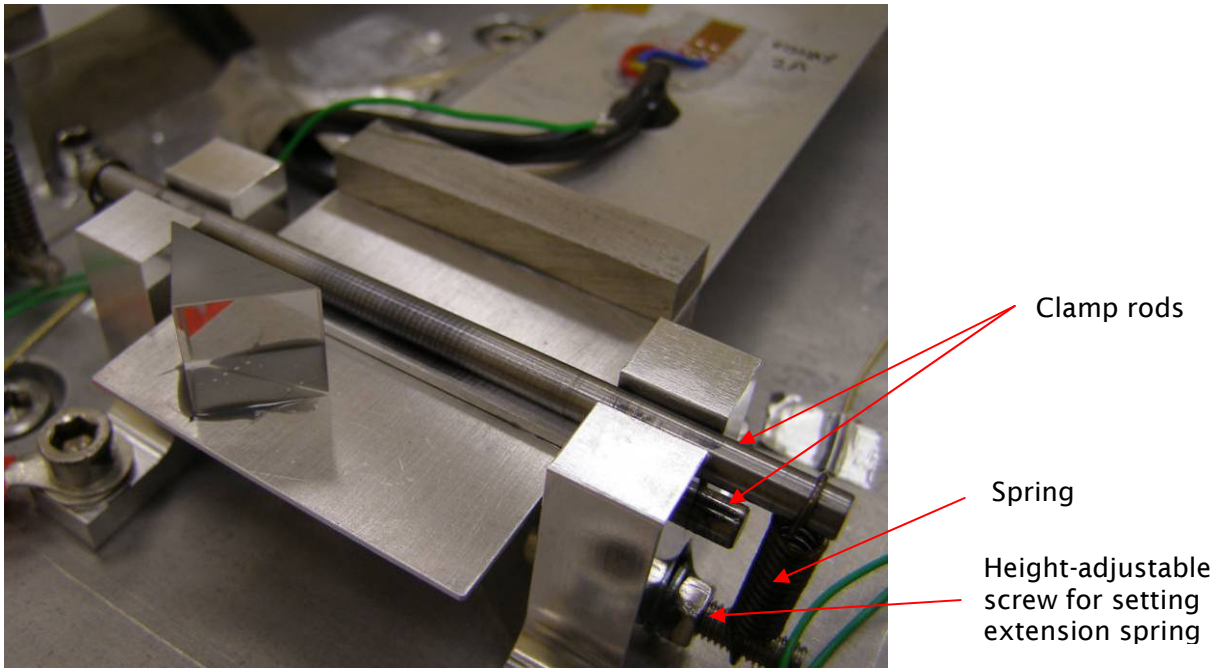

Figure 34. Support of Al alloy sample showing clamp rods and springs.

A test rig was produced that was capable of simultaneously testing three samples under identical dynamic loads (see Figure 35).

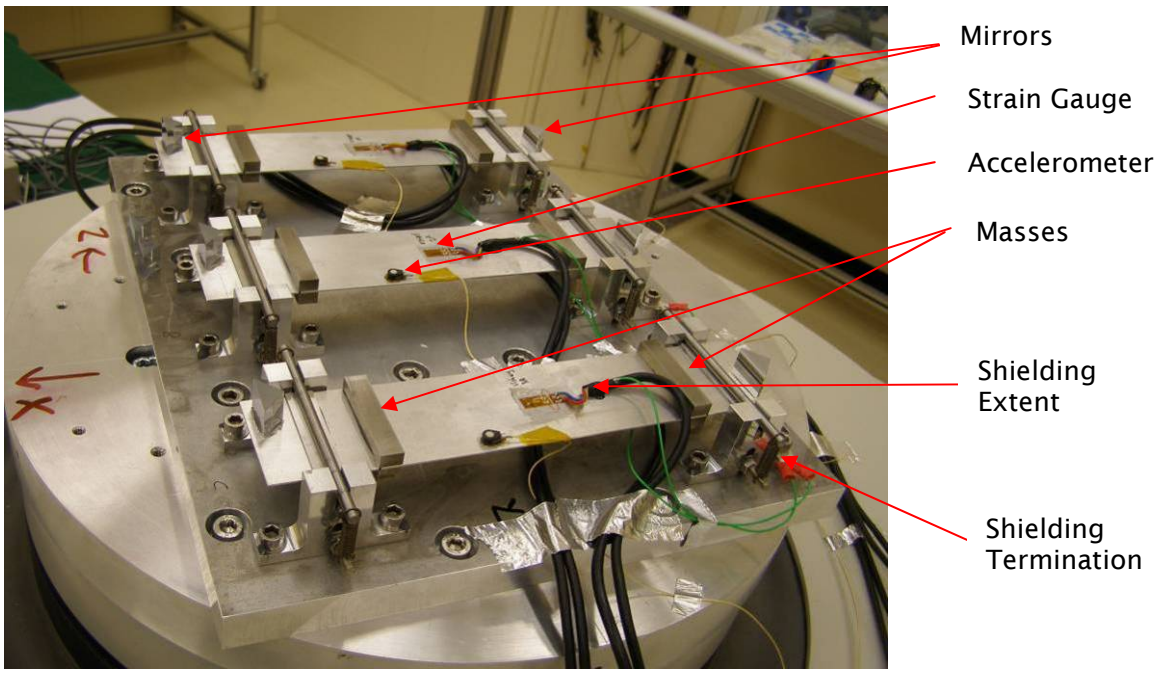

Figure 35. Overall test setup showing three samples.

4.2.3 Materials

Two materials were tested – aluminium alloy 2024 T3 and a CFRP composite.

The Al alloy was chosen because there were some test data available in the literature for microyield and also cyclic plasticity for similar grades. The material was procured in 1 mm thick sheet form, and machined to produce the correct size strips. It was annealed at 200°C for 1 hour to relieve internal stresses.

The CFRP was chosen because it is a material that is widely used in stable optical structures. It was a skin composed of 8 unidirectional plies in a (0°, 90°, +/-45°) quasi-isotropic layup. The fibres were high-modulus M55J, and the resin was Advanced Composites Group LTM123, a cyanate ester. A low temperature cure was used (to minimise thermal strain between fibres and resin on cooldown), with a long postcure (to complete cross-linking of the resin polymer chains). The thickness of the final strips was about 1 mm. This is also he same material that was used for many of the structural areas of the BBM.

The masses were bonded-on stainless steel blocks. For the aluminium samples, the masses were 0.050 kg at either end; for the CFRP samples, they were 0.031 kg. For the aluminium samples, the natural frequency was 41 Hz and for the CFRP it was 81 Hz (the reason for the difference between the two is that following higher-than-expected damping during the CFRP tests, it was sought to increase the dynamic stress levels for the subsequent Al alloy tests – this is explained in more detail later).

4.2.4 Test Procedure

Following assembly, metrology was performed on the three samples. The test rig was then set up on the shaker, and metrology performed again. Vibration test runs of 60s duration were performed, with metrology performed on each sample between each run. The procedure required two phases of testing – a microstrain “Search” phase and an “Evolution” phase. During the Search phase, the test levels were sequentially increased in 3dB steps, starting very low relative to some “baseline”, until observable yield was seen (with observable yield defined as unambiguous residual strain in the 5 – 20 μstrain region). At this point, the Search phase would finish and the Evolution phase would start. Any higher-level Search phase tests would be missed, and instead

the evolution of residual strain would be examined with further repeated tests at and around the observable yield level. The procedure is shown schematically in Figure 36.

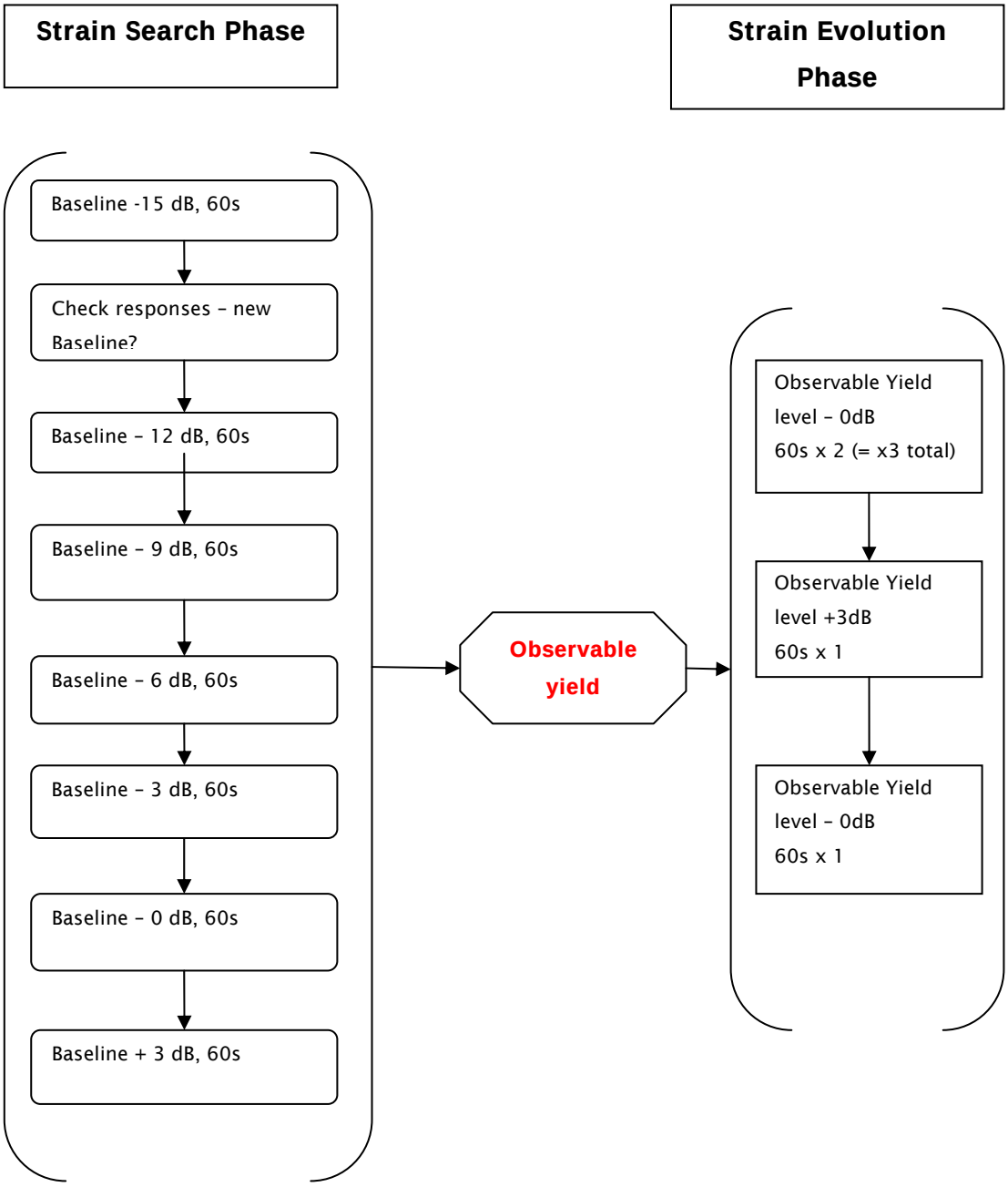

Figure 36. Nominal test procedure

In practice, observable yield was not reached in the CFRP samples, so additional higher-level tests were added to the Search phase, going up to +15 dB.

4.2.5 Loading

For the CFRP test, a baseline load spectrum was derived, using FEA iterations to predict the level at which 1-σ stresses of 60 MPa would be seen (the stress level thought to have induced microyield during BBM testing). The spectrum shape is typical of qualification testing[99], and includes the first resonance on a 0.1 g^2/Hz plateau (Table 8). The FEA model was conducted using ANSYS v12. It was a simple 3-D model using shell elements (see Figure 37, Figure 38 and Figure 39). Damping was assumed to be 1%.

Figure 37. FEM of the CFRP samples, showing supports (pale blue) and masses (red).

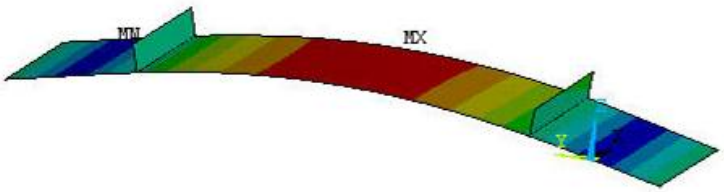

Figure 38. First modeshape of CFRP sample (81 Hz).

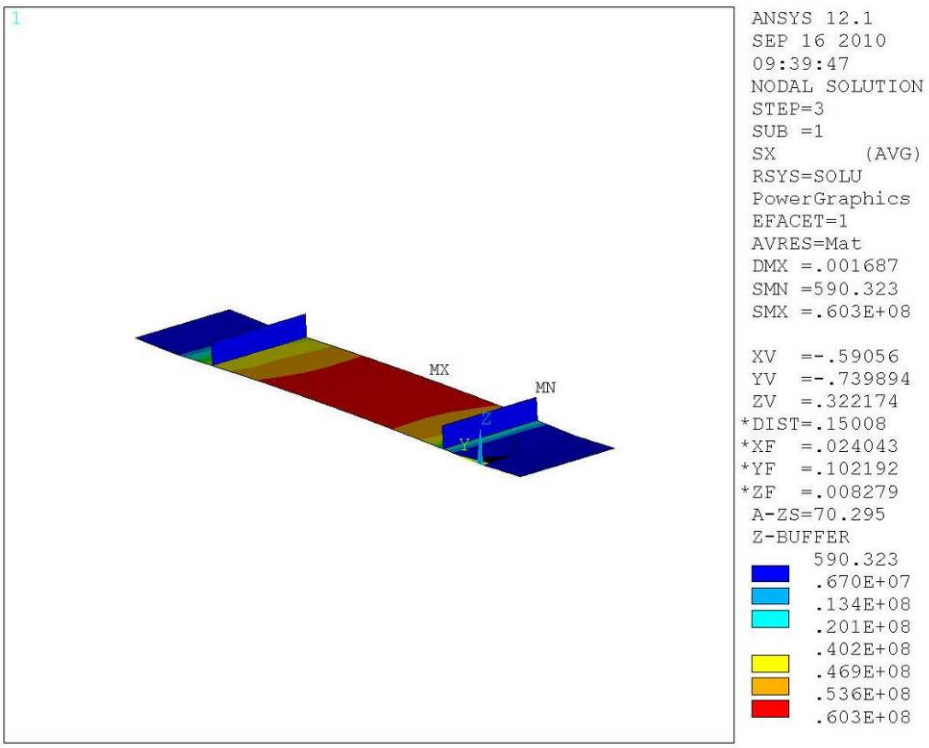

Figure 39. 1-σ axial stress response to baseline spectrum (max. stress = 60.3 MPa).

Frequency	Level
20-70 Hz	+3dB/oct
70-300 Hz	0.1 g^2/Hz
300-2000 Hz	-3dB/oct

Table 8. CFRP baseline test spectrum 7.66 gRMS.

A similar test spectrum was used for the Al alloy test, albeit with the plateau starting at 30 Hz in order to fully encompass the first peak. The spectrum is shown in Table 9.

Frequency	Level
20-30 Hz	+3dB/oct
30-200 Hz	0.1 g^2/Hz
200-2000 Hz	-3dB/oct

Table 9. Al alloy baseline test spectrum 6.44 gRMS.

4.2.6 Metrology

Two methods were used to measure residual strain between each test run. They were strain gauges and curvature measurement of the beam optically. The execution of these methods varied slightly between the CFRP tests and the Al alloy ones. In addition, CMM measurements were used.

Strain Gauges

The instrumentation setup limited the number of strain gauges to two per sample. The Al alloy samples used strain gauges located on the upper and lower surfaces, directly opposed in the centre of the sample (see Figure 35). For the CFRP samples, both strain gauges were positioned on the top surface – one in the centre, and one offset towards one of the stainless steel masses (as shown in Figure 40). The reason for this was to assess the RMS bending strain at two points along the stressed portion of the sample for comparison with FEA results.

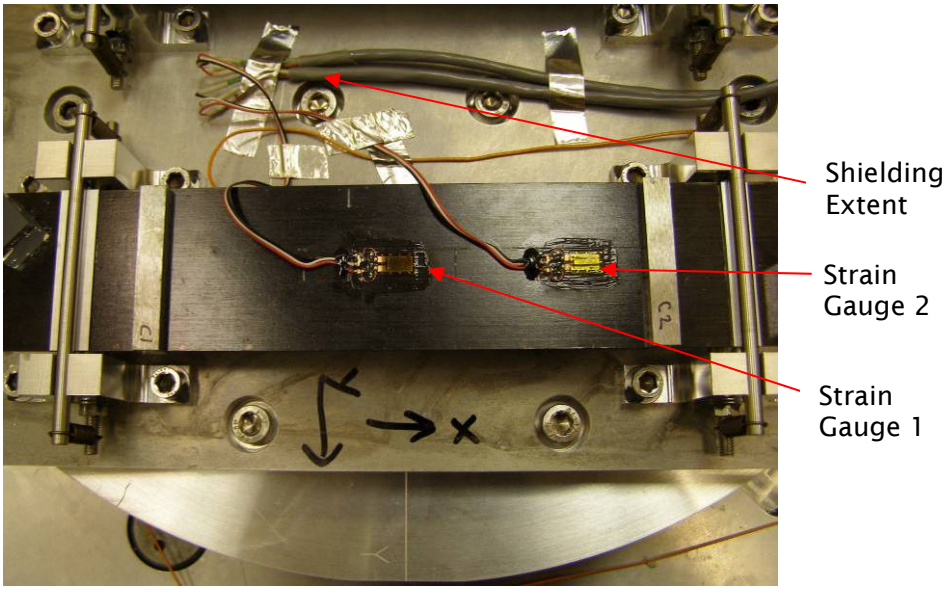

Figure 40. CFRP sample strain gauge positions.

Shielding was applied slightly differently for the two tests, due to lessons learned during the first test. For the CFRP samples, strain gauge leads were shielded only at the strain gauge amplifier end, with the shielding extending only as far as the test fixture, leaving about 150 mm of wire un-shielded (see Figure 40). The Al alloy samples used shielding terminated at both ends, with the shielding extending right up to the strain gauge. For both tests, strain gauge measurements were made directly from the amplifier using a voltmeter. The voltmeter leads were shielded for all measurements apart from the first CFRP ones. In the case of the Al alloy tests, facility data acquisition equipment was also used to capture strain information during the dynamic tests (providing a strain spectral density response).

A seventh gauge, located on a fourth sample that was not subject to vibration, was also recorded to act as a "control" sample and assess any long-term effects over the duration of the test (ie temperature and humidity fluctuations – see Figure 41).

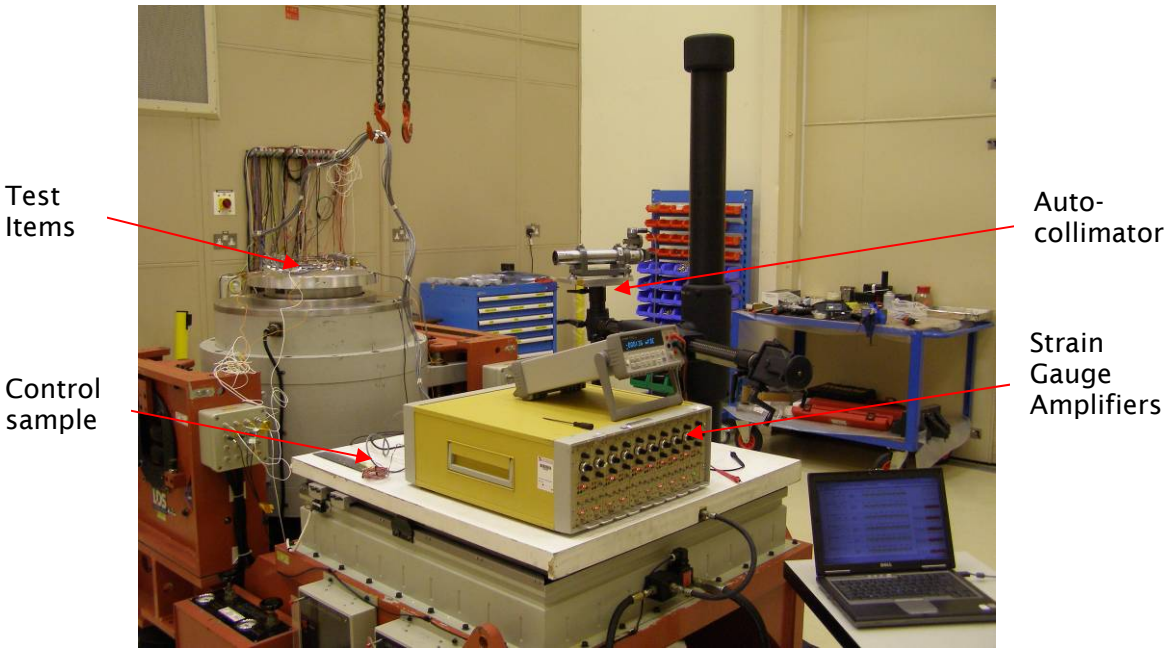

Figure 41. Test setup.

Autocollimator

The curvature measurement relied on a pair of parallel flat mirrors bonded to either end of each beam (Figure 42). The mirrors were located outside the supports, in a region that was nominally un-stressed. The resulting measurement therefore gave an average residual strain over the stressed area, rather than the local measurements provided by the strain gauges. An autocollimator with arcsecond-level accuracy was used to measure this angle before and after each vibration run. The geometry was such that a 1 μstrain average residual strain would produce a tilt of 0.97 arcminutes, easily measurable.

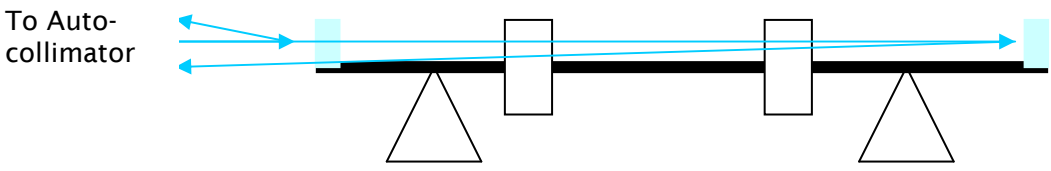

Figure 42. Tilt measurement using mirrors.

Figure 43. Samples on shaker

CMM

The third measurement was using a CMM to probe points at 20 mm intervals along each sample. The CMM was located in a different facility and was not portable, so it was only practical to perform measurements before and after the entire series of tests. The main purpose of this measurement was to verify the results of the other two metrology techniques, and to assess the final shape of the deformed samples.

4.2.7 Static Test

A fifth sample of each material was subjected to static four-point bend testing. The test configuration was nominally identical to the dynamic test setup, though with different support structure (the samples simply rested on the rods, and were not clamped). Loading was applied at the same locations as the two masses, using a tensile test machine (Figure 44). The load was cycled, starting with a low load (5 – 10 N) and increasing in increments of 5 – 10 N. Loads were completely relaxed between cycles, and residual strains were recorded at these points using the strain gauges. A typical time history for this test is shown in Figure 45 for a strain gauge on the CFRP sample (the signal was clipped above 1000 μstrain).

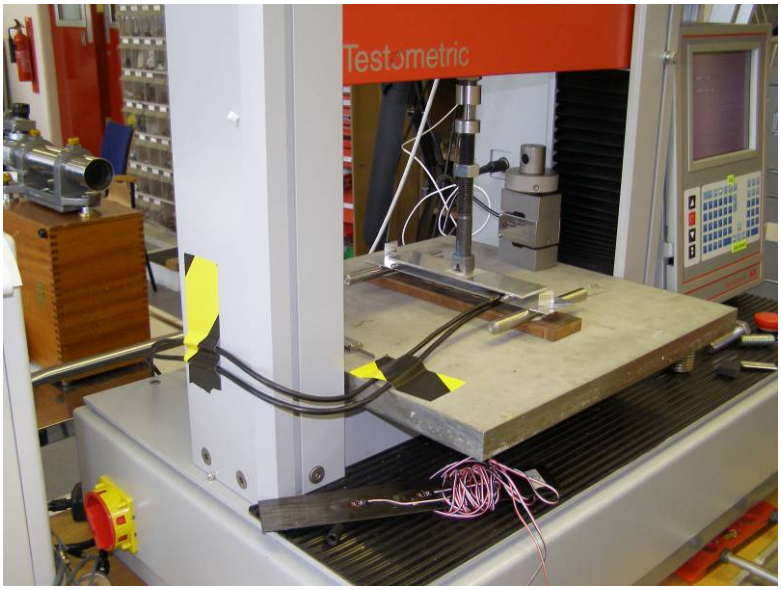

Figure 44. Static test setup

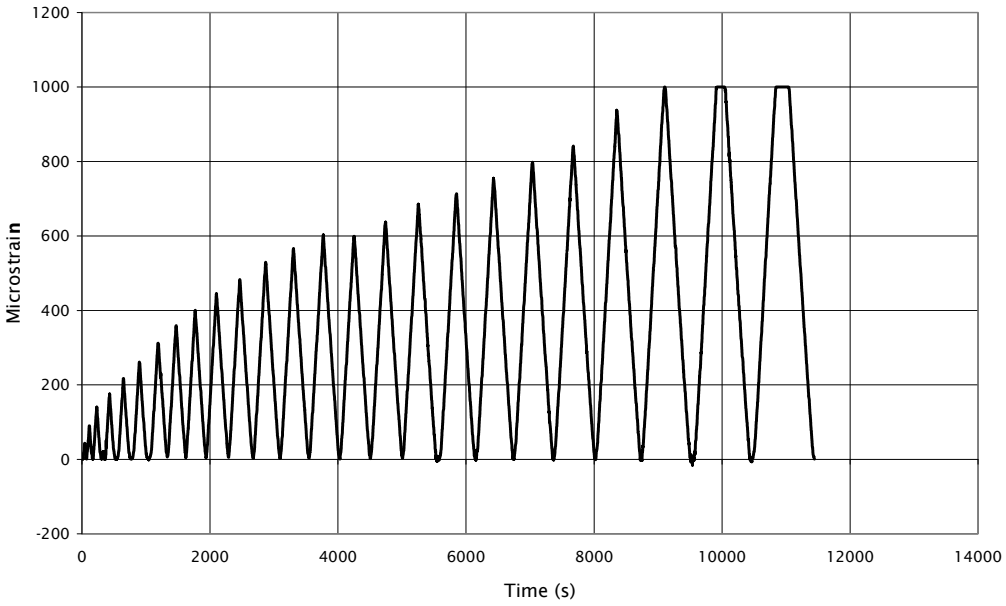

Figure 45. Strain history for the static test of the CFRP sample.

4.2.8 Instrumentation

The CFRP test took place on a 40 kN Ling Dynamic Systems Model 954 MkII. The aluminium samples were tested with a 60 kN LDS V8-440 SPA56K shaker. Acceleration was measured with Bruel & Kjaer Type 4517 miniature accelerometers.

The strain gauges on the CFRP samples were Vishay CEA-00-250UW-350 devices (CTE-matched to the samples). The Strain gauges on the aluminium test samples were Vishay CEA-13-250UW-350 devices (CTE-matched to aluminium). Both sets of gauges were bonded to the test samples with Vishay M-Bond AE-10 by Vishay Measurements Group UK Ltd. Both sets of gauges were shielded, as described previously.

For both test setups, strain gauge amplification was via a Vishay 2200 Signal Conditioning System with internal temperature compensation. All strain gauges were wired in a quarter-bridge configuration. Strain response was measured directly from the 2200 System with a digital voltmeter.

The autocollimator was a Taylor-Hobson Model TA51.

The static test used a Testometric AX500 machine. The strain gauge amplifiers for this test were RDP Electronics model 628s.

4.3 CFRP Test Results

4.3.1 In-Situ Measurements

Strain gauge and autocollimator results are shown in Figure 46, Figure 47 and Figure 48 for CFRP samples A, B, and C respectively. The horizontal scale shows the event that precedes the measurement, the vertical scale shows μstrain and arcminute measurements, which are approximately equivalent. For each strain gauge, “1” is the one in the centre, and “2” is the off-centre one, as shown in Figure 40.

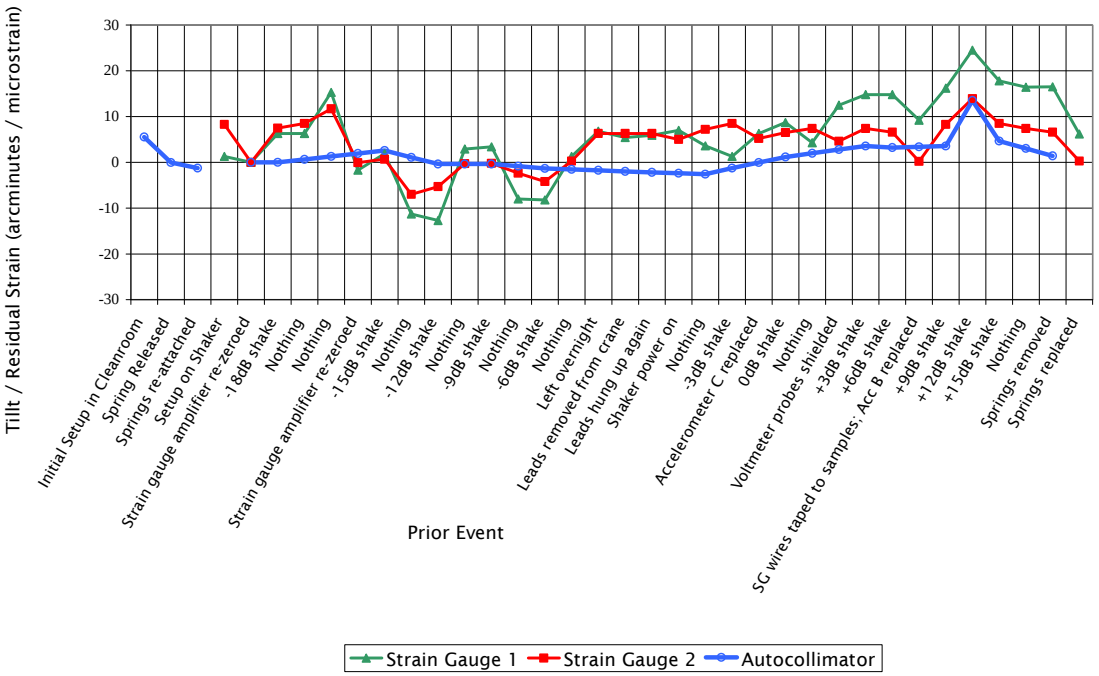

Figure 46. Sample A Results

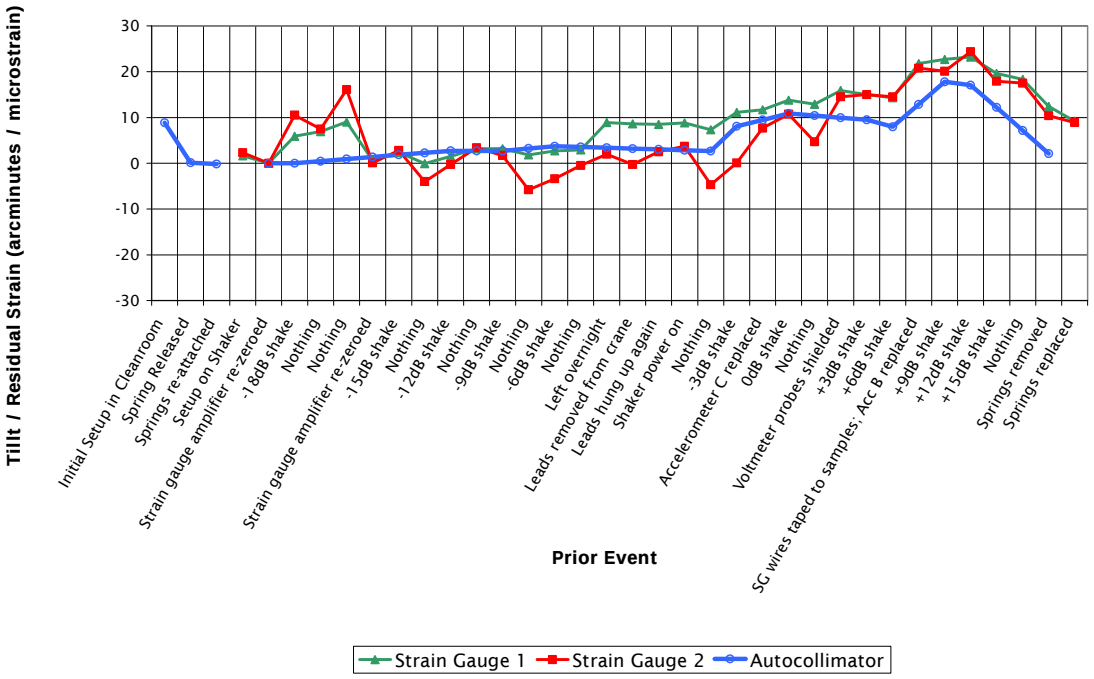

Figure 47. Sample B Results

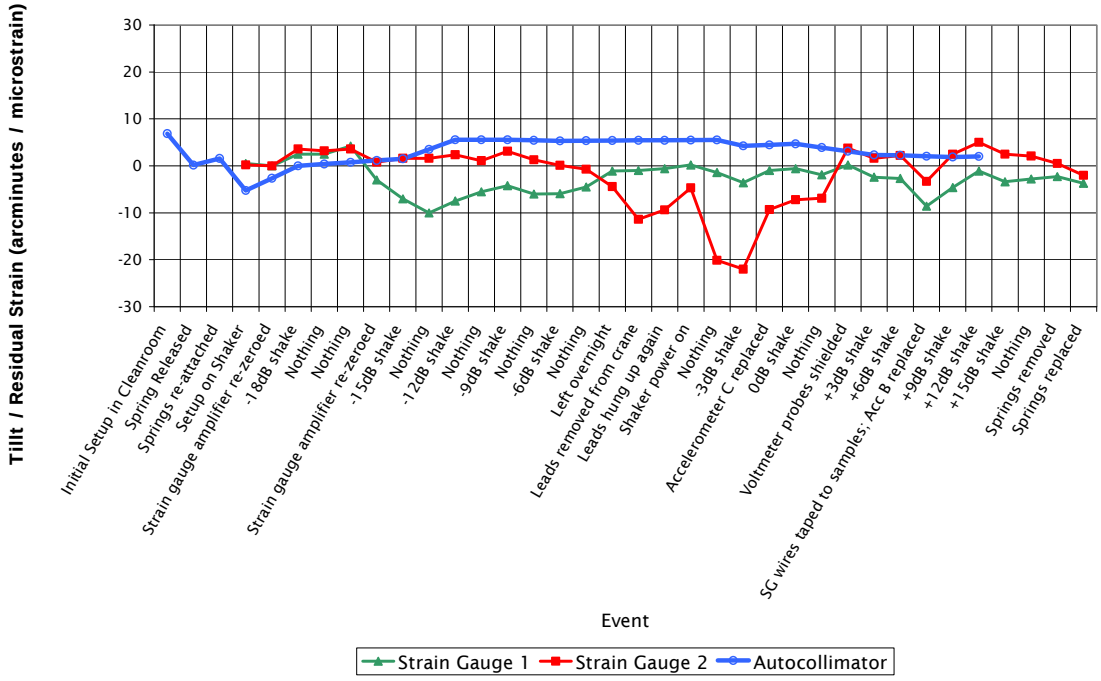

Figure 48. Sample C Results

The plots show for all three samples that a reduction in tensile strain on the upper surface occurred after the initial assembly when the clamping springs were released. The magnitude of the change was 5-10 arcminutes. Subsequent re-application of the spring load did not affect change this angle by more than about 1.5 arcminutes. This suggests an experimental error in the system due to the spring clamping force – this is investigated in further detail later in this chapter. Large residual strains were induced either during the CMM measurements, transport between facilities, or set up on the shaker. The magnitude of this change was in excess of 10 arcminutes, and outside the measurement range of the equipment.

For sample A, high noise levels on the strain gauge measurements are apparent for all tests until the "overnight" event. Following the addition of shielding to the voltmeter wires, the results were fairly stable until after the +6 dB shake. Then, the strain gauge wires were taped to the samples in order to prevent them damaging the strain gauges. At this point, a compressive strain was observed due to the wire-taping process, which was recovered on the subsequent +9dB shake. Angular measurements were not made at this point, so no corresponding dip is seen in the tilt angle curve. A large tensile strain of about 10 μstrain is seen on the +12dB shake, observed with both strain gauges and the autocollimator. This strain was recovered during the next shake.

Removal of the springs reduced the tensile strain only slightly, but re-application of them reduced it about another 10 μstrain.

The results for sample B followed a similar pattern, the main difference being a permanent tilt of about 6 arcminutes being observed following the -3dB shake. A further increase in strain, observed with both techniques, was seen for the 9dB shake. This was partially recovered following the +15dB shake, and reduced even further by the relaxing of the clamping springs.

The results for sample C show large variations between both strain gauges and the angular results up to the point where shielding was added. In particular, a reduction of 20 μstrain was observed on one strain gauge during a period when the sample was not exposed to any stresses (just prior to the -3 dB shake). This jump was not observed with either the other strain gauge or the autocollimator. Angular results show a jump at the -12dB shake, followed by a long period of being constant, with a gradual return to its original position between the 0 and +6dB shakes. The strain gauge results following the addition of shielding were very constant, with the only variation occurring when wires were taped to the sample.

Comparison of Residual Strain With Prior RMS Stress

In order to better assess the contributions of individual vibration levels to plastic strain, the residual strain results were compared with prior RMS vibration stresses (Figure 49, Figure 50 and Figure 51). Here, the RMS tensile stress in the outer fibres of the samples was produced using data from the accelerometers on each sample – a Displacement Spectral Density function was computed from the PSD response, and the RMS displacement used to compute the RMS strain in the outer plies. PSD response results could not be obtained for sample C due to data acquisition problems, so the (horizontal) stress axis uses the results from sample B. Note that these curves follow the convention of Figure 46 to Figure 48 with residual strain on the vertical axis and prior loading condition on the horizontal axis (rather than the usual stress-strain curve axes with stress plotted on the vertical axis and strain horizontal).

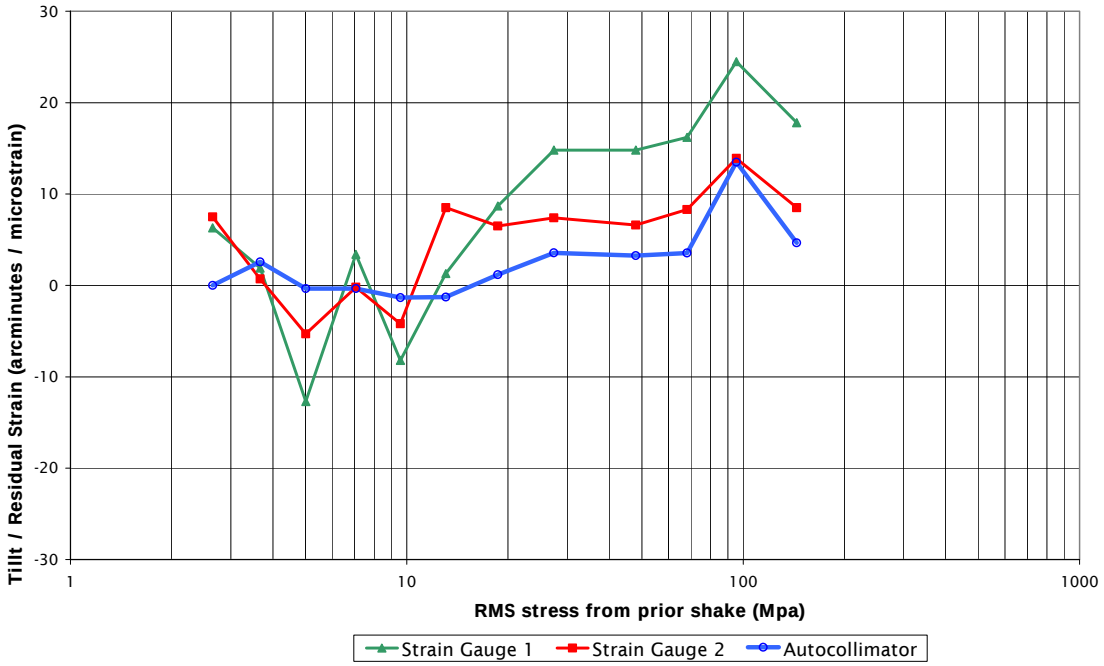

Figure 49. Residual strain RMS stress for sample A.

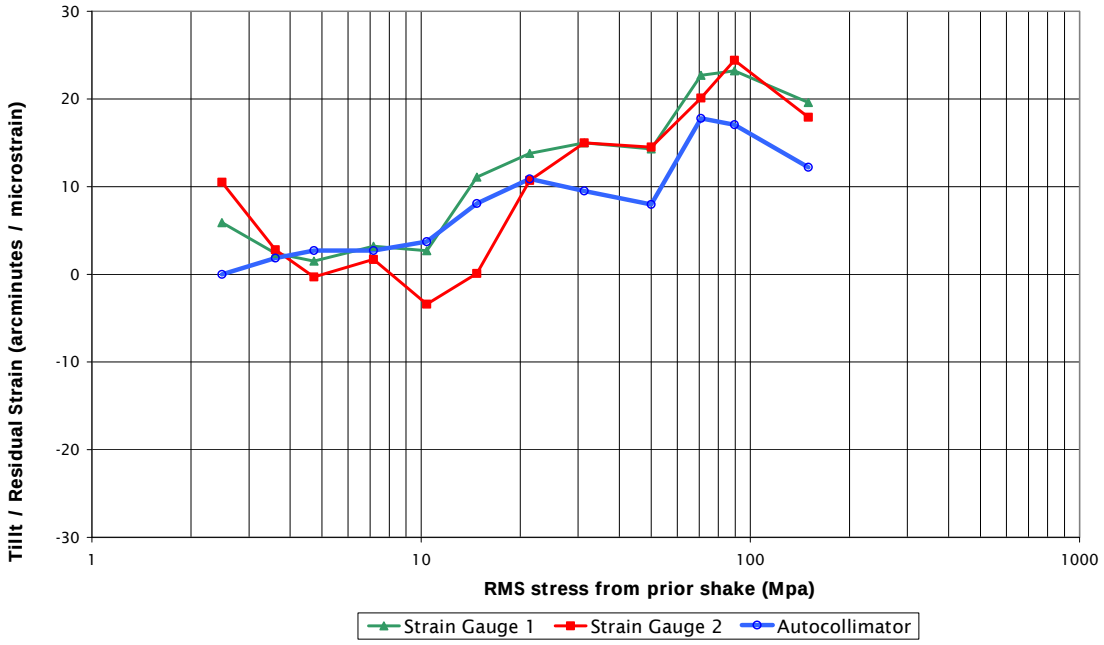

Figure 50. Residual strain Vs RMS stress for sample B.

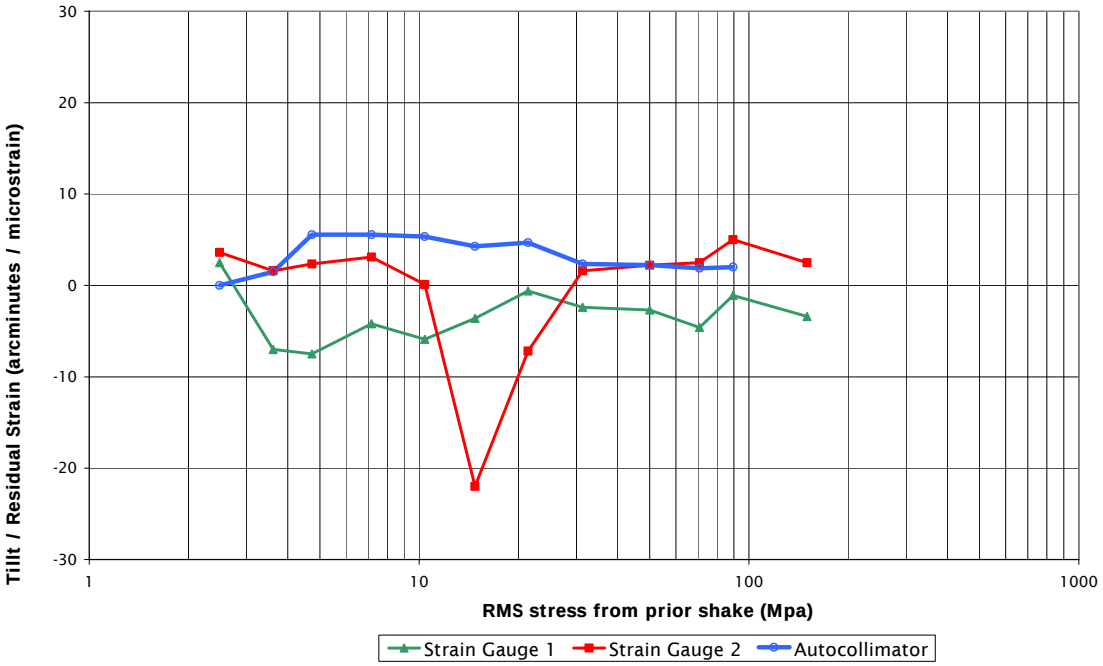

Figure 51. Residual strain Vs RMS stress for sample C.

Recalling that a 1 arcminute tilt equates approximately to a 1 μstrain average residual strain, correlation between strain gauge and angular data was very good after shielding had been used on strain gauge measurement wires (from the +3dB shake onwards) for all samples. Therefore it is assumed that prior to this point, residual surface strains are best inferred from the angular measurements.

For sample A, residual strains are very low until about 27 MPa where there is a small jump of about 5 μstrain. Sample B shows a gradual increase to 10 μstrain, with most movement happening from about 15 MPa onwards. Both samples show large jumps of about 10 μstrain at 71 MPa for B and 95 MPa for A. Both A and B then show a decrease in strain of almost the same amount following the final shake, 150 MPa. Up to this point, both samples followed a similar pattern, with movements all in the same direction. This may be indicative of a non strain-free setup, the effects of gravity, or asymmetry in the test samples. However no such cumulative strain effect is observed in sample C, whose residual strain slightly decreases during the higher-level tests.

Interpretation of Results

The residual strains seen here are low – the highest observed was only 25 μstrain. To put this in context, a 1m long aluminium alloy strip would expand

this much for every 1°C temperature increase. Over the length of a whole metering structure, such a change would be significant. For the BBM structure, this would move M2 with respect to M1 by 15 μm. However in reality, only small areas of the tube would suffer high stress, particularly those around attachment points.

These results offer some useful engineering guidance: they show that an accumulation of residual distortions over several tests is more likely to be "sided" than randomly distributed about a centreline for a nominally strain free structural member. Such information could be useful in performing final alignment operations, and test campaign management.

Peak stresses in the sample were lower than expected, as damping was found to be significantly greater than predicted (6% as opposed to 1%). A comparison of test results with analysis predictions is shown in Figure 52 and highlights the sensitivity in response to damping assumptions.

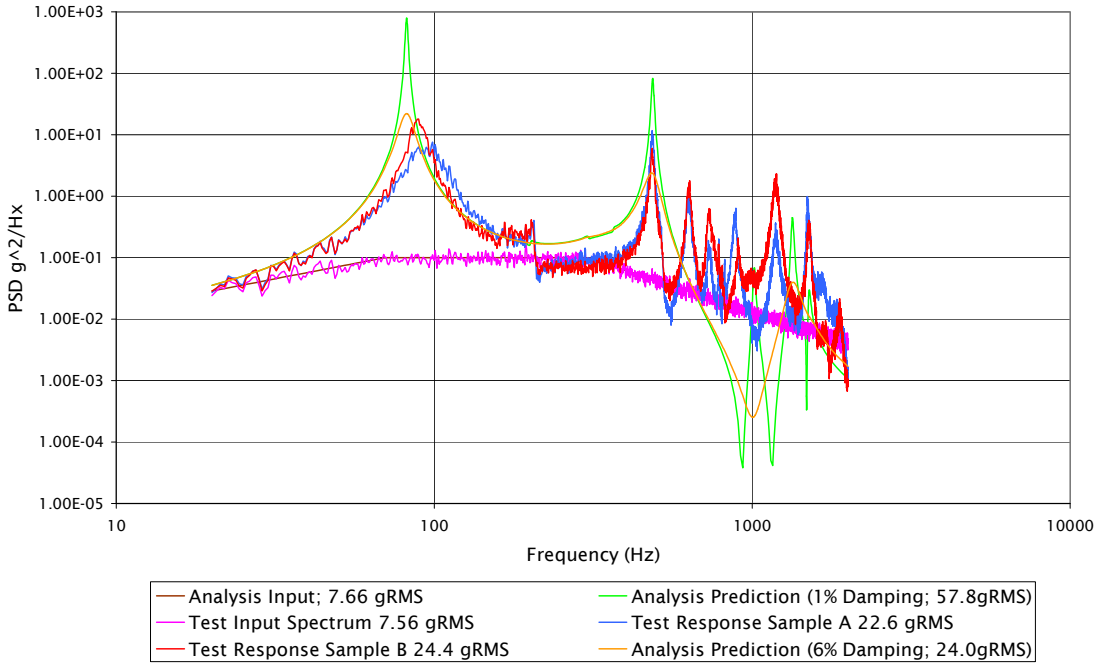

Figure 52. Analysis predictions and test responses for CFRP tests

Residual strain results for each level of dynamic stress are presented in Figure 53 in a more traditional stress vs residual strain format. The results shown are the average values for all three centre strain gauges, all three off-centre ones, and all three tilt measurements respectively.

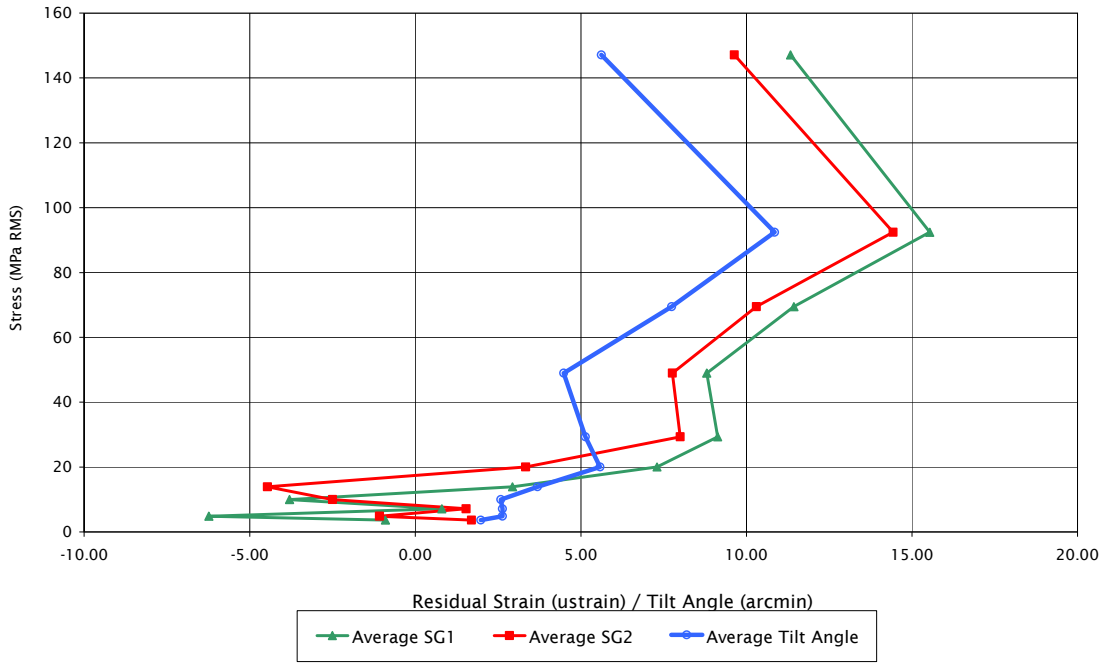

Figure 53. Dynamic stress/residual strain plots for CFRP samples.

These results all follow a similar pattern, giving good confidence in their accuracy and also suggesting a low spread amongst identical samples. The strain gauge results are noisy at low stress levels, but match the tilt measurements well above about 10 MPa RMS (the exception being strain gauge 2 on sample C – as shown in Figure 51, the large negative residual strain actually occurred prior to the -3 dB shake (during a period of inactivity), and is therefore likely to be due to noise). For samples A and B, most measurements show general movements in the positive residual strain side of the graph. These measurements tend to be "sided", increasing in magnitude in the same direction on subsequent shakes. The exception to this is the very last measurement, where some residual strain is recovered (about 5 μm). The results for sample C were generally flat over the same test range.

4.3.2 CMM Measurements

Points along each sample were probed in the vertical direction before and after vibration testing. Measurements were taken only in the vertical direction to measure residual bending. The measurements took place with the samples mounted in their test fixture.

CMM Results

The CMM results are shown in Figure 54, Figure 55 and Figure 56. These results have been normalised by adding a small translation and rotation to the "after" response such that the displacements around either support point are zero. This is necessary, as the test setups were bound to be in slightly different locations for the before and after measurements, with the only common datum being the support points. The adjustments preserve the shapes of the samples, which is the area of interest for estimating the surface strain. Note that measurements were not taken actually at the support points, so the measurement point that was closest was used instead (slightly inboard of the actual support points).

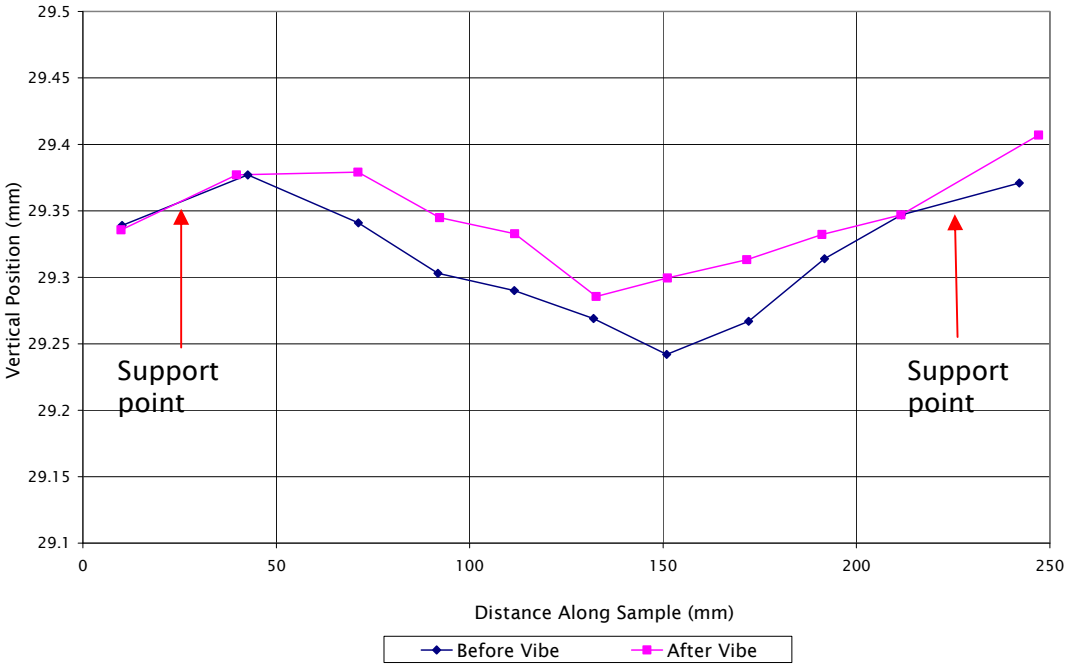

Figure 54. CFRP sample A CMM results

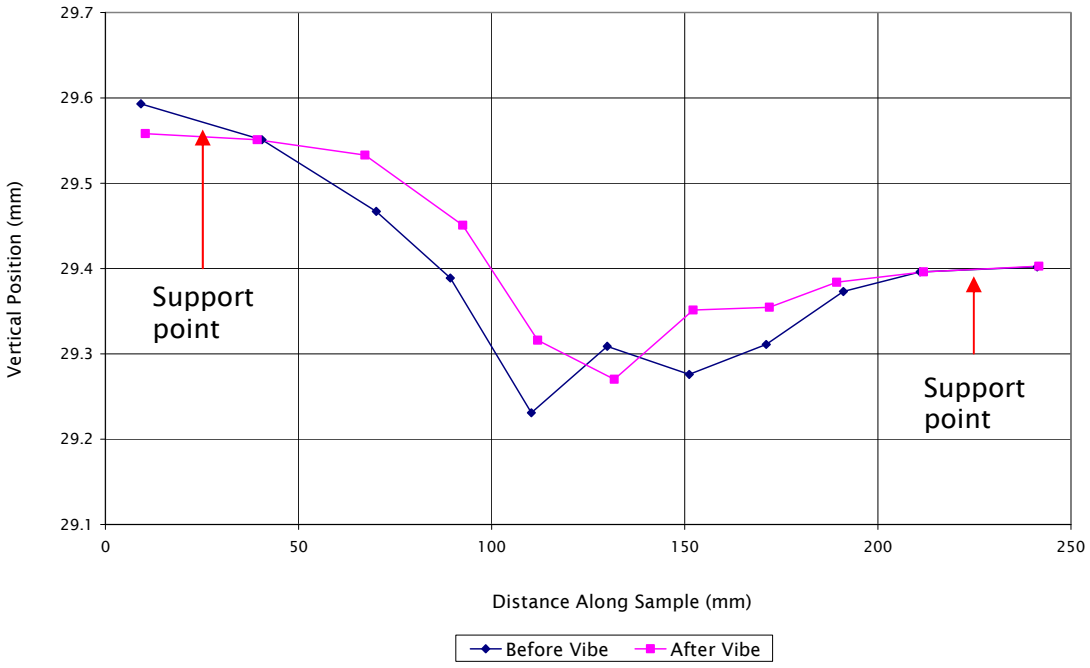

Figure 55. CFRP sample B CMM results

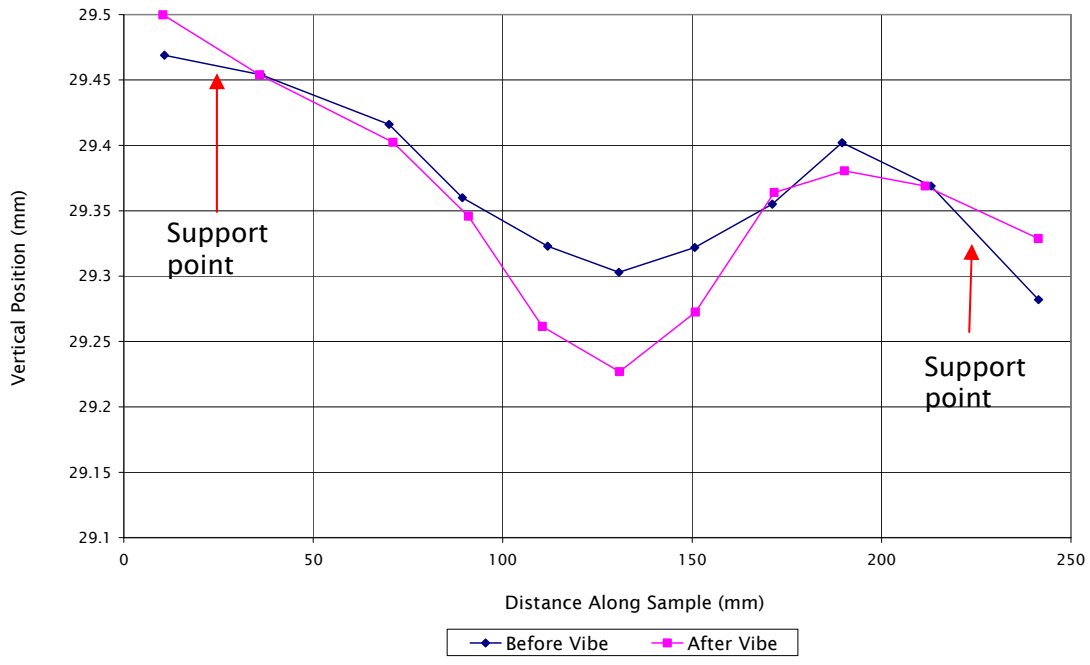

Figure 56. CFRP sample C CMM results

During probing, the samples visibly deformed slightly under the force of the probe around their centres. Thus these three curves do not represent the true shape of the samples, and include a central downward shift. If this effect

was repeatable and common to both the “before” and “after” measurements, then the resulting error should be nulled when subtracting one from the other.

Before/After Vibration Difference

The differences between the before and after vibration measurements were determined, and are shown in Figure 57:

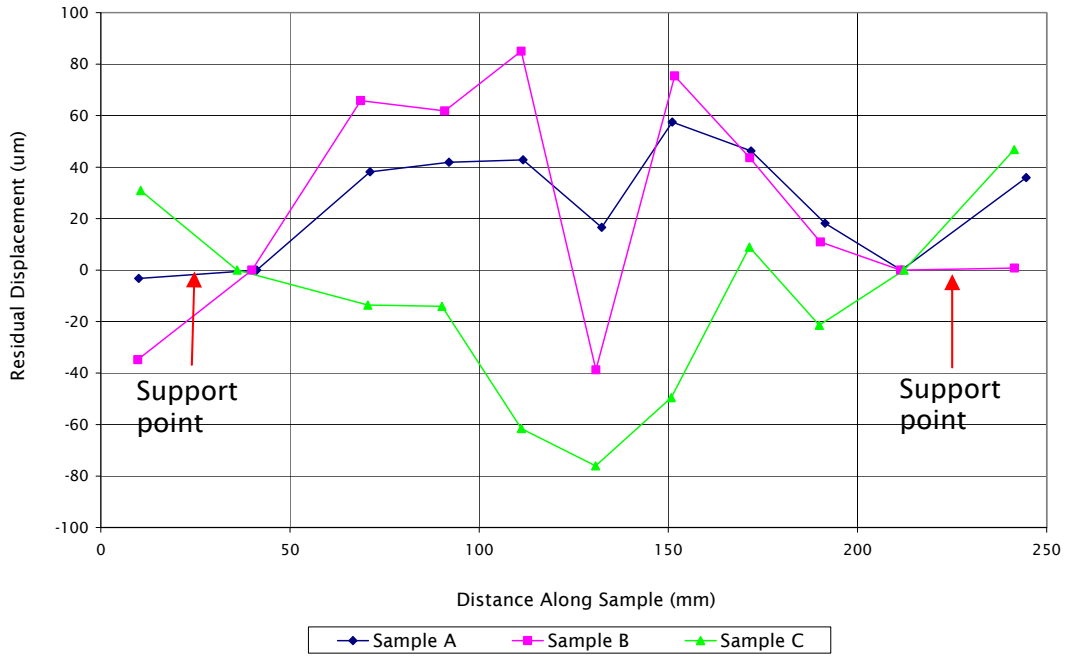

Figure 57. CFRP samples CMM results – difference between before and after measurements

Thus we see peak deflections in samples B and C of around 80 μm. Samples A and B display an anomaly in the centre, which is difficult to explain. This could be caused by excessive elastic movement in the samples during probing around the sample centres. Ideally, these residual bending shapes can be used to estimate the residual surface strain. A simple linear elastic FEA model was used to estimate the relationship between vertical deflection and surface strain at the centre of the sample, assuming a bending shape caused by a static acceleration. This model predicts about a 10μm vertical displacement for every 1 μstrain on the surface. Thus, with approximate peak deflections on samples A, B and C respectively of 80, 60 and -80 μm (from Figure 57, ignoring the dips for samples A and B), the peak residual strain on the top surface of the samples is estimated at 8, 6 and -8 μstrain (for samples A, B and C respectively). This compares to 6.2, 9.2 and -3.7 μstrain respectively for the

final strain gauge readings – a relatively poor correlation. However such a comparison assumes that the strain gauge measurements are measuring pure residual bending, assuming that there is no constant-through-thickness tensile/compressive component to the residual strain response. Also, the test results of Figure 57 suggest that more complex residual bending shapes are present than the simple ones assumed for this approach. A better comparison was possible for the Al alloy sample tests – having a strain gauge on either side enabled a decomposition of the response into bending and axial components.

4.3.3 Static Test Results

The static test results are shown in Figure 58:

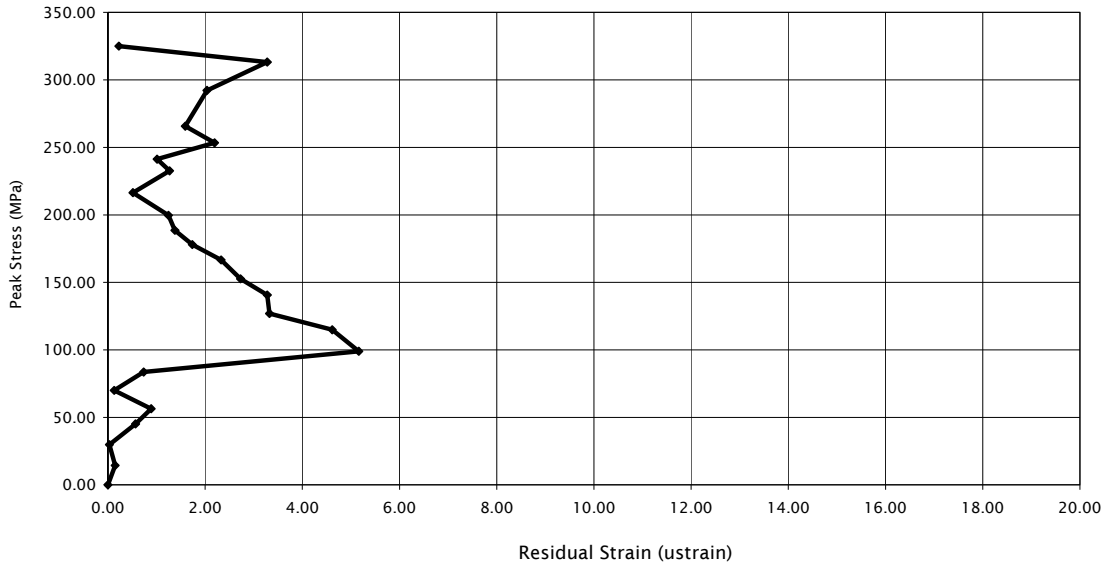

Figure 58. CFRP residual strain results under static loading.

During static CFRP tests, an anomaly was seen when stress in the outer fibres reached about 100 MPa – at this point, a significant strain was seen, which was gradually recovered on subsequently higher stress cycles. It is unclear what caused this anomaly. It may have been a fibre pulling out, with an effect that was gradually compensated-for by visco-elastic creep behaviour in the resin. Interestingly, the dynamic results appear to follow a similar pattern to the static ones (see Figure 53). This suggests a real event occurs in this material at this threshold. It is probably not transverse microcracking, the behaviour that can cause residual strains under thermal cycling, as such strains would not be recovered. It is unclear from the test data whether the recovery is time-dependent, or due to subsequent stress cycles.

4.4 Al alloy samples

The CFRP sample tests provided some useful test data and enabled the refinement of the test setup. They also proved the metrology technique. However significant large-scale microyield behaviour was not observed in the test samples. This was partly due to the shaker not being able to provide sufficient acceleration, partly due to the higher-than-expected damping, and partly due to the high strength of the material. As a result, it was thought that further work was required to better validate the test setup. To do this, it was decided to re-run the tests using a material with a lower strength and more predictable yield characteristics. Al alloy 2024 T3 was chosen for this, and provided the added advantage of having been studied in the literature.

The Al alloy sample tests took place a year after the CFRP ones. The test setup was nominally identical, being conducted in the same test facility and making use of the same test fixture and metrology gear. There were a few differences though:

- The shaker used had been upgraded, however, enabling higher acceleration levels.
- The strain gauges were bonded on the upper and lower faces, not just the upper one (as described in the Test Setup section).

Photos of the test setup were shown in Figure 34 and Figure 35.

4.4.1 In-Situ Measurements

The strain gauge results are shown in Figure 59. These results represent two slightly different test setups used on consecutive days of testing. At the end of the first day's testing, it was suspected that experimental error due to the mounting arrangement was occurring. Therefore, a second round of tests was conducted (on the same samples) with the clamping springs removed, and the clamping rods bonded into position. This new arrangement provides no clamping force, which was thought to be responsible for the experimental error. The revised mounting arrangement is shown in Figure 60. It worked well, though with no clamping force, the lower rods had nothing to prevent them sliding out of their housings during testing. This started to happen to

one of the lower rods on sample B following the -6 dB shake, so adhesive tape was added to secure them.

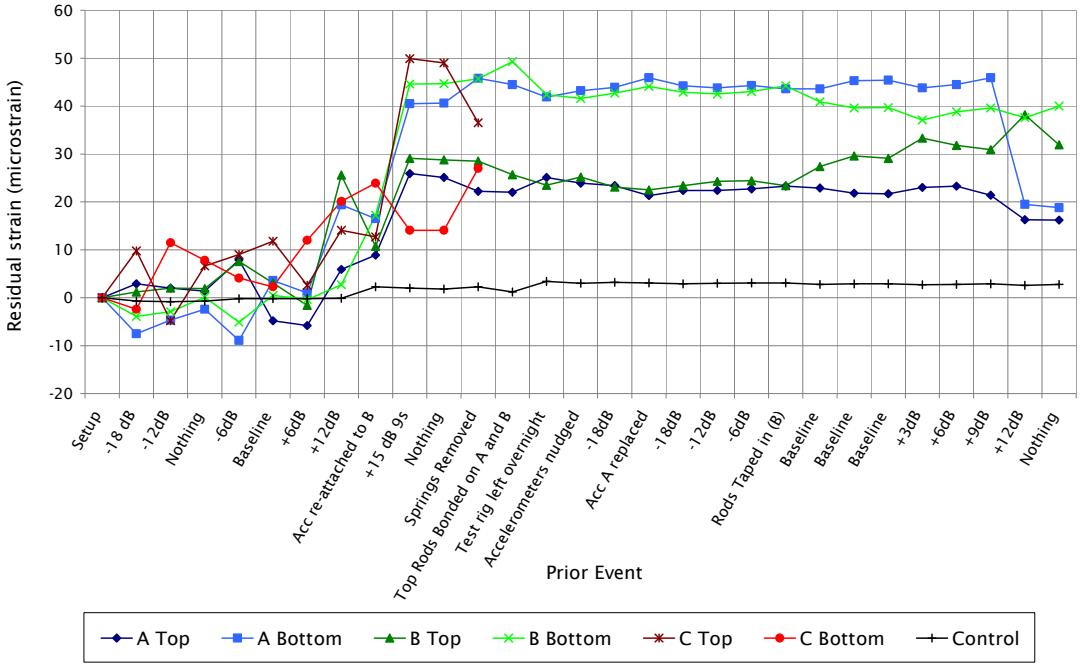

Figure 59. Al alloy strip test summary.

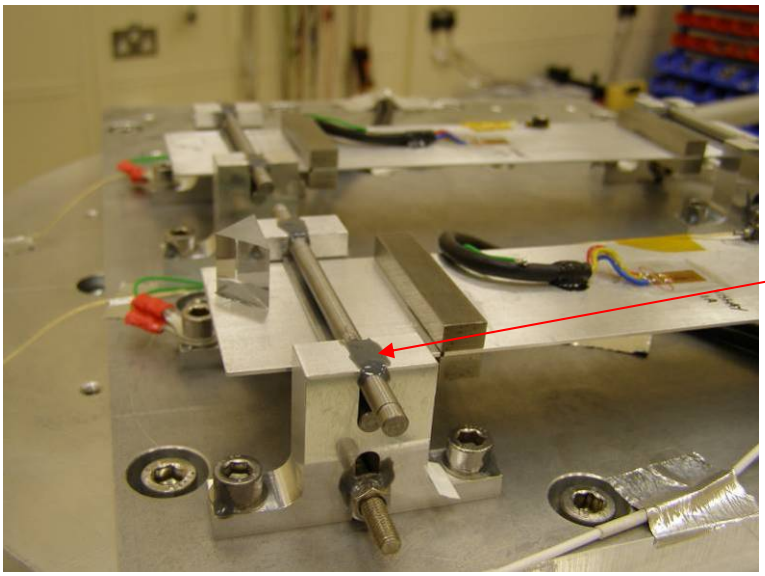

Figure 60. Bonded-in clamp rods.

All samples show small residual bending strains (up to +/- 10 μstrain) for the series of tests up to +6 dB. During the +12 dB test, significant movements are seen for all strain gauges. These movements are all in a positive sense, indicating that the samples were exhibiting a tensile residual strain, rather

than equal tensile/compressive strains which would indicate pure bending (ie, the samples are growing in length). The accelerometer on sample B came loose during this test and was re-bonded for the subsequent +15 dB test. The +15 dB test lasted only 9 seconds, though significant additional movements were seen in both net tension and bending on all samples.

Removal of the Clamp Springs had little effect on samples A and B, though appeared to significantly relax the bending strain in sample C. These tests were repeated the following day on samples A and B only, with the Clamp Rods bonded in position. Both samples were very stable up to the Baseline load, when bending strain started to reduce in sample B. Sample A showed a large reduction in strain on the bottom strain gauge following the +12 dB test, which appears to be due to a reduction in both tensile and bending strain.

Decomposition of Results

The strain gauge results were decomposed into bending and tensile results. The residual bending strain was estimated to be half the difference between the top and bottom strain gauge results. This was compared with the autocollimator tilt measurements in Figure 61. For the first part of the test, the trends in tilt measurement match the trends in bending strain well. For the second part of the test, tilt measurements were only made on sample A, as the mirrors on sample B had become damaged in the +15 dB shake on Day 1. The tilt measurement trend matches the bending strain trend well for sample A during the second round of tests, albeit with an offset of several microstrain.

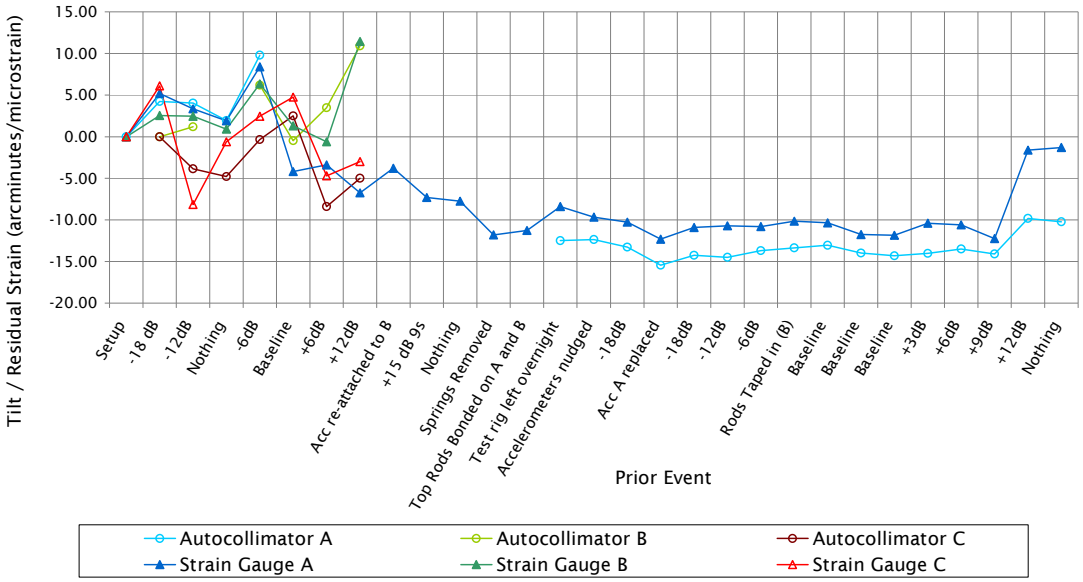

Figure 61. Residual tilt measurement compared with residual bending strain from strain gauges.

It is evident from Figure 59 that all samples displayed significant axial strain as well as bending strain (pure bending strain would be manifested in upper and lower stain gauge responses that are equal and opposite, with a zero mean). Estimates for these were derived from the data and plotted against RMS stress in Figure 62 and Figure 63 for the Day 1 tests. Axial strain is assumed to be simply the average of the upper and lower surface strain gauge results.

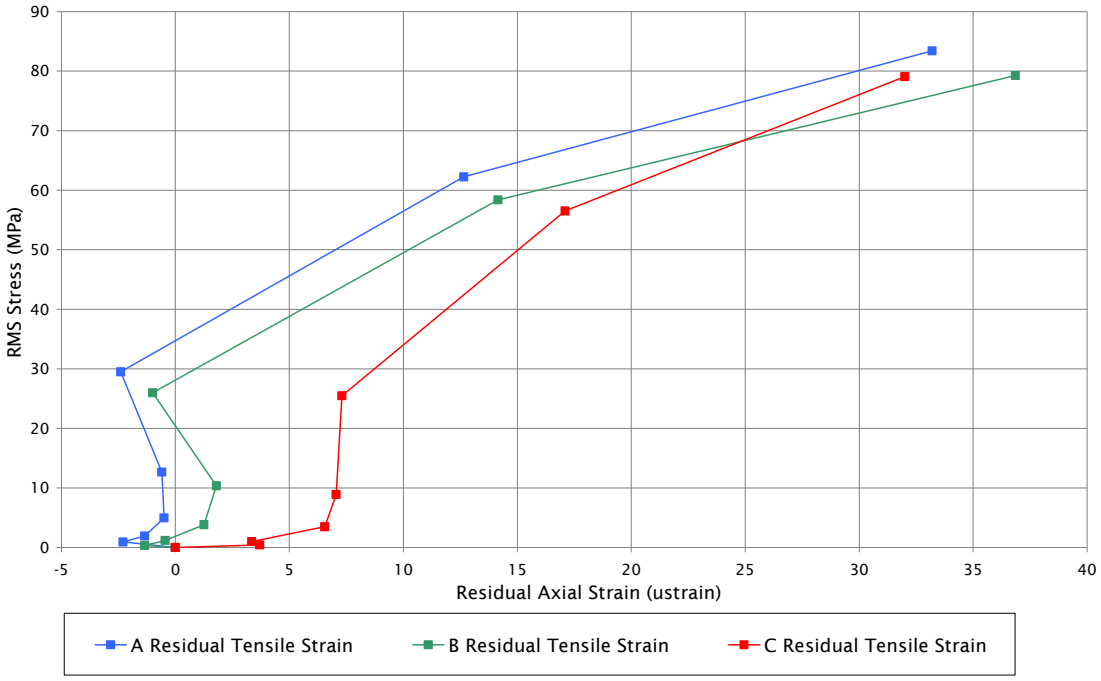

Figure 62. Al alloy samples: RMS stress vs residual axial (tensile) strain (Day 1 tests only).

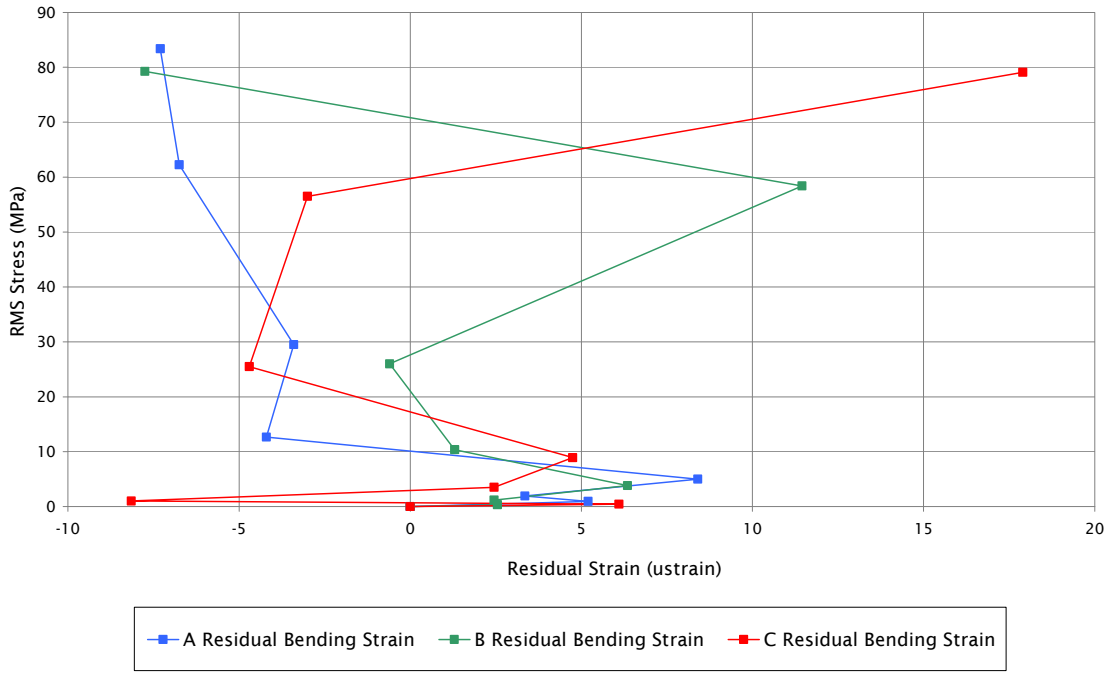

Figure 63. Al alloy samples RMS stress vs residual bending strain (Day 1 tests only).

Figure 62 shows that the axial residual strains follow a very similar trend to one another. The negative slope at very low stresses seen on samples A and

B is probably due to test setup bedding-in. Ref. 8 reports an interesting observation with instances of low-stress negative yield in static microyield tests for a number of materials (including aluminium), resulting in a very similar-shaped curve.

The bending residual strains shown in Figure 63 are of a lower magnitude, and follow a very different pattern. They generally increase in magnitude with increasing dynamic stress, though the sign is not consistent with changes between tension and compression on subsequent shakes. The mean value of all three is roughly zero for all tests, suggesting that the residual bending component is random with zero-mean, rather than evolving in a particular direction as the residual axial strains do.

4.4.2 CMM Measurements

CMM measurements were made on the Al alloy strip samples using a similar technique as for the CFRP samples. The same CMM was used, in the same controlled environment. The only difference was that all measurements, before and after vibration testing, were performed with the clamp springs removed. This was to eliminate the clamp spring force as a possible source of experimental error.

CMM Results

The results for all three samples are shown in Figure 64 to Figure 66. Again the “after” curves have been adjusted with a translation and rotation such that the measurements at the mounting points are the same as the “before” curves. The common points for the “before” and “after” curves are again the measurement points slightly inboard of the actual support points.

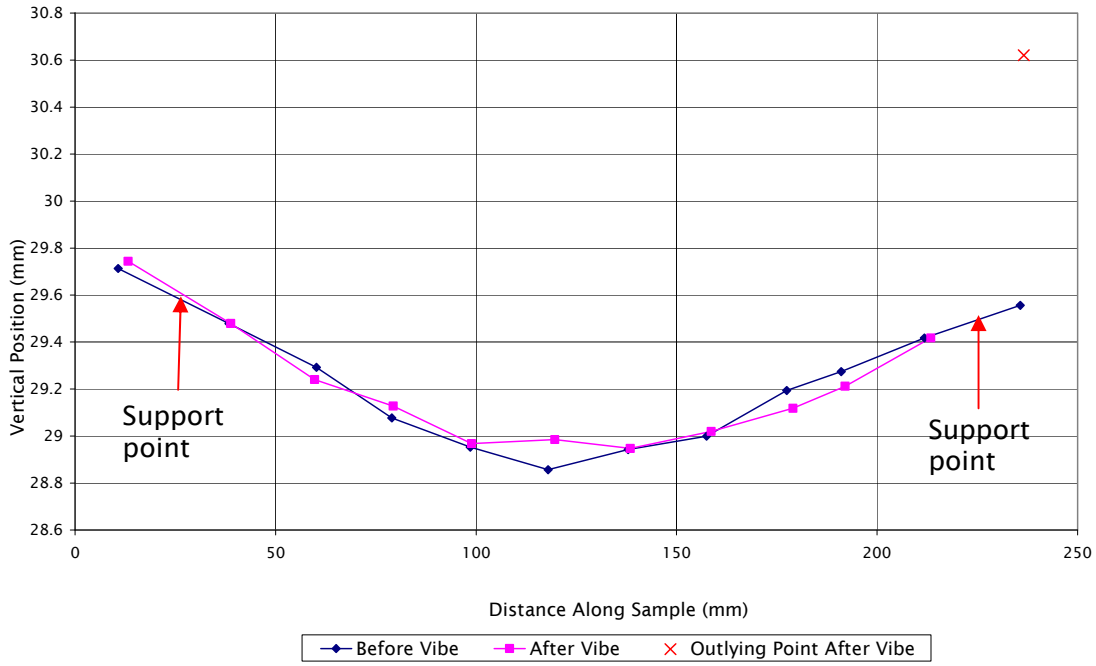

Figure 64. Al alloy sample A CMM results.

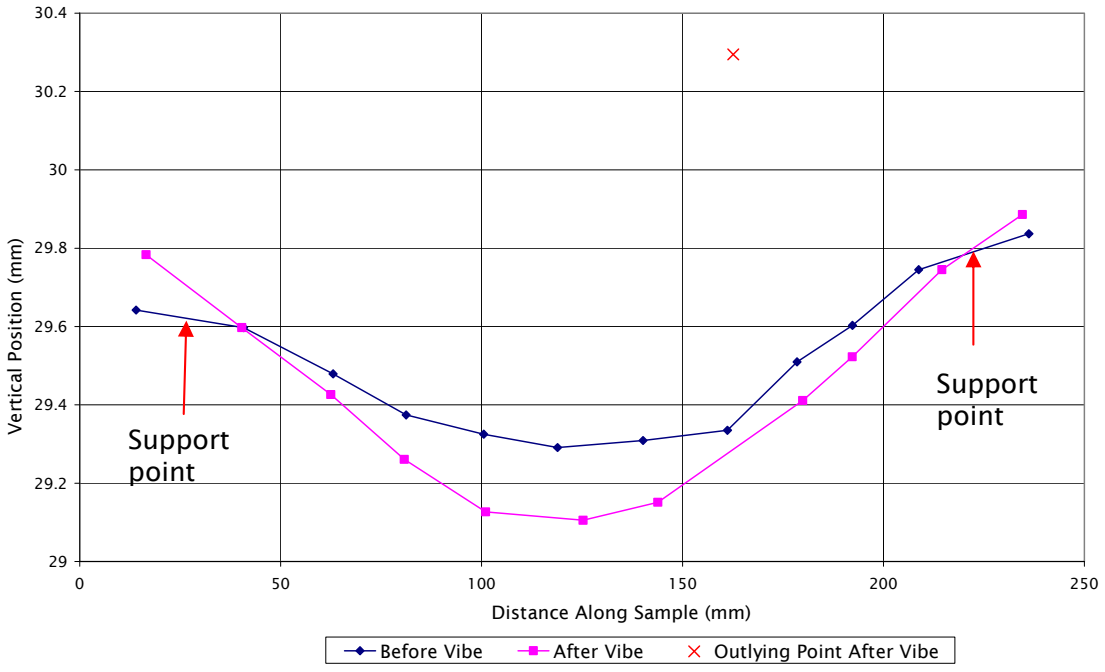

Figure 65. Al alloy sample B CMM results

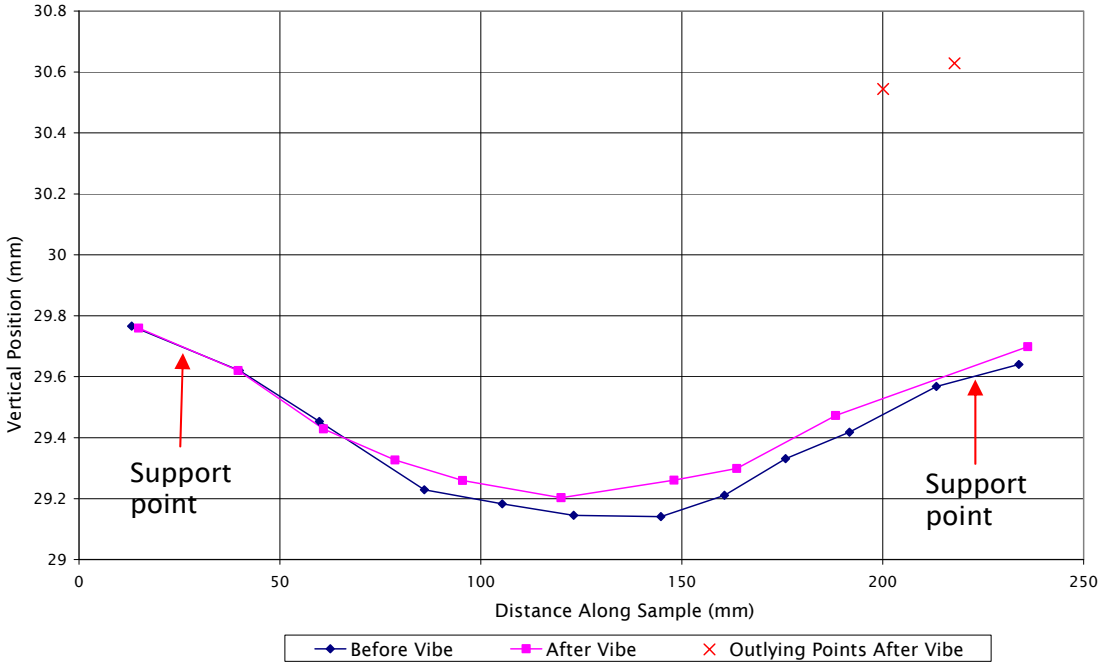

Figure 66. Al alloy sample C CMM results

Sample A showed similar before and after shapes, with a large deflection on the right hand side of the support point following vibration. This may be due to material yield or measurement error, but is not in a region of interest for these tests. Sample B has an anomalous measurement at the 163 mm point, which may be operator error or debris on the surface of the sample. Sample C also shows anomalies, though these are close to the right hand support point and may again be due to localised yield around the support or operator error.

Before/After Differences

The differences between before and after measurements are shown in Figure 67, effectively showing the residual bending shape.

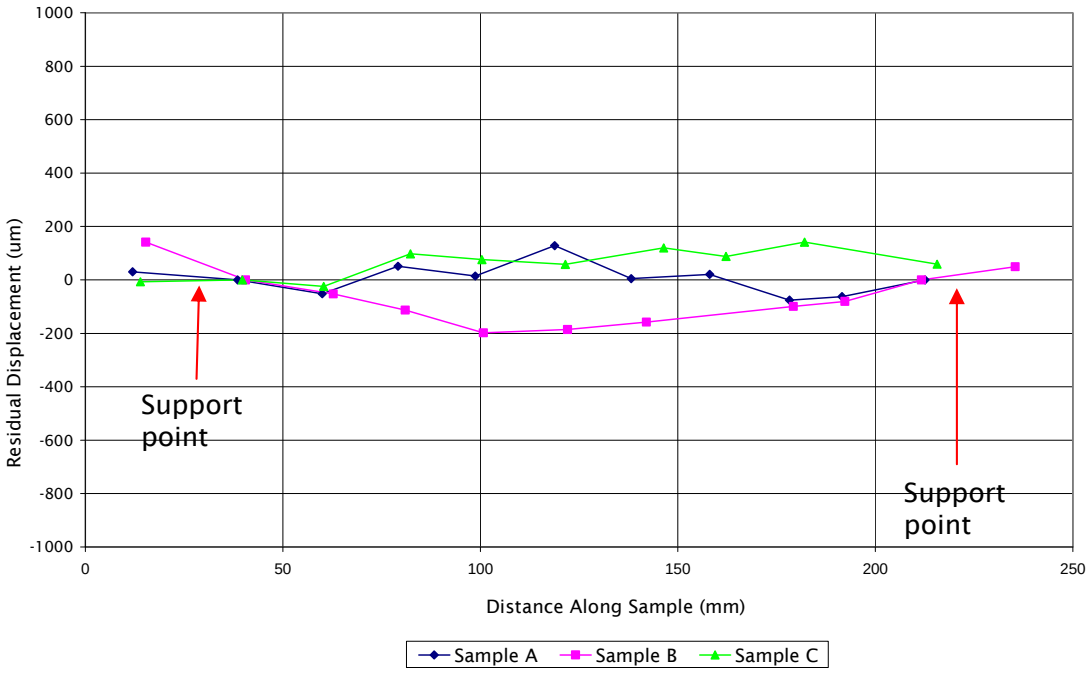

Figure 67. Al alloy samples CMM results – difference between before and after measurements (anomalous points not shown).

The curve for sample B follows a pattern that one would generally expect to see with residual bending strain in a beam. The peak displacement at the centre of sample B is -185 µm. The same technique that was used for the CFRP CMM data to estimate residual surface strain was applied to this result. Note that the displacement-strain relationship is the same, as it depends only on the test specimen geometry (and not material properties), which is the same in both tests. Thus the CMM measurements predict a surface strain, due to bending only, of -19 µstrain for sample B. This compares poorly with the strain gauge result in bending of -4.1 µstrain (derived from the final measurements on Day 2 – see Figure 59). The discrepancy is greater than the expected experimental error for this technique (see Section 4.5). Samples A and C were not assessed this way, as their residual shapes were different to the pure bending shapes assumed in the analysis.

4.4.3 Static Test Results

The static test results are shown in Figure 68.

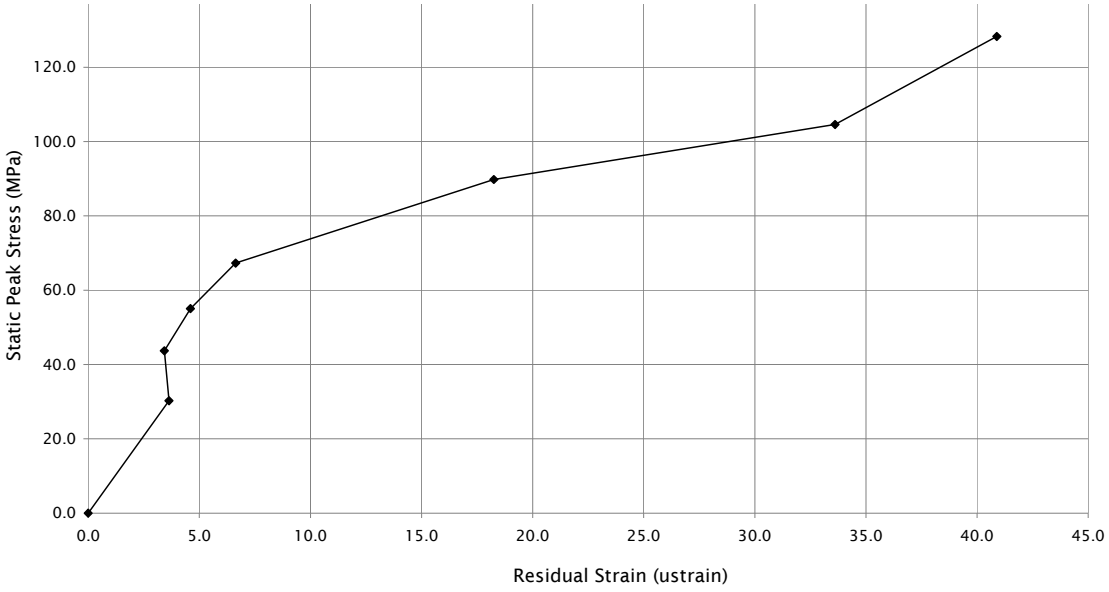

Figure 68. Peak stress vs residual strain for the Al alloy static test.

The apparent residual strain between the first two data points (ie, up to about 4 μstrain) is probably an artefact of the test setup, with the first observed residual strain occurring at about 44 MPa. This is effectively the elastic limit for this material, stressed in this configuration. The MYS is slightly higher than this, at about 55 MPa.

4.5 Error Estimation

Experimental errors were high at the start of these tests, though refinements of the test setup throughout testing substantially reduced them.

Strain Gauges and Autocollimator

The CFRP tests were the first ones to be conducted. It was evident from the start of these that electronic noise in the vicinity of the shaker was a problem. Strain gauge readings fluctuated rapidly by about +/- 5 μstrain, with occasional excursions of 15 μstrain. Several strategies were employed to reduce this, such as suspending the strain gauge leads from an overhead crane, as far as possible from the shaker armature. The most significant reduction in noise came with the addition of shielding to the voltmeter probes used for taking readings between the 0 dB and +3 dB shakes. This reduced fluctuations to below 1 μstrain.

A summary of the control sample results is shown in Figure 69. The control sample was located on a platform next to the shaker head (see Figure 41). This shows that the autocollimator measurements are very stable, but there is an error of up to 5 μstrain on the strain gauge. The standard deviation for autocollimator results is 0.16 arcminutes (0.16 μstrain), and for the strain gauge it is 2.3 μstrain. The aluminium control sample strain gauge results were shown in Figure 59, and show a drift over the whole test of approximately 3 μstrain.

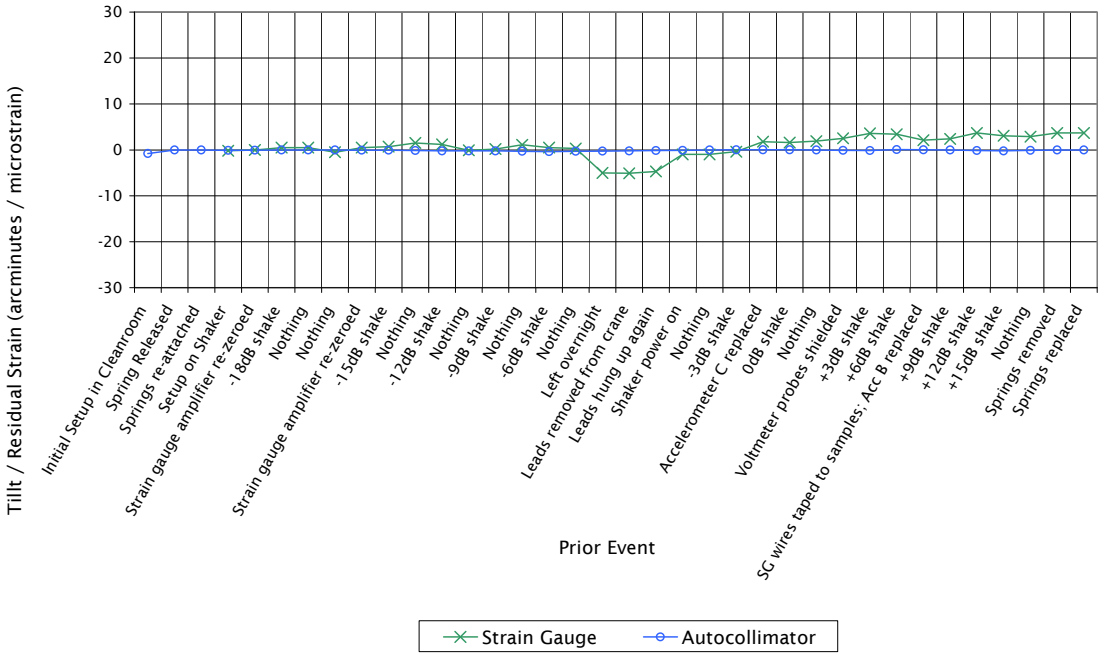

Figure 69. CFRP control sample results.

The Al alloy tests were subsequently performed on an updated-model shaker. The strain gauges on these had better shielding, that extended directly to the gauges. The maximum excursion seen on the Al alloy control sample was 4 μstrain, seen after the test setup was left overnight.

Strain gauge sensitivity was quoted by the manufacturer as ± 0.5%, or about 0.25 μstrain for the maximum values measured here. Strain gauges were thermally matched to the substrate material, and the tests were conducted in a thermal environment that was stable within 3°C. Taking into account slight mismatches between the strain gauge and substrate CTEs, the maximum possible error due to thermal effects is ± 0.3 μstrain for the CFRP test and ± 0.45 μstrain for the Al alloy one. It should be noted, however, that

temperature (and humidity) fluctuations over the time between metrology runs (several minutes) would have been extremely small, with thermally-induced errors occurring over relatively long time-frames.

For the angular measurements, the resolution was about 10 arcseconds, or about 0.17 μstrain (though it could have easily been a tenth of this if greater care had been taken during measurement). Other sources of error are the bond layers between the mirrors and the CFRP top layers. For this, it is instructive to analyse the results for a pair of mirrors bonded directly to the vibration fixture (the autocollimator results in Figure 69). Here, the tilt angle remained at almost exactly zero for the duration of the test, with a peak fluctuation of 0.8 arcminutes. This may point to a thermal influence. Therefore, it is assumed that the worst-case error observed here is 0.8 arcminutes (~0.8 average μstrain).

Mounting Errors

The other main source of error was from the mounting technique. The test rig undoubtedly produced elastic bending strains in the samples. Application and removal of spring preloads was observed to induce or relax bending strains. To quantify this effect, small bending strains were induced by hand on a sample of each material in a static test setup. The elastic strain induced was enough to cause approximately a 10 arcminute tilt (equivalent to 0.7 MPa for the Al alloy and 3.1 MPa for the CFRP). The apparent residual deformation was measured with the autocollimator. This was performed three times in each direction, under several mounting configurations. The results are shown in Figure 70. It is clear that even small perturbations to the test setup can cause apparent residual strains of 13 arcminutes for the CFRP, and 8 arcminutes for the Al alloy when the springs are attached. Without the springs, errors are reduced to below 2 arcminutes for both.

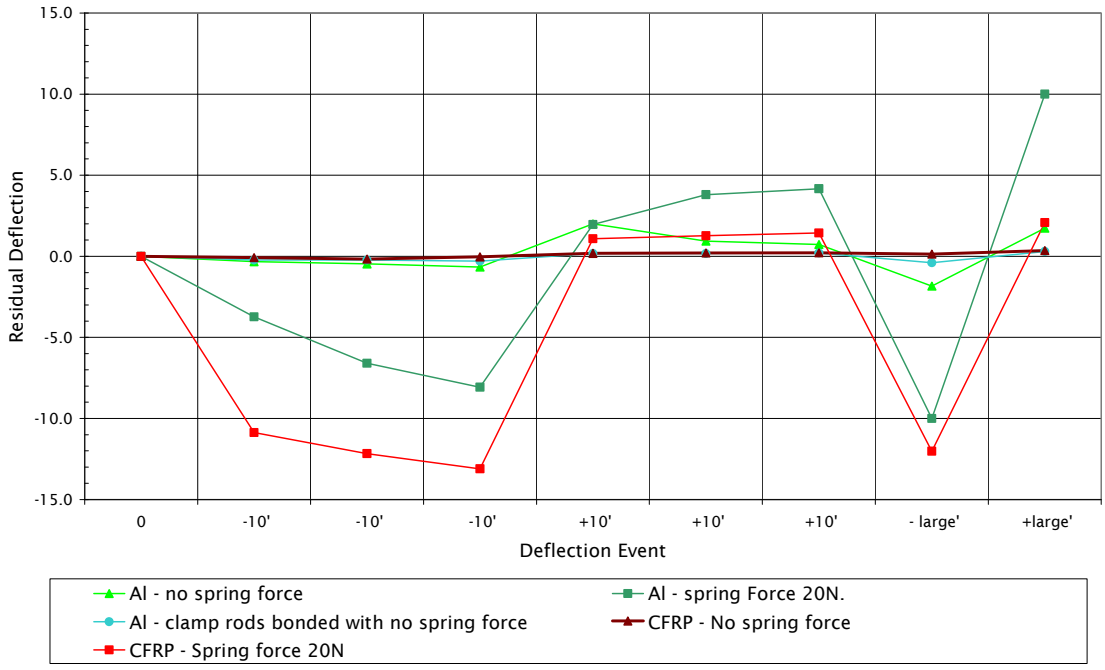

Figure 70. Measurements of experimental errors due to mounting.

The final day of dynamic testing of the Al alloy samples made use of this better mounting concept, dispensing with springs and using epoxy to secure the upper Clamp Rods (Figure 60).

CMM Errors

For the CMM results, the calibration certificate shows that the measurement uncertainty should be about +/- 5 μm over this measurement range, or about +/- 0.5 μstrain depending on the residual shape. During metrology, force from the probe visibly deformed the samples on contact, though the magnitude of this effect was not assessed. To assess repeatability, one of the samples was subjected to three identical measurement runs, 10 minutes apart. The results are shown in Figure 71.

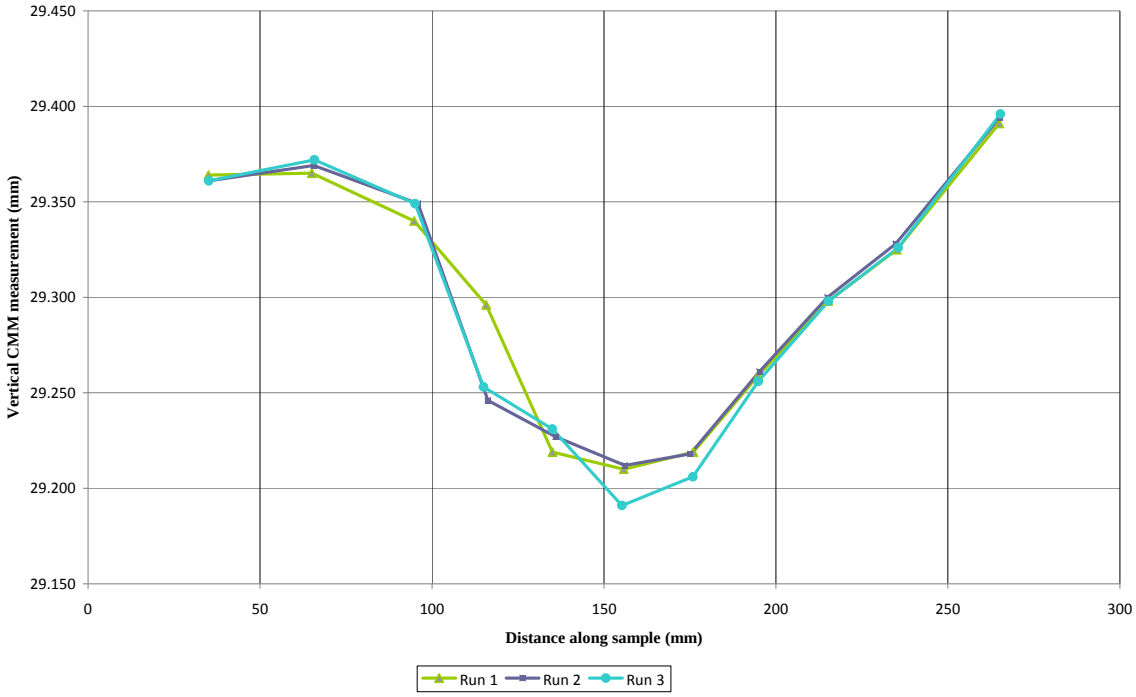

Figure 71. Repeatability of CMM measurements on CFRP sample A.

These results are very similar, showing a good degree of repeatability, for the CFRP samples at least. The peak discrepancy between Runs 2 and 3 at the half-way point along the sample is about 20 μm, or about 2 μstrain (for our assumed bending shape). The lack of good correlation between CMM results and strain gauge/autocollimator results is probably due to handling and transport to the new facility. During this time, the test rig would have been subject to loading whose impact on residual strain was not monitored by strain gauges or the autocollimator, but would have impacted on the CMM results.

4.6 Discussion

4.6.1 Test Setup

As discussed, experimental errors were initially high, though the test setup was refined to the point where they were in the 1 μstrain region. The main source of error was due to the clamping force at the support points, eliciting a stick-slip response in the samples rather than smooth movement at the rod/sample interface. This was despite the use of a lubricant here. The removal of the clamp springs during the second day of Al alloy sample testing is thought to have significantly improved the test setup. An alternative method

of mounting based on rotary and linear bearings with zero preload may give even better results, though for more complexity.

Another issue with the clamping springs is that they make the test mounting depart from a simple support. The “fixed” end of the simple support, that is constrained axially, is the end where the clamp rods are in contact with the contact pad. The other end, where the pads are flat, should ideally be free to move axially, but in reality it is not. There is a small frictional resultant at this location in the axial direction as a result of the clamping force. This force will be examined in greater detail in a later chapter as it is thought to be responsible to the sample elongation witnessed with the Al alloy samples.

In all, the final iteration of the test setup is thought to have been able to provide a good basis for examining microyield in materials under random vibration, and is recommended for use in the future. Ideally, more samples could be tested to examine result variability. The use of three samples was sufficient to demonstrate that some variability exists, however insufficient to adequately quantify it.

Correlation between accelerometer data and FEA was also very good, though some (upwards) adjustment of the damping factor was required to get a well correlated model. This resulted in the problem of not being able to achieve the highest levels of dynamic stress originally planned. To ensure that high stresses can be achieved, a relatively large shaker is required. Alternatively, the sample geometry or the test masses could be adjusted to provide a lower natural frequency. Assuming that residual strains are predominantly due to first-mode resonance, lowering the frequency of this mode should result in higher displacements, and therefore higher dynamic strains at the surface of the samples.

Metrology Techniques

The correlation between most of the results from different metrological methods is encouraging, particularly between autocollimator and strain gauge measurements. The shaker environment was clearly an electronically noisy one, which adversely affected the early stain gauge measurements. The use of shielding on strain gauge wires and voltmeter probes made a large improvement. For the Al alloy tests, the shielding was terminated at both ends of the wire. This is understood to be an unusual scheme, but was

recommended in the strain gauge amplifier manual[109] for use in a noisy environment, and appears to have worked well.

Another useful feature of the strain gauges was the ability to provide real-time strain data during dynamic testing, producing a strain spectral density plot for each test. This is valuable information for determining the dynamic stresses seen by the material prior to residual strains being measured. The alternative method, employed for the CFRP tests, is to use accelerometer data integrated twice to give a displacement spectral density. This can then be used to estimate the strain spectral density at the surface by assuming a certain bending shape (ie, the shape of the first mode).

Strain gauge positioning was an important factor. The Al alloy tests, with mutually opposing strain gauges on the top and bottom surfaces gave the ability to separate axial from bending strain. The CFRP tests used gauges that were both on the same surface, but at different locations along the length. There are two advantages to this – firstly, it provides a double-check of the results. For samples A and B, the strain gauge trends are very similar, increasing confidence in the results (this is not the case for sample C). Secondly, it provides an estimate of the degree to which the first bending modeshape departs from an ideal four-point bending shape. For a static four-point test, there is a notionally constant bending moment between the two load application points (ie, the masses in the dynamic case). The first modeshape is slightly different to this idealised shape, and results in a slightly higher bending strain in the centre than towards the edges of the stressed region. This effect is seen with CFRP samples 1 and 2, where in both cases, the residual strain for strain gauge 1 is generally higher than that for strain gauge 2. This effect could not be investigated further due to the dynamic strain data not being recorded at both points.

The autocollimator results followed the strain gauge trends very well for the measurements where there was good confidence in the strain gauges. The autocollimator technique measures average residual strain over the whole stressed surface, rather than the more localised strains. A significant limitation on this method is provided by the field-of-view, which is only 10 arcminutes for the device used. This means that the dynamic range for measurements is only 10 – θ arcminutes, where θ is the angle between mirrors at setup. However the autocollimator method offers a far higher level of

accuracy than the strain gauge method. With care, measurements could have been made with an accuracy of about 0.017 μstrain.

The CMM method proved to be of limited use for these tests. While contact probes are useful for measuring the positions of spherical tooling balls around a complicated structure, they are not ideal for measuring the shape of a relatively flexible beam. Although the repeatability of measurements was good, the results did not correlate well with the other two methods. Another limitation of this method was that the measurements were made out-of-situ. Therefore only two measurements were made, one before and one after all the shakes, meaning that there was no information about residual strains following individual shakes. Also, the handling and transport events that occurred between the CMM and vibration facilities may have affected the results. To improve on this method, it is suggested that a non-contact (optical) probe is used, and a CMM or metrology "arm" is used in-situ next to the shaker so that measurements can be taken easily between shakes. Such devices are commercially available for "shop floor" metrology.

4.6.2 Test Results

CFRP

Samples A and B displayed low levels of residual strain at low load levels. Between about 10 and 20 MPa RMS, there is a gradual increase in residual strain. Then there are larger residual strain events at 70 and 95 MPa RMS for samples A and B respectively - in the region of a 10 μstrain increase. This is partially recovered on a subsequent higher-level shake in both cases, though the mechanism for the recovery remains unclear. An interesting feature is the directionality of changes – they are mostly in the same direction, suggesting either asymmetric loading is present, or internal pre-stresses are being released.

The CFRP test suffered from high experimental errors due to the mounting configuration and strain gauge noise. The total experimental error was about ±15 μstrain for these test runs. Therefore it is difficult to draw any robust conclusions from the trends for samples A and B. However the peak results are low, and added to the error are still less than 40 μstrain. This suggests that the material is very stable under random vibration loading at these levels. Although this level of residual strain could cause problems over

the length of a camera structure, it is unlikely that a constant high stress would be present over this whole length – in reality high stresses causing microyield would be fairly localised around mounting areas and points where masses are attached.

There are a number of possible mechanisms for composite yield at this level. The most likely is microcracking in the resin matrix, where strains are already present from the manufacturing process. Fibre pull-out is another possible cause. Fibre fracture is a less-likely possibility at these stress levels. As noted in the Literature Review, there are in general a number of possible failure mechanisms, and also a large number of failure models that can be used for analysis at a macro-yield level. The specific nature of the residual strains observed in the CFRP tests is not investigated as part of this research. There do not appear to be any suitable material models in the literature that could be used to predict test results using FEA.

Al Alloy

The Al alloy samples displayed recognisable yield behaviour at a lower stress value. The elastic limit was around 45 MPa for the static test, and 25 MPa for the dynamic ones. This is somewhat lower than expected from the literature – Ref. 27 reports a value of 205 MPa for the elastic limit in tension of Al alloy 2024-T4. The difference can be attributed to differences in processing and heat treatment, as well as the different test setup (yield in bending is a combination of tensile and compressive yield, rather than the pure tension applied in Ref 27).

The Al alloy samples also exhibited greater residual strains in tension than in bending – they effectively became slightly longer during vibration. This was a somewhat unexpected result, as FEA and hand calculations both showed that bending stresses due to the first modeshape were substantially higher than any tensile stresses that could be caused under large deformations (approximately 0.53 MPa axial stress due to frictional resistance at the sliding end, compared with 55.8 MPa due to bending). This was true assuming either frictional resistance at the axially-floating end or the extreme case of both ends fully constrained axially (in fact the natural frequency results were very close to those predicted by the FEA model with no axial constraint at the floating end, suggesting that this end was moving freely as intended). That all

three samples demonstrated this effect, and it was outside the range of experimental error, suggests that it is a real effect.

Ref 27 also reports test performed on materials samples under alternating stresses. It found a similar trend to that seen here – that samples tended to grow in length, even when the stress amplitudes were significantly below the MYS. The materials tested were several grades of Al alloy (including 2024 T4) and titanium alloys.

There are several possible explanations for this. Firstly, it could be due to long range internal stress relief. Internal stresses were not measured, though they were minimised with heat treatment. However as the internal stress in the outer faces should be compressive, and the stress at the neutral axis tensile[8], it would be more likely that stress relief would cause an apparent shortening of the samples (as the regions most highly stressed – the faces – are already closer to yield in compression than tension).

The effects seen here could also be seen if yield behaviour in tension was slightly different to that in compression. Adrien et. al.[110] describe an effect called the Strain Differential Effect (SDE), where the stress-strain curves for a material are slightly different in tension and compression for low strains (<<0.2% permanent strain). As strains increase, the stress-strain curves converge to be the same at the strain levels of usual interest to engineers. The effect is somewhat dependent on prior strain history. For the current study, the static Al sample static test showed that the side in tension exhibited higher residual strains than the side in compression (Figure 72), even though peak stresses were the same or higher for the compressive side. Note that the behaviour of these curves above about 90 MPa was affected by the test samples bottoming-out on the test rig.

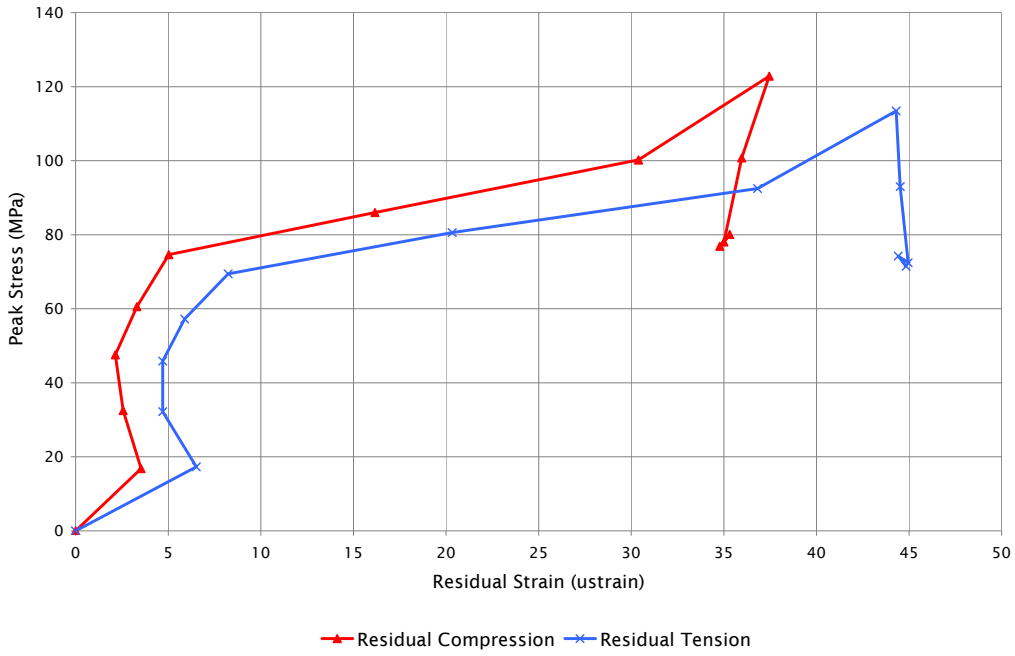

Figure 72. Tensile and compressive residual strains for the Al alloy static test.

Although this trend is consistent with the length increase observed in the dynamic tests, the SDE is a small effect, and single peak events during the test could not be responsible for the large tension-bending discrepancy observed. Cyclic plasticity models that incorporate differences in tensile and compressive post yield behaviour were not available in the FEA package used however (ANSYS 12.1), so this could not be verified analytically.

A final possibility is microplastic yield occurring under a cyclic load imposed on constant static load, such that the combination of the two stressors results in a stress level high enough to initiate plastic flow only in one direction. For cyclic plasticity problems on the macro scale, this is known as shakedown[29]. A similar effect has been described by investigators of creep in materials under load – its rate has been found to increase with the addition of a small alternating stress[8]. For analysis work, cyclic plasticity models, based on nonlinear kinematic hardening rules, are available, and these are capable of replicating the shakedown effect. These were used to model shakedown in the Al alloy samples under a slight load asymmetry caused by friction. This analysis is discussed in detail in Chapter 6.

4.7 Conclusion of the Material Tests

A novel test rig was developed to assess dimensional instability in materials subject to random vibration. The test setup and metrology methods were refined to the point where useful experimental data with relatively low levels of experimental error is achievable. This goes some way to fulfilling the second main goal of this research:

- "To develop empirical methods for the quantitative assessment of dimensional instability in structures subjected to random vibration."

The second main area of stability loss, at structural joints, is investigated in the next chapter.

In addition to the development of test setups, some useful material data were obtained for two materials commonly used in spacecraft structures. In particular, a CFRP composite was found to be very stable, and an Al alloy was found to grow in length under cyclic bending stresses. Several important behaviours were observed that also go some way towards achieving the analytical part of this goal – for both materials, there was some correlation in test results between static and dynamic tests. This suggests that for these materials, the use of material parameters obtained from (simple) static tests can be used to model behaviour under dynamic loading analytically. Further, for the Al alloy tests, residual strains tended to continue in the same direction throughout testing, suggesting that an analytical model based on ratchetting or shakedown effects may be appropriate.

5 Dimensional Stability Testing of Bolted Joints Under Random Vibration

5.1 Introduction

This chapter examines the second main structural area identified as being of interest for stable structures under random vibration – bolted joints. Together with the previous chapter, it answers part of the second main goal of this research:

- "To develop empirical methods for the quantitative assessment of dimensional instability in structures subjected to random vibration."

The joints examined in this chapter are simple bolted joints. The main alternative to this joint type is adhesive bonding. Adhesive bonding is commonly used for making glass-metal joints, or CFRP-metal joints, and is also of interest as a potential source of dimensional instability (discussed briefly for reference in the Appendix). However it is usually necessary to incorporate bolted joints in stable structures, particularly around optical mounting sub-structures that are required to be adjustable during the optical alignment process (though this is not necessarily the case for monolithic structures incorporating both optics and structure in one part, such as silicon carbide instruments – see Ref. 100 for example).

The main aim of the research presented in this chapter was to develop a test setup for assessing micron-level slipping at a bolted interface. As with the material tests of the previous chapter, such work does not appear in the literature, and requires the design of bespoke test and metrology rigs.

Several related tests have been documented in the literature. Baylis[67, 68] performed tests on bolted joints for spacecraft structures under vibration. However his test setup was designed to obtain data for gross slipping, rather than micron-level slip. Lobitz et. al.[79] describe an experiment performed at Sandia National Laboratory in the USA to measure microslipping at a faying interface under vibration. Ostensibly the purpose of this research was to better understand the damping effects of preloaded joints. The test setup

used a simple shear joint, with preload applied using a pair of rollers. Microslip was not directly measured at points throughout the joint, instead being determined from accelerometer data gathered either side of the joint. Although of interest for this research, the test setup was deemed to be too non-representative of a real joint, as it made use of a line preload rather than fastener preload. Also, the metrology technique was aimed at measuring force-displacement hysteresis loops at certain frequencies, rather than full-joint slippage following a relatively broad band of vibration frequencies.

The test setup developed for this research made use of three identical bolted joints on a single test fixture. The joints were aluminium-aluminium, with an M4 screw. The configuration was such that slippage at the faying surface would result in a rotation of one joint member relative to the other. The fixture was subject to a variety of dynamic load tests (so all three samples saw the same vibration levels). Loading was applied in the shear direction, and micron-level slipping at the bolted interface was measured. Metrology was primarily by measuring the relative member rotations optically. CMM measurements were also performed.

A second area of interest was residual movements in the axial direction of the screws, particularly those that are fastened into inserts in honeycomb panels. The BBM test results of Chapter 3 suggest that such movements occurred at the primary mirror mounting interfaces. One likely cause of this is if the inserts within the bulkhead panel were able to move a very small amount within the panel. Therefore this area was also investigated by test.

5.2 Test Description

5.2.1 Test Configuration

The aim of the bolted joint test was to assess micron-level slipping at the faying interface of a typical joint used in space structures. Loading was via random vibration in the direction of slip measurement. The joint was designed not to resonate over the test frequency range, and was free from preload in the slip direction.

For metrology, it was sought to use a setup that could resolve a small joint slip into an angular movement that could be measured with a sensitive autocollimator. The test configuration was based on a rigid element bolted to

a test fixture with a single fastener (at point *b* in Figure 73), and hinge-jointed at one end (point *a*). At point *b*, the point of interest, the joint is fixed – therefore resultant moments are possible here as well as resultant shear forces. However it can be shown that for a Rigid Element of constant section and density, an acceleration load on the Element will produce a resultant force at point *b*, with no resultant moment, if the length La = 2Lb (using beam theory). This was verified with a simple FEA model.

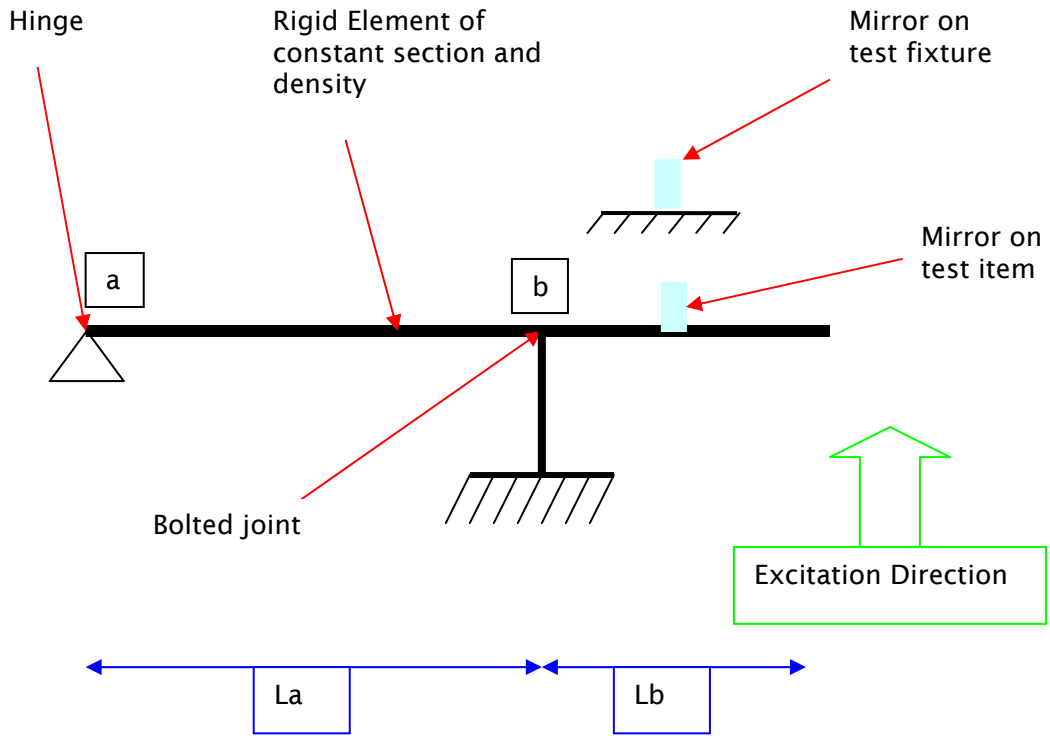

Figure 73. Conceptual layout of bolted joint slip test

The test configuration thus comprised a Rigid Element fixed to a vibration test Fixture on a shaker slip table with a single screw at the test surface (*b*), and a hinge at the end (*a*). Ideally, the hinge would have made use of a device that offers free rotation, such as a bearing. This was considered early in the design process, but was discounted for practical reasons – firstly it would add complexity and cost to the test rig. Secondly, radial bearing runout, even if only several microns, could significantly add to the expected levels of experimental error.

An alternative idea was to use a flexure at this point. This was in fact the initial design for this test rig. It was discounted because early calculations showed that it would be difficult to realise a flexure that would not provide a significant restorative force on the joint once it had slipped, and this force could bias the bias the results.

The final design made use of a second screw at point *a*. It was positioned such that under a lateral load, the Rigid Element would tend to rotate about *a*, with the bulk of the resistive force being provided by friction at *b*. A small resistive moment was nonetheless provided at *a* under this configuration. This assumption is examined in detail with FEA in Chapter 6, which shows that ¼ of the total moment resisting slipping would be due to *a*, and ¾ due to *b*. Note that the equivalent hand calculation is problematic, as the system is now statically indeterminate.

5.2.2 Test Setup

A CAD model of the Rigid Element is shown in Figure 74), showing the salient features.

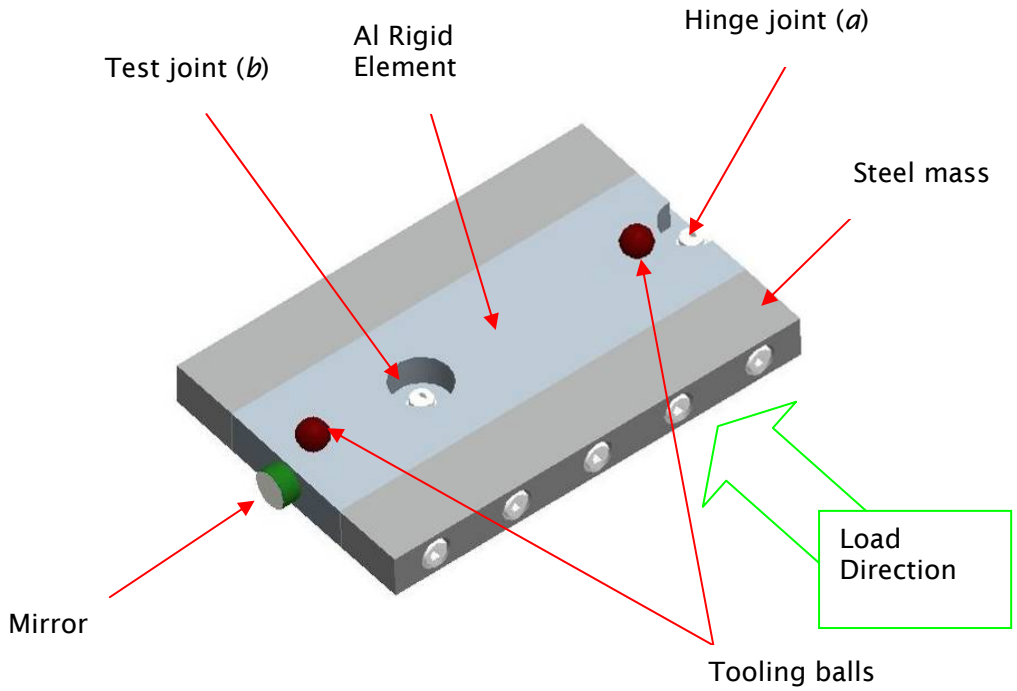

Figure 74. Bolted joint test Rigid Element.

When slipping occurred at *b*, the entire Rigid Element would rotate slightly about *a* with respect to the test Fixture. This rotation was measured

optically, and used to determine the distance of slip. A cross section view of the setup is presented in Figure 75, showing the extent of the faying surfaces and the depth of the clamped portion of the joint.

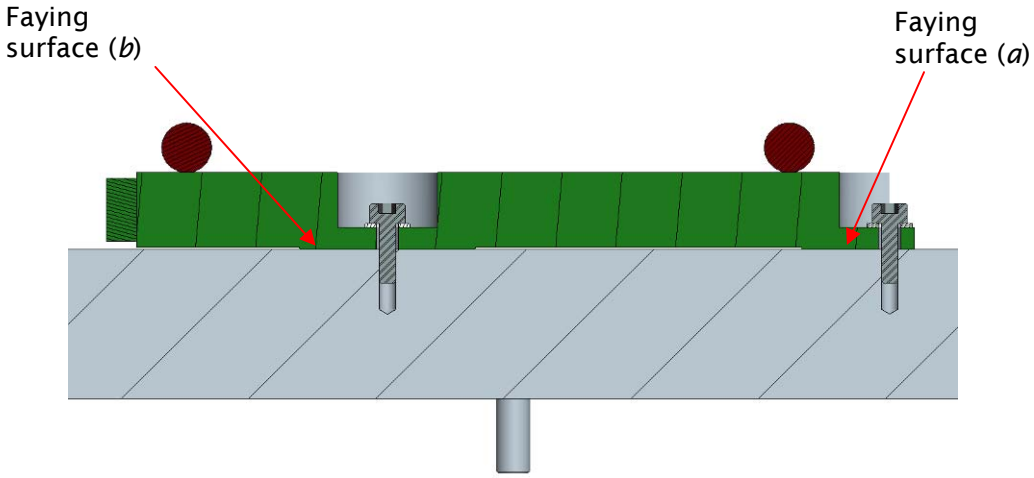

Figure 75. Cross section view of bolted joint sample.

The material used on both sides of the joint was Aluminium alloy 6082. Raised areas (35 mm diameter) on the underside of the Rigid Element were used to control the contact area (see Figure 76). All faying surfaces were machined. Surface micro-roughness was measured with a Mitutoyo Surftest machine, and found to be about 0.15 μm RMS on the Rigid Elements, and 0.2 μm RMS on the fixture. Both faying surface s were cleaned with isopropyl alcohol.

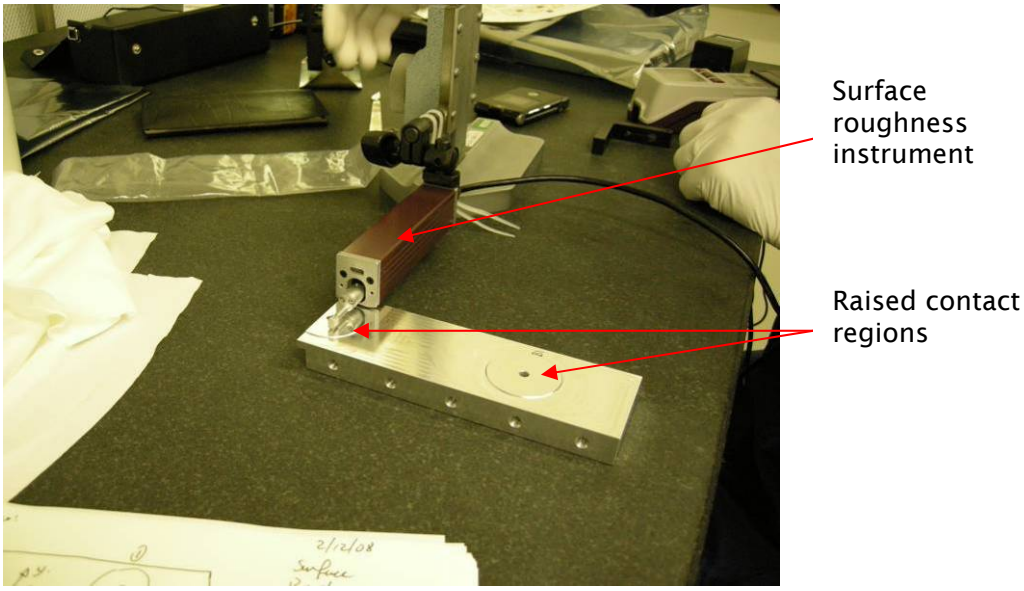

Figure 76. Surface roughness measurement.

The static friction coefficients between the Rigid Elements and the test fixture were measured using an inclined plane with an inclinometer (Figure 77). The results are given in Table 10 for five test runs. For this test, loading normal to the faying surface was provided only by the mass of the Rigid Element.

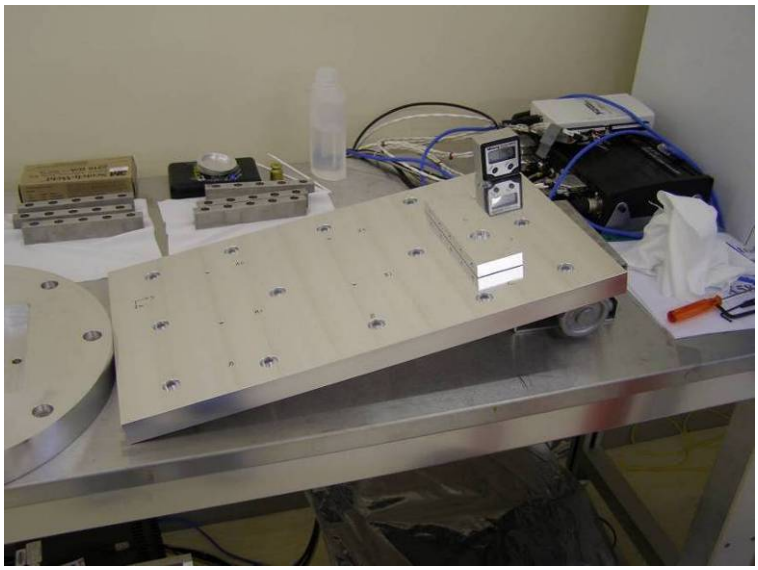

Figure 77. Static friction measurement setup

Sample	Mean Static Coefficient	Standard Deviation
A	0.41	0.02
B	0.32	0.05
C	0.36	0.05

Table 10. Friction coefficient measurement.

The fasteners used at both joints were standard metric M4 x 0.7 socket cap head screws. The screw material was A2-70 stainless steel. Preload was applied by torque-tightening. Preload was not directly measured, but inferred from the torque. The torque-preload relationship was improved by using a lubricant (Fomblin grease) on the threads. This provides more repeatable thread friction with less scatter. The torque was determined using the software Boltcalc V5.87 based on a 90% yield condition. The torque was 2.56 Nm and the estimated preload was 3090 N. Clearance holes in the Rigid Element were of 4.5 mm diameter. Fastener heads were locked with epoxy to prevent rotation.

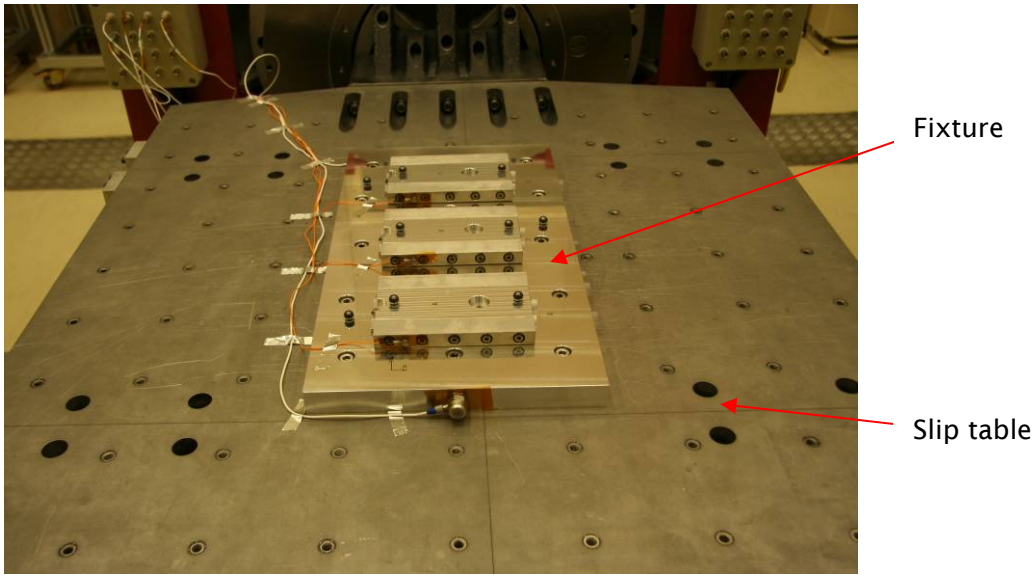

Figure 78. Bolted joint test setup on shaker slip table.

5.2.3 Loads

The Baseline load spectrum was derived from a typical space instrument test specification from Ref 99, and is shown in Table 11 and Figure 79.

Frequency	Level
20-100 Hz	+3dB/oct
100-300 Hz	1.092 g^2/Hz
300-2000 Hz	-5dB/oct

Table 11. Baseline Test Spectrum (25 gRMS)

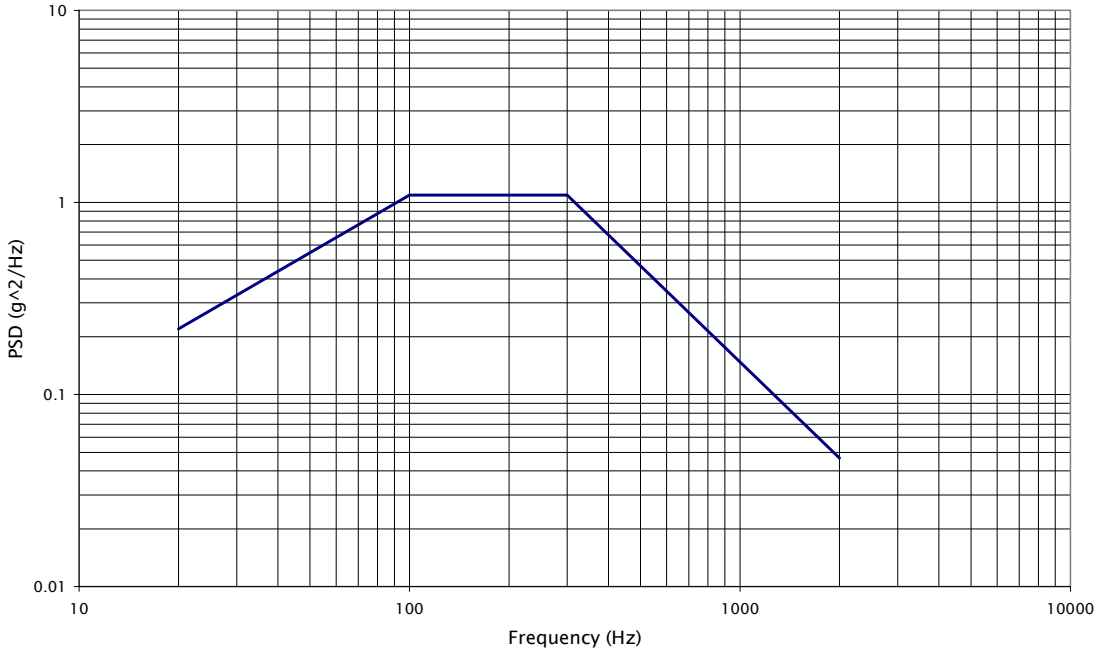

Figure 79. Baseline test spectrum

The plateau value, 1.092 g^2/Hz was determined such that the 3 x RMS value, applied as a quasi-static acceleration load, would initiate gross slipping (assuming a friction coefficient of 0.2). This would be a typical criterion for the assessment of a structural joint that was non-stability critical. Steel masses were required as part of the Rigid Element in order to achieve sufficient interfacial shear forces at these levels (Figure 74).

This approach to loading is slightly different to that used for the material tests, as the test rig was designed not to resonate within the band of the test spectrum, with the direct test levels being sufficient to initiate microslip. Thus

this test simulates a joint in an area which is highly loaded but not subject to additional loading due to resonances in the attached structure. The material tests, conversely, relied on resonance to achieve stresses high enough to initiate microyield.

The procedure required two phases of testing – a slip "Search" phase and an "evolution" phase. During the Search phase, the amplitude of the test vibrations was gradually increased (3 dB increments), starting with very low levels (Baseline -12 dB), until an unambiguous slip of 2µm was seen. At this point, the Evolution phase was started, and further tests conducted at this level, and at subsequently higher and lower levels in order to assess bedding-in effects. This is shown schematically in Figure 80.

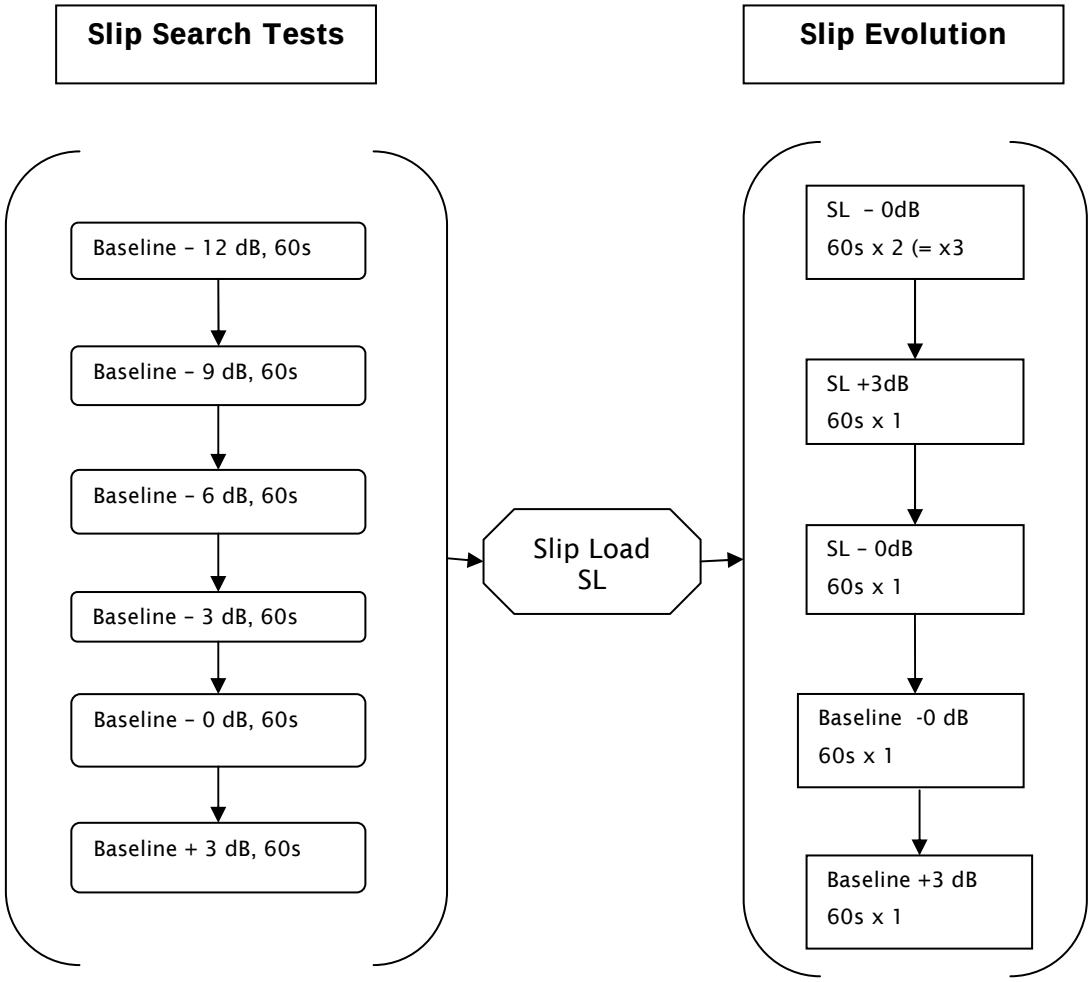

Figure 80. Schematic test plan.

5.2.4 Metrology

Two methods were used for metrology, angular measurement with an autocollimator, and CMM probing of tooling balls.

Mirrors were bonded to each Rigid Element Sample, and again to the test Fixture in such a way that both could be seen simultaneously with the autocollimator, and hence angular changes measured (Figure 81). The geometry means that a 1µm slip at the joint results in a 2 arcsecond tilt response, assuming pure rotation about *a*. The autocollimator was able to resolve to about 1 arcsecond. A pair of control mirrors were bonded directly to the fixture, to assess experimental errors.

To check the assumption about rotation with no linear slip, and to confirm the autocollimator results, contact measurements were performed on each sample before and after the series of shakes with a CMM. A pair of high-sphericity tooling balls were attached to each Rigid Element, and three tooling balls were attached to the test fixture to act as a datum.

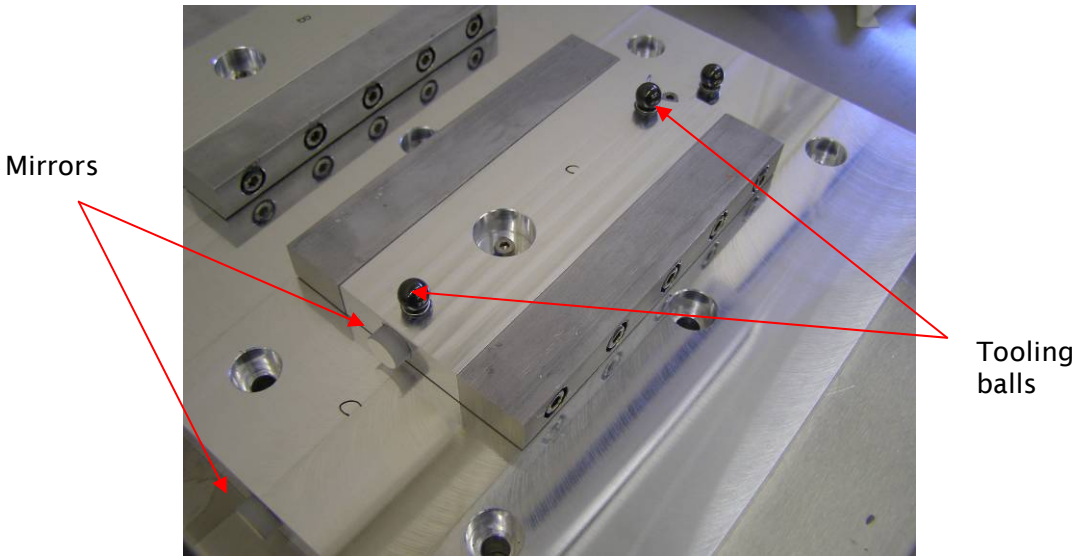

Figure 81. Metrology features.

5.2.5 Test Instrumentation

The test took place at RAL's vibration test facility (Figure 82). The shaker was a 40 kN Ling Dynamic Systems Model 954 MkII. Acceleration was measured with Bruel & Kjaer Type 4517 miniature accelerometers. The autocollimator was a Taylor-Hobson Model TA51. The CMM was an Etalon Derby, with a Tesa Star sapphire probe.

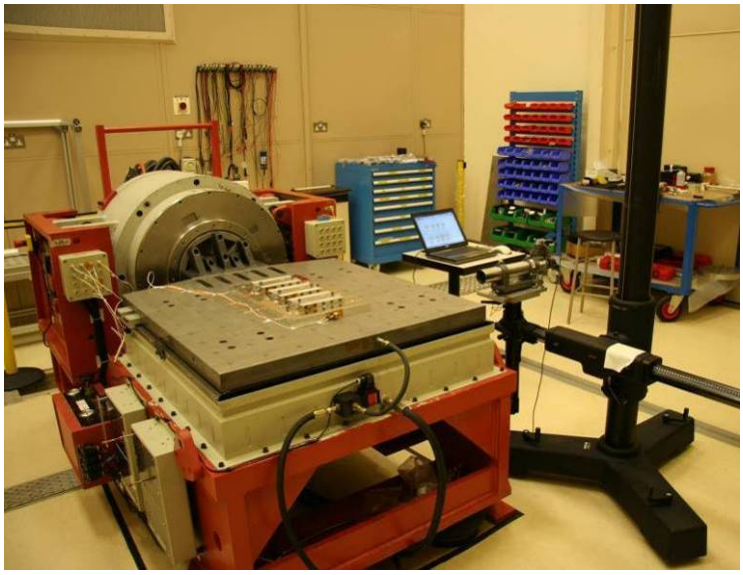

Figure 82. Test setup.

5.3 Test Results

5.3.1 In-Situ Measurements

A summary of the autocollimator results is shown in Figure 83, normalised to zero at the initial test setup. The horizontal axis shows the RMS slip force seen at the faying interface (ie, ¾ of the total slip force seen by the Rigid Element). These results show that movements are low up to the -3dB shake, where all three Rigid Elements move by up to 10 arcseconds (5µm) – this level then became the Slip Load of Figure 80. Two subsequent shakes at the same level resulted in minimal movements. Large movements were seen during the next shake (at full level), of up to 24 arcseconds (12 µm) for sample C.

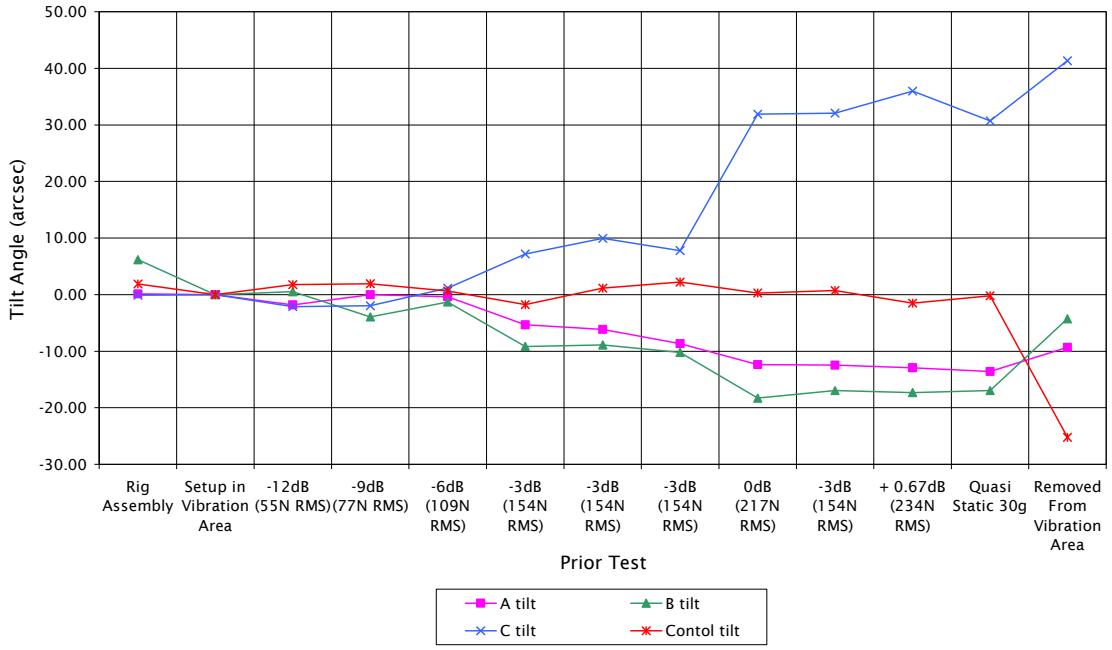

Figure 83. Autocollimator tilt measurement summary.

A further shake at the Slip Load (-3dB) did not result in any movement. The 0dB input levels were very high, and +3dB was unachievable on the shaker. The highest random level that was possible was +0.67dB, and this test was run for 40 seconds. Following this, a final sine test was run, providing an input load of 30 g at 30 Hz. A small movement was seen at C only, of about 2.5 μm. Large tilts were seen on all three samples when the test rig was removed to a different location and re-measured.

Tilt measured between the control mirrors did not vary from its original position by more than 2.2 arcseconds (~1μm) for the duration of the test, but did move significantly following transport to a new laboratory. It is possible that mirrors were disturbed by handling in this period.

5.3.2 CMM Measurements

For the CMM results, the tooling ball labels in Figure 84 are used.

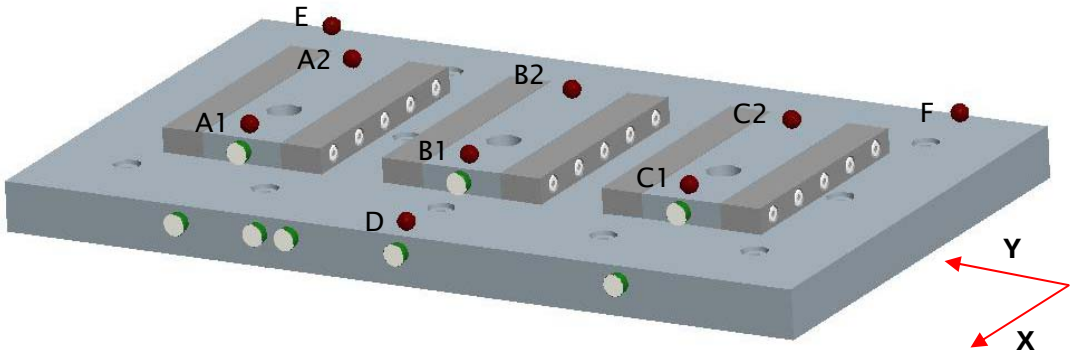

Figure 84. CMM tooling ball labels and direction definition.

Six measurement runs were performed before vibration, and four afterwards. The "after" results were rotated slightly such that the datum balls D, E and F were the same as the "before" measurements. Thus normalised, the X and Y movements for each tooling ball are shown in Table 12. Also shown is the rotation about the hinge-end balls (the number 2's in Figure 84). This is determined from the arctangent of the Y-direction movements over the distance between balls in the X direction.

Ball	ΔX (μm)	ΔY (μm)	Rotation (arcsec)
A1	-2.2	14.0	-8.5
A2	1.6	9.1	
B1	-0.7	3.7	-5.8
B2	3.7	0.3	
C1	1.7	-25.8	44.5
C2	5.1	0.6	
D	0.0	0.0	
E	1.6	1.7	
F	3.3	-1.9	

Table 12. CMM results.

These results compare relatively well with the final autocollimator tilt results, of -9.3, -4.3 and 41.3 arcseconds for A, B and C respectively.

Following these measurements, the test rig was disassembled and inspected. All the faying surfaces showed some signs of fretting, with blackening over both sides of joint (Figure 85). There is no indication that the blackening was worse for any particular sample.

Figure 85. Blackening of joint observed following testing.

5.4 Error Estimation

Using the technique described above for tilt measurements with the autocollimator, the average standard deviation obtained over the duration of the tests was 0.45 arcseconds, or about 0.2μm.

For the CMM results, the calibration certificate shows that the measurement uncertainty should be about +/- 5 μm. The standard deviation of these measurements ranged from 0 to 5μm. A check of the distance between the (fixed) tooling balls D, E and F reveals that they appear to move relative to each other by between 2 and 4 μm, which is most likely to be due to CMM precision errors rather than experimental error (ie, the balls moving).

5.5 Discussion

5.5.1 Test Setup

The correlation between results obtained with the two different methods is encouraging. The assumption that point *a* acts as a hinge can be assessed by examining the movements at A2, B2 and C2 in Table 12. Here it is seen that B and C behave as predicted with sub-micron movements in the lateral (Y) direction, though A includes a significant (9μm) movement. Possible improvements to the test rig include the replacement of the screw at *a* with either a rotary bearing or a flexure. As already discussed, both these methods introduce new problems and sources of error that would need to be assessed.

The autocollimator method was shown to be able to resolve μm-level movements between shakes. In order to achieve this precision however, five measurement runs were required for each result, and this resulted in lengthy measurement runs between each shake.

The CMM method produced useful data to back up autocollimator results. Its main shortcoming is that it was not possible to produce measurement data between shakes. Also, the test fixture was potentially subject to unexpected handling and transport loads on being moved between the CMM and vibration facilities

The general test setup is recommended for future tests in this area. It was relatively simple to manufacture and assemble. The actual test performed here was simplistic though – in reality, loading conditions would be more complex. For future tests it is suggested that modifications to this setup could be used to examine the effects of resonance, out of plane loads, and joints with a preload in the slip direction. This last test in particular would be valuable for determining whether a jointed structure must be notionally free of inbuilt strains to maximise dimensional stability under random vibration. If such inbuilt strains can cause directional movement analogous to ratchetting in materials, then the threshold strain for this behaviour should be determined.

Tests on other screw sizes and preloads should also be investigated. It is probable that joints with preloads much higher than those tested for this research would require large shakers, or the inclusion of a resonant mass to achieve sufficient slip loads.

5.5.2 Test Results

It is clear from Figure 83 that movements up to the -6dB point are very small, and the first significant movements for all three samples was at -3dB. The input level at -6dB was 12.53 gRMS, producing a quasi-static 3-σ shear resultant on the joint of 326 N. Given that the bolt preload was 3089 N, and assuming a friction coefficient of 0.36 (the average static value measured), a safety factor of (3089x0.36)/326 = 3.4 on 3-σ resultants would have prevented this initial slip. When the levels are increased to those designed to produce gross slip, a large slip is observed (albeit with a friction coefficient of 0.36 rather than 0.2 assumed for this load).

The distances moved for each slip event were generally similar for all three samples except during the 0 dB run, when sample C moved significantly more than A or B. This suggests some inherent variability in the slip response for nominally identical samples under identical loading.

Movements tended to be "sided", and therefore to accumulate over tests of increasing severity. Bedding-in with the joints was observed at levels equivalent to the peak levels so far tested. Therefore short duration bedding-in shakes at levels as high as the maximum qualification levels (or higher) would be suitable for improving joint stability.

5.6 Insert Test

5.6.1 Insert Design

The BBM tests of Chapter 3 showed that the primary mirror dummy mass moved substantially in the axial direction under random vibration (see Figure 27). There are several possible causes for this – one being the inserts within the honeycomb panel moving slightly within the panel (ie micron-level pull-out). This possibility was further investigated by test.

The insert design used for the BBM bulkhead panel made use of CFRP cylinders containing metallic thread inserts. The CFRP cylinders spanned the thickness of the panel, being bonded to both the upper and lower skins in order to facilitate load transfer to both sides of the panel. Additionally, they were "potted" within the honeycomb core with a foaming adhesive. The general layout is shown in the CAD image of Figure 86.

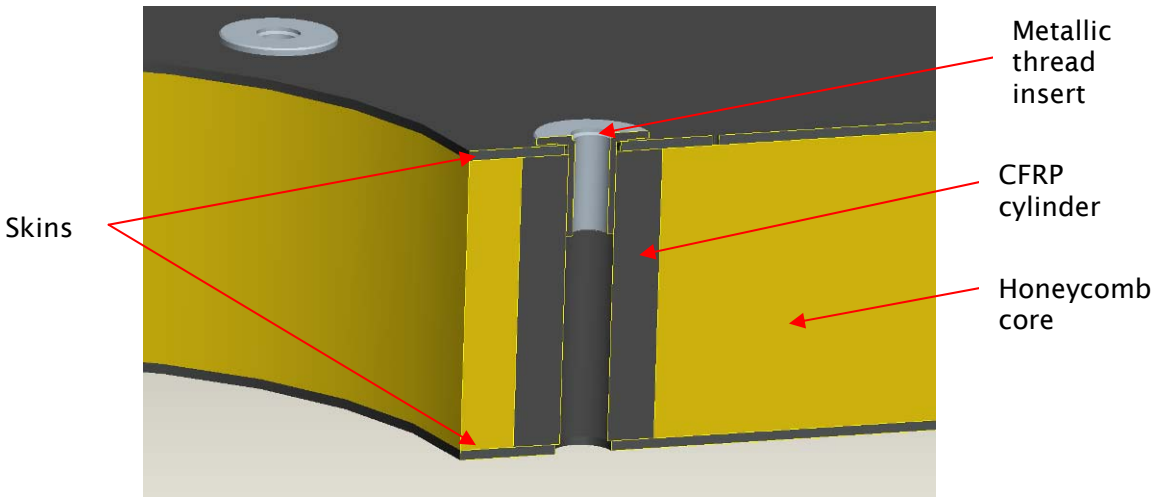

Figure 86. CAD model of insert.

A number of insert test specimens had been procured with the BBM structure. Several of these had been tested to destruction with a tensile test rig in order to determine safety factors on ultimate tensile failure. A test was performed on one of the remaining samples in order to determine the dimensional stability response to a tensile load. The specimen was essentially a single insert in a 100 mm square piece of panel. The insert, adhesives and materials were all identical to those used in the BBM bulkhead panel.

5.6.2 Insert Test Setup

Only static loading was considered, with tensile (pull-out) forces acting on the insert. This is because the test samples that were available could not be easily incorporated into a vibration test setup that imparted a load spectrum in a controlled manner in a single direction at a time (ie, the load imparted by a vibrating mass on the inserts would have included shear, bending and axial components that could not easily be separated).

The test sample was a small panel section of 80 mm x 80 mm size (see Figure 87). It was clamped in a test mount with a circular (70 mm diameter) aperture for the insert. This test geometry was suggested in the ESA Insert Design Handbook[111] for insert tensile pull tests.

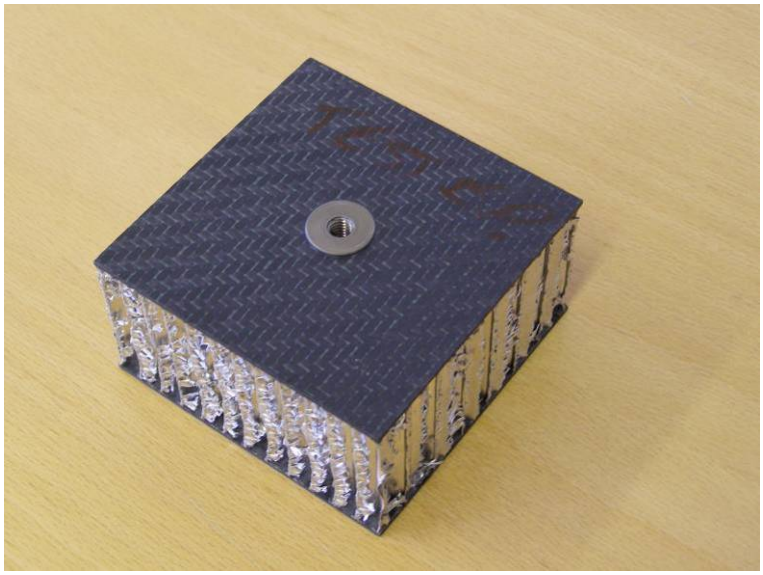

Figure 87. Test sample.

The test was arranged horizontally (ie, with the axis of the insert pointing horizontally). This was to facilitate the use of optical metrology equipment that needed sensitive alignment. The tensile test rig used was the Testometric AX500 machine previously used for static testing of the material samples. This rig was vertically-arranged, so a cable with a pulley was used to apply the tensile load to the test rig.

Metrology used two methods – laser interferometry to measure axial movement of the insert with respect to the front skin, and autocollimation to measure residual angular movements of the insert with respect to the front skin. Thus, flat mirrors ad retroreflectors were bonded to the front skin to act as reference points. Commensurate reflectors were attached to the insert via a stainless steel bar screwed onto it. This is shown in Figure 88.

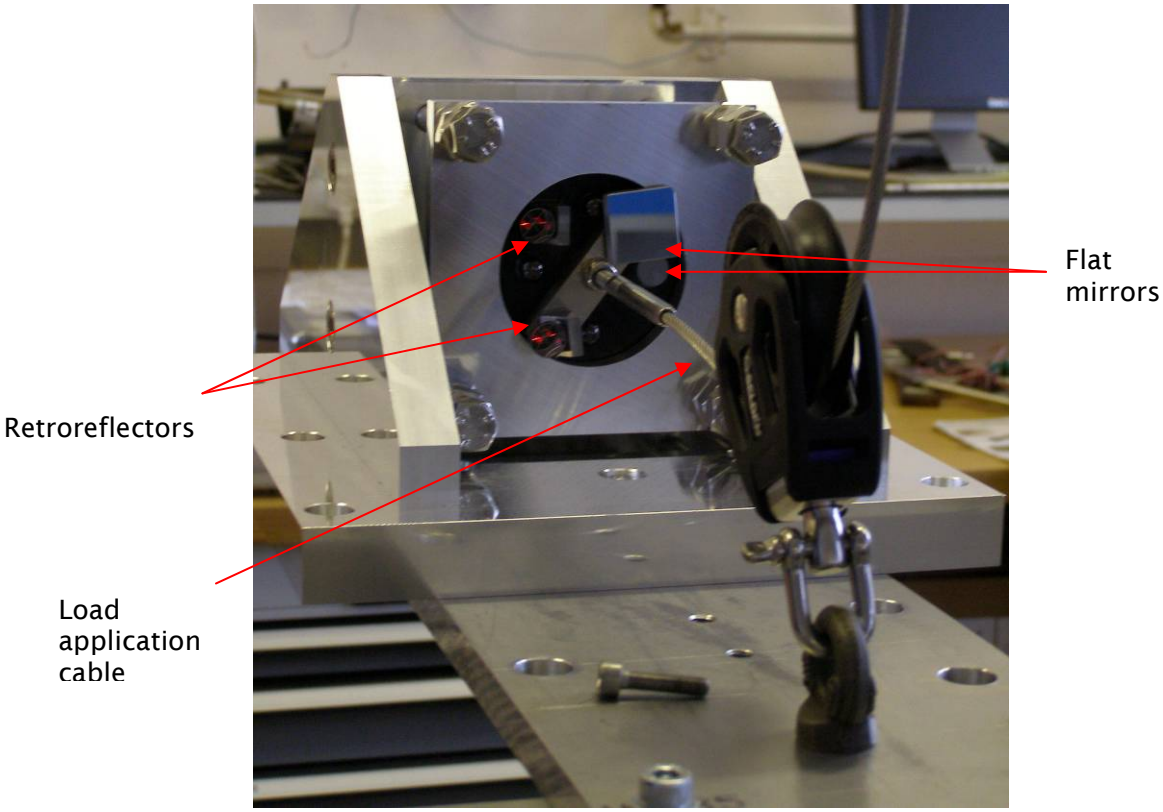

Figure 88. Insert test specimen.

The full test setup, including the autocollimator and laser interferometer heads is shown in Figure 89.

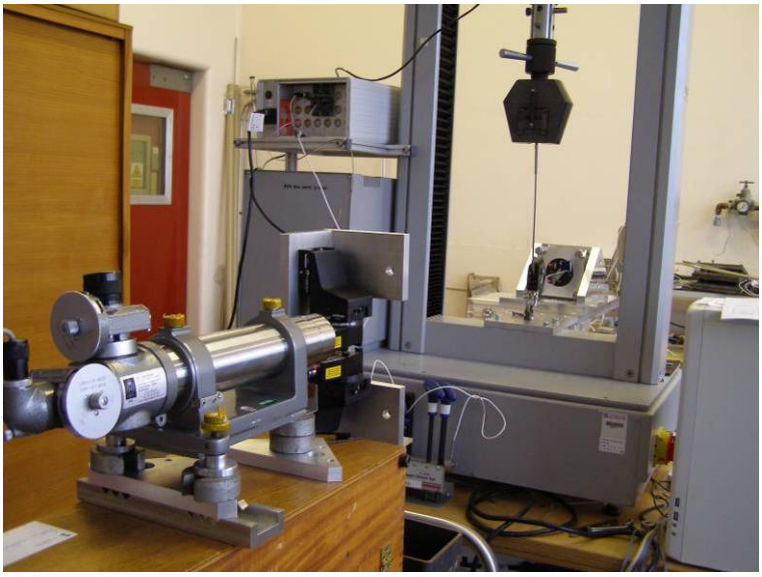

Figure 89. Full test setup.

5.6.3 Loading

As in the material sample static tests, the load was applied in increasing steps, and relaxed between them to measure the residual strain. The step size started at 50 N, then increased to 100 N, and then to 250 N as the test progressed. The final load achieved was 4000 N. This compares with an average pull-out force of 5.8 kN, determined from previous tensile tests on identical samples.

5.6.4 Results

The results are shown in Figure 90. The laser interferometer results are cut-off at 900 N, as lock was lost on one of the retroreflectors. Also, tilt was only measured about one axis due to the setup angle between the mirrors in the other axis being too great.

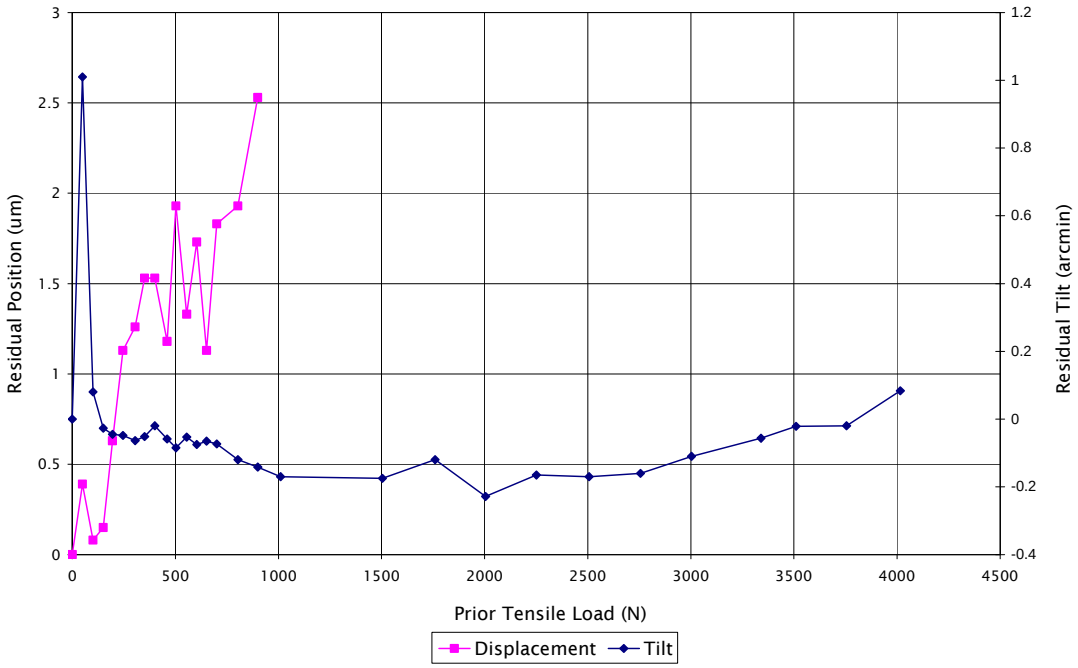

Figure 90. Insert residual strain test results.

The tilt angle was very small apart from an early peak following the very first load-unload cycle. From 2500 N onwards, it shows a gradual increase of about 0.3 arcminutes to the final 4000 N cycle. The displacement results show a gradual increase of about 2.6 μstrain over the first 900 N range.

These results are fairly small compared to the movements observed for the BBM primary mirror dummy mass in the axial direction, of up to 95 μm.

The force resultants at the BBM panel inserts were not measured during BBM vibration testing, but were determined from an FEA model to be between 630 and 970 N RMS. Higher peaks (at say, 3-σ) may have pushed the BBM inserts past some yield threshold, that was not reached with displacement metrology in the presently-described static test. The tilt measurements were achieved at a much higher load level – these suggest that such a threshold was not achieved within the 3-σ range though (unless the yield was manifested in a pure tensile pull-out with no tilt).

It is also possible that cyclic loading produces much higher levels of insert microyield than equivalent static loads. The presence of pre-strain at the joint may have a large influence here. Even so, the relatively low residual movement values observed here suggest that other effects were possibly more dominant. Other possible causes for the high BBM M1 movements are load conditions being much higher than expected, microyield in the titanium M1 flexures, or slippage at the M1-flexure interface.

5.7 Conclusion of the Bolted Joint Tests

A test rig was developed to assess micro-slipping at a bolted interface subject to random vibration loading in the slip direction. This partly meets the second goal of this research:

- "To develop empirical methods for the quantitative assessment of dimensional instability in structures subjected to random vibration."

The test method used optical and contact methods to measure slipping. Both methods correlated well with each other for the three samples tested. For the case tested here (with no shear-direction preload and no resonance), it was found that a safety factor of 3.4 would have been required (based on measured preload and friction coefficient values, and 3-σ resultants) to prevent micro-slip initiation.

The possibility of residual movements in the axial direction due to the micro pull-out of panel inserts was also investigated with static tests. It was found that although this makes a small contribution to dimensional instability, it probably can't explain some of the large M1 movements seen with BBM testing.

A further important conclusion of these tests is that bedding-in shakes at high levels for short durations could enhance the resilience of dimensionally stable bolted joints under random vibration.

6 FEA Modelling of Dimensional Instability

6.1 Introduction

The aim of this part of the research was to investigate ways of modelling the residual strain behaviour seen during testing using commercial FEA software, hence addressing the third main goal of this research project:

- To assess the potential for predicting dimensional instability under random vibration using FEA techniques.

The focus of this chapter is modelling the effects seen during the material sample tests, in particular the metallic ones. FEA modelling of bolted joints is also assessed.

Vibration Analysis

There are a number of challenges in attempting to predict plastic microyield behaviour in materials subject to random vibration. Firstly there is the random nature of the test loads. Inherently, we are trying to predict deterministically the outputs from a random process. Such an exercise must therefore be considered as an estimate, rather than a closed-form solution.

For random vibration effects, the literature is mainly concerned with fatigue damage. There are well-established methods for predicting gross failure in materials under cyclic loading using S-N curve data and Miner's Cumulative Damage Ratio[112]. However there do not appear to be any procedural methods for predicting plastic strain in the 10^{-5} - 10^{-6} region resulting from random cyclic loads.

A structure subject to harmonic excitation is relatively straightforward to analyse. With simple mathematical models (using mass, stiffness and damping parameters), it is possible to deterministically predict stress amplitudes which do not vary from cycle to cycle. Such problems lend themselves to the use of tension-compression cyclic plasticity test data to predict residual strain. While such an analysis may be of use for structures undergoing harmonic testing, random vibration is more problematic, and can be more severe in terms of its effect on dimensional stability. This is for two reasons – firstly, random

vibration simultaneously excites modes over a wide frequency range, including primary modes and their harmonics. Harmonic excitation acts at only one particular frequency at a time, which may not be a resonance. Exposure to random vibration - either during ground testing or during launch - typically lasts for several minutes, with the power spectrum of the excitation remaining constant throughout. Harmonic testing generally sweeps through from a low frequency to a high frequency, resulting in exposure to resonance lasting for a smaller duration.

Cyclic Plasticity Prediction

Predicting plastic strain resulting from random vibration can be problematic and there does not seem to be an established method to perform these calculations. The difficulties in carrying out predictions arise for two reasons. Firstly, it can be difficult to determine a useful stress response to compare with an established yield criterion. Random vibration results in cyclic stresses at a number of different frequencies and amplitudes simultaneously, giving rise to a complex stress state that requires a probabilistic description. It is relatively straightforward to obtain a solution for stress components that are Gaussian with a zero mean. Combining these - to produce a von Mises equivalent resultant for instance - produces a probability distribution that is no longer Gaussian with a zero mean, complicating the calculation[107]. The probability distribution function (PDF) of the von Mises response is in fact governed by a chi squared distribution[113]. Composites have more complex failure modes. These typically require combination of several component stress resultants, each with its own PDF to compare with the failure criterion of interest.

Secondly, it is not clear how to use such a stress response to predict residual plastic strains. Is the residual strain response dependent on instantaneous high peak stresses that might occur only a few times during the vibration exposure, or is it more likely to depend on lower-amplitude stresses cycles that may occur many thousands of times (or both)? Also, the plastic strain response can be somewhat dependent on the rate of the applied stress. A number of metals tested by Nicholas[114] using a shock loading test rig demonstrated higher strength at faster strain rates.

The analysis presented in this chapter starts with the premise that the growth in length observed for the Al alloy samples was due to cyclic hardening under a non-symmetric load. It is assumed that static test data is sufficient to

determine the necessary material constants. For loading, an approach similar to Miner's rule for fatigue analysis was used, combining the effects of several stress amplitude levels. The number of cycles of each is dependent on the probability of exceedance during exposure. This is then to be used to approximate a time-history stress response that can be input as sequential load cases in an FEA model for solution in the time domain.

6.2 Model Description

The model was a simple 2-D FEM produced in ANSYS 12.1. It was produced in 2-D in order to minimise the solution time taken. With a large number of load steps to solve, each one a nonlinear iterative solution, minimising model complexity to ensure a reasonable solution time was important. The model is shown in Figure 91. It included 232 elements and 1658 degrees of freedom. The elements were type "Plane 183", which are 8-node 2-D elements. The boundary conditions were applied as simple supports – these are shown in blue in Figure 91.

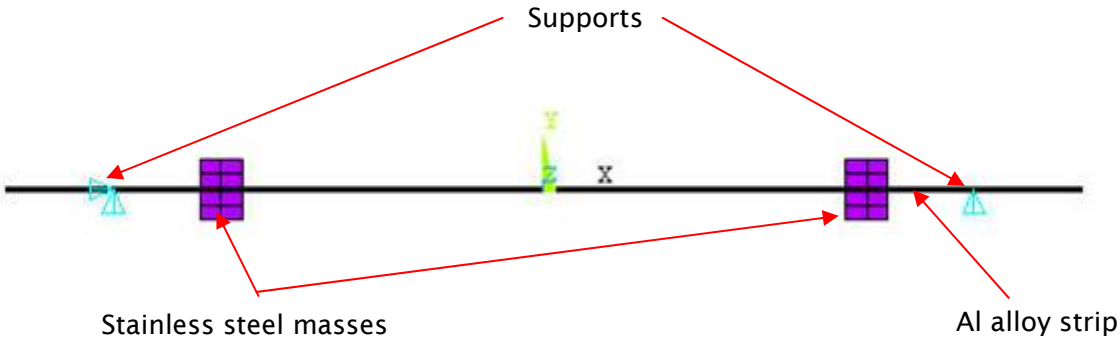

Figure 91. FEA model.

6.2.1 Material Properties

The material model used was nonlinear kinematic hardening. This is a rate-independent cyclic plasticity model that can predict ratchetting and shakedown effects in ductile materials[10]. This model assumes that under monotonic loading above the material yield stress, hardening occurs (ie, the yield stress shifts). On reversal of this load, hardening also occurs. Over a number of cycles, hardening occurs but at an ever decreasing rate (governed by a tanh function). This allows the shapes of stress-strain hysteresis curves to

be accurately predicted (as opposed to the linear case, which would assume simple bilinear hysteresis curves). In the presence of a purely cyclic symmetric load, this behaviour will not result in accumulating plastic strains. However in the presence of a non-symmetric cyclic load, the hysteresis curves can gradually move along the plastic strain axis (with a reduction in the movement every cycle). This behaviour is called "shakedown"[29] – see Figure 3. The yield surface is governed by the von Mises criterion.

Hardening Rule

The model uses a hardening curve that is modified every cycle with a "back stress" term that takes the following form[115]:

$$\alpha = \frac{C}{\gamma}(1 - e^{-\gamma\varepsilon^{pl}})$$

Although it is possible to obtain an accurate hardening curve over a typical strain range of interest, it is harder over a large range. Thus, additional values of *C* and γ (representing additional kinematic models) can be superimposed to better represent additional strain ranges. For *n* superimposed models, this provides a term of the form[10]:

$$\alpha = \frac{C_1}{\gamma_1}(1 - e^{-\gamma_1\varepsilon^{pl}}) + \frac{C_2}{\gamma_2}(1 - e^{-\gamma_2\varepsilon^{pl}}) + ... + \frac{C_n}{\gamma_n}(1 - e^{-\gamma_n\varepsilon^{pl}})$$

This requires some basic parameters to be defined from cyclic test results: *k*, C_i and γ_i. Here, *k* is the elastic limit, C_i is the initial hardening modulus, and γ_i is a parameter that controls the rate at which the hardening modulus decreases with increasing strain. Ref. 115 provides a good guide to the identification of these parameters. It is basically a curve fitting procedure, performed in $\Delta\sigma/2$ - $\Delta\varepsilon^{pl}/2$ space using the following identification equation[10, 115]:

$$\frac{\Delta\sigma}{2} - k = \frac{C_i}{\gamma_i}\tanh\left(\gamma\frac{\Delta\varepsilon^{pl}}{2}\right)$$

where $\Delta\sigma$ and $\Delta\varepsilon^{pl}$ are the stress range and plastic strain range for a developed hysteresis loop. Thus, hysteresis loops are required for several stress amplitudes in order to obtain the parameters. The first step in the procedure is to determine k, the elastic limit (or yield stress for some applications). Next the asymptote C_i/γ_i is obtained from the data curve. Finally, γ_i (and hence C_i) is obtained using an arbitrary curve-fitting algorithm.

The data collected from the static Al alloy tests of Chapter 4 were for monotonic loading in only one direction. Thus it was not possible to deduce the full hysteresis loops, and therefore the exact values of $\Delta\sigma/2$ and $\Delta\varepsilon^{pl}/2$. However it still is possible to estimate the parameters from such data using a single tension curve, and assuming that the shape of this curve is the same as that of a developed hysteresis curve[115]. This is the approach that was taken here.

Parameter Identification

Another problem with the data of Chapter 4 was that although plastic strain was observed in the strain range of interest, the data did not extend into a range where it was possible to determine an asymptote, necessary for determining the ratio C_1/γ_1 and hence C_1 and γ_1. Therefore the test data were combined with data from the literature for a much higher strain range that included this asymptote. Constants C_2 and γ_2 were obtained from Ref. 116. The result is a model with the constants k, C_1, γ_1, C_2 and γ_2. The constant k, the elastic limit, was determined from Figure 68. Next, the value C_1/γ_1 was obtained by ensuring that the asymptote of the calculated curve was the same as that in Ref. 116. Finally γ_1 was obtained by curve fitting against the test data using MS Excel's "Solver" add-in. The final constants are shown in Table 13 and a summary of the relevant curves is in Figure 92.

Constant	Value	Units
k	4.37e7	Pa
C_1	1.94e12	Pa
γ_1	6748	-
C_2	1.18e10	Pa
γ_2	103	-

Table 13. Nonlinear kinematic hardening constants.

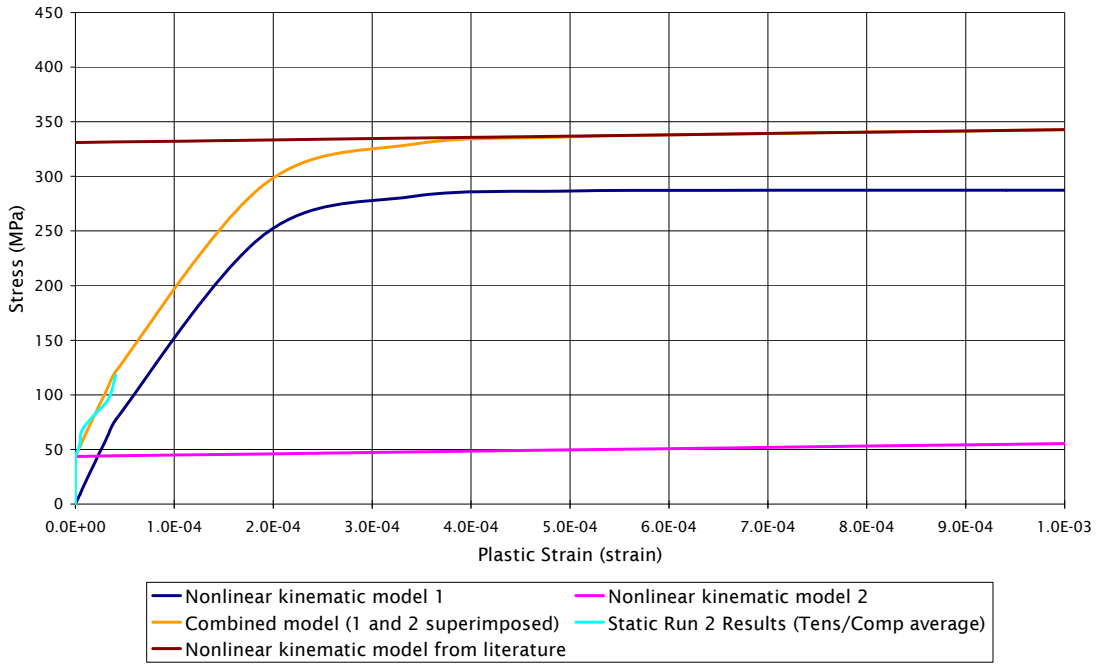

Figure 92. Nonlinear kinematic hardening curves, showing how two models (1 and 2) were superimposed to obtain a curve that matches both the test results and the curve from Ref. 116.

The "Combined model" in Figure 93 was the one used for analysis. There is a clear interpolation in the data between about 125 MPa and 335 MPa. This should not cause a problem for the analysis, as most of the cyclic loading occurs below 125 MPa, with the peak 3-σ loads resulting in stresses only slightly exceeding 130 MPa.

6.2.2 Loads

The +12 dB (58.4 MPa RMS) test was used for analysis, as this was the first load case that produced significant residual strain events, with roughly similar results for samples A and B. Firstly, the FEA model was correlated with the test results by adjusting the damping values for each mode. As noted in Chapter 4, damping was higher than originally expected. This was probably due to sliding at the clamped mounting supports. Correlation was based on the accelerometer response for sample B (see Figure 93). The responses are well correlated for the first two modes, but not after this. The difference in high frequency behaviour is probably due to the FEA model being only two-dimensional, excluding torsional modes and other modeshapes that act across the width of the beam rather than along it.

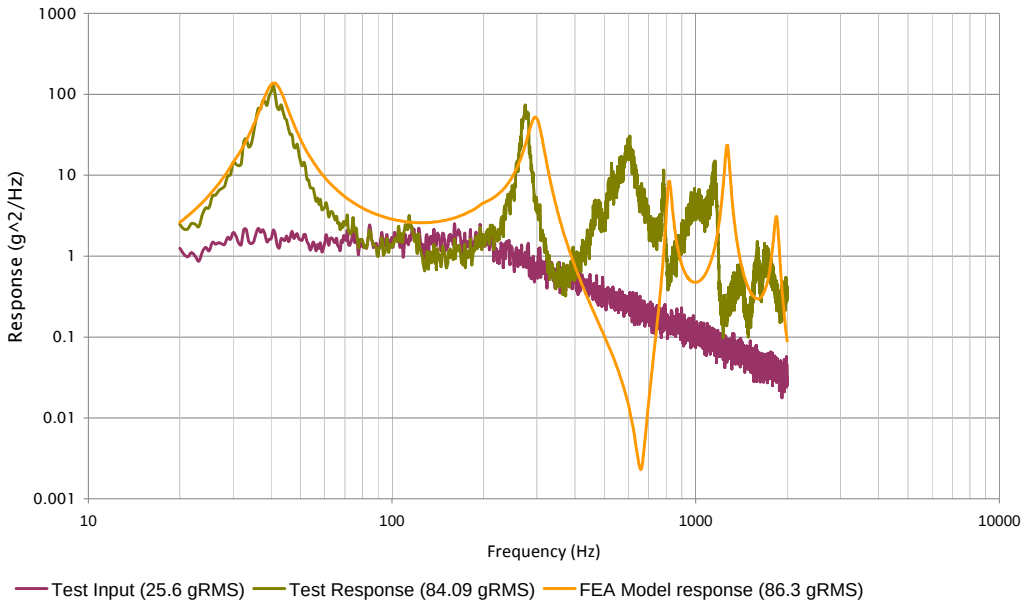

Figure 93. Al alloy sample B +12dB run - correlation between accelerometer data and FEA model. Modal damping values of 10% and 6% for first and second modes respectively were used.

While the test response in Figure 93 shows significant peaks well beyond the first natural frequency, these peaks are less of a concern for stress analysis. This is because the resulting displacements (and therefore the stresses and strains) are inversely proportional to the square of the frequency. The power-spectral density response for one of the strain gauges on sample B is shown in Figure 94 to illustrate this.

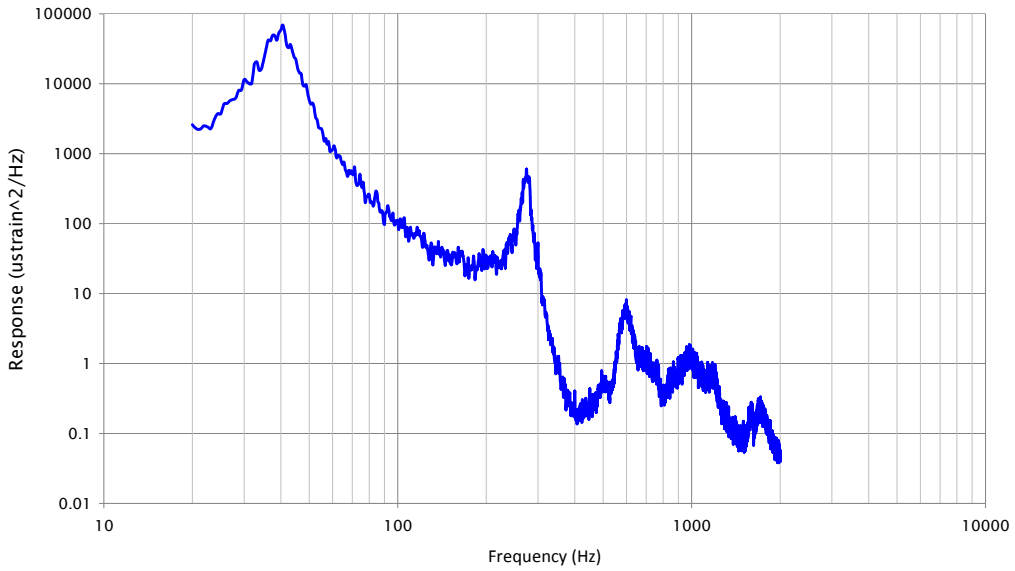

Figure 94. Power spectrum of the microstrain response for the sample B +12 dB run.

To determine the quasi-static load to be applied, it was assumed that the residual strain response was entirely due to the first bending mode of the samples, with no contribution from the higher modes. The response due to the first mode only was obtained by truncating the full response at a factor of 1.414 from the first natural frequency. The RMS value of this truncated response was then used as a quasi-static input acceleration for the time-domain analyses. The FEA-determined RMS stress response at the centre of the sample compared well with the RMS value measured by the strain gauges (56.2 and 58.2 MPa respectively, assuming an elastic modulus of 73 GPa).

Axial Force Due to Clamp Rod Friction

The load non-symmetry was provided by an axial frictional force at the axially-free end. Friction was measured directly from the test rigs with a force transducer to have static coefficient of 0.376. The axial frictional load was applied at point *x*2 in Figure 95 and Figure 96, and was based on the sum of the resultant force at this point and the spring clamping force.

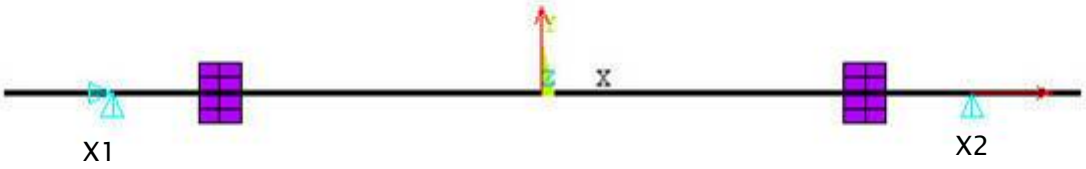

Figure 95. FEA model showing quasi-static acceleration upwards.

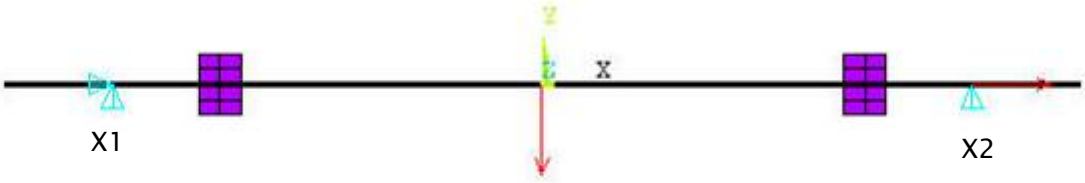

Figure 96. FEA model showing quasi-static acceleration downwards.

Load Cycles

Next, the cyclic plasticity analyses were performed by applying a series of bending load cycles, applied as quasi-static accelerations. A Miner's Rule approach was taken, assuming there would be contributions from stress cycles over a range of amplitudes. Accelerations were determined at the 1-σ, 2-σ and 3-σ levels, with the number of cycles commensurately determined from the probability of exceedance to be 779, 112 and 7 respectively (based on the test duration and frequency of the first mode). For ease of generation of the load step input files, the cycles were applied in groups of the same level – ie, the 3-σ cycles were applied first, followed by the 2-σ and 1-σ cycles. This is shown in Figure 97. A summary of the load amplitudes is shown in Table 14.

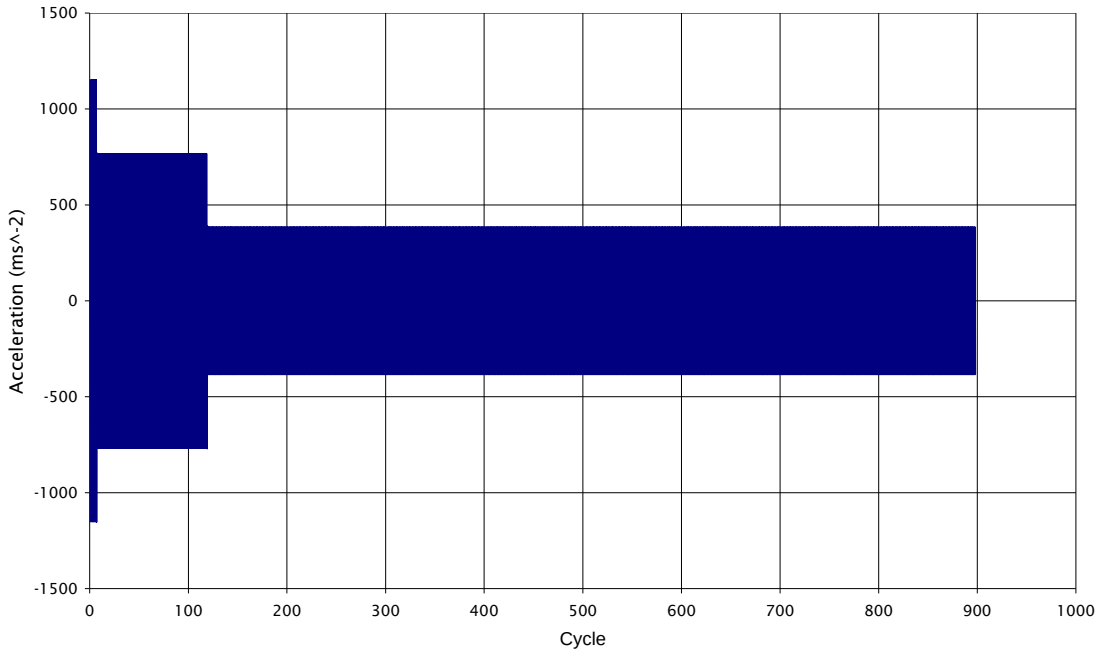

Figure 97. Quasi static acceleration cycles applied to the FEM.

	Probability of Exceedance	No. Cycles	Acceleration	Lateral Friction Force
			m/s^2	N
1-sigma	0.3173	779	383.6	24.8
2-sigma	0.0455	112	767.1	34.5
3-sigma	0.0027	7	1150.7	44.2

Table 14. Summary of FEM loads.

Each full load cycle used two load steps, with 20 intermediate sub-steps. Although the model is very simple with few degrees of freedom, the large number of nonlinear (iterative) loadcases led to a long solution time – several hours using a high-specification analysis PC. This is likely to be the limiting factor for more complex geometries representing real hardware.

6.2.3 Results

The results are shown in Figure 98 for the time-domain plastic strain response. There is a clear trend from equal tensile and compressive plastic

strains in the first cycle to purely tensile residual strains at the end of all cycles. Figure 99 shows this behaviour with stress vs plastic strain hysteresis curves. These commence with the 7 large 3-σ cycles, followed by the 2-σ and finally the 1-σ cycles. By the time the 1-σ cycles are complete, both the tension and compression sides of the cycles are on the residual tensile strain (positive) side of the graph, indicating an overall elongation of the sample. The final values were 21.1 μstrain and 8.2 μstrain on the upper and lower surfaces respectively, giving an average axial extension of 14.7 μstrain. The equivalent values observed with strain gauges for sample B during the +12 dB test were of 27.2 μstrain and 3.1 μstrain, giving an average of 15.2 μstrain.

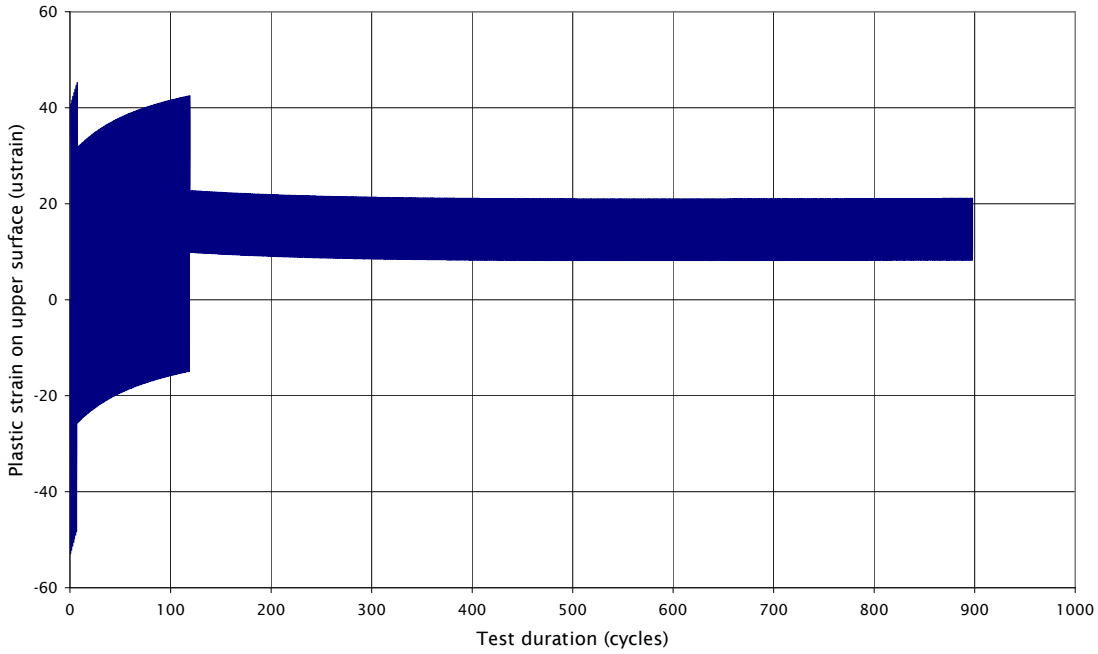

Figure 98. Plastic strain results at upper surface node representing a strain gauge.

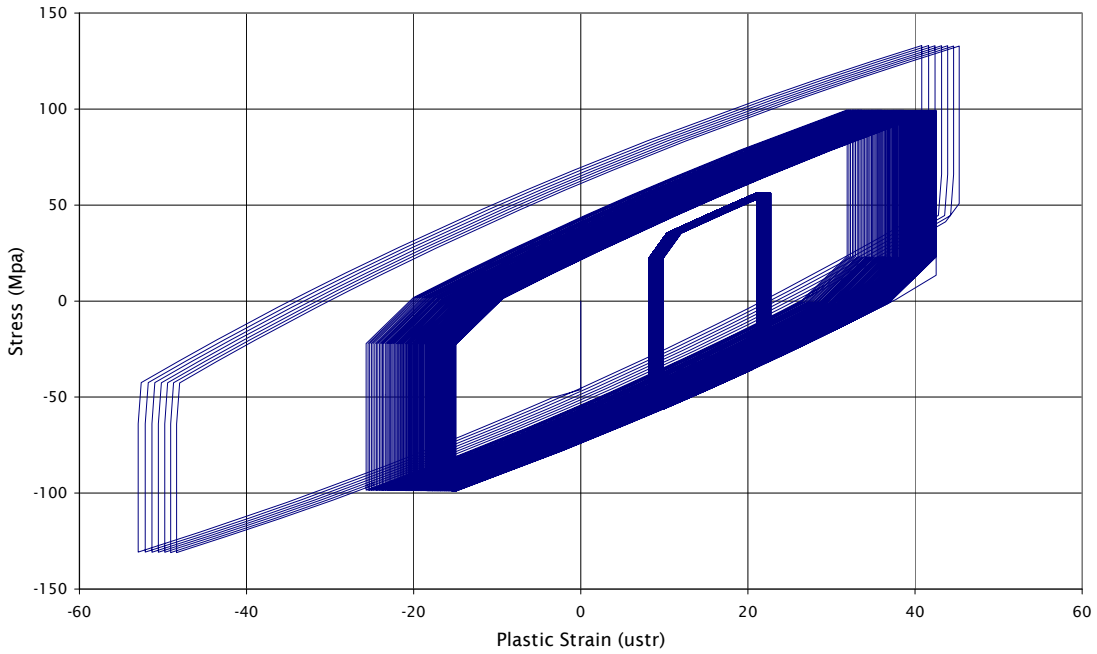

Figure 99. Stress vs plastic strain hysteresis curves for the analysis.

Thus this simple FEA model has been able to predict the extension behaviour of this sample with reasonable accuracy. The difference between the final upper and lower values is dependent on the amplitude of the final stress cycle applied, in this case 1-σ. The test results suggest that a final cycle of slightly more than 1-σ would have been appropriate for the FEA model.

The peak stresses seen in the material, about 130 MPa (3-σ), are of a level that may potentially occur in a spacecraft structure. Such structures are often dimensioned using gross structural failure based on UTS and 0.2% proof strength as failure criteria. These values are over 400 and 300 MPa respectively, and likely to provide positive safety margins in this case.

It should be noted that the nonlinear kinematic hardening rule used here is based on von Mises equivalent stresses. The use of von Mises stresses with random vibration analysis can be problematic, as they do not follow a normal distribution (see Chapter 2). For the analysis presented here, the simple geometry and loading means that the peak von Mises stresses are nearly identical to the peak component (X-direction in Figure 91) stresses, which are Gaussian. For more complex analyses, other methods would be required to determine the probability density function (probably based on a chi squared distribution – see Ref. 113) and therefore estimate the number of cycles at each stress level.

6.2.4 Discussion

The behaviour seen during test was successfully modelled with nonlinear kinematic hardening. The key point in this analysis is that a relatively small stress asymmetry can have a large impact on the dimensional stability response of a structure over a large number of cycles. For a real structure, it is difficult to foresee a situation where there is no asymmetry. Most structures contain some in-built pre-stress following assembly. This can be minimised in critical areas (such as mirror mounts) by employing a kinematic fastening philosophy, so that constrained degrees-of-freedom do not conflict. However there are other sources of asymmetry that would be harder to address. Gravity is an obvious case. A more problematic source is static acceleration loading during launch – this obviously is beyond the capability of standard electrodynamic shaker testing.

Apart from minimising the load asymmetry, minimising the cyclic stresses is a logical approach. In general, maximising the natural frequency of a system is beneficial in this respect, as peak displacements are generally lower. However, increasing the natural frequency will result in a larger number of stress cycles. The effect of increasing the number of cycles is likely to be outweighed by the effect of reducing the peak stresses. This is borne out in Figure 98, where the larger number of low-amplitude cycles has less effect on residual plastic strain than the smaller number of high-amplitude cycles. Also, deformations in the breadboard testing of Chapter 3 were observed to be more dependent on input test levels than durations.

Finally, the use of a safety factor against yield failure could be extended to microyield. If there is good knowledge of the microyield properties of a material, then a suitable safety factor can be used during the design process to ensure that that stress threshold is not exceeded.

6.3 Bolted Joint Analysis

6.3.1 Introduction.

A finite element model was produced to investigate the behaviour of the bolted joint test setup of Chapter 5. The main aim of the model was to test the assumptions made in Chapter 5 about the way the test setup responds to lateral loads. A secondary aim was to investigate the prediction of shear

slippage evolution under random vibration in the lateral direction using a sequence of load cycles solved in the time domain (in a similar manner to that used in the previous sections for cyclic plasticity).

6.3.2 Test Setup Verification.

It is a somewhat counter-intuitive aspect of the test setup used in Chapter 5 that the end that is supposed to be hinge-jointed (point *b* in Figure 73) is actually fastened with a screw of the same size and preload of that used at the slip joint (point *a*). An analysis was performed to assess this, and also to assess the relative proportions of the whole slip load that the test mass sees that are resisted by the slip joint and the hinge end.

The model was a solid 3-D model, constructed and solved in ANSYS Workbench V13 and 14. Both sides of the joint were included (the rigid element and the test fixture). The screws were not included – instead constant forces were used to represent their preload (3090 N). These were applied as distributed loads over the areas of contact with the screw heads (see Figure 100).

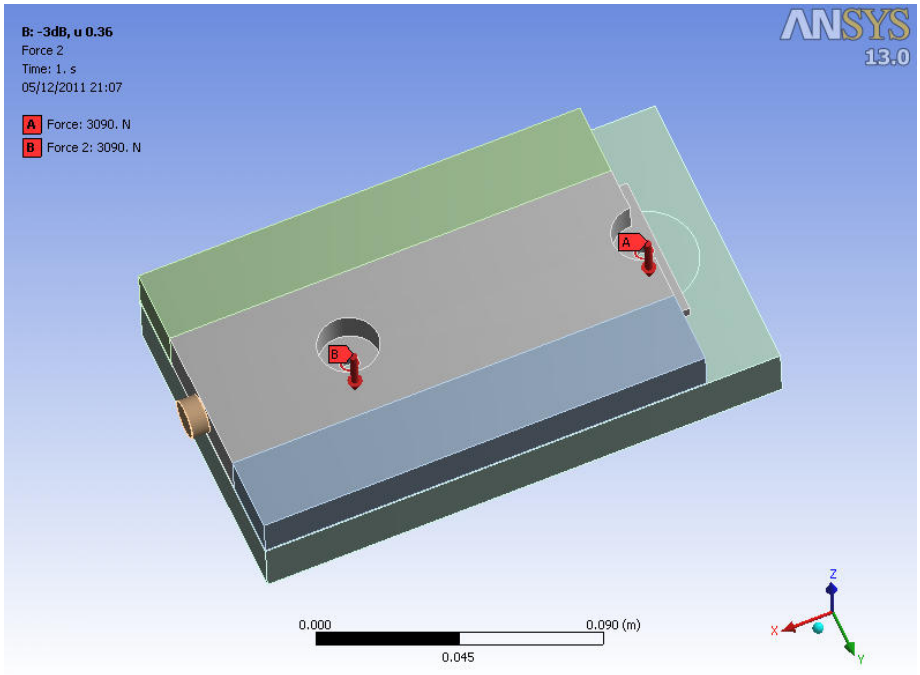

Figure 100. FEA model showing screw preloads (note that A and B are reversed from *a* and *b* in Figure 73).

This model contained 14,618 elements and 27,431 nodes. There are several different methods available for modelling frictional contact, depending on such factors as the accuracy required for the solution, the contact stiffness, and the contact behaviour (ie: sticking, slipping, gapping etc). For this analysis, contact was modelled at both faying interfaces using the ANSYS default "pure penalty" algorithm. The mesh was specifically refined around the two faying surfaces (see Figure 101).

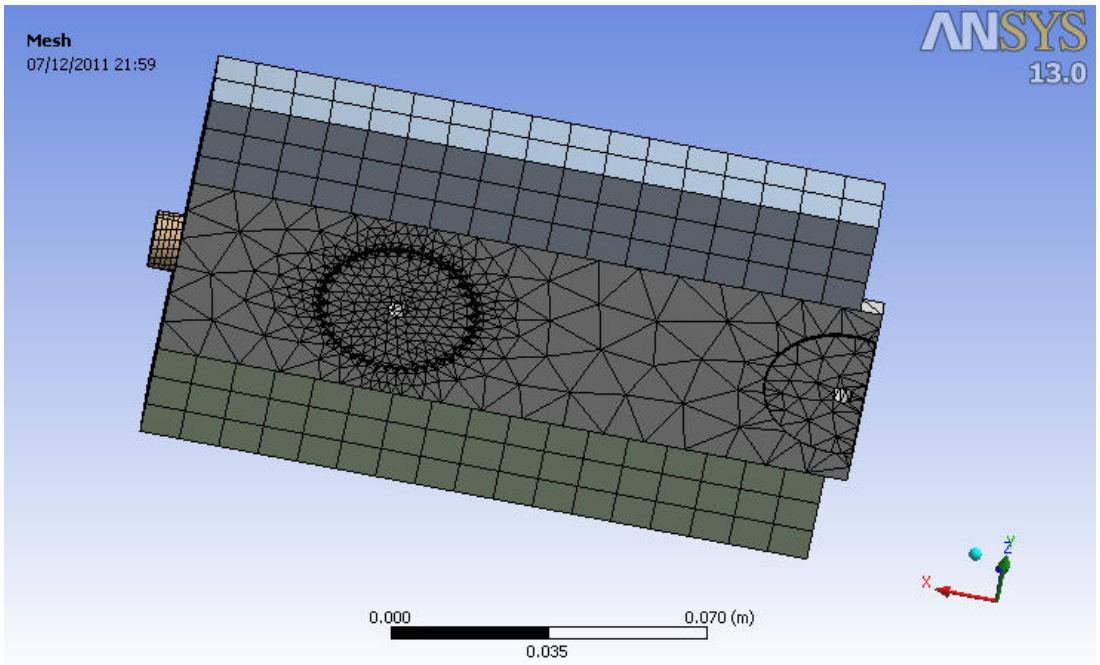

Figure 101. Surface mesh of rigid element, showing refinement around contact areas.

Friction was assumed to be the mean value measured statically (see Table 10), 0.36.

A lateral acceleration load was applied (in the Y direction in Figure 100). This load was then released, and the resulting position of the rigid element was assessed. The magnitude of this load was derived from the test data. It was based on the peak acceleration loads experienced during the -3 dB shake, as this was the lowest level test that produced significant movements in all three samples. The acceleration applied, 520.9 ms^{-2}, was simply the RMS figure multiplied by 3.

Loading was applied in five sequential load-steps:

1. No loads.
2. Screw preloads added.
3. Shear load(s) added.
4. Shear load removed, screw preloads remain.
5. No loads.

The deformation results are displayed in Figure 102. This figure shows the deformation after load-step 5, as the preload screw preload causes large local deformations that mask the overall movement.

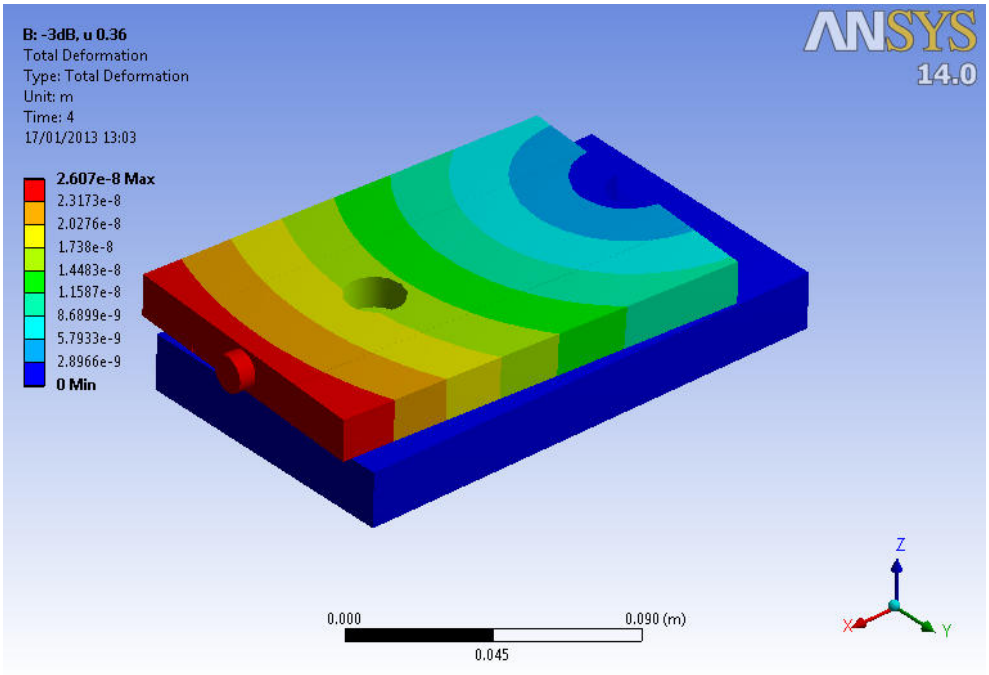

Figure 102. Displacement results after a single load half-cycle.

This clearly shows that the rigid element has tended to rotate about the hinge end following the relaxation of the load, as assumed in Chapter 5. The magnitude of this displacement is low – the movement of a faying surface node between load-steps 2 and 4 (while screw preloads are still present) is 0.168 μm (as opposed to about 5 μm from the tests). This suggests that the movements observed during testing were not the result of single peak acceleration events, but repetitive acceleration cycles.

The reaction force in the Y direction at point *a* (the test interface) was 450 N, providing a resistive moment about point *b* (the hinge end) of 45 Nm. The moment reaction at point A was 14.7 Nm. Thus, around 75% of the slip

resistance is provided by the test joint *a*. The remaining 25% is provided by the screw at *b*, effectively a very stiff hinge.

6.3.3 Cyclic Loading

Applying a series of load cycles, with magnitudes in proportion to probability of exceedance is problematic in this case. This is because the loading at the shear plane is broad-band, unlike the material sample test where stresses were largely attributable to a single resonant frequency. Therefore it is impossible to say how many cycles would have reached a certain threshold.

In order to investigate the effects of cyclic loading on the FEA model, a simplistic approach was taken – the quasi-static 3-σ acceleration from the previous section was used, and reversed 50 times (this is an arbitrary number of cycles – it was chosen as a good compromise between a large number of cycles and a sensible solution time). The results are shown in Figure 103, again for the displacement of the rigid element after load-step 5 with no screw preload. The residual displacement at the faying surface was again low: 0.151 μm between the cases with screw preload (load-steps 2-4). This result is slightly different to the single shear load case, and may become more significant over a much larger number of cycles.

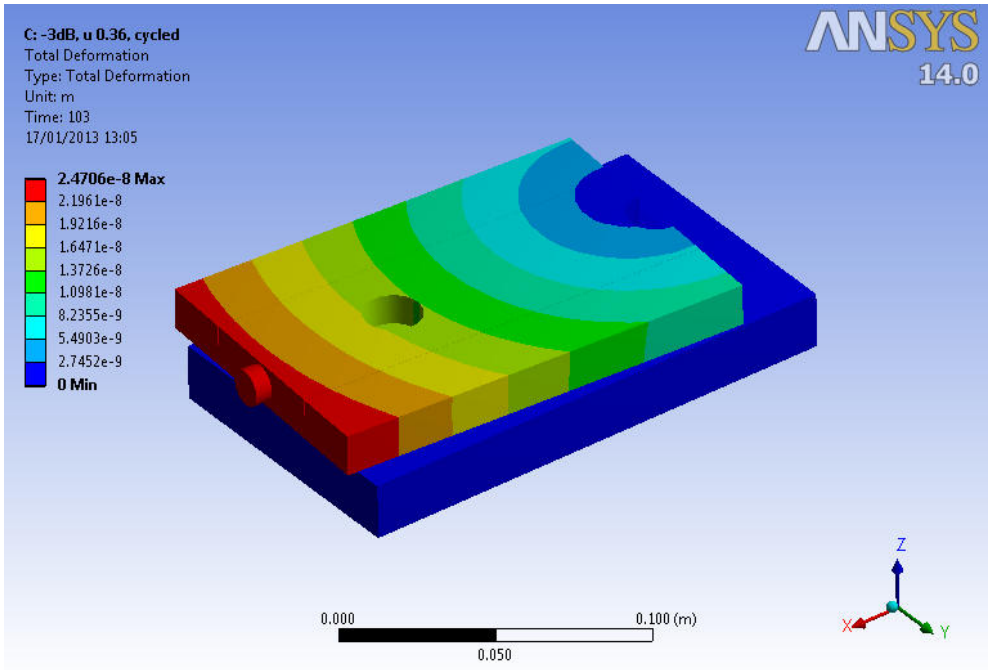

Figure 103. Final displacement results after 50 shear cycles.

Next, a load non-symmetry was applied in the form of a static 1g acceleration in the Y direction, superimposed on the cyclic loads. The results of this are shown in Figure 104, again for 50 cycles with screw preloads removed (load-step 5).

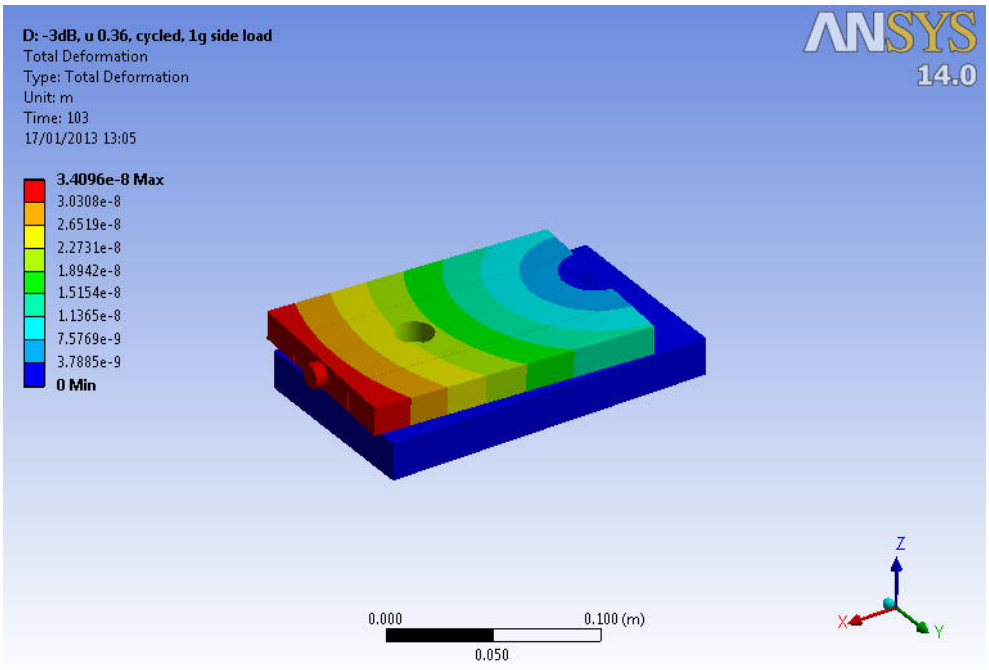

Figure 104. Final displacement results after five non-symmetric shear cycles.

Here, the (load-step 2-4) residual displacement is 0.132 μm. This result is slightly less than the symmetric cyclic case, since the acceleration non-symmetry means that the final load half cycle was slightly less than the final load half cycle in the symmetric case. This result does not really provide conclusive evidence that load non-symmetry has an effect. It is possible that a larger number of cycles or a larger non-symmetry would provide a more conclusive result. Certainly, the test results show a "sidedness" to the residual strain response, suggesting that some form of load non-symmetry is at play, possibly due to residual strains in the joint. However in the specific case of this analysis, it can be concluded that the effect of load cycling on residual displacements may be as significant as the addition of load non-symmetry on otherwise identical finite element models. It should be noted that these results under-predict the test results by an order of magnitude.

6.4 Conclusion.

The main aim of this chapter was to address the third main goal of this research project:

- "To assess whether it is possible to predict dimensional instability under random vibration, and if so, what methods are best."

It was demonstrated that the cyclic plasticity behaviour seen during the Al alloy sample tests could be successfully predicted using a finite element model with nonlinear kinematic hardening material properties. Loading was applied using a Miner's rule analogy, with the number of cycles of a certain level being dependent on the probability of exceedance, the test duration and the natural frequency. It requires an assumption that all the cyclic plasticity effects are due to a single well defined and well understood modeshape. It also requires a load asymmetry, of a large-enough magnitude to cause shakedown.

The bolted joint test was modelled using frictional contact at the faying surfaces. It was shown that the assumptions made in Chapter 5 about load sharing between the two ends of the sample were correct. Movement under cyclic symmetric and non-symmetric loads was also investigated, and found to be significant, though FEA results did not correlate well with the test results.

7 Recommendations and Conclusions

7.1 Recommendations for Future Stable Structures Projects

A number of useful findings have come from this research that could provide good guidance for future stable structures projects. For instance the sided movements observed could be minimised by ensuring that structural preloads is minimised through careful design and assembly.

To minimise the possibility of material yield in the microstrain region, the microyield strength of materials should be assessed, and used as a criterion during material selection. Large safety factors are recommended when considering bolted joint slippage. The addition of dowel pins may help, but for the BBM tests, this operation itself had a small detrimental effect on stability.

A significant finding of this research is the possibility of conditioning a structure to be more tolerant to the effects of random vibration through the use of bedding in shakes. The shakes should have high amplitudes, but small durations are sufficient.

These suggestions (and some others) have been summarised together as a protocol for the design, development and testing of stable structures for space optics. This is presented in the Appendix.

7.2 Recommendations for Future Work

There are a number of areas where further work, building on the current research, could be performed to better understand dimensional stability under random vibration.

For material testing, the test setup developed here is considered to now be good enough for further testing, without further refinement being necessary. The effect of the size of the load non-symmetry should be investigated. It would be relatively straightforward to alter the test setup of Chapter 4 to incorporate controlled preloads of various levels. Another area of interest is the effect of the resonant frequency. This can be altered by simply changing the masses attached to otherwise identical test samples. Also, the non-sided component of the residual strain response should be further

investigated – after all, it will be present even when load non-symmetry is not. This may require a statistical approach, and a large number of test samples.

For the bolted joint test rig, the proportion of the lateral load resisted at the joint of interest was never actually measured, just predicted from FEA. It is suggested that the test setup could be further refined by replacing the hinge joint bolt with a precision instrument bearing setup. This will complicate the test setup, but reduce any uncertainty about the proportion of the slip load resisted at each mounting point. Another important refinement would be a method to directly measure the bolt preload, rather than relying on a torque measurement. This could be achieved with load cells, or simple Belleville washers (disc springs) that provide a known force when fully compressed. Further areas of investigation for bolted joints include the effects of resonance, different material combinations, surface finishes and textures, different bolt sizes, dowels, lateral preload and the effect of non-perpendicularity between the preload direction and the faying surface.

It was found that the specific type of insert tested was very stable under static axial loading. Similar tests could be performed with loading in shear. Dynamic tests could also be performed on these, with a view to determining whether it is possible to predict the stability response to dynamic loads with static tests.

Bonded joints are widely used in spacecraft structures, and are sometimes necessary in areas of high dimensional stability. For example the mounting of mirrors and lenses often requires a glass-to-metal structural joint to be made. Bonded joints were not investigated as part of this research, though a brief survey of the literature on bonded joints (summarised in the Appendix) suggests that they too have not received much attention in terms of dimensional stability under dynamic loading. Therefore, it is suggested that this area is further investigated experimentally, and analytically if appropriate.

The final area that could be investigated further is FEA modelling. While the method used in Chapter 6 worked well for predicting the sided stability response for this particular material and test setup, it should be assessed for other situations, including more complex geometries. The order in which load cycles are applied was not investigated here, and should be investigated in the future. Ideally a random order of 3, 2 and 1-σ cycles could be applied. The nonlinear kinematic hardening model used here does not lend itself to analysis

of composite materials, due to von Mises failure criterion being used. However there may be other models that can predict cyclic plasticity based on other criteria that are more suitable for composite materials – these should be investigated.

Another useful route of investigation is all-up modelling of large complex structures. As already noted, the method used here is only suitable for simplified models of small areas of a structure. It may be possible to simulate the results of these submodels accurately with new element technologies or novel applications of existing ones. For example a stick-slip element could be used to model a bolted joint. Such an approach might enable complex optical structures to be analysed in a single model.

7.3 Conclusions of this Research

The research presented in this thesis is an improvement to the state of the art in stable structures for space optics subject to random vibration loading.

At the start of this thesis, it was proposed that while much attention has been focused in the literature on some aspects of structural dimensional stability in precision structures for space optics, the effects of random vibration during launch and ground-testing had been neglected. This point was supported by an extensive literature survey (Chapter 2), which found that thermal and hygral effects in stable materials had been widely researched. However, little evidence was found of work on stability loss due to random vibration, or even mechanical load cycling of any sort.

The first goal of this research was:

- "To better understand dimensional stability in structures subjected to random vibration, identifying key problem areas. Also to understand this in the context of a space-based structure that is subjected to a number of other environmental conditions that promote dimensional instability."

This goal was addressed by performing a series of environmental tests on a structural breadboard model of an Earth-imaging camera (Chapter 3). These tests compared the dimensional stability response of thermal cycling, moisture

desorption, vibration, assembly operations (dowelling) and transport. The unequivocal finding was that random vibration is capable of bringing about a significant and detrimental dimensional instability response.

The dimensional stability of the structure was monitored throughout testing, which involved a sequence of tests of increasing severity. Significant findings were:

- That dimensional instability appears to be more dependent on the magnitude of test input levels, rather than the duration (ie, the number of cycles).
- The dimensional instabilities induced tended to be "sided", increasing in the same direction throughout testing.
- Dimensional instability seems to have been introduced both at joints and in structural materials, suggesting that both joint slippage and material microyield are potential problems.

Having highlighted these two specific areas, it was time to move on to the second main goal:

- "To develop empirical methods for the quantitative assessment of dimensional instability in structures subjected to random vibration."

This was the subject of Chapters 4 and 5.

Chapter 4 describes a novel test setup and procedure designed to measure the dimensional stability response of material samples subject to random vibration. The four-point bending test setup relied on sample resonance to generate high loads. Several metrology techniques were trialled, with the most successful being strain gauges with a large amount of shielding against electronic noise. Contact metrology tended to affect the results, and could not be performed in-situ between each shake. Optical measurements, to determine the residual change in angle of the samples, offered the best experimental accuracy, at the expense of a relatively poor dynamic range. The test setup itself was progressively refined to reduce experimental errors.

Random vibration tests were performed on two different material types – a CFRP of a type that had previous heritage in space instrument structures, and

a standard grade Al alloy. Static tests were also performed. Both materials exhibited some instability. For both materials, there were two apparent components to the plastic strain response – a "sided" effect, which gradually moved the plastic strain in a constant direction over a number of tests, and a non-sided random effect, manifested in a plastic strain response that increases in magnitude with increasing vibration levels but with a random direction. These two effects are exemplified in Figure 62 and Figure 63 respectively. For the Al alloy samples, repeated tests with identical levels resulted in comparatively little additional plastic strain, compared with an increase in test levels. This supports the finding of the BBM tests, that vibration amplitudes have more effect than test durations.

Chapter 5 describes a novel test setup for assessing slipping at a bolted interface under a lateral vibration load, making use of test masses pinned at one end so that a measurable rotation is induced on interfacial slipping. Slip forces were induced directly by virtue of the shaker acceleration, with no need to use resonance. The pinned end was not truly pinned, and offered a degree of resistive torque, slightly reducing the actual slip load seen at the joint of interest. This was verified with an FEA model in Chapter 6. Two metrology methods were used, again with the optical method suffering from a small dynamic range. The CMM method was limited by being only able to make measurements before and after all the tests, but not during testing. It was a good cross-reference though, verifying the angular measurements made with the optical method.

The results all showed a significant sided response above a certain threshold. The direction of the response was not the same for all samples, and neither was the amplitude. Repeated shakes at the same amplitude did not introduce further instability, adding further weight to the conclusion that induced instability in precision structures is more dependent on peak amplitudes than number of cycles. The cause for the sided response is unclear. It is possible that it was due to ratchetting as a result of surface features at the interface. However all samples were identically machined, so should have moved in the same direction.

Another possibility is a slight sideways component to the preload in the screws. This may be possible if the washer or under-head surfaces are not perfectly flat and perpendicular to the preload direction. For instance in the

case of the tests presented in section 5, a 1° angle between the preload direction and the faying surface will provide a sideways resultant force of 54 N at the joint – a small but potentially significant result.

While the results gathered here have offered some useful insights into the general behaviour of joints under vibration, the tests performed were for very specific bolted joint material, geometry and loading conditions. It is probably valid to assume that the slipping behaviour observed is likely to occur in other similar (though not identical) situations (ie, different sized screws, different surface finishes and different materials). However for joints with more substantial differences (ie, dowel pins, resonances or out-of-plane loads), the test setup would need to be modified to provide a more accurate representation of the problem. The test setup used for this research could be used on a number of different materials, joints and loads in order to provide a useful comparative guide for future stable structures projects.

Thus the second main goal of this research has been met. The third main goal was the subject of Chapter 6:

- "To assess the potential for predicting dimensional instability under random vibration using FEA techniques."

Here, the sided part of the dimensional instability response of an Al alloy sample was correctly modelled using a time domain FEA model. The random effect was dependent on assumptions made about the amplitude of the final load cycle applied to the model. It is proposed that this method could be used for instability predictions in more complex structures, such as mirror mount flexures, which exhibit a well-defined first resonance. This would of course require good knowledge of cyclic hardening behaviour in order to determine the correct material parameters. There appears to be little information of use in the literature for materials commonly used in stable structures over the small strain ranges of interest – therefore bespoke material testing may be required. Also, good knowledge of the load asymmetry is required – this may be due to assembly stresses or simply gravity. The main drawback of the method is the long computation times involved. It is suggested that heavy de-featuring and coarse meshing is applied in all areas of the model not subject to high dynamic stress.

Similarly, the proposed method for estimating slip at bolted interfaces requires a large number of sequential quasi-static nonlinear solutions, posing a potential problem for solution times. This analysis was not performed on the test setup of Chapter 5, as there was no resonant frequency for determining the peak load. Also, there was no knowledge of any specific load asymmetry that would cause the sided response. Nonetheless, the method was demonstrated using arbitrary loads and numbers of cycles.

In summary, the novel features of this work are tests to assess the dimensional stability of stable structures subject to random vibration, metrology techniques for controlled tests on specific structural items in order to assess their contribution to dimensional instability, and the prediction of dimensional instability using FEA techniques.

Appendix

A1 Protocol for Minimising Dimensional Instability due to Random Vibration

This section summarises the main findings of this research in a way that can be useful to developers of future stable structures projects. It is split into steps that represent typical development project phases, and provides suggestions for maximising dimensional stability at each stage:

A1.1 Design and Analysis

Material selection

An important factor in material selection should be microyield strength, available for a number of materials from several sources (ie, Refs. 8, 9, 40). This should be as high as possible. Note that 0.2% proof strength is not a reliable indicator of microyield behaviour. Material conditions should be selected to minimise internal material stresses from forming and heat treatments (for composites, this suggests that low-temperature curing resin systems are preferable to medium of high temperature ones).

Structural stiffness

The structure should be as stiff as feasibly possible. A stiffer structure will see smaller displacements during a resonant response to random vibration, and hence smaller peak loads. With a higher natural frequency, a larger number of cycles will be seen for a given exposure time. However the peak loads are likely to be more important from the point of view of dimensional stability than the number of cycles.

Structural preloads

Any form of structural pre-stress should be minimised. Any pre-stress will potentially form non-symmetries in the stress response of critical areas, leading to ratchetting or shakedown. To minimise the possibility of such stresses, fully kinematic mounting techniques are suggested. Where these are not practical, the use of tight tolerances or shims may be required.

Material allowable design stress

The rule of thumb suggested for CFRP materials in Ref. 37. (which applies a factor of 1/3 on composite tensile failure strength to derive a maximum allowable "microyield" stress) was found to be appropriate for the CFRP samples tested here, based on a comparison with 3-σ dynamic stresses.

The Al alloy samples had an elastic limit during static testing of 45 MPa, and 25 MPa RMS during dynamic testing. Thus a factor of 0.56 on static microyield strength would have been appropriate against 1-σ stresses.

Although these factors are for very specific cases, they could be used as a good starting point in the absence of any further information about dynamic microyield.

Slip loads

The tests found that a factor of 3.4 on 3-σ resultants would have prevented microslip. Again, though this is for a very specific case, it remains a good starting point for design purposes.

An alternative method of preventing slip is with dowel pins. If these are to be used, small amounts of deformation can be expected during the fitting process.

FEA predictions

The sided response of materials under dynamic non-symmetric loading can be predicted using the modelling method proposed in Chapter 6. The non-sided part of the response is dependent on the size of the final load cycle applied during the analysis. In this case, the correct load is slightly higher than 1-σ.

A1.2 Assembly, Integration and Testing

Assembly and integration pre-stresses

It is critical that assembly occurs in a stress-free manner. If the design does not allow fully kinematic mounting techniques, then great care must be taken when fastening screws. They should be sequentially tightened in a way that minimises the risk of pre-stress. The interface of the optical structure to both the vibration test fixture and the spacecraft require similar attention.

Vibration testing

It is clear that vibration can be used to condition structures to become more resilient to further shaking. This research has shown that random vibration amplitudes are more important then durations, so short bursts of high-amplitude vibration are appropriate. During optical alignment operations, several such tests could be used, with any necessary optical re-alignment taking place between each in order to "bed-in" the structure in its optimum position.

Transport

BBM testing showed that transport between facilities could cause dimensional instability. It is not clear whether this was due to handling shocks or vehicle loads, however it shows that transport equipment and procedures also require special attention.

A2 Space-Based Earth Observation Structures in the Literature

The following is a description of some relevant missions that are currently either operating successfully or being developed.

A2.1 TopSat

TopSat was developed in collaboration between RAL, SSTL, Qinetiq and Infoterra with funding from the BNSC Mosaic program[13].

The TopSat camera was launched in 2003 on an SSTL mini satellite bus, and has been a good success. It is designed to produce 2.5m images in panchromatic, and 5m images in colour. It weighs 30kg and is about 0.7m in length.

The camera is a three-mirror off-axis design, making use of Zerodur glass for all three optical substrates. The mirrors are housed in a stiff CFRP open-sided box structure. Stability requirements along the length of the box are +/-10μm and +/-10 arcseconds before image quality becomes too degraded. A sequential alignment process was used, with M1 being aligned first, then M2 aligned to M1 and M3 aligned to M2, and finally the Focal Plane Assembly containing the CCDs aligned to M3 to complete the optical system. Mounting for each of these subsystems was designed so that they could be adjusted in

the important degrees of freedom, and then locked in position using dowel pins and adhesives.

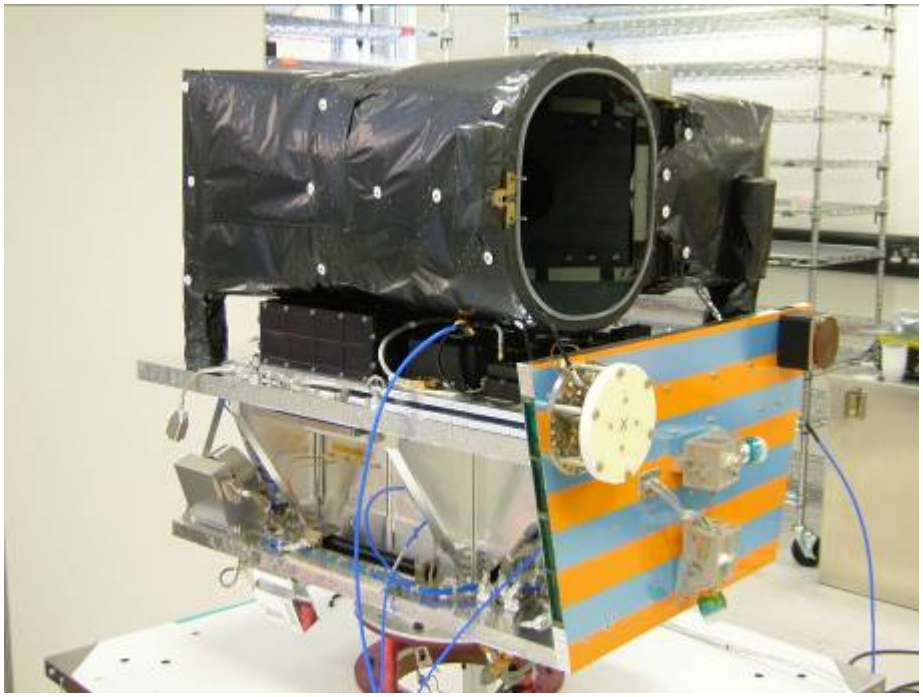

Figure 105. The TopSat camera and SSTL satellite bus.

A structural engineering model of the camera was produced with dummy optics, and subjected to vibration testing. Stability was assessed using spherical tooling balls whose locations were measured with a coordinate measurement machine (CMM) before and after testing. Although the primary structure was found to be suitable, problems were encountered with the individual mirror mounting techniques and their interface to the CFRP structure. In particular the primary mirror mount design went through several iterations and required features for dowel pins to be retro-fitted to the design in order to achieve the necessary degree of stability. Verification of stability due to thermal and vacuum conditions relied on FEA modelling and tests on material samples for CTE (coefficient of thermal expansion) and CME (coefficient of moisture expansion).

A2.2 Tacsat-2

TacSat is a technology demonstrator mission funded by the USAF and launched in 2006[117]. The primary payload is a camera capable of sub-1m GSD

from LEO. It makes use of an off-the shelf telescope of 0.5m aperture. The telescope has been ruggedised to withstand the launch and space environments, though there is little information available on this.

The commercial version of the telescope is a Richey-Chrétien optical design, comprising a 0.5m hyperbolic primary and a hyperbolic secondary. The stability of these two mirrors must be a key issue for the programme. The commercial version of the camera incorporates a refocus mechanism on the secondary mirror, though it is unclear how this would operate from orbit and may take a long time to adjust if using reference targets on the ground. The primary structure of the commercial version consists of a CFRP tube, and the optics are low-expansion glass.

A2.3 Dobson Space Telescope

Dobson Space Telescope is a spinout company from the Technical University of Berlin[118]. For a number of years, it has been developing a space camera based on a deployable secondary mirror. This has many advantages in terms of mass and packaging for launch. The deployment mechanism is based on stiff trusses and hinges, and has been successfully tested on parabolic flights. The alignment of M2 is done via a 5-axis actuator. The literature has no mention of the on-orbit alignment process, or how image verification is performed. This is likely to be a major hurdle for the programme.

A2.4 Formosat-2

Formosat-2, formerly ROCSAT-2 is a Taiwanese satellite that carries a camera developed by EADS Astrium called RSI (remote Sensing Instrument). The instrument makes use of silicon carbide for both the structure and the optics[100]. The primary mirror is 600mm, and the mass is 60kg. Image resolution is 2m panchromatic. Refocus is achieved by controlling the temperature of the metering tube between the two mirrors, and allows a +/- 200μm adjustment. A structural model using mirror blanks was vibration tested, and stability was assessed with a "3-D machine". Following this, protoflight model tests were performed. Interestingly, acoustic testing was used instead of random vibration.

Formosat-2 was launched in 2004, and the RSI instrument has proved to be successful. It was used to assist with rescue efforts following the Asian tsunami of 2004.

A2.5 Hirise

The HIRISE camera was launched aboard NASA's Mars Reconnaissance Orbiter in 2005, and has been very successful so far. It is a three-mirror Cassegrain telescope with a 0.5m primary mirror and a mass of 65kg[119, 120], and was built by Ball Aerospace. The primary structure is CFRP, and the mirrors are Zerodur. It is capable of imaging in red, green, blue and NIR with a GSD of 1m from a 300km altitude. Metering of the secondary mirror is via a truss structure. The main truss elements are CFRP with a slightly negative axial CTE, with metallic endfittings designed to null the overall CTE. The CFRP is an M55j high modulus fibre in a cyanate ester resin matrix. The whole metering structure is temperature-controlled with heaters. The beam is folded behind the primary mirror, and one of the fold mirrors is moveable, giving a refocus capability. There is no information about how the correct focus is achieved on-orbit.

The requirements for alignment between M1 and M2 were 12μm de-centre and 5 arcseconds relative tilt. This was achieved in a vertical alignment rig using theodolites. Alignment changes due to gravity release were verified, though there is no information on thermal-vacuum or vibration test verification. The primary mirror is a double-arch design. Two primary mirrors were produced, with the first one being distorted as a result of bonding fittings for three-point mounting. The second was more successful, though a significant trefoil distortion was still seen due to gravity. This was not sufficient to compromise the quality of the optical system.

A2.6 COROT

COROT is a French mission to investigate stellar seismology and planetary transits. It is an off-axis optical design based on three bulkhead panels spaced axially with CFRP tubes in a hexapod arrangement[121]. ESA metrology, vibration and materials specialists were called upon to help meet "extremely rigorous mechanical requirements" for the main stray-light baffle[122].

A2.7 Pleiades

This is another French camera, designed by Alcatel Space and intended for civilian and military use[38]. Its goal is 0.7m GSD panchromatic imagery. The optical layout is a four-mirror Cassegrain system in a "Korsch" arrangement, with a 660mm diameter primary mirror. There is little information about

verification. The primary structure is carbon-carbon, with carbon-cyanate ester CFRP for secondary mirror spider elements. The mirror mounts are Invar, which are machined using wire electro-erosion to minimise machining stresses. There is a refocus mechanism on M2 that essentially makes use of an aluminium cylinder which is temperature controlled.

A2.8 Quickbird

The Quickbird cameras were developed by Ball aerospace for commercial Earth imaging. They are designed to give a 1m GSD image from LEO. The camera structure weighs around 300kg, and is based around a three mirror off-axis optical design with a 600mm primary mirror[123]. The large mass is justified by "saving money, time and risk"[124]. The Structure is composed of a pair of stiff CFRP-honeycomb bulkhead panels joined by CFRP box structure.

All the optical components are fixed to one of the bulkheads. The primary mirror is 50% lightweighted Zerodur, while the other mirrors are solid Zerodur. Mirror mounting is via "flexural standoffs" and a "monoball" interface in a kinematic arrangement. The bonding of the fixtures to the glass substrate was investigated with a destructive test program that covered 20 adhesives and bonding processes.

FEA models were used, with Zernike polynomials used to investigate the effects of mirror deflections on image quality. Test results were correlated, and the FEA-to-optical software translation helped with alignment under 1g. The structural model was tested under random vibration and thermal vacuum, with wavefront measurements before and after. Deflections were acceptable.

A test facility was devised to accommodate the optical alignment and test requirements of the project[125]. This included an optical integrating sphere and an interferometer on a traversing stage that could scan across the camera image plane. A large-structure metrology setup makes use of four theodolites and can determine positions of discrete points to within 25μm.

A2.9 SNAP

The SNAP telescope is a space-based astronomical instrument being developed by NASA for assessing the expansion history of the universe by measuring the redshift and intensity of supernovae[126]. The optical system is a Korsch layout, using three mirrors, with M1 and M2 on-axis and M3 oriented perpendicular to these behind M2. The aperture is 2m.

Low expansion glasses and silicon carbide are being considered for the mirror substrates. M1 mounting concepts that have been investigated include methods that achieve a near ideal kinematic system[93]. These rely on ball-in-cone type arrangements that require a hard preload that must be controlled and maintained in service. This would require a caging mechanism for launch. One method of manufacture being considered for M1 is fusion bonding with an egg crate core[37]. Different pocketing geometries were investigated, with little difference seen between square, hexagonal and triangular arrangements and 80% lightweighting achievable.

The stability requirements between M1 and M2 are “several microns”. A CFRP tripod is currently planned for the metering structure for this. Additionally, a “five-axis motorised adjustment” mechanism is planned for M2. For the metering struts, they have suggested using high modulus fibres in an axially dominant layup, with layers of metal that would bring the CTE to zero, while presumably acting to prevent moisture ingress.

A3 Optical Drivers of Stability

A3.1 Typical Optical Systems

Most space-based optical systems rely on reflective components. Typically there is a large primary mirror with a revolved conic section profile which focuses light on to a smaller secondary mirror, then on to further mirrors, corrective lenses, and to a focal plane assembly containing filters and detectors.

The capabilities of the telescope are highly dependent of the size of the primary mirror. The larger the mirror, the more light is collected and the greater signal/noise ratio will be achievable. In terms of focal plane image, larger diameters result in smaller Airy disks on the (the size of the diffraction ring pattern generated by a point light source that contains enough energy to be detectable). Hence detectors with smaller pixels can be used before the system becomes “diffraction limited”. The amount of light collected by the primary mirror goes up with the square of the mirror diameter, but the mass goes up with the cube of this figure.

There several telescope configurations that are popular for space use[127]. One is the Cassegrain class of telescopes (Figure 106), which are on-axis

systems where the primary mirror is partially obscured by the secondary. The Ritchey-Chrétien system is an example of this class in which both primary and secondary mirrors are complex hyperboloids. Another popular design is the three mirror anastigmatic (TMA) system, in which the mirrors can all be positioned off-axis. This offers the advantage of having no central obscuration, giving a potentially better quality image for a given package size (Figure 107).

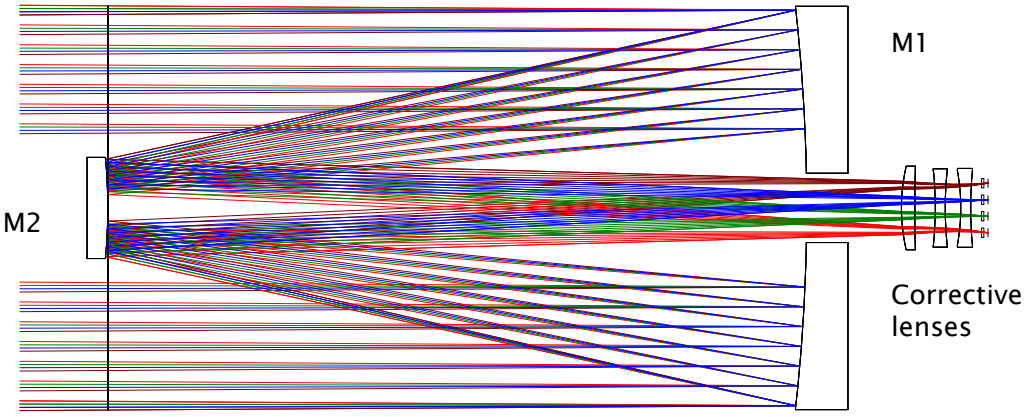

Figure 106. A Cassegrain optical system, showing red, green, blue and near-infrared rays and separate detectors.

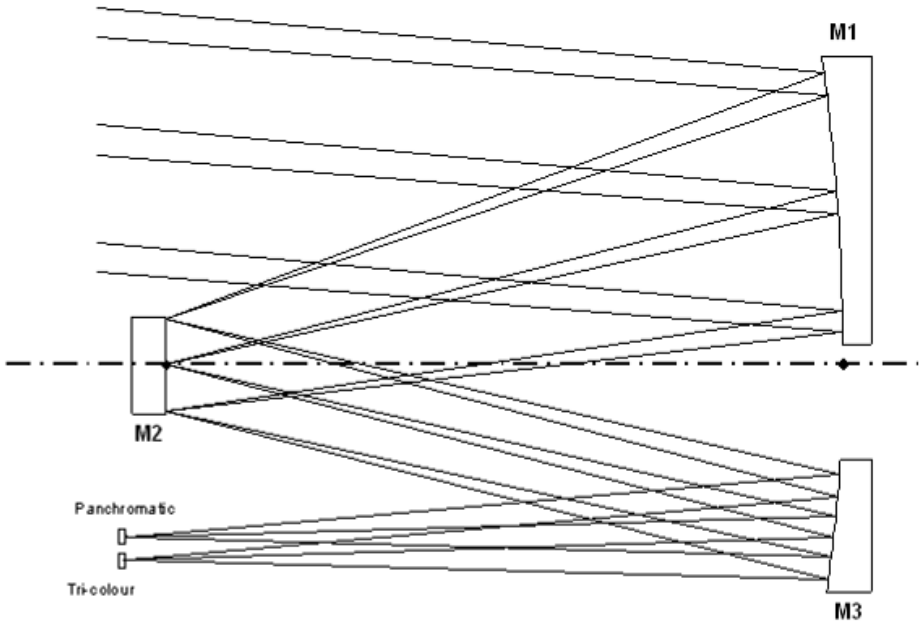

Figure 107. The three mirror off-axis system used on TopSat, showing the panchromatic and colour ray traces.

A3.2 Image Quality and Optical Performance

Optics engineers tend to deal with deviations from the ideal, or aberrations. Given perfect optics in perfect nominal positions, much of the optical design process is concerned with assessing how sensitive the wavefront at the image plane is to small changes in system geometry. The wavefront is an imaginary surface that joins all points in an optical beam that share the same phase angle[128]. Ideally, the telescope optics would produce a wavefront that is perfectly spherical. Any deviation from this is a "wavefront error" (WFE).

Unfortunately there is no single parameter that is sufficient for appraising the performance of an optical system. The shape and magnitude of the WFE can be used, expressed as either a peak-valley difference or as an RMS value integrated over the wavefront. These figures do not necessarily give an indication of the quality of the image produced though. A commonly-used measure is the modulation transfer function (MTF), which is presented as a curve of image contrast versus spatial frequency[129]. Taking into account the detector performance, signal/noise ratio is another performance indicator. Radiometric performance is another issue – the optical performance of the system may differ from one wavelength of interest to another. Ray-tracing software can give a good indication of expected system performance, determining the route through the optical system that is taken by individual rays of light and what level of error is incorporated in their final position on the focal plane.

A3.3 Optical Tolerancing and Design

There are a large number of independent degrees of freedom in an optical system that can affect image quality, and assessing their combined effect can be difficult. For instance each optical component in the system can be subject to 3 translations and 3 rotations. Additionally, deviations from the ideal shape of the optical surfaces must be assessed. No optical manufacturing process is perfect, and deformations in mirror substrates due to changing gravity vectors and thermal excursions, although small, may be highly significant at the wavelengths of interest.

Typically, an early stage in the optical design process is to perform a sensitivity analysis. Some indicator of image quality is used, and the various

degrees of freedom are altered individually to assess their impact. At this stage, the important degrees of freedom are identified. The levels of deflection that are deemed acceptable from this analysis are then used as requirements for early structural design work.

The net effect of a number of deflections can be assessed using a root-sum-of-squares approach to summing the individual contributions[103]. A more analytical method that is often used later in the design process uses a Monte Carlo simulation, with square functions to describe the inputs of various deflections, resulting in a probabilistic image quality result.

A3.4 Optical Testing

During space instrument AIV (assembly, integration and verification) activities, optical performance can be measured very accurately with optical interferometers and wavefront measuring equipment. This equipment is typically used to align mirrors in their nominally perfect positions before integration of the camera to the spacecraft. This equipment is not easily used in a thermal vacuum test environment though – Telkamp[12] noted vibration noise from vacuum pump equipment was a problem for Mars Observer Camera tests. Other ways of assessing image quality under these test conditions must be considered (ie, measuring mechanical deflections separately, and computing their effect on system performance[7]).

Measurement of optical performance from orbit can be difficult. MTF measurements can be made by looking at objects with a distinct contrast. For astronomical instruments, bright stars are good for this. For EO instruments, black and white marks are sometimes painted on the ground for this purpose, or bright spotlights used at night. Long re-visit times to these targets, combined with weather variability, can make this a very long process[130].

A4 Composite Materials

A4.1 Types of Composite

A composite material is one that "consists of at least two discrete phases, whose geometrical arrangement and individual properties tend to be significantly different"[16]. Many different engineering materials meet this definition, including reinforced concrete, plywood, glass-ceramics and

carbon/glass fibre reinforced plastics (CFRP/GRFP). Usually a composite will consist of a "matrix" phase, with one or more "reinforcement" phases. The matrix phase is usually a polymer, but can also be a metal or ceramic. The reinforcement typically takes the form of long fibres, short chopped fibres, woven cloth, whiskers and particulates. Reinforcement orientation can be highly controlled to give macroscopic orthotropic properties, or completely random to give anisotropic or quasi-isotropic properties.

From now on, the discussion will be limited to conventional composite materials that are used in aerospace structures and stable optical structures. Unless stated otherwise, the term "composite" will now refer only to these.

The main matrix systems used for aerospace applications are thermoplastics and thermoset resins. Thermoplastics do not "cure", and rely on viscoelasticity at high temperatures for forming. They are generally very tough, but can include high residual stresses due to the high forming temperatures[45]. Nonetheless, they have been investigated for stable space structures as very low CTEs and high moduli are possible[131]. Thermosets are composed of monomers or partially-formed polymers capable of "cross-linking" when fully polymerised on cure[132]. Of these, epoxies are historically the most widely used, as they are strong and relatively cheap. A new group of thermosets emerged in the early 1990s, the cyanate esters. These offered the mechanical strength of epoxies, with lower moisture absorption[95, 133, 134]. Cyanate esters are now the materials of choice for stable structures, and are popular for space use due to their low outgassing – in fact some are specifically targeted at the space market[86]. Matrix materials continue to be developed, and it is likely that there will be further developments that will be of benefit for stable structures in the coming years.

A large number of types of fibre are used in aerospace composites. The three main types are carbon, glass and aramid[45]. Glass fibres are not as stiff or strong as carbon, but they are cheap, easy to machine, and available in many useful forms. They are mentioned here not as potential elements in a stable structure, but as useful parts in the ancillary structure that are thermally and electrically insulating. Aramid fibres, such as Kevlar, are of interest because they have a slightly negative CTE. They can therefore be used with a matrix whose CTE is positive to produce a composite of very low CTE. Aramids tend to absorb moisture, leading to swelling.

Carbon fibres offer the best combination of properties for stable structures. There are a large number of fibres available, with a large variety of tensile properties. Traditionally, fibres have been characterised as either high modulus (HM) or high strength (HS) or intermediate modulus (IM)[132]. A typical HS fibre, the T300, has a Young's modulus of 235 GPa and a tensile strength of 3.5 GPa; a typical HM fibre, the M55J, has a modulus of 540 GPa and a strength of 3.9 Gpa. HM fibres are usually significantly more expensive. These fibres are all produced from acrylic fibres that are converted to carbon of varying degrees of purity by applying tension and heat treatment and are known as PAN (polyacrylonitrile) fibres. A second class of fibres is produced by spinning coal tar pitch, which enables higher stiffnesses than even the HM PAN fibres – up to 900 GPa is possible (the UHM range). Despite this, pitch fibres have historically been out of favour with the aerospace industry because of difficulties in obtaining consistent mechanical properties during manufacture.

A4.2 Prepregs, Layups and Curing

Having chosen a suitable matrix and fibre, there are a number of ways to combine them. The easiest way to do this in a controlled and repeatable manner is using prepregs – these are sheets or rolls of fibre pre-impregnated with wet partially-cured resin. Fibres can be laid out unidirectionally (UD) or in a woven fabric. They can be cut to size, and "laid up" with specific orientations to generate a laminate with predictable mechanical and thermal properties.

For complex shapes, the laminate can be formed using a male or female mould tool. Care must be taken that fibre orientations are maintained around tight corners. Pitch fibres can be difficult to bend around corners without breaking. The laminate must be cured at an elevated temperature, so the CTE of the tooling must be taken into account (as well as tool removal post-cure).

Curing is done at temperatures from about 80°C to 200°C under pressure for most epoxies and cyanate esters. There are two main methods of achieving this – using an autoclave (a high-pressure oven) or a vacuum-bag in an oven at atmospheric pressure. In both cases, a "bleeder" cloth is employed around the outside of the laminate to soak up excess resin. Most manufacturers will claim that these methods will result in a laminate that is 60% fibre and 40% resin by volume – ie the fibre fraction Vf = 60%, although this is rarely achieved. After cure, sometimes a post-cure is recommended[86].

This post-cure ensures that the cross-linking of resin molecules is as complete as possible. It does not result in further dimensional changes – the final dimensions are set during cure. The post-cure temperature may significantly exceed the cure temperature though, so tooling and mounting CTE differences may require evaluation.

A4.3 Analysis of Composites

There are two steps in analytically determining the elastic response of a laminate under load. The first is to calculate the elastic engineering properties for individual layers, and the second is to use these values to generate constitutive equations that relate stress to strain[45, 135, 136].

The stress-strain relationship for an orthotropic layer (or ply) is of the form:

$$\begin{bmatrix} \sigma_1 \\ \sigma_2 \\ \sigma_6 \end{bmatrix} = \begin{bmatrix} Q_{11} & Q_{12} & 0 \\ Q_{21} & Q_{22} & 0 \\ 0 & 0 & Q_6 \end{bmatrix} \begin{bmatrix} \varepsilon_1 \\ \varepsilon_2 \\ \varepsilon_6 \end{bmatrix}$$

Where σ_1 is longitudinal (in the direction of the fibres) stress, σ_2 is transverse stress and σ_6 is shear stress; the Q_{ij} terms are stiffness terms for longitudinal, transverse, shear and 1-2 coupling behaviour; the ε terms are strains. Making the assumption (validated in Ref. 45) that $Q_{12} = Q_{21}$, this means that four material parameters are required to predict elastic behaviour (as opposed to two parameters for a metal).

For an individual ply, the longitudinal elastic modulus, CTE and Poisson's ratio are determined with good accuracy from the "rule of mixtures". This simply sums the constituent values in the proportion of their volumes, or cross-sectional areas. This method is poor at predicting transverse properties though. For this, a number of alternatives are suggested in the literature[45, 135]. Ref. 135 suggests the "Haplin" method, which is based on advanced models that account for 3-D effects.

For a laminate composed of a number of plies, the stress strain relationship is expressed is the form:

$$\begin{bmatrix} N_x \\ N_y \\ N_{xy} \\ M_x \\ M_y \\ M_{xy} \end{bmatrix} = \begin{bmatrix} A_{11} & A_{12} & A_{16} & B_{11} & B_{12} & B_{16} \\ A_{12} & A_{22} & A_{26} & B_{12} & B_{22} & B_{26} \\ A_{16} & A_{26} & A_{66} & B_{16} & B_{26} & B_{66} \\ B_{11} & B_{12} & B_{16} & D_{11} & D_{12} & D_{16} \\ B_{12} & B_{22} & B_{26} & D_{12} & D_{22} & D_{26} \\ B_{16} & B_{26} & B_{66} & D_{16} & D_{26} & D_{66} \end{bmatrix} \begin{bmatrix} \varepsilon_x \\ \varepsilon_y \\ \varepsilon_{xy} \\ \kappa_x \\ \kappa_y \\ \kappa_{xy} \end{bmatrix}$$

Where N_{ij} and M_{ij} are laminate forces and moments respectively; ε_{ij} and κ_{ij} are strains and bending curvatures; A_{kl}, B_{kl} and D_{kl} are all stiffness coefficients that are calculated by summing individual ply properties with respect to the laminate mid-plane with a transposition to a common coordinate system.

This matrix is commonly referred to as the A-B-D matrix. The A terms represent extensional stiffness, the D's represent bending stiffness and the B's are coupling terms. If the laminate is symmetric about its mid-plane, the coupling B terms become zero. If the laminate is also balanced in-plane (all plies are in +/- pairs), then the A_{16} and A_{26} terms also become zero. Most composites for stable applications are symmetric and balanced. There are a number of commercial software packages for laminate design that can be used to determine these constitutive equations. For the purpose of this study, an Excel spreadsheet has been produced by the author, "Composite-V1.xls" – it was used in the design of a breadboard camera model described in Chapter 3.

These relationships are not necessarily linear, even without plasticity and crack formation. For example, under tension, unidirectional fibres tend to become better aligned with the load direction, and the tensile modulus increases slightly[132]. For woven fabrics, the fibres must cross each other, reducing in-plane stiffness typically by 15-20% from the equivalent 0°/90° UD layup.

A4.4 Microcracking and Temporal Stability of Composites

It is possible to predict the critical temperature for the onset of microcracking. Using a simple rule-of-mixtures type approach, the temperature–residual stress relationship can be evaluated. This requires knowledge of the stress-free temperature (usually slightly less than the cure temperature), and the temperature dependencies of the other relevant properties such as modulus and CTE. Unfortunately the comparison of theory

with observation is not good using such methods[53]. Energy methods are more accurate - these require the empirical determination of the "critical energy release rate" for a particular laminate[137]. The use of a failure criterion that includes both deviatoric (ie von Mises) and hydrostatic components has also been recommended in the literature. This criterion, along with a strain energy method that predicts matrix cavitation, was verified by Fielder et. al.[138] for composite plies of various fibre fractions under transverse loading.

A long-term study by Deev and Nikishin[139] on composites exposed to the space environment outside the Mir and Salut space stations found that resin erosion and microcracking on the surface of a CFRP composite could be expected after a year or so in orbit. Though the damage did not appreciably affect the bulk material structural properties, it may have implications for stability.

Little work seems to have been done on creep in CFRP, though tests have shown that it is an issue for stable structures under load[140].

It stands to reason that creep should be possible in unloaded CFRP simply due to inherent processing stresses. Hobbiebrunken et. al.[141] found that residual stresses in CFRP were lower than predicted by FEA modelling, and put this down to plasticity and stress redistribution on the initial cooldown. Wolff[142] assumed that composite creep was due to viscoelastic behaviour in the matrix. He used a series of short term creep tests on CFRP tubes to identify the viscoelastic parameters required (time-dependent compliances), and was able to predict creep recovery strains in the microyield region with reasonable success. The assumption of temperature-dependent viscoelastic matrix behaviour has also been made to predict residual cure stresses and strains[143, 144]. A simple method of evaluating such stresses is simply to cure a non-symmetric laminate, and measure the resulting curvature as a function of temperature[145].

A study by Cohen et. al.[18] looked at temporal stability of a cyanate ester-based CFRP structure at room temperature over about a year. They found that the material grew, initially at a rate of several ppm per year. This growth rate decreased exponentially with time, and was attributed to creep in the matrix material, which was not completely cured.

A4.5 Improving Composite Stability

A number of qualitative suggestions are made by Wolff[16] to minimise microcracking. They include:

- Post-curing or annealing.
- Not drying-out the laminate.
- The use of woven fabrics as surface plies.
- Particulate additives to the matrix to lower its CTE.
- Low modulus fibres with a higher CTE.
- Avoiding large bunches of 0° and 90° plies.
- Avoiding large angles between adjacent plies – ie (0/45/90/-45) is better than (0/90/45/-45).
- Structural conditioning postcure (ie, low temperature thermal cycling).
- Use thin surface plies.
- Use thin 90° plies.

To minimise CTE, it is relatively easy to design a quasi-isotropic layup using HM fibres. To minimise changes in CTE during the lifetime of the instrument, it is common to condition the structure by thermally cycling it. The microcracks that would otherwise result during operations can thus be produced before sensitive optical alignments are made[146].

Variability in material properties between samples is a factor that should be taken into account for any precision structure, and is particularly pertinent for composite-based structures. Here, variations in the properties of the constituent parts, as well as in the manufacturing process, can all contribute to variability in bulk properties[37]. Therefore, any bespoke composite materials test should make use of a statistically significant number of samples. Sable[147] demonstrated a technique for predicting the variance in various bulk properties by summing the standard deviations of the various relevant component and layup properties. An alternative (more costly) approach would be Monte Carlo simulation. Various defects were purposely introduced in an early ESA study on the stability of CFRP-aluminium honeycomb panels[148], which found that there was generally little net effect on various stability parameters, apart from areas that were very “resin dry”. Small misorientations in ply angles can also have an effect, the extent of which is dependent on the nominal

angles[50]. Tests performed by McMahan[54] on a spacecraft optical bench structure showed that CTE sensitivity to resin content was of the order of 0.016ppm/°F per % fibre fraction. In the same set of tests, the variability in properties amongst six identical CFRP tubes was found to be very low.

Microcracking can be minimised by careful layup design (avoiding big angles between adjacent plies), using toughened resins, and designing to avoid large operational stresses. There is some evidence (based on CTE changes after cryogenic excursions) that very thin laminates are less susceptible to microcracking than thick ones[149]. Thermal cycling to purposely introduce microcracks before any critical alignments are performed is fairly routine for stable structures. As noted previously however, this needs to be limited before other bulk material properties such as MYS are adversely affected.

Creep may be a problem for loaded structures. It therefore makes good design sense to ensure that long-term loads are not seen by stability-critical CFRP elements during operations, or storage in 1g.

A4.6 Moisture Barriers for Composites

The use of Pitch fibres, with their higher modulus and lower CTE, allows the use of matrix constituents, barriers or thermal finishes with high positive CTEs whilst maintaining a zero laminate CTE. Pitch fibres have the additional benefit of significantly improved thermal conductivity over HM fibres[150]. On the minus side, these same properties will result in higher residual stress levels, and reduced resistance to microcracking.

To minimise moisture ingress, moisture barriers applied on all exposed surfaces can be used. These typically rely on a thin coating of a metal alloy with a eutectic composition to minimise the melting temperature. Such barriers do not completely prevent moisture uptake, as flaws are present depending on the quality of the coating process, but they can slow it down. Barriers for space composites were tested extensively by Brand[151], who performed tests on various resin systems with barriers of various qualities. He proposed several different options for maximising hygral stability. The most stable option involved sealing a very controlled amount of moisture into the resin with a eutectic barrier. The rate of outgassing in space is very slow for the level of saturation chosen – expected dimensional changes are sub-ppm during ground storage and operations. The barrier also affects the CTE, making it more positive. In order to maintain a near-zero CTE with such a

laminate, Brand suggests using Pitch fibres due to their high moduli and high-negative CTE. Other costs for this method are in mass and cost. Barriers have been used successfully in space before, such as for the MSX spacecraft[15].

Metallic barriers have been proposed or used for other purposes as well. On the outside of a structure, they help to reduce matrix degradation by atomic oxygen. On the Japanese Solar-A experiment, an aluminium foil was bonded to the inside of the main metering tube to control the direction of outgassing, directing volatiles away from cold optics[152].

The cheapest option identified by Brand was to use a combination of HM fibres, a cyanate ester resin and good humidity control during processing, which can achieve stability in the region of 5-10 ppm over the material lifetime. Abusafeih et. al.[146] propose taking this approach a step further, and using a continuous dry nitrogen purge, or regular periodic bakeouts to reduce moisture expansion to sub-ppm levels in a cyanate ester. Control of the amount of time spent in a lab environment (9 hours) before returning to a dry environment was successfully used during the Mars Observer Camera alignment[153]. A similar approach was taken on the UVCS structure for SOHO, where test coupons were used to assess both allowable “wet times” and the duration of the bakeouts between them[154].

The relationship between moisture content and hygral strain can also be subtly “tuned” in the layup design. During moisture ingress, there will always be a moisture gradient that sees a maximum concentration in the surface plies. Wolff[52] found that hygral strain could be reduced for any given moisture content simply by ensuring that the outer plies were aligned with the fibres in the direction of interest for stability.

A5 Glasses for Stable Structures

Glasses are typically used in stable optical structures for the optical substrates, either as lenses or mirrors. Most glasses have very low CTEs, and a specific stiffness similar to that of aluminium. It is also relatively easy to produce glass parts with the very specific and accurate surface profiles required by optical designs, and also to polish them to obtain RMS surface roughnesses in the order of fractions of a wavelength of visible light. Glasses can exhibit some temporal instability, which has been measured, and appears

to asymptote at between about 25 and 100ppb after 100 days for stable glasses of interest[155, 17].

Glasses have also been used for structural items. The SMART-2 optical bench was a solid slab of Zerodur[156] to which optical components were attached. The key to using glass in this way is to devise methods of attachment that do not impose significant strains on the material due to environmental loads. Another use for glasses is as a reference length when conducting accurate measurements on other materials, or as part of a contacting probe used for metrology whose temperature (or thermal gradient) will not affect the results.

Failure in glass is usually due to the very rapid exponential growth of cracks (brittle failure). Prediction of failure under tensile load is statistical, and assumes a Weibull distribution for the failure probability[40].

The most popular stable glasses are Corning ULE, and Schott Zerodur, though there are several others. ULE is a titanium-silicate glass, with a typical room-temperature CTE of 0.03-0.05 ppm/°C[22] (though this can be much higher at low temperatures[157]). Zerodur is a nanocomposite, consisting of crystalline quartz with a negative CTE component embedded in an amorphous glass matrix with a positive CTE. It is available in different "expansion classes", and 0.02 ppm/°C is possible. Under thermal cycling, Zerodur can exhibit hysteresis[31], though this is more a problem around "anomalous" temperatures of 240K and 440K.

A6 Unconventional Materials for Stable Structures

These materials are generally expensive or would require bespoke development programs – they are therefore not directly relevant for low-cost structures, but are mentioned here as technical competitors.

Metal matrix composites (MMCs) are similar in many ways to the polymer composites already discussed – the main difference is that the matrix is a metal, usually aluminium or magnesium. The reinforcement fibres are usually carbon, boron or silicon-carbide. For UD composites of this type, very low CTEs and high specific stiffnesses are achievable in the direction of the fibres. There are, however also considerable particulate reinforced MMCs. For anisotropic composites using small chopped filaments of reinforcement, these properties are harder to obtain. High processing temperatures mean that

residual stresses are high[16]. Hysteresis on thermal cycling, annealing, and Bauschinger effects in the matrix are all potential problems.

These materials are generally difficult to obtain as "off-the shelf" solutions, and often require specific development programs to solve particular structural problems. Space heritage includes the high-gain antenna on Hubble, and structural parts of the space shuttle.

Silicon Carbide has properties that are very attractive for stable optical structures. In particular, it has very good structural properties (high specific stiffness), a low CTE (approximately 1.5 – 5 ppm/°C), good thermal conductivity, and the ability to polish to an optical finish. This last property raises the possibility of an inherently athermalised structure – one in which the optics and structure have an identical CTE, so that focal length will change exactly the same amount as the structural length during a temperature variation.

There are several methods of producing it. It is used in industry, such as automotive, where it is mass-produced. A French company, Boostec[158], produces parts for spacecraft structures in a process that involves sintering, which "shrinks" the structure by 17% (making design difficult). It has seen used in space in both structural and optical roles on the Formosat-2 spacecraft[100]. The Herschel primary mirror is composed of SiC segments, and was the largest ever launched (3.5m).

SiC can be reinforced with carbon, to produce even better mechanical and thermal properties. This has been done on the optical bench for the NIRspec instrument on JWST, developed by Alcatel for cryogenic optics[159].

Carbon nanotubes have great potential for use in stable structures. They are expected to have extraordinary strength, stiffness and thermal properties. Before this is possible, techniques will need to be developed that can produce them in large quantities cost-effectively. Recent studies have highlighted difficulties with incorporating them into composite materials due to poor cohesion with matrix materials[160]. Other possible techniques for forming solid structures may include sintering and cross-linking them.

Carbon fibre reinforced graphite offers excellent mechanical and thermal properties. It has been used for metering structures on space telescopes such as Pleiades[38]. Its principal advantage over conventional CFRP is that it does not absorb moisture, and exhibits excellent long-term stability[103]. It has also found

uses in cryogenic instruments at CERN[161] due to its high thermal conductivity. However, it is difficult and expensive to process and it requires the pyrolysis (conversion to carbon) of an organic matrix material, then exposure to a gas at high temperature to minimise porosity.

A7 Bonded Joints

Where joints are not required to be broken once made, or joint materials are unsuitable for threaded fasteners (ie, glass), adhesive bonding is the best solution. In general, adhesive bonds are very strong in shear, but not in tension or under "peeling" type loads. There are a number of adhesives that have been recommended in the literature for use in space due to low outgassing and high strength properties[162]. The most common space adhesives are epoxies, though cyanoacrylates (superglue), RTV rubbers and UV-curing adhesives are popular in some areas.

The analysis of bonded joints in the literature is geared towards sizing calculations for macroscopic strength rather than stability. As with bolted joints, there are various rules of thumb and empirically-derived, simplified calculations[163] to determine bond thicknesses and lengths for various geometries and load conditions. Very thin bondlines may be treated as nearly incompressible, which has the effect of increasing their stiffness[164].

The use of FEA for analysing bonds is also a mature technique[165]. The main issue with these is deciding on the best material model to use, and then determining the material parameters that are required. The National Physical Laboratory (NPL) in the UK has produced a comprehensive guide to using FEA with adhesive joints[166]. Several material models are recommended for different classes of adhesive. These include various forms of the Drucker-Prager criterion, which has von-Mises and hydrostatic components (similar to methods already mentioned for CFRP matrix yield), and is easily implemented in commercial FEA codes. The material parameters required for these analyses are determined by curve fitting the stress-strain results of adhesive specimen tests in tension, compression and shear.

A particular area of concern that has received some attention is in the adhesives used for glass-metal bonds for mirror mounts. Such bonds were responsible for significant distortions of optical surfaces on the TopSat primary mirror[13]. Part of the problem is that epoxies tend to shrink on cure, and

therefore can induce high residual strains. The solution to this issue was to perform the final polishing of the mirror after the bonds had been made. An investigation of distortions in FUSE Zerodur mirrors due to epoxy-bonded flexures revealed that there were additional distortions due to the high CTE and moisture-swelling of the adhesive, with significant additional distortion seen during thermal-vacuum testing[167]. A study was performed by Daly and Daly[168] which compared epoxy with UV curing adhesives in terms of the stability of glass-metal bonds, using various glasses, metals and geometries. Their conclusion was that the UV class has significant advantages over epoxies. Unfortunately, Zerodur – the glass of choice for many space optics – does not transmit in the UV band, so curing would be a problem. One potential solution to the epoxy-shrinkage issue is to load it with glass spheres. This may have the multiple benefits of controlling the bondline thickness, reducing the cure shrinkage, reducing the adhesive CTE, and increasing its stiffness.

Creep in lightly-loaded epoxy joints was assessed by Patterson et. al.[169] using laser interferometry, and was found to be of the order of 4nm per day for a "lightly-loaded" joint.

For joining glass-to-glass, a technique recently developed at the University of Glasgow is Hydroxide Catalysis bonding[156]. This form of bonding requires an optical-quality finish on both sides of the joint. A solution containing hydroxide ions is introduced, which starts a reaction that results in silicon-based polymers that rigidly joins the surfaces. It was used successfully on the SMART-2 optical bench.

A8 Example of BBM Tooling Ball Data

An example of metrology data obtained for tooling ball positions during the BBM test campaign is shown in Table 15.

TB No.	Dir'n	Run 1	Run 2	Run 3	Run 4	Run 5	Run 6
7	X	175.7265	175.7271	175.7278	175.7282	175.7282	175.7287
	Y	-180.0424	-180.0424	-180.0415	-180.0421	-180.0414	-180.0412
	Z	98.1512	98.1508	98.1505	98.1507	98.1512	98.1514
8	X	69.1612	69.1624	69.1606	69.1600	69.1594	69.1598
	Y	239.8948	239.8948	239.8958	239.8957	239.8959	239.8956
	Z	97.1829	97.1829	97.1827	97.1828	97.1826	97.1827
9	X	-241.9527	-241.9523	-241.9531	-241.9526	-241.9512	-241.9499
	Y	-62.4279	-62.4274	-62.4276	-62.4277	-62.4268	-62.4258
	Z	97.1351	97.1355	97.1356	97.1362	97.1377	97.1386

Table 15. Typical tooling ball results, showing six measurement runs for the positions of tooling balls on M1 (mm).

References

[1] "Earth Observation History on Technology", http://www.eoportal.org/documents/kramer/History.pdf

[2] Sandau R., "Small Satellites – What are the Prospects for Topographic Mapping in the Next Decade", *DLR Competence Centre Optical Information Systems*, Berlin.

[3] Edeson R. L., Aglietti G. S., Tatnall A. R. L., "Conventional stable structures for space optics: The State of the Art" *Acta Astronautica*, 66, (1-2), 13-32. (doi:10.1016/j.actaastro.2009.06.015), 2010.

[4] Edeson R. L., Morris N., Aglietti G. S., Tatnall A. R. L., "Dimensional Stability Testing of a Space Optical Bench Structure", *AIAA Journal* Vol 47, No 1, Jan 2009.

[5] Edeson R. L., Aglietti G. S., Tatnall A. R. L., "Dimensional Stability Loss in Structures Subject to Random Vibration", *COMPDYN Thematic Conference on Computational Methods in Structural Dynamics and Earthquake Engineering*, Corfu, Greece, 2011.

[6] Edeson R. L., Aglietti G. S., Tatnall A. R. L., "The Effects of Random Vibration on the Dimensional Stability of Precision Structures", *12th European Conference on Spacecraft Structures, Materials and Environmental Testing*, Noordwijk, The Netherlands, 2012.

[7] Kilpatrick M. C., Girard J. D., "Design of a Precise and Stable Composite Telescope Structure for the Ultraviolet Coronagraph Spectrometer (UVCS)", *SPIE Proceedings,* Vol. 1690, 1992.

[8] Marschall C. W., Maringer R. E., "Dimensional Instability – An Introduction", Permagon Press, 1977.

[9] Paquin R. A., "Dimensional Instability in Materials: How Critical is it in the Design of Optical Instruments?", *SPIE Proceedings*, CR43, 1992.

[10] Lemaitre J., Chaboche J-L., "Mechanics of Solid Materials", Cambridge University Press, 1990.

[11] Calvi A., "An Overview of the ECSS Handbook for Spacecraft Loads Analysis", *COMPDYN Thematic Conference on Computational Methods in Structural Dynamics and Earthquake Engineering, Corfu*, Greece, 2011.

[12] Telkamp A. R., "Recent Developments With the Mars Observer Camera Graphite Epoxy Structure", *SPIE Proceedings*, Vol. 1690, 1992.

[13] Greenway P., Tosh I., Morris N., "Development of the TopSat Camera", *ESA-SP-554,* 2004.

[14] Kim E. D., Choi Y-W., Kang M-S., Kim E-E., Yang H-S., Rasheed A. A. A., Arshad, A. S., "Medium Sized Aperture Camera for Earth Observation" *ESA-SP-554*, 2004.

[15] Skullney W. E., Kreitz Jr H. M.., Harold M. J., Vernon S. R., Betenbaugh T. M., Hartka T. J., Persons D. F., Schafer E. D., "Structural Design of the MSX Spacecraft", *Johns Hopkins APL Technical Digest*, Vol. 17, No.1, 1996.

[16] Wolff E. G., "Introduction to the Dimensional Stability of Composite Materials", Destech Publications Inc, 2004.

[17] Jacobs S. F. "Variable Invariables – Dimensional Stability With Time and Temperature", *SPIE Proceedings*, CR-43, 1992

[18] Cohen L. M., Freeman M. D., Podgorski W. A., "Temporal Stability of Graphite-Cyanate Ester Composites and its Effect on the High Resolution Mirror Assembly of the NASA Advanced X-ray Astrophysics Facility", *Society of Experimental Mechanics Conference Proceedings*, Grand Rapids, 1995.

[19] Canay Luhia M. A., "Sudden Stress Release Tests Performed on GOCE Spacecraft Component samples", *ESA-SP-581*, 2005

[20] Do N. B., "Modelling Frictional Contact Conditions in Structures", MSc Dissertation, *Georgia Institute of Technology*, 2005.

[21] Neam D. C., Gerber J. D., "Structural Design and Analysis for an Ultralow CTE Optical Bench for the Hubble Space Telescope Corrective Optics", *SPIE Proceedings*, Vol. 1690, 1992.

[22] Roy R., Agrawal D. K., McKinstry H. A., "Very Low Thermal Expansion Coefficient Materials", *Annual Review of Materials Science,* 1989.

[23] Dolgin B. P., Moacanin J., O'Donnell T. P., "Theoretical Limits of Dimensional Stability for Space Structures", *SPIE Proceedings,* Vol. 1533, 1991.

[24] Domber J. L., Hinkle J. D., Peterson L. D., "Experiment to Quantify Material Microyield", *AIAA-2003-1539*, 2003.

[25] Bates S. J., Bacon D. J., "Microyielding in Alpha Titanium", *Journal of Materials Science,* Vol 15, 1980.

[26] Trigo J., "Dimensional Stability Characterisation of Carbon Fibre with Epoxy and Cyanate Ester Resins Laminates Due to Moisture Absorption", *ESA-SP-386*, p. 371, 1996.

[27] Maringer R. E., Cho M. M., Holden F. C., "Stability of Structural Materials for Spacecraft Application: Final Report", *NASA-CR-97844*, 1968.

[28] Domber J. L., Peterson L. D., "Implications of Material Microyield for Gossamer Optical Reflectors", *43rd Structures, Structural Dynamics and Materials Conference, Denver, Co.,* 2002.

[29] "Plasticity", *ANSYS Advanced Structural Nonlinearities Course Notes*.

[30] Chaboche J-L., "On Some Modifications of Kinematic Hardening to Improve the Description of Ratchetting Effects", *International Journal of Plasticity*, Vol.7, pp. 661-678, 1991

[31] Jacobs S. F., "Dimensional Stability of Materials Useful in Optical Engineering", *Applied Optics and Optical Engineering X,* 1987.

[32] Marschall C. W., "Microyield and Microcreep of Invar", *The Invar Effect: A Centennial Symposium, ed. J. Wittenauer,* The Minerals, Metals and Materials Society, 1997.

[33] Wittenauer J., Yaney D. L., Lewis R. E., "Microyielding in Fe-36Ni: Role of Carbon and Thermal Processing", *Scripta Metallurgica et Materialia,* Vol. 31, No. 11, 1994.

[34] "36% Nickel-Iron Alloy", datasheet from *The International Nickel Company Inc*.

[35] Stumm J. E., Pynchon G. E., Krumweide G. C., "Graphite/Epoxy Material Characteristics and Design Techniques for Airborne Instrument Application", *SPIE Milestone Series*, Vol. 770,1981.

[36] Ozores E., Arevalo F., Ayuso A., Bonet A., Lareo S., Pradier A., "Development Tests for a High Stability Optical Bench", *ESA-SP-336,* 1992

[37] Ponslet E., Smith R., "Structural Engineering for the SNAP Telescope: Status Report", http://snap.lbl.gov/pubdocs/Hytec_11_3a.pdf.

[38] Lamard J-L., Gaudin-Delrieu C., Valentini D., Renard C., Tournier T., Laherrere J-M., "Design of the High resolution Optical Instrument for the Pleiades HR Earth Observation Satellites", *ESA-SP-554,* 2004.

[39] "IMI Titanium 318", datasheet from *Imperial Metal Industries Ltd.*

[40] Vukobratovich D., "Rugged Yet Lightweight: How Can We Achieve Both in Optical Instruments?", *SPIE Proceedings*, CR-43, 1992.

[41] Dudarev E. F., Kashin O. A., Kolobov Y. R., Pochivalova G. P., Ivanov K. V., Valiev R. Z., "Microplastic Deformation of Polycrystalline and Submicrocrystalline Titanium During Static and Cyclic Loading", *Russian Physics Journal*, Vol. 41, No. 12, 1998.

[42] Imam M. A., Gilmore C. M., "Room Temperature Creep of T1-6Al-4V", *Metallurgical Transactions A,* Vol. 10A, 1979.

[43] Yoder P. R., "Design and Mounting of Prisms and Small Mirrors in Optical Instruments", *Tutorial Texts in Optical Engineering TT32,* SPIE Opt. Eng. Press, 1998.

[44] Sun C. T., "Strength Analysis of Unidirectional Composites and Laminates", *Comprehensive Composite Materials*, Ch. 1.20, Elsevier, 2000.

[45] "Structural Materials Handbook Volume 1: Polymer Composites", *ESA-PSS-03-203,* 1995.

[46] Kaiser C., Weihs H., Zuknik K-H., Obst A., "Failure Criteria for FRP and CMC: Theory, Experiment and Guidelines", *ESA-SP-581,* 2005.

[47] Bathias C., "An Engineering Point of View About Fatigue of Polymer Matrix Composite Materials", *International Journal of Fatigue,* Vol. 28, 2006.

[48] DeLacey T. J., Dharan C. K. H., "Characterisation of Stability Mechanisms in Advanced Composites", *Proc. 8th Airforce/DARPA Symposium on Quantitative Nondestructive Testing, Boulder Co.,* 1982.

[49] Favre J-P., Raud C., "Acoustic Emission to Monitor Crack Accumulation in Cross-Ply CFRP In Conditions of Mechanical Loading or thermal Cycling", *5th International Symposium on Acoustic Emission From Composite Materials, Columbus,* 1995.

[50] Wolff E. G., "Dimensional Stability of CFRP Tubes", *29th National SAMPE Symposium,* 1984.

[51] Kim R. Y., Crasto A. S., Schoeppner G. A., "Dimensional Stability of Composite in a Space Thermal Environment", *Composites Science and Technology*, Vol. 60, p.2601, 2000.

[52] Wolff E. G., "Moisture and Viscoelastic Effects on the Dimensional Stability of Composites", *SPIE Proceedings*, Vol. 1335, 1990.

[53] Nairn J. A., "Matrix Microcracking in Composites", *Comprehensive Composite Materials*, Ch. 2.12, Elsevier, 2000.

[54] McMahan L. L., "Space Telescope Optical Telescope Assembly Structural Materials Characterisation", *AIAA - Technology For Space Physics: The Next 30 Years, Danbury, Ct.,* 1982.

[55] "Guidelines For Threaded Fasteners", *ESA-PSS-03-208,* 1989.

[56] Al-Hunti N. S., "Computation of Member Stiffness in Bolted Connections Using the Finite Element Analysis", *Mechanics Based Design of Structures and Machines*, Vol. 33, 2005.

[57] Manring N. D., "Sensitivity Analysis of the Conical-Shaped Equivalent Model of a Bolted Joint", *ASME Journal of Mechanical Design,* Vol. 125, 2003.

[58] Marshall M. B., Lewis R., Dwyer-Joyce R. S., "Characteristics of Contact Pressure Distribution in Bolted Joints", *Strain*, Vol. 42, 2006.

[59] Groper M., "Microslip and Macroslip in Bolted Joints", *Experimental Mechanics*, Vol. 25, Pt. 2, 1985.

[60] Pratt J. D., Pardoen G., "Numerical Modelling of Bolted Lap Joint Behaviour", *Journal of Aerospace Engineering*, Jan 2002.

[61] Ferrero J. F., Yettou E., Barrau J. J., Rivallant S., "Analysis of a Dry Friction Problem Under Small Displacements: Application to a Bolted Joint", *Wear,* Vol. 256, 2004.

[62] Ferrero J. F., Barrau J. J., "Study of Dry Friction Under Small Displacements and Near-Zero Sliding Velocity", *Wear,* Vol. 209, 1997.

[63] Reid J. D., Hiser N. R., "Detailed Modelling of Bolted Joints With Slippage", *Finite Elements and Design,* Vol. 41, 2005.

[64] Panait A., He Q-C., Bary B., Cossavella M., Morcant K., "A Coupled Experimental and Numerical Approach to the Integrity of Friction Grip Connections in Glass Structures", *Engineering Failure Analysis*, Vol. 14, 2007.

[65] Benabdallah H. S., "Static Friction Coefficient of some Plastics Against Steel and Aluminium Under Different Contact Conditions", *Tribology International,* Vol. 40, 2007.

[66] Karamis M. B., Selcuk B., "Analysis of the Friction Behaviour of Bolted Joints", *Wear,* Vol. 166, 1993.

[67] Baylis R. J., "Slip Coefficients for Shear Joints", Advanced Structural Materials Workshop, *ESA-WPP-004,* 1988.

[68] Baylis R. J., "Slip Coefficients for Shear Joints: The Effects of Dynamic Loading and Surface Treatment", *ESA-SP-303*, 1990.

[69] Starikov R., "Fatigue Behaviour of Mechanically Fastened Aluminium Joints Tested in Spectrum Loading", *International Journal of Fatigue,* Vol. 26, 2004.

[70] Light D. J., "Vibration Loosening of Threaded Fasteners", *Chartered Mechanical Engineer*, May 1983.

[71] Smallwood D. O., Gregory D. L., Coleman R. G., "Damping Investigations of a Simplified Frictional Shear Joint", *71st Shock and Vibration Symposium*, 2000.

[72] Barber J. R., Ciavarella M., "Contact Mechanics", *International Journal of Solids and Structures*, Vol. 37, 2000.

[73] Gorbatikh L., Popova M., "Modelling of a Locking Mechanism Between Two Rough Surfaces Under Cyclic Loading", *International Journal of Mechanical Sciences,* Vol. 48, 2006.

[74] Segalman D. J., "An Initial Overview of Iwan Modelling for Mechanical Joints", Sandia Report, *SAND2001-0811*, 2001.

[75] Chen W. and Deng X., "Structural Damping Caused by Micro-slip Along Frictional Interfaces", *International Journal of mechanical Sciences*, Vol. 47, p. 1191, 2005.

[76] Segalman D. J., "Modelling Joint Friction in Structural Dynamics", *Structural Control and Health Monitoring*, Vol. 13, 2006.

[77] Song Y., McFarland D. M., Bergman L. A., Vakakis A. F., "Modelling, Identification and Simulation of Structures with Joints and Interfaces", web-article, http://3icee.njut.edu.cn/download/paper/ch3/ch3_48.pdf.

[78] Heald J. C., "Deployment Repeatability in Mechanically Jointed Precision Structures", Doctoral Dissertation, *University of Colorado, Boulder*, 2003.

[79] Lobitz D. W., Gregory D. L., Smallwood D. O., "Comparison of Finite Element Predictions to Measurements from the Sandia Microslip Experiment", *International Modal Analysis,* 4359 Vol. 2, 2001.

[80] Ouyang H., Oldfield M. J., Mottershead J. E., "Experimental and Theoretical Studies of a Bolted Joint Excited by a Torsional Dynamic Load", *International Journal of Mechanical Sciences,* 2006.

[81] Gaul L., Lenz J., "Nonlinear Dynamics of Structures Assembled by Bolted Joints", *Acta Mechanica,* Vol. 125, 1997.

[82] Wentzel H., "Modelling of Frictional joints in Dynamically Loaded Structures – a Review", http://www.hallf.kth.se/forskning/publikationer/rapport_419.pdf.

[83] Oldfield M., Ouyang H., Mottershead J. E., "Simplified Models of Bolted Joints Under Harmonic Loading", *Computers and Structures,* Vol. 84, 2005.

[84] Block J., Brander T., Lambert M., Lyytinen J., Marjoniemi K., Schutze R., Syvanen L., "Carbon Fibre Tube Inserts – a Light Fastening Concept With High Load Carrying Capacity", *ESA-SP-581*, 2005.

[85] Cabeza I., Pradier A., “Dimensional Stability Verification of an Optical Bench for Space Applications Under Thermal-Vacuum Environment”, *ESA-SP-386*, p. 353, 1996.

[86] LTM123 (Cyanate Ester) datasheet, *Advanced Composites Group Ltd*.

[87] Dawson R., Moffat D. G., “Vibratory Stress Relief: A Fundamental Study of its Effectiveness”, *Journal of Engineering Materials and Technology*, Vol. 102, 1980.

[88] Peterson L. D., Hinkle J. D., “Microdynamic Design Requirements for Large Space Structures”, *AIAA-2003-1451*, 2003.

[89] Hammerschlag R. H., “Friction and Stick-Slip in a Telescope construction”, *Wear*, Vol. 113, 1986.

[90] Romeo R. C., Martin R. N., “Progress in 1m-Class Lightweight CFRP Composite Mirrors for the ULTRA Telescope”, *SPIE Proceedings,* Vol. 6273, 2006.

[91] Thompson S. J., Doel A. P., Whalley M. S., Edeson R. L., Tosh I., Poyntz-Wright O., Atad-Ettedgui E., Montgomery D., Nawasra J., "Large Aperture Telescope Technology: A Design for an Active Lightweight Multi-Segmented Fold-Out Space Mirror", *International Conference on Space Optics*, Rhodes, Greece, 4-8 October 2010.

[92] Iraninejad B., Lubliner J., Mast T., Nelson J., “Mirror Deformations Due to Thermal Expansion of Inserts Bonded to Glass”, *SPIE Proceedings*, Vol. 748, 1987.

[93] Heetderks, “Notes on Telescope Design”, SNAP Project Technical Note, snap.lbl.gov/pub/bscw.cgi/S4753b1bc/d104085/SNAP-TECH-04021.doc

[94] Lord J. D., “Measuring the Dimensional Stability of Composites”, *NPL Measurement Note,* CMMT (MN) 014, 1997.

[95] Blair C., Zakrzewski J., “Moisture Absorption and Mechanical Properties for High-Modulus Pitch 75 Graphite-Fibre Modified Cyanate Ester Resin Laminates”, *SPIE Proceedings,* Vol. 1690, 1992.

[96] James J. D., Spittle J. A., Brown S. G. R., Evans R. W., "A Review of Measurement Techniques for the Thermal Expansion Coefficient of Metals and Alloys at Elevated Temperatures", *Measurement Science and Technology,* Vol. 12, 2001.

[97] Giaretto V., Miraldi E., Ruscica G., Cabiati F., Dosio D., "The Dimensional Stability of a CFRP Structure Probed with Sub-Millimetre Accuracy in Varying External Conditions", *ESA-SP-386*, p. 345, 1996.

[98] Roose S, Stockman Y., Rochus P., Kuhn T., Lang M., Baier H., Langlois S., Casarosa G., Optical methods for non contact measurements of membranes, *International Astronautical Congress IAC-07-C2.2.1* September 2007

[99] "Space Engineering – Testing", *ECSS-E-10-03A,* ESA Publications Division, 2002.

[100] UguenG., Luquet P., Chassat F., "Design and Development of the 2m Resolution Camera for Rocsat-2", *ESA-SP-554,* 2004.

[101] Wolff E. G., "Thermal Expansion of Asymmetrical Laminates", *Thermal Conductivity*, 1997.

[102] Di Carlo A., Usinger R., "Development of a Dimensionally Stable CFRP Structure for supporting Optical Instruments in a Laser Communication Device", *Proceedings of the 1st CEAS; 10th European Conference on Spacecraft Structures, Materials and Mechanical Testing*, Berlin, 10-13 Sept 2007.

[103] Bailley, B., Cornu, J. L., Capdepuy, B., Leleu, F., Kornmann, M., Pradier, A., "Dimensionally Stable Structures", *ESA-SP-386,* p. 361, 1996.

[104] Cloud G., "Moiré Interferometry for Measurement of Strain Near Mechanical Fasteners in Composites", *Handbook of Moiré Measurement, Institute of Physics*, 2004.

[105] "Modelling Material Nonlinearities", *ANSYS User Guide*, Sect. 8.4.

[106] "Dynamics Testing and Analysis", Proceedings from the *NAFEMS Awareness Workshop*, Tuesday 18th September 2007, Bristol.

[107] Segalman D., Reese G., Field R. Jr., Fulcher C., “Estimating the Probability Distribution of von Mises Stress for Structures Undergoing Random Excitation”, *Transactions of the ASME,* Vol. 122 pp. 42 – 48, 2000.

[108] Gupta S., Manohar C. S., “Probability Distribution of Extremes of von Mises Stress in Randomly Vibrating Structures”, *Journal of Vibration and Acoustics,* Vol. 127 pp. 547 - 555, 2005.

[109] “2200 Signal Conditioning System Instruction Manual”, *Vishay Micro-Measurements*, PO Box 27777, Raleigh, North Carolina, March 2001.

[110] Adrien J., Maire E., Estevez R., Ehrstrom J. C., Warner T., "Influence of the Thermomechanical Treatment on the Microplastic Behaviour of a Wrought Al-Zn-Mg-Cu Alloy", *Acta Materialia* 52 pp. 1653 - 1661, 2004.

[111] Hertel W., Paul W., Wagner D., "Insert Design Handbook", *ESA Contract No 3442/77/NL/PP*, 1980.

[112] Steinberg D. S., "Vibration Analysis for Electronic Equipment", John Wiley & Sons Inc., 2000.

[113] De la Fuente, "Von Mises Stresses in Random Vibration of Linear Structures", *Computers and Structures*, Vol 87, Iss 21-22, 2009.

[114] Nicholas T., "Dynamic Tensile Testing of Structural Materials Using a Split Hopkinson Bar Apparatus", *Wright-Patterson Aeronautical Laboratories Report AFWAL-TR-80-4053*, 1980.

[115] Sheldon I.,"Chaboche Nonlinear Kinematic Hardening Model", *ANSYS Memo STI0805A*; http://ansys.net/tips_sheldon/STI0805_Chaboche.pdf, 2008.

[116] Francois M. L. M., "A Pasticity Model with Yield Surface Distortion for Non Proportional Loading", *International Journal of Plasticity*, Vol. 17, No. 5, pp. 703 - 718, 2001.

[117] http://en.wikipedia.org/wiki/TacSat-2#Camera_.2F_Telescope

[118] Segert T., Danziger B., Gork D., Leider M., “Dobson Space Telescope – Development of an Optical Payload of the Next Generation”, *ESA-SP-621,* 2006.

[119] Bergstrom J. W., Delamere W. A., McEwen A., "MRO High Resolution Imaging Science Experiment (HIRISE): Instrument Test, Calibration and Operating

Constraints", *International Astronautical Congress IAC-04-Q.3.b02*, Vancouver, 2004.

[120] Gallagher D., Bergstrom J., Day J., Martin B., Reed T., Spuhler P., Streetman S., Tommeraasen M., "Overview of the Optical Design and Performance of the High Resolution Science Imaging Experiment (HIRISE), *SPIE Proceedings* Vol 5874, 2005.

[121] Viard T., Bodin P., Magnan A., "Corot telescope Development", *ESA-SP-554*, 2004.

[122] "ESA ESTEC Expertise and Facilities Assist COROT Project", http://www.esa.int/SPECIALS/COROT/SEMSZEANMUE_0.html

[123] Miers T. H., Munro R. H., "Ball Global Imaging System for Earth Remote Sensing", *SPIE Proceedings,* Vol. 4169, 2001.

[124] Figoski J. W., "The Quickbird Telescope: The Reality of Large, High-Quality Commercial Space Optics", *SPIE Proceedings,* Vol. 3779, 1999.

[125] Figoski J. W., "Alignment and Test Results of the Quickbird Telescope Using the Ball Optical Systems Test Facility", *SPIE Proceedings,* Vol. 3785, 1999.

[126] Lampton M. et. al., "SNAP Telescope", *SPIE Proceedings,* Vol. 4849, 2002.

[127] Cutter M., Lobb D., Purll D., Cawthorne A., Sweeting, Sir M., "The Trade-off Space of High Resolution Imagers on Small Satellites", *International Astronautical Congress, IAC-08-B4.6.A9*, Glasgow, 2008.

[128] Sacek V., http://www.telescope-optics.net/.

[129] Cook M. K., Peterson B. A., Dial G., Gibson L., Gerlach F., Hutchins K., Kudola R., Bowen H., "IKONOS Technical Performance Assessment", *SPIE Proceedings,* Vol. 4381, 2001.

[130] Latry C., Despringre V., Valorge C., "Automatic MTF Measurement Through a Least Square Method", *SPIE Proceedings*, Vol. 5570, 2004.

[131] Silverman E. M., Sathoff J. E., Forbes W. C., "Design of High Stiffness and Low CTE Thermoplastic Composite Spacecraft Structures", *SAMPE Journal,* Vol. 25, No. 5, 1989.

[132] Smith P. A., "Carbon Fibre Reinforced Plastics - Properties", *Comprehensive Composite Materials*, Ch. 2.04, Elsevier, 2000.

[133] Almen G. R., Mackenzie P. D., Malhotra V., Maskell R. K., "Fiberite 954: Cyanate Ester Systems", *SPIE Proceedings,* Vol. 1690, 1992.

[134] Brand R. A., Derby E. A., "Evaluation of High-Modulus Pitch/Cyanate Ester Material Systems for Dimensionally Stable Structures", *SPIE Proceedings,* Vol. 1690, 1992.

[135] Hyer M. W., Waas A. M., "Micromechanics of Linear Elastic Continuous Fibre Composites", *Comprehensive Composite Materials*, Ch. 1.12, Elsevier, 2000.

[136] Hyer M. W., "Laminated Plate and Shell Theory", *Comprehensive Composite Materials*, Ch. 1.17, Elsevier, 2000.

[137] Pagano N. J., Schoeppner G. A., Kim R., Abrams F. L., "Steady-State Cracking and Edge Effects in Thermo-Mechanical Transvers Cracking of Cross-Ply Laminates", *Composites Science and Technology,* Vol. 58, 1998

[138] Fielder B., Hojo M., Ochiai S., Schulte K., Ochi M., "Finite Element Modelling of Initial Matrix Failure In CFRP Under Static Transverse Tensile Load", *Composites Science and Technology,* Vol. 61, 2001.

[139] Deev I. S., Nikishin E. F., "Effect of Long-Term Exposure in the Space Environment on the Microstructure of Fibre Reinforced Polymers", *Composites Science and Technology*, Vol 57, 1997.

[140] Helwig G., "Highly Dimensionally Stable Composite Structures", *Proceedings of the International Workshop on Advanced Materials for High Precision Detectors, CERN 94-07,* 1994.

[141] Hobbiebrunken T., Fielder B., Hojo M., Ochiai S., Schulte K., "Microscopic Yielding of CF/Epoxy And the Effect on the Formation of Thermal Stresses", *Composites Science and Technology,* Vol. 65, 2005.

[142] Wolff E. G., Crane S. T., "Prediction of the Microyield Strength of Polymer Matrix Composites", *Journal of Composites Technology and Research,* Vol. 10, Pt. 4, 1988.

[143] Marchetti M., Morganti F., Tizzi S., "Evaluation of the Built-in Stresses and Residual Distortions on Cured Composites for Space Antenna Reflectors Applications", *Composite Structures,* Vol. 7, 1987

[144] Kim B. S., Bernet N., Sunderland P., Manson J. A., "Numerical Analysis of the Dimensional Stability of Thermoplastic Composites using a Thermoviscoelastic Approach", *Journal of Composite Materials,* Vol. 36, No. 20, 2002.

[145] Kim K. S., Hahn H. T., "Residual Stress Development During Processing of Graphite/Epoxy Composites", *Composites Science and Technology,* Vol. 36, 1989.

[146] Abusafeih A., Federico D., Connell S., Cohen E., Willis P. B., "Dimensional Stability of CFRP Composites for Space Based Reflectors", *SPIE Proceedings,* Vol. 4444, 2001.

[147] Sable W. W., "Probabilistic Model of the Thermal Dimensional Stability of Composite Structural Components", *SPIE Proceedings,* Vol. 1690, 1992.

[148] Keates T. F., Drucker S. C., "Report on the Study of the Dimensional Stability of Carbon Fibre Reinforced Plastic Skinned Honeycomb Cored Structures", *ESA CR(P) 1616*, Contract No. 4252/80/NL/AK, BAe Dynamics, 1982.

[149] Manders P. W., Maas D. R., "Thin Carbon Fibre prepregs for Dimensionally Critical Structures", *SPIE Proceedings,* Vol. 1303, 1990.

[150] Pottish N., "Designing for Dimensional Stability in Space", http://www.compositesworld.com/hpc/issues/2005/July/920/1, 2005.

[151] Brand R. A., "Strategies for Stable Composite Structural Design", *SPIE Proceedings,* Vol. 1752, 1992.

[152] Jurcevich B. K., Bruner M. E., "Use of Graphite Epoxy Composites in the Solar-A Soft X-Ray Telescope", *SPIE Proceedings,* Vol. 1303, 1990.

[153] Telkamp A. R., Derby E. A., "Design Considerations for Composite Materials Used in the Mars Observer Camera", *SPIE Proceedings,* Vol. 1303, 1990.

[154] Austin J. D., "Moisture Effects and Control for the UVCS Composite Structure", *SPIE Proceedings,* Vol. 1690, 1992.

[155] Berthold J. W., Jacobs S. F., Norton M. A., "Dimensional Stability of Fused Silica, Invar, and several Ultra-low Thermal Expansion Materials", *Metrologia,* Vol. 13, 1977.

[156] Middleton K., Caldwell M., Edeson R., Munro G., Killow C., Robertson D., Hough J., Ward H., Heinzel G., Braxmier C., Plate M., "The LISA Technology Package Engineering Model Interferometer: Construction and Alignment Techniques", *Photon 04* (Glasgow 2004).

[157] Wolff E. G., "Development and Testing of Zero CTE Materials", *Proceedings of the 8th International Symposium on thermal Expansion*, 1981.

[158] http://www.boostec.com/

[159] Devilliers C., Krodel M. R., "CESIC – A New Technology for Lightweight and Cost Effective Space Instrument Structures and Mirrors", *ESA-SP-581*, 2005.

[160] Yamamoto G., Sato Y., Takahashi T., Omori M., Hashida T., Okubo A., Tohji K., "Single-Walled Carbon Nanotube-Derived Novel Structural Material", *Journal of Materials Research,* Vol. 21, No. 6, 2006.

[161] Olcese M. et. al., "Ultra-Light and Stable Composite Structure to Support and Cool the ATLAS Pixel Detector Barrel Electronics Modules", *Nuclear Instruments and Methods in Physics Research,* 518, 2004.

[162] "Adhesive Bonding Handbook for Advanced Structural Materials", *ESA-PSS-03-210,* 1995.

[163] Chen W. T., Nelson C. W., "Thermal Stresses in Bonded Joints", *IBM J. Res. Develop.,* Vol. 23, No. 2, 1979.

[164] Michaels G., Genberg V. L., "Finite Element Modelling of Nearly Incompressible Bonds", *SPIE Proceedings,* 2002.

[165] Thompson T. C., Grastataro C., Smith B. G., "Recent Developments in Low Cost Stable Structures for Space", *International Workshop on Advanced Materials for High Precision Detectors,* 1994.

[166] Dean G., Crocker L., "The Use of Finite Element Methods for Design With Adhesives", NPL Measurement Good Practice Guide No. 48, 2001.

[167] Ohl R. G., Barkhouser R. H., Kennedy M. J., Friedman S. D., "Assembly and Test-Induced Distortions of the FUSE Mirrors – Lessons Learned", *SPIE Proceedings,* Vol. 3356, 1998.

[168] Daly J. G., Daly D. J., "Structural Adhesives for Bonding Optics to Metals: a Study of Optomechanical Stability", *SPIE Proceedings,* Vol. 4444, 2002.

[169] Patterson S. R., Badami V. G., Lawton K. M., Tajbakhsh H., "The Dimensional Stability of Lightly-Loaded Epoxy Joints", *Lawrence Livermore National Laboratory report,* https://e-reports-ext.llnl.gov/pdf/235105.pdf.